The Mysteries of the Surface First Part: The Characteristic Features of the Microgeometry of the Machined Surface

Béla Palásti-Kovács, Sándor Sipos, Szabolcs Bíró

Bánki Donát Faculty of Mechanical Engineering and Security Technology, Óbuda University, Népszínház u. 8, H-1081 Budapest, Hungary;
e-mail: palasti@uni-obuda.hu; sipos.sandor@bgk.uni-obuda.hu;
biro.szabolcs@bgk.uni-obuda.hu

Abstract: In these days, the key elements for the reliability and the safe operation of technical devices are the following: surface of the tools, the surface quality and the roughness of the connecting elements. The present work is going to introduce the idea that different machining methods that create microgeometries that are very much different from each other and of diverse roughness parameter proportions. It will be shown that the wear and the change of the tool edge(s) – resulting from the deterioration process of the tools, used during production – cause significant arithmetical, average and form deviations. The uncertainties of the roughness measuring technique, arising during the evaluation of the real and filtered surface profiles, will be shown via samples.

Keywords: machined surface; microgeometry; roughness; wear process

1 Introduction

Production, quality and operations — terms, being inseparable, depending on each other and mutually determinant of each other. Each specification and problem, arising during the production process of connecting components, may have a significant influence on the operation.

This research work has been oriented to examine surface microgeometry by a skidless stylus method, to the modernization and extension of the evaluation possibilities of the surface profiles and topographies, gained from measurements at Bánki Donát Faculty of Óbuda University, for more than three decades [1-4].

The research and development works started in 1975, with a surface roughness measuring device, type “Kalibr 201”; the first evaluation programs in FOKAL programming language run on TPA computers. The set of devices of the research work has now been significantly updated. We have workshop machines, works

manager "pocket" devices (Perthen, Taylor-Hobson), surface roughness measuring instruments to carry out quality works of higher level (Perthen, Mitutoyo); furthermore, to the execution of up-to-date examinations there is research equipment (type: Perthometer Concept): its outgoing digital signals can be directly processed by a computer. The education and research works are supported by the wide range of ancillaries and a whole assortment of styluses. Measurements, carried out on outer or inner arcs or on holes, having a diameter of 1.5 mm or measurements of edge roughness and edge rounding off, performed on cutting tools (Figure 1) are just few from the measuring applications yet to be mentioned.

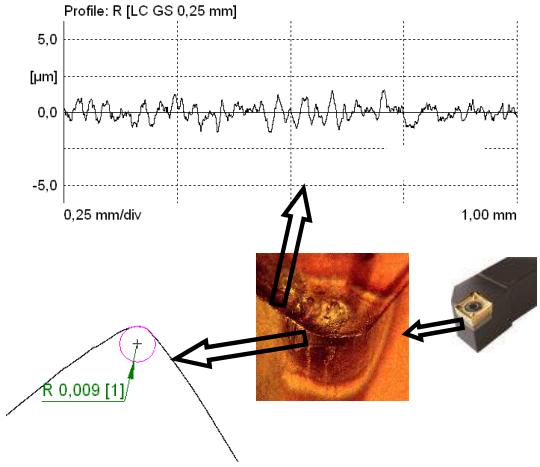

Figure 1
Edge roughness and rounding off in case of cutting insert

2 Roughness of Surfaces as Machined with Different Methods

In the 21st Century it is needed to have technical specialists to meet the quality requirements of the manufacturing technology industry, at a high level, to identify surface roughness, not only with roughness parameters Ra or Rz, but to identify the possibilities for improvement for the products using more sensitive quality characterizations on the connecting surfaces. Parallel with the dynamic development of the machining technology and surface finishing processes, the machines currently are characterized by new technical surfaces, being different in their character and quality and having been consciously planned and produced, when techniques that were well-proven earlier, are losing in their importance or they require more careful consideration. In industrial practice, the change in this way of thinking has evolved very slowly (Figure 2) [5].

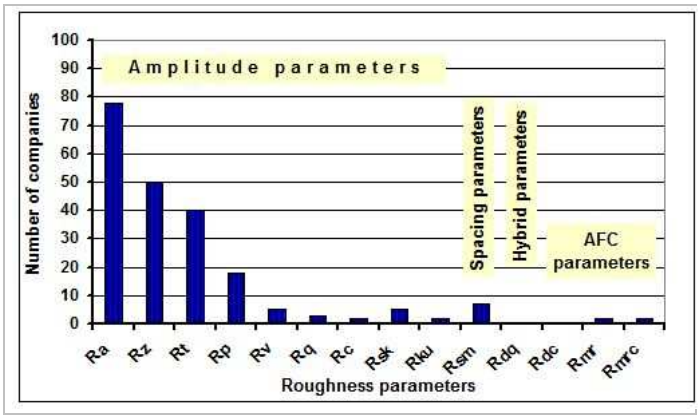

Figure 2

The roughness parameters, measured/applied in the industrial practice [5]

In the manufacturing technology of our globalized world, we can notice that the arithmetic parameters (Ra, Rz, Rt, Rp) are dominant and other attributes, describing the working behavior in a better way, are still pushed into the background. The drawings, prepared for components, usually contain only one parameter, therefore, the following questions arise: Can we reconvert one parameter into another with certainty? Is there a correlation, for example, between Ra and Rz that may be used for machining and described by a formula?

The formulas "Rz=4×Ra" or "Rz=4.5×Ra" have been used in professional training and in the practice of manufacturing technology for at least 6 or 7 decades. Occasionally, there are publications, revising and trying to modify this way of thinking [6, 7, 8], but until now, they were not able to achieve a real breakthrough in this question. If we analyze the roughness of surfaces, machined with different methods, the values, shown in Table 1, are gained. It can be seen that there are significant differences in the ratio of Rz/Ra as the measured values scatter in the range of 5.36 and 9.2.

Table 1

Roughness of surfaces, formed with different machining methods

Milled groove surface			Ground milling cutter shaft			Super finished shaft		
Ra	Rz	Rz/Ra	Ra	Rz	Rz/Ra	Ra	Rz	Rz/Ra
0.39	2.09	5.36	0.15	1.3	8.67	0.05	0.46	9.2
0.31	1.72	5.55	0.15	1.29	8.6	0.07	0.53	7.57
0.29	1.69	5.83	0.15	1.25	8.33	0.07	0.53	7.57

Having analyzed the values, it can be noticed that the tool edges, the cutting data, the machining system and its surroundings may 'produce' surfaces that have very different micro-geometric characteristics. The micro-geometric profiles of surfaces, have nearly the same average surface roughness Ra and are machined by

different processes such as milling, spark erosion machining, grinding and super finishing operations. These are shown in Figure 3. Every profile has well determined characteristics, and this means that there are surfaces with significantly different formal features with obviously different Rz/Ra ratios and they have different behavior during the operation as well.

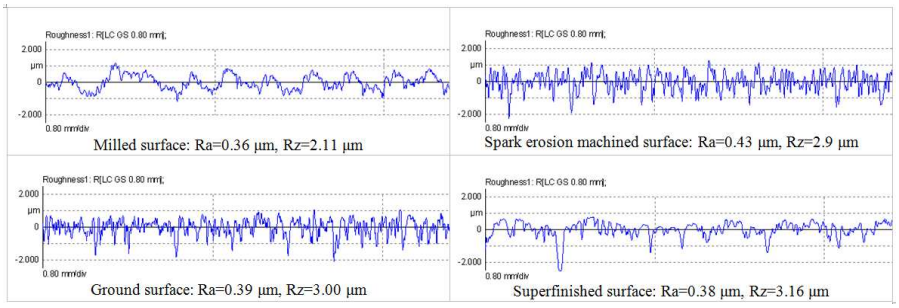

Figure 3

Surface roughness profiles in case of different machining methods

(Ra=0.36…0.43 µm; Rz/Ra=5.8…9.5)

Several cutting processes (turning, planing, drilling, peripheral milling, grinding, super finishing, spark-machining, etc.) were examined in order to discover the micro-geometric characteristics, the relationships among the roughness parameters of each machining method and to observe the variance of the features on the surfaces [9].

The measurements were carried out on a roughness measuring device, type Mahr-Perthometer and the values were evaluated by MarSurf XCR-20 software. On each workpiece, formed with the same machining operation, 25 standardized profile measurements were carried out on different places on the material. The roughness (R) and unfiltered (P) parameters of measurements, performed in the earlier described way, were evaluated; and the data, such as maximum and minimum values of the range, variance of the values, average values and range/minimum values and were collected in a form of a table. Only part of the test results are presented in this paper. The roughness parameters of a steel surface, machined with a coated carbide tool, are shown in Table 2.

Although the surface is supposed to have the same roughness parameters, from the measured data it can be seen that there are significant differences in the parameter values and their ratios, as well as, in different moments of the machining operation (it depends on the contact between the tool and the workpiece). According to the data, indicated in Table 2, the deviation is 27% in case of Ra, average roughness, being generally known and the most often used parameter on the machine drawing, 46% in case Rz (height of unevenness) and it is nearly 200% in the case of Rt parameter [10]. A significant variance was observed in case of skewness index number Rsk as well.

Table 2
Turning operation with sharp tool, v_c= 250 m/min; a=1.5 mm, f= 0.05 mm

Roughness	Max.	Min.	Range, R	Dispersion, s	Average	R/Min.
Filtered R-profile						
Ra	0.254	0.201	0.054	0.018	0.229	27%
Rz	1.983	1.358	0.625	0.150	1.577	46%
Rt	4.794	1.621	3.173	0.651	2.229	196%
RSm	65.458	31.730	33.728	8.337	42.299	106%
Rsk	4.412	-0.698	5.110	0.966	-0.089	
Rdq	0.091	0.059	0.032	0.008	0.077	54%
Unfiltered P-profile						
Pa	0.425	0.229	0.197	0.048	0.342	86%
Pz	2.697	2.024	0.672	0.191	2.353	33%
Pt	5.015	2.229	2.786	0.574	2.905	125%
PSm	197.729	45.856	151.873	42.587	109.784	331%
Psk	3.197	-0.271	3.468	0.652	0.211	
Pdq	0.091	0.058	0.033	0.008	0.077	57%

The component surfaces, having (fitting, moving away or frictional) connection with each other, are in touch with each other not along the filtered R-profile, but along the unfiltered P-profile. The evaluation is made even more difficult, if the parameters of P profile is examined as well and they are compared to the values of the filtered profile. The deviations are significantly greater, compared to the R profile: for example, in case of Pa parameter it is 86%, while the difference between the Pt parameters is greater than 100%. It can be seen as well that the change in the increase of the arithmetical parameters of the P profile is significantly greater, compared to the R profile, as it is nearly 50% (in case of Pa and Pz). Parallel with roughness parameters, the earlier described changes are extremely well demonstrated by the surface profiles, taken in the same magnification (Figure 4).

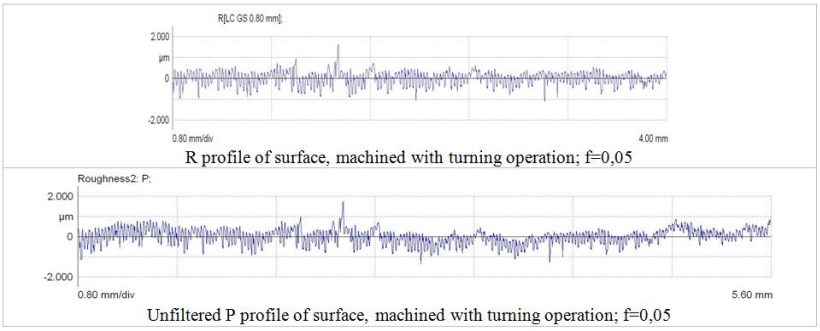

Figure 4
R and P surface profiles during turning operation in case of new and worn out tool

The same can be observed in case of machining operations carried out with an irregular edge geometry, or with grains, having a geometrically nondescribable shape, i.e. in the case of grinding. For this machining type, a typical stochastic surface structure develops (see Figure 5), being significantly different from the periodicity of the surface development, arising during machining with tools of regular edge geometry (turning, milling operation etc.). The surface, machined with grinding operations contains numerous cutting scratches of irregular shape and different depth size and results in a great diversity of surface profiles.

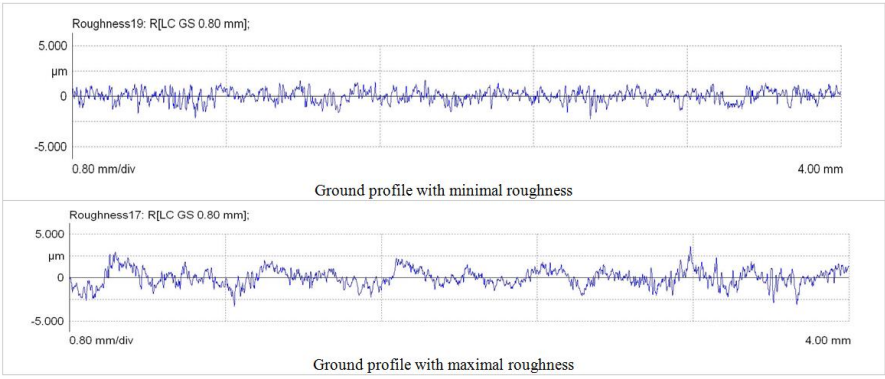

Figure 5

Minimal and maximal roughness values of R profile of surfaces, gained with grinding operation

As it can be seen well in Table 3, there is a variance of 63% in the average roughness value Ra and height of unevenness Rz, while in case of Rmax and Rt values the difference is 70-80%. The negative value of Rsk refers to a good load bearing capacity of the surface. The coefficient of formula, used in practice to convert the values Rz and Ra, has an increasing tendency in this type of machining and it achieves a value of Rz≈7Ra on average.

Table 3

Parameters of steel surface, machined with grinding operations, cooling and spark-out; v_c= 50 m/s

Roughness	Maximum	Minimum	Range, R	Dispersion, s	Average	R/min.
R profile						
Ra	0.76	0.47	0.29	0.077	0.574	63%
Rz	5.14	3.16	1.98	0.469	3.994	63%
Rt	6.90	3.77	3.13	0.804	5.030	83%
RSm	106.00	41.95	64.05	15.693	61.694	153%
Rsk	0.02	-0.63	0.65	0.173	-0.335	
Rdq	0.20	0.17	0.04	0.011	0.181	123%
P profile						
Pa	1.15	0.55	0.59	0.166	0.762	107%
Pz	7.91	4.08	3.83	1.007	5.415	94%

Pt	9.08	4.26	4.83	1.170	6.246	113%
PSm	216.20	54.61	161.59	49.746	110.257	296%
Psk	-0.04	-0.84	0.80	0.203	-0.337	
Pdq	0.21	0.17	0.04	0.010	0.181	124%

The variance between the maximal and minimal values of unfiltered P-parameters, indicated in Table 3 is above 100%. The parameter values of Pa, Pt and Pdq oscillate in the range of 105-125% and they can cause serious work in production in order to keep the prescribed surface roughness values in the prescibed range [11].

3 The Change in the Characteristics of a Turned Surface during Machining

When analyzing a turned surface, at an appropriate magnification, the geometric marks developed during machining can be observed. These are peaks, tool marks, outstanding peaks (built-up edges) and cavities (extracts), their sizes, shapes and distance from each other are quite different (Figure 6). The micro-geometric shape, developed on the surface, is determined by the kinematics of the machining process, the direct and indirect effects of the chip detachment, the geometric features of tool and by the physical-mechanical characteristics of the workpiece, to be machined. To these elements amounts the effect of further several important factors, such as cutting speed, the condition of the cutting edge of tool, the presence of cooling and lubricating, the dynamic behavior of machine - device - workpiece - tool system, the features of the surroundings and process, they mainly determine the irregularity of the part microgeometry, to be developed on the surface, and the waviness. Significant differences may be caused by the change of these factors in the surface microgeometry during the machining process [1, 7, 9, 11, 12]. In the case of serial production it means a serious challenge to continuously maintain the prescribed surface roughness measures.

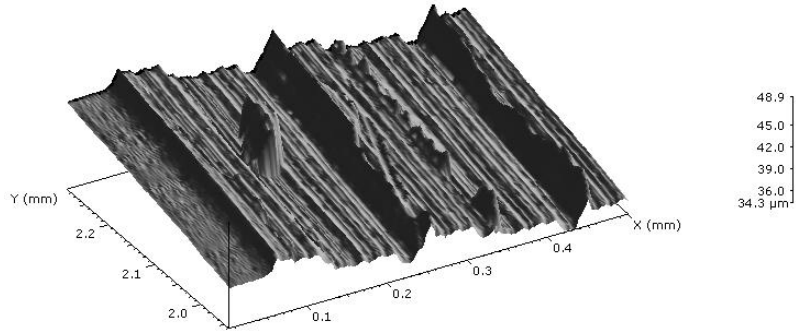

Figure 6

The micro-geometric features of surface, machined with turning operation

As it can be seen, from the above-mentioned examples, the connection between microgeometry, developed on the surface and the machining operation is quite versatile and complicated. The effect of some factors are described by theoretical formulas, these are Bauer-formula (1) and Brammertz-formula (2):

$$Rz \approx R_e = 125 \cdot \frac{f^2}{r_\varepsilon} \quad [\mu m] \qquad (1),$$

and

$$Rz \approx R_{eBr} = 125 \cdot \frac{f^2}{r_\varepsilon} + h_{min} \cdot \left(0.5 + \frac{r_\varepsilon \cdot h_{\min}}{2000 \cdot f^2} \right) \quad [\mu m] \qquad (2),$$

Whereas:

- f Applied feed, mm
- r_ε Nose radius of the tool, mm
- h_{min} Minimum detachable chip thickness, i.e. h_{min} = f (v_c, r_n, etc.) = 3-8 µm
- r_n Rounding off radius of the tool edge (on average approx. 25 µm)

Although formulas (1) and (2) do not include several factors, their application is widespread in technology planning practice, for example, when determining the feed limits.

There is a great uncertainty in the common effect of all influencing factors and among them, the temporal change may have a significant role as well. Based on publications [13-15], prepared on turning examinations, the general conclusion can be drawn that a cutting operation, lasting for 15-20 minutes, results in an increase of Ra value by 1 µm. Only the trend and size of the change may be predicted by this information, and the changes in the micro-geometric shape on the surface, developing as a result of the tool deterioration process, may not be seen. The research carried out in this topic, focused on the analysis connected with the generally considered trend and on the on deeper changes that develop during the deterioration process.

Several cutting tests were carried out on C50 (constructional) and Ko36 (corrosion-resistant) steel, using CNMG120408 type, PVD-coated cutting inserts and applying the same machining data (a=1.5 mm; f= 0.2 mm). In order to determine the deterioration behavior of the tool, not only the wear and force values were measured (depicted on the time, spent in machining), but Ra and Rz surface roughness values as well. Parallel with the temporal increases of the wear values and in certain cases, serious changes were observed in the roughness parameters, while a general increasing tendency was registered in the majority of cases (Figure 7).

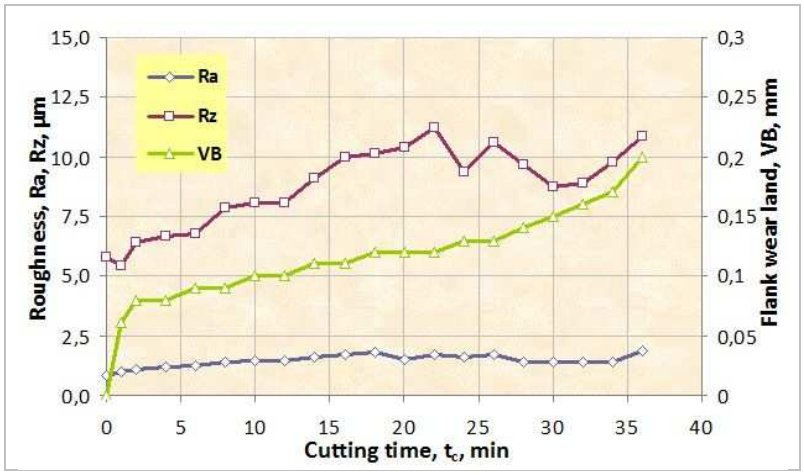

Figure 7
The connection between flank wear-land and roughness in case of turning operation in C50 steel (v_c=315 m/min; coating: nACoX3)

In case of turning operation with another PVD-coated tool, change in surface roughness, resulting from the wear process, was 100%, the degree of irregularity scattered in the range of 25-30%. As a result of it, there was obviously an oscillation in the ratio of Rz/Ra in the range of 5.3-7.2 (Figure 8).

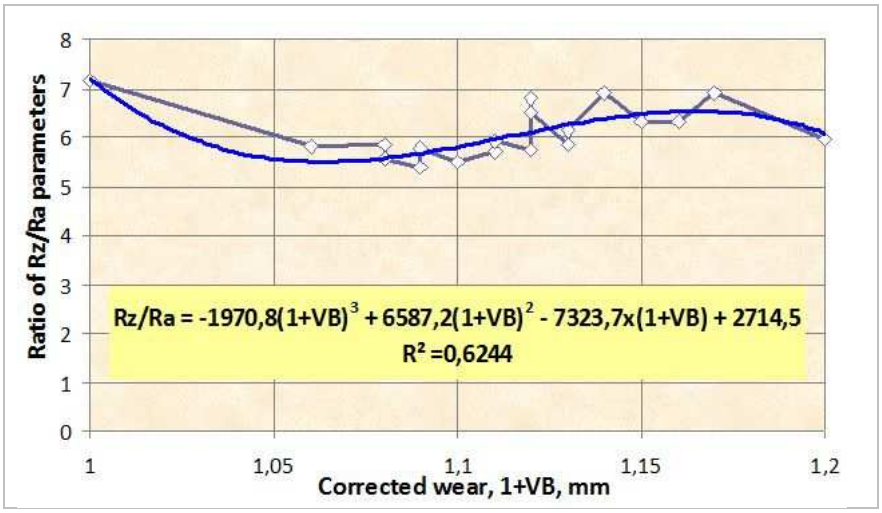

Figure 8
The connection between roughness and corrected wear in case of turning operation in C50 steel (v_c=315 m/min; coating: nACo3)

The same changes in the surface roughness were observed during the turning operation in the Ko36 material, tested in the second phase, but they occurred much faster than expected, due to the greater abrasive effect and adhering character effect of the corrosion-resistant material.

Based on our experiences, it can be noticed that the diversity of the surface shapes is the consequence of the wear changes, developing on the flank wear-land area of the tool, when the sectional profile of the wear mark on the flank wear-land area, changing continuously and being determining, is "copied" onto the surface of the workpiece (Figure 9).

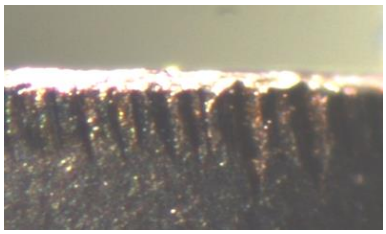

C50 steel; v_c= 315 m/min; t_c=22 min

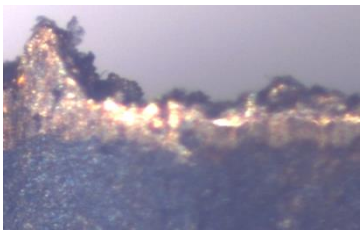

Ko36 steel; v_c=160 m/min; t_c=10 min

Figure 9
Photo about flank-land wear, taken by stereomicroscope (magnification: 45x)

4 Connection between the Tool Edge and the Machined Surface

An extra research series was carried out in material qualities, mentioned earlier, in order to examine the micro-geometric connection between the tool edge and the surface machined by it, in a deeper way. The dry turning operation was performed with DNMG150608R-K GC4025 (made by Sandvik) insert, the depth of cut was 1 mm, the applied cutting speed values were in case of constructional steel v_c=300 m/min and 160 m/min in case of more difficult to machine corrosion-resistant steel, respectively. A feed value of f=0.1 was determined by us as in order to better observe the change in the wear marks on the micro-geometric profile diagrams. Every minute, stereomicroscopic pictures were taken of the flank wear-land of the tool edge section, forming the surface microgeometry. At the same time, filtered (R profile) and unfiltered (P profile) profiles, together with the surface profile pictures were registered by MarSurf XCR-20 evaluation software on Mahr-Perthen surface roughness measuring instrument (in every minute). After having finished the tests, the surface forming insert and cutting tool were examined in details: 3D optical microscopic and electron microscopic pictures were taken, additionally, topographic measurements were performed with the help of surface roughness measuring instrument.

In Figure 10, the values of Ra and Rz parameters are shown as a function of the cutting time (t_c) in the case of tests, carried out in C50 material. In regards to the Rz parameter, the degree of differences, resulting from the tool wear, is more than 3X. It is typical for the change that it has a slightly increasing (cca. 0.3 µm/min) tendency in the first 20 minutes. During this period of time, the regular edge shape disappears and a typical transcriptional mechanisms develops [1]; after that a definite decrease can be observed (parallel with further deterioration of the edge shape, the formation of a "ironing" edge section can be observed). The temporal changes can be described by a three-degree polynomial, drawn on the change of the values, with adequate accuracy. Although the coefficient of determination (R^2) values scattered in a range between 0.65 and 0.75, the correlation (R) had a value above 0.8. In technical practice, the variance of wear processes of cutting operations can be properly characterized by this last-mentioned value.

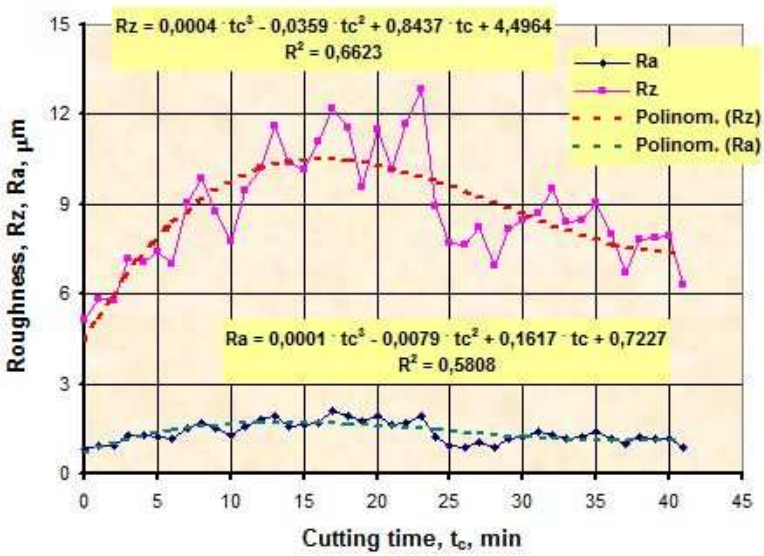

Figure 10

The development of Ra and Rz value in function of cutting time in case of turning operation in C50 steel (v_c=300 m/min; coating: CVD, type 4025)

The development of surface microgeometry is well demonstrated by the roughness profile diagrams, shown on Figure 11; on these the interactions between the edge shape and the machined surface, described earlier, can be well seen.

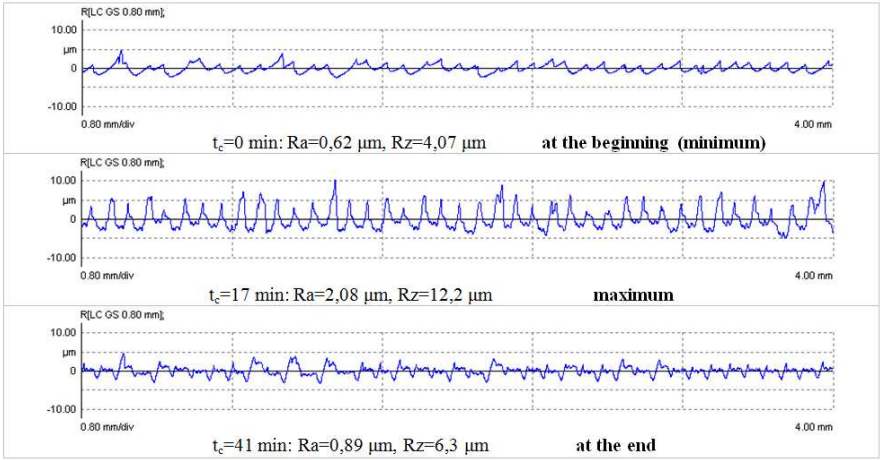

Figure 11

The development of roughness profile diagrams in function of cutting time in case of turning operation in C50 steel

In Table 4 the development of the main surface micro-geometric parameters, observed during the time of examination, is summarized. A greater value than 100% was achieved in differences among the measured minimum and maximum values in case of Ra average roughness, Rz height of unevenness, Rt maximum unevenness and Rdq mean square of average profile slopes. The greatest change was observed in the values of Rsk: the strong transformation of microgeometry, resulting from the tool wear, is demonstrated the best by it. The unfiltered parameters of the R profile were exceeded by the similar values of the P profile, the degree of differences is similar as earlier described.

Table 4

Surface, machined with turning operation, material: C50; v_c=300 m/min; a=1 mm; f=0.1 mm; r_ε =0.8 mm

Roughness	maximum	minimum	Range, R	Dispersion, s	Average	R/min
R profile						
Ra	2.08	0.83	1.25	0.35	1.36	151%
Rz	12.2	5.13	7.07	1.84	8.76	138%
Rt	16.8	7.12	9.68	3.25	10.71	136%
RSm	149.3	98	51.3	11.27	112.70	52%
Rsk	1.09	-0.13	1.22	0.35	0.64	-938%
Rdq	0.279	0.106	0.173	0.04	0.20	163%
P profile						
Pa	2.3	0.91	1.39	0.37	1.46	153%
Pz	15.2	6.68	8.52	2.32	10.31	128%
Pt	23.8	7.41	16.39	4.05	12.65	221%

PSm	216.5	101.7	114.8	20.76	121.86	113%
Psk	1.97	-0.07	2.04	0.49	0.74	-2914%
Pdq	0.28	0.115	0.165	0.04	0.20	143%

In Figure 12, the values of the Ra, Rz parameters, as a function of cutting time, are shown from tests carried out with corrosion-resistant steel. The character and the generating reasons of the change are the same, the wear process takes place in a much more intensive way in case of more difficult to machine and inclined to burr formation steel assortments. In the first 6 minutes of machining, the surface roughness has an increasing tendency (approx. 1 µm/min), after that a definitive decrease can be observed. The differences, resulting from the tool wear, achieved treble value in case of Rz parameter treble value of differences. The temporal changes (especially in case of average roughness values) were described by a three-degree polynomial, drawn on the change of the values, with adequate accuracy.

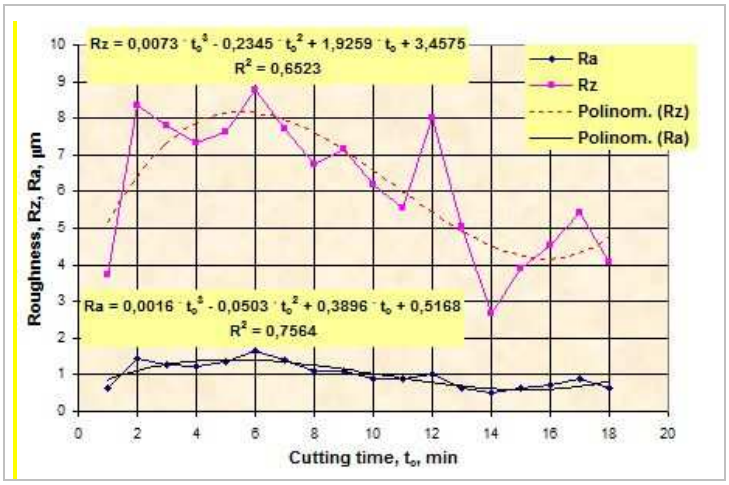

Figure 12

The development of Ra and Rz values in function of cutting time in case of turning operation in Ko36 steel (v_c=160 m/min; coating: CVD, type 4025)

In the roughness profile diagrams of Figure 13, presenting the changes in the surface microgeometry, the phenomena, described earlier in connection with Figure 11, can be recognized. As a result of "wandering" of the momentary cutting edge, the arithmetic parameters of surface roughness may achieve lower values, than those gained with a sharp tool.

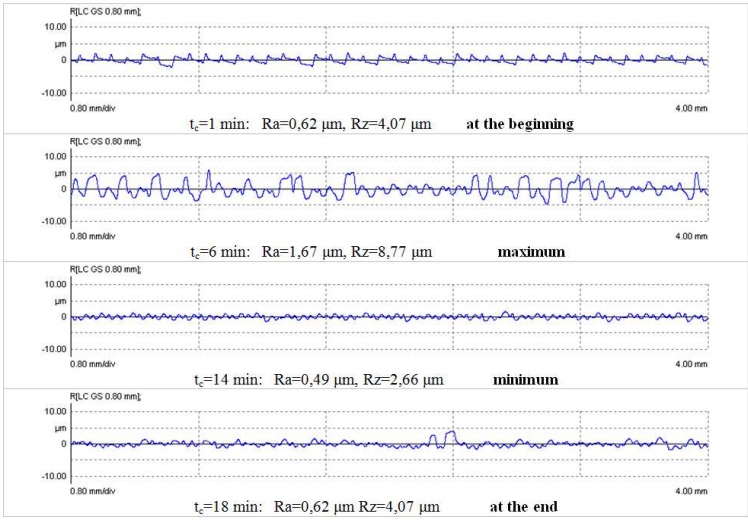

Figure 13

The development of roughness profile diagrams in function of cutting time in case of turning operation in Ko36 steel

The change in the parameters that occurred during the examination time is shown in Table 5, for the case of a turned surface. Analyzing the data, it is clear that the change, resulting from the tool wear, is greater than 200% – due to the bad machinability features of the corrosion-resistant material – in case of Ra average roughness, Rz height of unevenness and Rt maximal unevenness; while in case of Rdq values, the change is greater than 100%. In regard to the Rsk values, the change is greater: the drastic transformation of microgeometry, resulting from the tool deterioration, is confirmed. The parameter values of R profile is obviously exceeded by the P profile parameter values, but the degree of change is smaller (lower than 200%).

Table 5

Surface, machined with turning operation, material: Ko36; v_c= 160 m/min; a=1 mm; f=0.1 mm; r_ε =0.8 mm

Roughness	maximum	minimum	Range, R	Dispersion, s	Average	R/min
R profile						
Ra	1.67	0.49	1.18	0.34	1.00	241%
Rz	8.77	2.66	6.11	1.84	6.15	230%
Rt	12.98	3.12	9.86	2.37	8.25	316%
RSm	211.4	58.6	152.8	33.23	123.78	261%
Rsk	1.72	-0.07	1.79	0.51	0.93	-2557%
Rdq	0.143	0.063	0.08	0.03	0.10	127%

P profile						
Pa	1.67	0.6	1.07	0.34	1.07	178%
Pz	9.58	4.43	5.15	1.85	7.39	116%
Pt	13.23	5.9	7.33	1.95	9.23	124%
PSm	195.2	75.5	119.7	31.25	138.21	159%
Psk	2.61	0.5	2.11	0.52	1.25	422%
Pdq	0.133	0.06	0.073	0.02	0.10	122%

The wear marks, registered in the case of certain feed values, are shown in the stereomicroscopic pictures taken of the surface forming tool edge section and its flank wear-land using a 45X magnification (Figure 14).

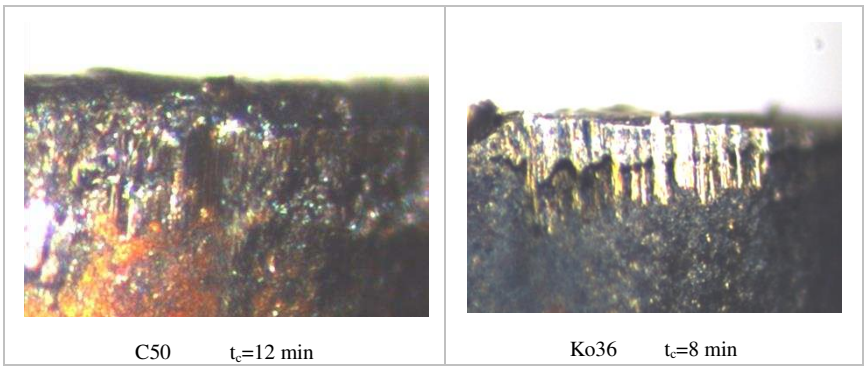

C50 t_e=12 min Ko36 t_e=8 min

Figure 14

Stereomicroscopic pictures, taken about the flank wear-land wear in case of the machined materials

On these, the form and shape of the edge wear is well recognizable, but they are not able to carry out detailed analyses or even more to compare it with the microgeometry of the machined surface based on these pictures.

In case of a turning operation in C50 constructional steel, devices, enabling greater resolution and registrations (2D roughness measurements, 3D topography and electron microscope) were invoked in order to compare the tool edge section and the microgeoemetry.

The flank wear-land of the tool edge was scanned with stylus method, starting from the tool edge section in 10 μm steps, similar as in case of machined surface. The best correspondence between the edge shape and the machined surface was registered in the section, when the wear on the tool edge point achieved approx. 0.12 mm (Figure 15), i.e. the momentary cutting edge stayed in this position after having machined 22 minutes. This statement can be made if the tool edge point is "traversed" by 180º (this is valid for further examination and analysis methods as well).

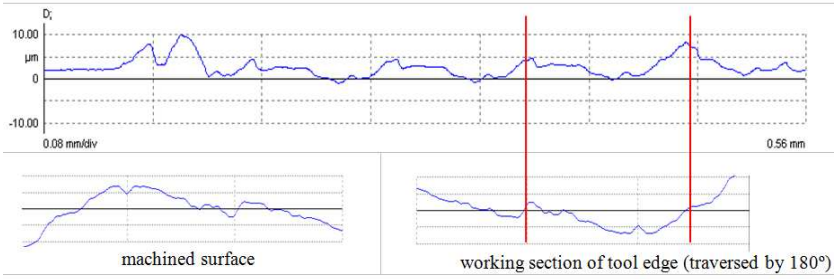

Figure 15

The flank wear-land wear on the tool edge ($VB_c \approx 0{,}12$ mm) and the micro-geometric section of the machined surface in case of turning operation in C50 material (t_c=22 min)

After having finished the cutting tests, there were further solutions to examine the inserts instrumentally. 3D topography was performed for the last section of the machined surface and for the flank wear-land of the tool edge on the Mahr-Perthen measuring instrument (Figure 16). The wear marks, indicated by a dart on the flank wear-land, can be compared easily with the shape of micro-profile of turned surface.

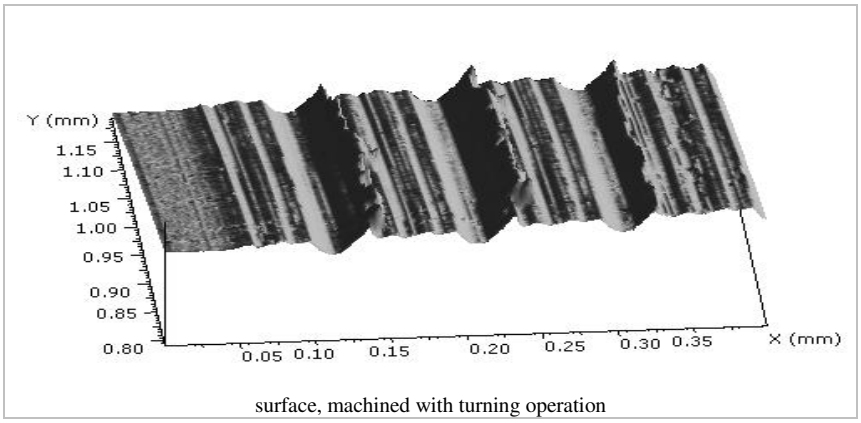

surface, machined with turning operation

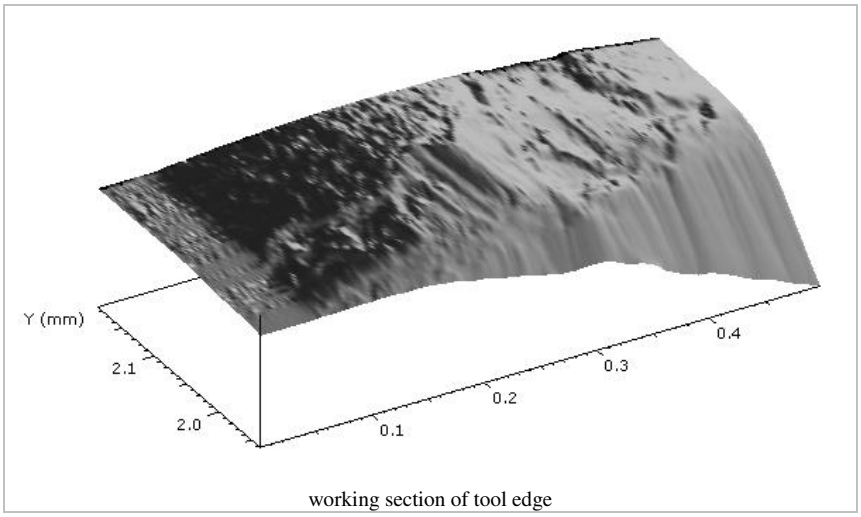

Figure 16

The machined surface and the topographic picture of tool flank wear-land in case of turning operation in C50 material (t_c=41 min)

Further and more detailed comparisons were carried out on 3D optical microscope with high resolution, type: Alicona InfiniteFocus and on Hitachi 3400 scanning electron microscope, located in the laboratory for material analysis at Széchenyi István University. The pictures, taken for these examinations, are shown in Figures 17-18.

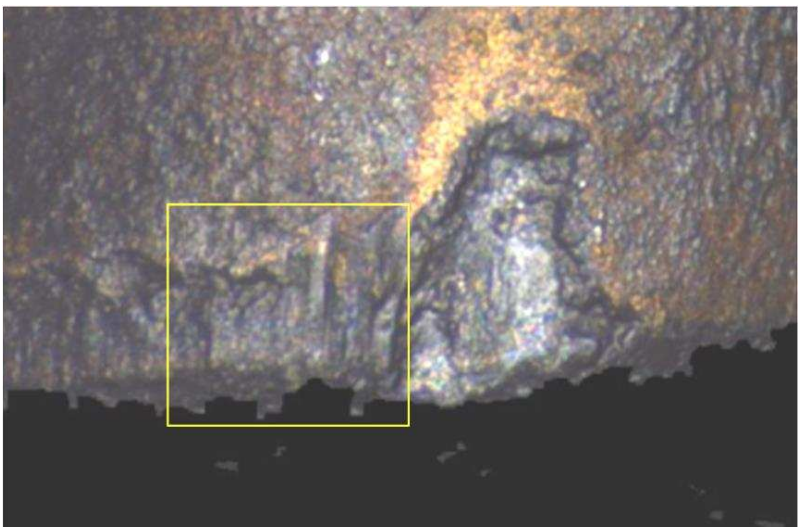

Figure 17

3D visualization of the flank wear-land of the tool edge

The picture, taken on Alicona, can be very well compared with the topographic pictures, made on Mahr-Perthen. On Figure 17 every typical wear mark can be well observed: the coating peel off, developed on the flank wear-land of the minor cutting edge and not influencing the tool in surface forming even as wear marks on the edges, forming the microgeometry of machined surface (for better visibility marked with a frame in the picture).

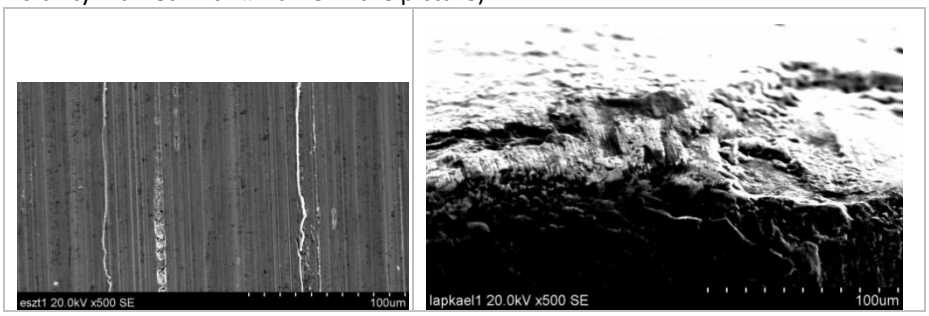

Figure 18
The machined surface and the picture, taken with electron microscope about the flank wear-land of the tool edge

Figure 18 was taken with an electron microscope, it shows the flank wear-land of the tool edge, compared to the statements, made untill now, as the details of the worn-out flank wear-land are well illustrated: the adhesion splits [16] and the wear marks of abrasive character are changing continuously.

Summary and Conclusions

A surface, machined by any method, cannot be considered homogeneous; no matter in regard to measurement technique, production or especially the operation. A significant difference may be shown, in the micro-geometric parameters that characterize the surface, in extreme cases it may achieve a value of 70-100%.

During production and quality control of a surface, consideration that surface formation takes place in the course of the deterioration process of the tool always needs to be noted. It means that the wear process of the tool and its temporal development intereacts with the surface as machined. This process can be traced back to the wear features of the flank wear-land of the tool edge: there is a change in the character of the micro-geometric profile, the generally known Ra and Rz roughness parameter values may even show a difference of 200-300%.

The R parameters of surface roughness do not characterize the microgeometry of the working, connected surfaces, quite reliably in and of itself, since − as a result of the filtering − there may be significantly differences in the existing surface. Therefore, the parameters of P profile, were always registered during the tests. Based on the comparison of the R and P parameters it is worth consideration to use features of the unfiltered P profile as they express the contact, friction and contact relations between the contact surfaces in a better way.

Acknowledgements

The project was realized through the assistance of the European Union, with the co-financing of the European Social Fund, namely: TÁMOP-4.2.1.B-11/2/KMR-2011-0001 Researches on Critical Infrastructure Protection.

References

[1] Palásti-K, B.: The Evaluation of Microgeometry of Machined Surfaces, CSc Thesis (in Hungarian: Forgácsolással megmunkált felületek mikrogeometriájának értékelése, Kandidátusi értekezés), MTA-TMB 10172, Budapest, 1984

[2] Czifra, Á.: The Change in Surface Microtopography during Sliding Friction between Metal-Metal and Metal-Ceramic Components, Phd thesis (in Hungarian: A felületi mikrotopgráfia változása fém-fém és fém-kerámia alkatrészek csúszó súrlódása során, PhD értekezés), BME, Budapest, 2007

[3] Horváth, S.: 2D and 3D Characterisation of Surface Waviness, Examination and Analysis of Its Effect, Carried Out on the Working Behaviour, Phd thesis (in Hungarian: A felületi hullámosság 2D-s és 3D-s jellemzése, a működési tulajdonságokra gyakorolt hatásának vizsgálata és elemzése, PhD értekezés), ZMNE, Budapest, 2008

[4] Farkas Gabriella: The Microtopographic Characteristics of Engineering Plastics' Surfaces Turned, Phd thesis (in Hungarian: Esztergált műszaki műanyagfelületek mikrotopográfiai jellemzői, PhD értekezés), SZIE, Gödöllő, 2010

[5] L. De Chiffre, P. Lonardo, H. Trumpold, D. A. Lucca, G. Goch, C. A. Brown, J. Raja, H. N. Hansen: Quantitative Characterisation of Surface Texture, Annals of CIRP, Vol. 49/2, pp. 635-652

[6] Palásti-K, B: The Information Content of Surface Roughness Characteristics (in Hungarian: Az érdességi jellemzők információtartalma), Gép, 1992/5 pp. 30-36

[7] Andó Mátyás: The Surface Roughness (in Hungarian: Felületi érdesség), Budapest, 2010-Gépész Tuning Kft

[8] Sipos, S. – Biró, Sz. – Tomoga, I.: The Simultaneous Increase of Productivity and quality with WIPER Edge Geometry (in Hungarian: A termelékenység és a minőség egyidejű növelése WIPER élgeometriával), Gépgyártás, XLVI. évf., 2006/4. pp. 17-24

[9] G. N. Tóth, Á. Drégelyi-Kiss and B. Palásti-Kovács: Analysis of Microgeometrical Parameters of Cutting Surfaces, 8th International PhD & DLA Symposium, 29-30 October 2012. University of Pécs, Pollack Mihály Faculty of Engineering and Information Technology in Hungary, Session 2.3, p. 12, ISBN 978-963-7298-48-6

[10] R. Horváth – Sz. Biró – S. Sipos: New Results on Wear Mechanisms of PCBN Inserts in Hard Turning *DMC 2007, Development of Metal Cutting, Kosice,* 15-16 November 2007, pp. 85-90, ISBN 978-80-8073-858-7

[11] Béla Palásti-Kovács, Sándor Sipos, Árpád Czifra: Interpretation of "Rz = 4×Ra" and Other Roughness Parameters in the Evaluation of Machined Surfaces, *Proceedings of the 13th International Conference on Tools, ICT, Miskolc*, 2012.03.27-28. pp. 237-244, ISBN 978-963-9988-35-4

[12] Kundrák, J; Gyáni, K; Bana, V: Roughness of Ground and Hard-turned Surfaces on the Basis of 3D Parameters, International Journal of Advanced Manufacturing Technology (2008) 38:(1-2) pp. 110-119 (DOI: 10.1007/s00170-007-1086-9)

[13] M. E. R. Bonifacio – A. E. Diniz: Correlating Tool Wear, Tool Life, Surface Roughness and Tool Vibration in Finish Turning with Coated Carbide Tools, Wear, 173 (1994) pp. 137-144

[14] W. Grzesik: Influence of Tool Wear on Surface Roughness in Hard Turning Using Differently Shaped Ceramic Tools, Wear, 265 (2008) pp. 327-335

[15] J-E. Stahl – F. Schultheiss – S. Hagglund: Analytical and Experimental Determination of the Ra Surface Roughness during Turning, Procedia Engineering, 19 (2011) pp. 349-356

[16] T. E. Tallian: Failure Atlas for Hertz Contact Machine Elements, ASME PRESS, New York 1992

Kinematic Quantification of Gait Asymmetry Based on Characteristics of Angle-Angle Diagrams

Patrik Kutilek[1], Slavka Viteckova[1], Zdenek Svoboda[2], Vladimir Socha[1], Pavel Smrcka[1]

[1] Faculty of Biomedical Engineering, Czech Technical University in Prague
nam. Sitna 3105, 272 01 Kladno, Czech Republic, e-mail: kutilek@fbmi.cvut.cz, vitecsla@fbmi.cvut.cz, sochavla@fbmi.cvut.cz, smrcka@fbmi.cvut.cz

[2] Faculty of Physical Culture, Palacky University of Olomouc
Tr. Miru 115, 771 11 Olomouc, Czech Republic, e-mail: zdenek.svoboda@upol.cz

Abstract: Our work focuses on studying gait symmetry with the use of bilateral angle-angle diagrams. The geometric characteristics of angle-angle diagrams can be used to characterize gait, as well as, identify and quantify the associated gait asymmetry. The angle-angle diagrams were created for ten patients with leg length inequality (LLI), to quantify gait symmetry before and after an application of the heel lift. In order to quantify the symmetry of human walking, we have invented and used the characteristics of an angle-angle diagram, which represent the evolution of the two joint angles, i.e. left and right knee angles or left and right hip angles. The novel methods are based on the area of the convex hull of the hip-hip diagram or knee-knee diagram, and can be used as an additional method for the determination of gait symmetry of the bipedal walking of human subjects or robots. Our method is not limited to gait studies, it can also be used to study arm swing symmetry.

Keywords: human walking; bipedal walking; convex hull; angle-angle diagram; length inequality

1 Introduction

Currently, several methods can be used in medical practice and in physiotherapeutic research to identify defects in bipedal walking. The most widely-used method for studying gait behavior in clinical practice is gait phase analysis by phase cycles of gait, [1] - [4]. Intensive research is now being done on studying leg movements by EMG signal measurements [5] - [7]. For the study of gait, we have used new methods based on the analysis of gait angles using angle-angle diagrams (also called cyclograms). The first mention of the cyclogram [8]

argued that a cyclic process such as walking can be better understood if studied with a cyclic plot. The creation of cyclograms is based on gait angles that are objective, reliable and well suited for statistical study [9] - [14].

We will focus on the use of the cyclogram for the evaluation of gait symmetry. Symmetry is an important indicator of a healthy gait or proper walking technique. Human gait symmetry can be influenced by various factors, such as limb asymmetry, injury and other mobility-affecting diseases. Several methods can be used for identifying defects in bipedal walking. At present, algebraic indices and statistical parameters represent two major classes of gait symmetry quantifiers [15] - [19]. Algebraic indices include a symmetry index and a ratio index. Symmetry and ratio indices compare bilateral variables such as, step period, maximum joint angle or step length. In the case of the evaluation of maximum joint angles, the basic formula is as follows:

$$\mathrm{R} = \frac{X}{Y}, \tag{1}$$

where R is the ratio index related to the maximum angles (maximum right angle X and maximum left angle Y). Notwithstanding, their successful use depends on discrete variables and are unable to reflect asymmetry, as it evolves over a complete gait cycle. Statistical methods such as paired t-test and Principal Component Analysis (PCA), and parameters such as correlation coefficients, coefficient of variation and variance ratio have also been used to measure gait asymmetry [14], [20]. Statistical parameters do not usually suffer from the limitations of the algebraic indices, however, their computation is more complex and interpretation is less transparent. Despite the broad agreement in the fundamentals of what constitutes symmetry, there is no appropriate measure of gait symmetry (reflecting asymmetry as it evolves over a complete gait cycle) [14], [15]. In paper [14], a technique was introduced based on the geometric properties of symmetric angle-angle diagrams. This technique is rooted in geometry and the symmetry measures are intuitively understandable. Depending on the cyclicity of the gait, cyclograms are closed trajectories generated by simultaneously plotting two (or more) joint quantities. In order to quantify the symmetry of bipedal walking, a cyclogram was obtained in the study [14], representing the same joint and two sides of the body, i.e. the evolution of the two (left and right) joint angles. The presented approach is based on the symmetry of joint angle evolution and comparison of the evolution of a single joint with that of its contra-lateral counterpart, [14], [21]. The papers also mentioned basic characteristics of the bilateral cyclogram, which can be used to evaluate symmetry. The area within the cyclogram, its orientation and its minimum moment are geometric parameters used to evaluate the symmetry, [14], [22], [23]. For the perfectly (i.e. absolutely) symmetrical gait, there is a zero area within the curve, its orientation is 45 degrees and the magnitude of its minimum geometric moment is zero [14]. However, angle-angle diagrams have never been used for

studying patients with Leg Length Inequality (LLI), hence the new shape characteristics of angle-angle diagrams can be very useful. Therefore, the main object of our study was to test and verify the application of the method based on the area of convex hull of angle-angle diagram to analyze the gait symmetry of bipedal walking of patients with LLI.

2 Methods and Materials

2.1 Participants and Test Procedure

The set of data to create and study angle-angle diagrams was measured on a sample of 10 volunteers/adult patients (age of 50 (SD 14.8) years) with leg length inequality (leg-length inequality of 0.85 (SD 0.32) mm) recruited from patients of the Rehabilitation Center Kladruby (Kladruby u Vlasimi, the Czech Republic). The subjects were asked to walk properly on a treadmill. A human walking speed of 2.3 km/h was selected for studying the proposed method. A constant speed was chosen because it directly affects the range of joint angles, [24], [25]. If we want to evaluate and compare shape characteristics of the angle-angle diagram, it is appropriate to measure the joint angles at a constant walking speed. We assume that improvement or deterioration of gait symmetry is not primarily influenced by walking speed.

First, patients were asked to walk without shoes and any support devices, while their joint angles (left/right knee angles and left/right hip angles) were measured. After that, the physician recommended appropriate shoes with a heel lift under the short leg side to stabilize and level the pelvis. Patients were asked to walk immediately after the application of the heel lift, and the joint angles were measured again.

2.2 Motion Capture Equipment

To create and study angle-angle diagrams, we used a model of the human body created in MatLab Simulink and SimMechanic software, [26]. The movement of the model of a body is controlled by data measured by the motion capture system (MoCap), which identifies the position of body segments in the Cartesian coordinate system. As a MoCap system, we used a very accurate Lukotronic AS 200 system (Lutz Mechatronic Technology declares, according to the EU Directive 93/42/EEC, that the system can be used in hospitals) with IR active markers placed on the following anatomical points on the person being measured: fifth metatarsophalangeal joint, malleolus lateralis, epicondylus lateralis,

trochanter major and spina iliaca anterior superior, Fig. 1, [16], [27]. The markers fastened with small adhesive double-sided tape were placed in accordance with the recommendation of the manufacturer of the MoCap system. Using this method, we were able to record and study the movement in 3D space, though we primarily studied the movement in a 2D sagittal plane. Maximum joint angles are small in the frontal plane and thus, one of the basic tools to study the gait is the analysis of the joint angles in the sagittal plane, [28], [29]. The MoCap system was calibrated accurately before the experiments, and the origin of the world coordinate system was set up so that the first axis is along the track of the treadmill and the other two axes are perpendicular to the track of the treadmill.

After obtaining the measured data, we identified joint angles and created the cyclograms in MatLab (The MathWorks Inc.) software. If we have information on the movement of anatomical points/markers in space, and the points characterizing the parts of human body, then we can use these to define the vectors of the positions and orientations of body segments. The difference in coordinates of two points in space defines a vector. The angles between each two segments are calculated by assuming the segments to be idealized rigid bodies. The angles are given by formula described in detail by Kutilek et al. [22].

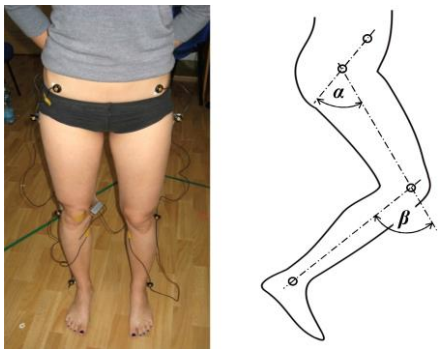

Figure 1
Placement of IR markers and angles measured during the examination, [22]

2.3 Gait Evaluation Methods

After the measurement and data processing, we used the method based on synchronization of two angle plots [14] to obtain bilateral knee-knee and hip-hip cyclograms. A prominent gait event such as the heel-touchdown was used to synchronize the two plots representing angles at the left and right joint. For a symmetric gait, properly synchronized twin trajectories from corresponding joints should be identical and a bilateral cyclogram should lie on a symmetry line, [14]. The symmetry line is a straight line passing through the origin inclined at an angle 45 degrees, see Fig. 2. We can mathematically measure cyclogram deviation from

the symmetry line to obtain a quantification of gait symmetry. We can also use the area within the cyclogram and its orientation to evaluate the symmetry, [14].

A bilateral cyclogram is not continuous curve, but it´s a polyline contour (i.e. irregular polygon), see Fig. 2. The smoothness of the contour is a function of the amount of noise in the measured data. We found that in some cases, the evaluation of the cyclogram using the area within the cyclogram and its orientation is incorrect. The cyclograms may consist of self-intersecting loops or they have a complex shape. Although the cyclogram may be complex and asymmetrical, its surface may also be very small. For example, a crescent shape can lead to a small area, although it is an asymmetrical gait, see Fig. 2.

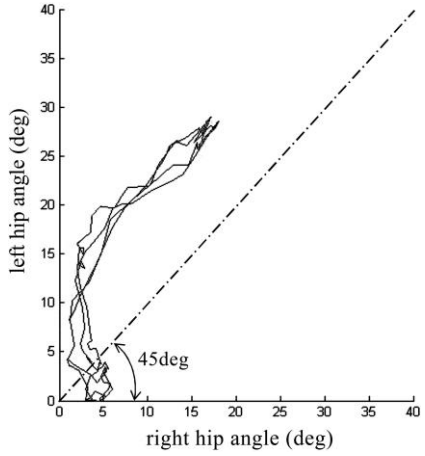

Figure 2
Example of a right hip vs. left hip bilateral cyclogram for measured patient with LLI, deliberately unfiltered, with symmetry line

For the above mentioned reason, we use the convex hull to calculate the area which represents the shape of the cyclogram. The convex hull of a cyclogram is more appropriate to describe the area which represents the gait asymmetry. A convex hull completely encloses a set of points with the fewest number of perimeter nodes. In our case, the set of points consists of all points on the cyclogram. The area of convex hull is usually larger than the area within the cyclogram if the cyclogram is asymmetric and with loops, see Fig. 3a. The second way to avoid improper evaluation of the area is based on the calculation of the area of the region enclosed by the curve of the cyclogram, the 45° straight line (symmetry line) and the lines perpendicular to the symmetry line, see Fig. 3b. The region is represented by the area above and below the symmetry line and is bounded by the outer curves of the cyclogram and lines perpendicular to the symmetry line. The positions of perpendicular lines are defined by the points of intersection on the symmetry line. The points are identified by projection of the points of the bounding curve of the cyclogram on the symmetry line, and are the

nearest and the furthest points of the projection of the cyclogram above/below the symmetry line from the origin of the symmetry line, Fig. 3b. We can also use the convex hull and/or the region enclosed by the curve of the cyclogram and symmetry line to calculate the second moment of area to describe the property of a two-dimensional plane shape of the cyclogram. Therefore, we can determine the second moment of area about the symmetry line.

The orientation of the planar geometric entity, i.e. convex hull and/or the region enclosed by the curve of the cyclogram and symmetry line, can be defined as the angle (bounded by +/-90°) between the symmetry line and the principal axis of the planar geometric entity, [14]. We can also use linear regression to determine the orientation of the planar geometric entity. Simple linear regression fits a straight line (axis) through the set of the points on the cyclogram, or only through the set of the points of bounding curve. Hence, the orientation can be defined as the angle between the regression principal axis and the symmetry line, [27].

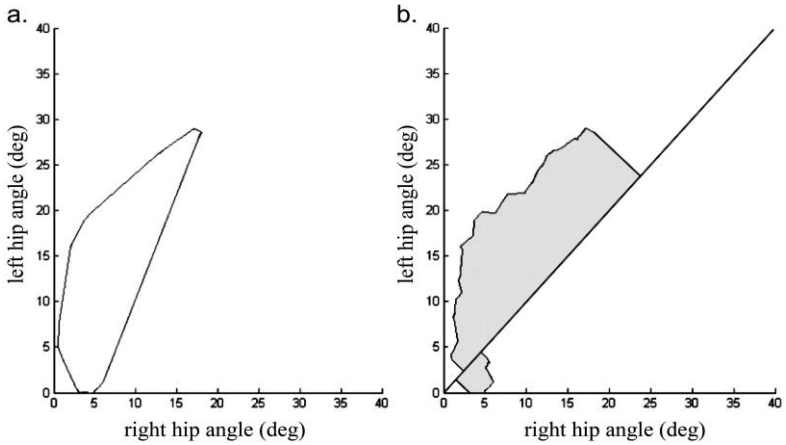

Figure 3

a) Example of the convex hull of the bilateral cyclogram (see Fig. 1); b) Example of the area of the region enclosed by the curve of the cyclogram (see Fig. 1) with symmetry line

The described symmetry quantification technique, based on convex hull and/or the region enclosed by the curve of the cyclogram, is sensitive to the precision of synchronization of the two signals. The area of the convex hull and/or the region enclosed by the curve of the cyclogram dramatically increases from zero for even a small time-shift, i.e. poor synchronization of the of two angle plots. In the next section, we describe the application of the method based on the area of convex hull. This method is easier and computationally faster than other methods/algorithms. The technique is also intuitively understandable.

We used convhull (i.e. MatLab function) to create convex hull of each bilateral cyclogram. The convhull, [30], returns the 2-D convex hull [31], of the points defined by coordinates (x, y), where x and y are values of the left joint angle and

right joint angle. The convhull function is based on Quick Hull method. This method computes the convex hull of a finite set of points in the plane. It uses a "divide and conquer" approach similar to that of a QuickSort sorting algorithm. We also used MatLab to calculate the area of the convex hull of each bilateral cyclogram.

The symmetry index (SI) was used as a comparative method to compare and quantify the symmetry of bipedal walking, [32]. The SI is a measure of the relationship between the discrete values obtained from the left and right sides. We used the "average" symmetry index:

$$\mathrm{SI}_{\mathrm{average}} = \frac{2 \cdot |X - Y|}{|X + Y|} \cdot 100\% \tag{2}$$

The symmetry index is related to the maximum angles (maximum right angle *X* and maximum left angle *Y*) formed when the right-side value is plotted and the left-side value is plotted. After the measurements, the area of convex hulls of cyclograms and the symmetry indexes were calculated. We assume that the decrease of the area of the convex hull indicates the improvement in symmetry of bipedal walking and the as well as the decrease of the symmetry index indicates the improvement in symmetry of bipedal walking, [33].

3 Results

The calculated areas of convex hulls and symmetry indexes are summarized in Table 1 and Table 2. The tables compare the area of convex hulls and symmetry indexes before the application of the heel lift and after the application of the heel lift. Table 1 represents the area of the convex hull and symmetry index of the right knee angle and left knee angle, and Table 2 represents the area of the convex hull and symmetry index of the right hip angle and left hip angle before and after the application of heel lift.

We used the measured data (Table 1 and Table 2) to test the proposed method and illustrate the relationship between the area of convex hull of the bilateral cyclogram and the symmetry index. The following plots (Fig. 4 and Fig. 5) display the minimum, maximum, median, first quartile (Q1), third first quartile (Q3), mean and standard deviation (SD) for the area of the convex hull of knee-angle cyclograms and hip-angle cyclograms before and after the application of heel lift, and the SI of knee angles and hip angles before and after the application of heel lift.

The data measured before and after the application of the heel lift indicates a decrease of the area of the convex hull of the knee-knee cyclogram in only three cases. The data also indicates a slight increase of the mean for the area of the

convex hulls, Tab. 3, Fig. 4. The gait symmetry index related to the maximum left and right knee angles decreased in five cases. The data indicate a slight increase of the mean for the SI, Tab. 4, Fig. 5. Improvements in the two characteristics, which describe the gait symmetry, are overlapping only in one case (i.e. 10%), Table 1.

Table 1

Area of the convex hull and symmetry index of the right knee angle and left knee angle before and after the application of the heel lift

patient with LLI	Area of convex hull [deg^2]		Symmetry index [%]	
	before application	after application	before application	after application
1.	884	733	13.4	14.3
2.	335	581	16.8	16.4
3.	567	526	18.6	28.7
4.	326	457	26.3	22.3
5.	841	610	57.7	55.3
6.	409	621	1.6	10.3
7.	696	785	1.4	3.3
8.	723	1098	29.7	22.9
9.	510	630	46.4	56.7
10.	386	553	38.6	24.9

Table 2

Area of the convex hull and symmetry index of the right hip angle and left hip angle before and after the application of heel lift

patient with LLI	Area of convex hull [deg^2]		Symmetry index [%]	
	before application	after application	before application	after application
1.	168	163	8.1	5.6
2.	123	135	5.3	2.1
3.	143	160	25.2	55.6
4.	142	171	0.5	1.3
5.	397	343	50.6	23.0
6.	235	348	16.5	6.7
7.	210	154	68.0	53.9
8.	154	271	4.5	12.8
9.	225	212	20.7	0.1
10.	223	201	13.0	1.4

The data measured before and after the application of the heel lift indicate a decrease of the area of the convex hull of the hip-hip cyclogram in five cases. The data indicate a slight increase of the mean of the area of the convex hulls, Tab. 3, Fig. 4. The gait symmetry index related to the maximum left and right hip angles

decreased in seven cases. The data indicate a decrease of the mean of the SI, Tab. 4, Fig. 5. Improvements in the two characteristics, which describe the gait symmetry, are overlapping in five cases (i.e. 50%), Table 2.

Table 3

Comparison of the area of the convex hull of knee-angle cyclograms and hip-angle cyclograms before and after the application of the heel lift

	Area (hip angles, before treatment) [deg^2]	Area (hip angles, after treatment) [deg^2]	Area (knee angles, before treatment) [deg^2]	Area (knee angles, after treatment) [deg^2]
Mean	202.00	215.80	567.70	659.40
SD	79.53	78.31	208.01	180.91
Median	189.00	186.00	538.50	615.50
Q1	145.75	160.75	391.75	560.00
Q3	224.50	256.25	716.25	707.25

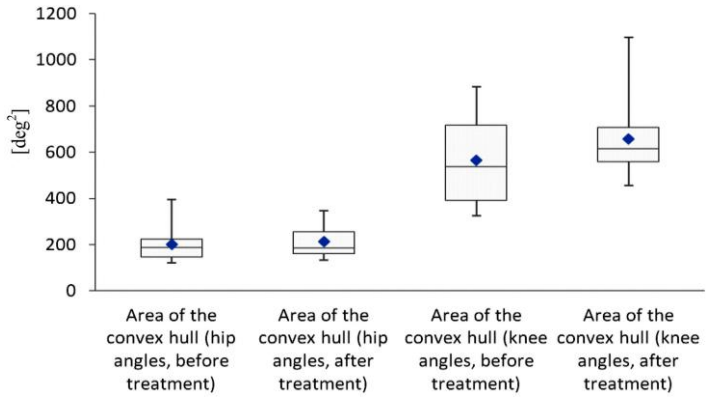

Figure 4

Comparison of the area of the convex hull of knee-angle cyclograms and hip-angle cyclograms before and after the application of the heel lift

The results of the comparison indicate that the methods show slightly different results. The evaluation method based on the area of convex hull shows improvement of the gait symmetry in fewer cases than the method based on the gait symmetry index. The reason is that the symmetry index depends on discrete variables and is thus unable to reflect the asymmetry, as it evolves over a complete gait cycle. The area of the convex hull depends on the complete gait cycle, i.e. relations and evolutions of joint angles over time, Fig. 6, which shows the bilateral cyclogram with large area of the convex hull and low SI. The SI is low because the maximum measured left and right hip angles are almost the same. However, we can see different sizes of the joint angles during specific phases of the gait cycle and the irregular curve of the bilateral cyclogram.

Table 4

Comparison of the SI of knee angles and hip angles before and after the application of the heel lift

	SI (hip angles, before treatment) [%]	SI (hip angles, after treatment) [%]	SI (knee angles, before treatment) [%]	SI (knee angles, after treatment) [%]
Mean	21.24	16.25	25.05	25.51
SD	21.84	21.43	18.51	17.71
Median	14.75	6.15	22.45	22.60
Q1	6.00	1.58	14.25	14.83
Q3	24.08	20.45	36.38	27.75

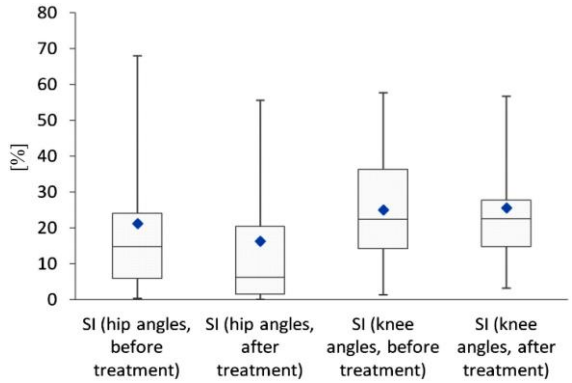

Figure 5

Comparison of the SI of knee angles and hip angles before and after the application of the heel lift

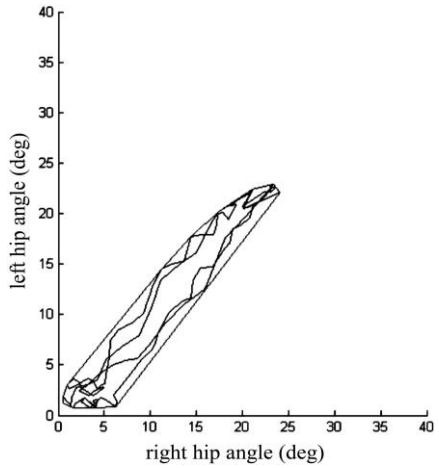

Figure 6

Example of right hip vs. left hip bilateral cyclogram (unfiltered data) with large area of the convex hull and supposed low SI

The measured data indicate that the improvement of the symmetry, i.e. the decrease of the area of the convex hull and symmetry index, is more pronounced in the case of hip angle measurements. In the case of knee angle measurements, we observed a small improvement of the symmetry. The data indicates a slight increase of the mean for the area of the convex hulls. Generally, the decrease of the area of the convex hull and symmetry index is up to 50% of the measured subjects.

4 Discussion

We tested and verified a new method, which is derived from the geometric properties of angle-angle diagrams. The described symmetry quantification technique based on the area of the convex hull of the bilateral cyclogram is sensitive to the precision of synchronization of the two signals and their quality, [32]. After obtaining the measured data, we created bilateral cyclograms using MatLab software and the MatLab functions were used to calculate the area of the convex hull for each bilateral cyclogram. As it can be seen from the examples above, it is not necessary to normalize the data because the standard ranges of angles are the same for the two sides of the body if the gait is symmetric.

We found that a study of symmetry based on an algebraic parameter (i.e. symmetry index) is not suitable for the study of complex movements, but the study of symmetry based on the bilateral cyclograms is influenced by many factors that affect accuracy and relevance, [32]. The area of the convex hull of the bilateral cyclograms can be used to study complex movements and describes the deviations of the measured angles from ideal angles. Using the area of the convex hull, we could also study, for example, the deviations of angles that are caused by a tremor. Note that algebraic indices (i.e. SI) cannot be used to identify gait asymmetry caused by a tremor, or similar movement disorders.

The results indicate that the new method, described in this work, has identified and quantified improvements of gait symmetry, but only in few cases. The method based on algebraic parameters, identified improvement of the gait symmetry after the application of a heel lift in more cases than the method based on the convex hull. The main reason for this result is the short application time of the heel lift. The subjects were measured immediately after the application of the heel lift and were not able to become accustomed to using the heel lifts. Also, the physician applied the heel lift and only maximum angles were used to evaluate the gait symmetry.

Conclusions

According to the method described here, bilateral cyclograms illustrate bipedal gait symmetry. This information is important for rehabilitation medicine, and also

could be used in control algorithms for lower limb prostheses or in the creation of bipedal robots. The method based on the convex hull of bilateral cyclograms can be used as an additional method for the determination of gait symmetry. Thus, future work can be focused on the comparison of other traditional methods based on algebraic indices and statistical parameters with the new method. In future studies, we plan to measure more patients with other types of disabilities and evaluate gait symmetry for a longer period of therapy.

This work has not attempted to describe all of the potential ways of applying the convex hull of the bilateral cyclograms. We have demonstrated new methods that have subsequently been tested on patients with Leg Length Inequality (LLI). The modified characteristics of angle-angle diagram have never previously been described and angle-angle diagrams have never been used for the study of patients with LLI. There is no limit for the research in field mentioned herin. However, the proposed method is sensitive to the precision of synchronization of the two signals and the quality of the signals. For this reason, it is necessary to use highly accurate and high quality MoCap systems and mathematical software. This may be the greatest problem in the use of the proposed methods for clinical practice. However, this can be overcome by cost reductions in MoCap systems in the future, and their introduction into clinical practice.

Acknowledgement

The work presented here was carried out at the Czech Technical University in Prague, Faculty of Biomedical Engineering within the framework of research program No. SGS14/094/OHK4/1T/17 CTU Prague.

References

[1] Gage R. J., Hicks R.: Gait Analysis in Prosthetics. Clinical Prosthetics & Orthotics, 1989; 9: 17-21

[2] Janura M., Cabell L., Svoboda Z., Kozáková J., Gregorkova A.: Kinematic Analysis of Gait in Patients with Juvenile Hallux Valgus Deformity. Journal of Biomechanical Science and Engineering, 2008; 3: 390-398

[3] Koktas N. S., Yalabik N., Yavuzer G.: Combining Neural Networks for Gait Classification. Proceedings of the 11th Iberoamerican Congress on Pattern Recognition, Mexico, Cancun; 2006; 11: 381-388

[4] Wang L., Tan T., Ning H., Hu W.: Automatic Gait Recognition Based on Statistical Shape Analysis. IEEE Trans Image Process., 2003; 12: 1120-1131

[5] Sepulveda F., Wells D., Vaughan C.: A Neural Network Representation of Electromyography and Joint Dynamics in Human Gait. J Biomech, 1993; 26: 101-109

[6] Heller B. W., Veltlink P. H., Rijkhof N. J. M., Rutten W. L. C., Andrevs B.: Reconstructing Muscle Activation during Normal Walking: a Comparison

of Symbolic and Connectionist Machine Learning Techniques. Biol Cybern, 1993; 69: 327-335

[7] Arsenault A. B., Winter D. A., Marteniuk R. G.: Bilateralism of EMG Profiles in Human Locomotion. Am J Phys Med Rehabil, 1986; 65: 1-16

[8] Grieve D. W.: Gait Patterns and the Speed of Walking. Biomed Eng, 1968; 3: 119-122

[9] Grieve D. W.: The Assessment of Gait. Physiotherapy, 1969; 55: 452-460

[10] Kutílek P., Viteckova S.: Prediction of Lower Extremity Movement by Cyclograms, Acta Polytechnica, 2012; 52: 51-60

[11] Hajny O., Farkasova B.: A Study of Gait and Posture with the Use of Cyclograms. Acta Polytechnica, 2010; 50: 48-51

[12] Giannini R. C., Perell K. L.: Lower Limb Coordination during Walking in Subjects with Post Stroke Hemiplegia vs. Healthy Control Subjects. Clinical Kinesiology, 2005; 59: 63-70

[13] Heck A., Holleman A.: Walk like a Mathematician: an Example of Authentic Education. Proceedings of ICTMT6 – New Technologies Publications, Greece, Athens; 2003

[14] Goswami A.: Kinematics Quantification of Gait Symmetry Based on Bilateral Cyclograms. Proceedings of the XIXth Congress of the International Society of Biomechanics (ISB), New Zealand, Dunedin; 2003

[15] Sadeghi H., Allard P., Prince F., Labelle H.: Gait Symmetry and Limb Dominance in Able-bodied Gait: A review. Gait Posture, 2000; 12: 34-45

[16] Legnani G., Zappa B., Casolo F., Adamini R., Magnani P. L.: A Model of an Electro-Goniometer and Its Calibration for Biomechanical Applications. Medical Engineering and Physics, 2000; 22: 711-722

[17] Herzog W., Nigg B. M., Read L. J., Olsson E.: Asymmetries in Ground Reaction Force Patterns in Normal Human Gait. Med Sci Sport Exer, 1989; 21: 110-4

[18] Vogt L., Banzer W., Bayer I., Schmidtbleicher D., Kerschbaumer F.: Overground and Walkway Ambulation with Unilateral Hip Osteoarthritis: Comparison of Step Length Asymmetries and Reproducibility of Treadmill Mounted Force Plate Readings. Physiotherapy Theory and Practice, 2006; 22: 73-82

[19] Roerdink M., Beek P. J.: Understanding Inconsistent Step-Length Asymmetries Gross Hemiplegic Stroke Patients: Impairments and Compensatory Gait. Neurorehab Neural Re, 2011; 25: 253-258

[20] Pierotti S. E., Brand R. A., Gabel R. H., Pedersen D. R., Clarke W. R.: Are Leg Electromyogram Profiles Symmetrical? J Orthop Res., 1991; 9: 720-729

[21] Goswami A.: New Gait Parameterization Technique by Means of Cyclogram Moments: Application to Human Slope Walking. Gait and Posture, 1998; 8: 15-26

[22] Kutilek P., Farkasova B.: Prediction of Lower Extremities Movement by Angle-Angle Diagrams and Neural Networks. Acta of Bioengineering and Biomechanics, 2011; 13: 57-65

[23] Goldstein H.: Classical Mechanics (2nd ed.) Boston: Addison-Wesley; 1980

[24] Segers V., Lenoir M., Aerts P., De Clercq D.: Kinematics of the Transition between Walking and Running when Gradually Changing Speed. Gait Posture, 2007; 3: 349-61

[25] Segers V., Aerts P., Lenoir M., De Clercq D.: Spatiotemporal Characteristics of the Walk-to-Run and Run-to-Walk Transition when Gradually Changing Speed. Gait Posture; 2006; 2: 247-54

[26] Kutilek P., Hajny O.: Study of Human Walking by SimMechanics. Proceedings of the 18th Technical Computing, Slovakia, Bratislava; 2010

[27] Kutilek P., Hozman J.: Prediction of Lower Extremities Movement Using Characteristics of Angle-Angle Diagrams and Artificial Intelligence. Proceedings of the 3rd International Conference on E-Health and Bioengineering - EHB 2011, Romania, Iasi; 2011

[28] Su P., Gard S., Lipschutz R., Kuiken T.: Gait Characteristics of Persons with Bilateral Transtibial Amputations. Journal of Rehabilitation Research and Development; 2007; 4: 491-501

[29] Haudum A., Birklbauer J., Müller E.: The Effect of an Acute Bout of Rubber Tube Running Constraint on Kinematics and Muscle Activity. Journal of Sports Science & Medicine, 2012; 3: 459-467

[30] Rovenski V.: Modeling of Curves and Surfaces with MATLAB, New York: Springer; 2010

[31] Adkin A. L., Bloem B. R., Allum J. H.: Trunk Sway Measurements during Stance and Gait Tasks in Parkinson's Disease. Gait Posture, 2005; 22: 240-249

[32] Zifchock R. A., Davis I., Higginson J., Royer T.: The Symmetry Angle: A Novel, Robust Method of Quantifying Asymmetry. Gait Posture, 2008; 27: 622-627

[33] Kutilek P., Viteckova S., Svoboda Z., Smrcka, P.: Kinematic Quantification of Gait Asymmetry in Patients with Peroneal Nerve Palsy Based on Bilateral Cyclograms. J Musculoskel Neuron, 2013; 2: 244-250

Architectural Design Patterns for Language Parsers

Gábor Kövesdán, Márk Asztalos and László Lengyel

Budapest University of Technology and Economics
Department of Automation and Applied Informatics
Magyar tudósok krt. 2, H-1117 Budapest, Hungary
{gabor.kovesdan, mark.asztalos, laszlo.lengyel}@aut.bme.hu

Abstract: Processing the textual scripts of computer languages is an important field in software development, which has been growing in popularity, recently. It is applied both for general-purpose programming languages and for domain-specific languages. There is a wide range of typical algorithms and patterns that are used to syntactically parse formal languages, each having specific characteristics and implying different software architectures. If we develop parsers at a higher abstraction level, it simplifies the problem domain and facilitates developing more robust software quicker, but there are always some tradeoffs to consider. The main guideline of this paper is abstraction: how to increase it in different patterns, how it helps parser development and what kind of tradeoffs are implied. The presented architectural design patterns are organized in a pattern catalog ordered by their abstraction level. This catalog is intended to assist developers in the industry in designing efficient parser software.

Keywords: modeling; model-processing; formal languages; parsers; design patterns; architectural patterns

1 Introduction

The complexity of systems is growing at a rapid pace, which promotes the use of modeling and formal methods in today's software environment. When modeling is used for a well-defined field and has a limited expressive nature, we usually speak about domain-specific modeling [1] [2]. This limited expressive potential reduces the problem domain and thus simplifies and facilitates software engineering. We can express models in two common ways: with graphical or textual representations. The latter has led to processing of textual scripts and formal language theory being used more widely than in the past [3]. Writing parsers for computer languages was formerly a very specific knowledge that was only necessary to design and implement compilers but was not a commonly required

skill. This situation has changed recently as software developers are more frequently facing the problem of processing textual representations of models. Although processing of domain-specific modeling languages is usually based on the theoretical background of compilers for general-purpose programming languages, their limited expressive power sometimes can lead to a simpler syntax, which allows other, often simpler, parsing approaches. This work presents processing methods of both types.

Despite the increasing use of domain-specific languages, we still lack catalogs that collect best practices for this field. Since the introduction of design patterns in [4], developers have a catalog of generally applicable object-oriented best practices and a universal terminology to refer to commonly used software recipes. This book had a great influence on the software development area, but it only contained a wide or general focus. Catalogs of more specialized patterns are still very much in demand, in order to collect more ideas and to create a common vocabulary among developers. In the field of domain-specific languages, [1] provides a pattern catalog, covering several different aspects of domain-specific languages. This is a rich source of information but it has a more general view than this paper and does not provide such a systematic organization of architectural patterns used in parsing as intended herein. Apart from this, [5] provides some practical uses of general object-oriented design patterns in recursive descent parsers and [6] describes how a parser generator uses object-oriented design patterns. These are just specific uses of general design patterns and these papers do not include more specialized patterns specific to parsers.

The goal of this paper is to fill the gap and provide a pattern catalog of design patterns that can be used to design parser software. We focus on architectural-level design patterns, which determine the software components and their interaction. Although some of the patterns described herein result in an identical runtime component structure, we judged that it was practical to describe them, because the development techniques and workflow that they suggest are very different. This also leads to deviating consequences, so we extended the notion of architectural design pattern to possibly include some aspects of development workflow. In fact, [1] also distinguishes some patterns that result in an identical runtime structure, though it does not explicitly merit this generalization. When creating the pattern catalog, we examined the interests of all actors within the industry that are concerned with parsing software: end-users, domain specialists, developers and tool developers. They have different focuses and goals, which were taken into account in the description of patterns, so that all actors can benefit from using this catalog.

The rest of this paper is organized as follows. In Section 2, the theoretical background is explained, which is necessary to understand the concepts outlined in the paper. In Section 3, the actual pattern catalog is presented. We provide an introductory section that summarizes its deliverables to different actors of the industry and then patterns are listed according to their level of abstraction. We

have intentionally avoided the terms maturity and evolution and consider it important to explicitly highlight that a higher level of abstraction does not necessarily guarantee a specific pattern is consistently more effective or practical. Higher abstraction usually means that less development work is necessary, but sometimes it may also include less flexibility.

2 Background

In the following, we summarize the principal concepts of parsing. This theoretical background is explained in more detail in [7] and [8].

First, we discuss the processing of textual scripts, we must divide this process into two major steps: parsing and execution. Parsing [1] is described here as a step in which the input is read and mapped to an internal representation, the semantic model, which is more meaningful than any intermediate abstract representation. Execution refers to the actual processing of the model, which can mean running some executable steps or a transformation executed on the model. Before describing the actual patterns, we briefly discuss the possibility of parsing and executing languages with increasing levels of abstraction. In software engineering, we identify some kind of systematic organization or commonly applicable steps, factor them out as reusable units and parameterize them with the parameters that change from one use case to the other. Abstraction is increased in this way. Later on, we discuss how this applies to language processors.

The least structured parser that we can imagine is a monolithic component, which reads an input and executes it immediately. One commonly used intuitive parsing solution that follows a more systematic approach is a delimiter-directed translation [1]. With this approach, the language is divided into chunks, called tokens, by identifying well-recognizable separator characters. Then the actual type of each token can be inferred from its position. For some simple languages, this is a quick and easy solution that can be developed. However, for a more complicated language, the notion of grammar [7] must be introduced. Grammar is a formalism that describes how the language constructs can be used together to create well-formed words[1]. The grammar uses two kinds of symbols: a terminal symbol is a symbol that can occur in well-formed words, while a non-terminal symbol is only used for substitutions, in an attempt to derive well-formed words from the grammar. There is a special non-terminal, the start symbol, from which the derivation starts. A grammar is composed of production rules, which have two sides and express a possible substitution while deriving a well-formed word. The

[1] A well-formed word is a statement expressed in the language that is considered valid and meaningful.

left side is the series of symbols that are substituted from the right side. If we can find a derivation from the start symbol that uses the production rules and successfully derives the word we are validating, then the particular word is considered well-formed in the language.

To simplify the process, production rules are usually phrased at the level of the tokens and not at the single characters. We construct a lexical analyzer (also called lexer or scanner) that creates a series of tokens from the input character stream. The syntactical analyzer then uses this token stream and a parsing algorithm to verify whether the word is well-formed in the language. While using the production rules to derive the input word, it also stores the parse tree or a simplified version of that, which is usually denoted as an abstract syntax tree. When the distinction between them is irrelevant, they are usually referred to as syntax trees. This phase is sometimes ambiguously referred to as parsing, identical to the entire process. With the help of the notion of grammar, we now have a more systematic method to build a parser: create a grammar, write a lexer that produces a token stream from the input and write the syntactical analyzer that uses the production rules of the grammar to decide whether the input belongs to the language. At the same time, it builds a syntax tree and if the derivation succeeds, this syntax tree can be used for the semantic analysis of the input. Figure 1 summarizes how a script is processed.

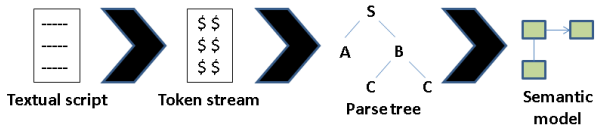

Figure 1
The processing steps of parsing a language

Since the parsing algorithms are generally applicable to a wide set of grammars (context-free grammars with some further limitations), the so called parser generators or compiler compilers (sometimes also referred to as compiler generators) have been developed to automatically generate parsers from a grammar in a well-specified notation. Using these tools, we can create a ready-to-use parser that provides us with a syntax tree that can be used to further process the language. This highly simplifies the development effort for a parser. Nevertheless, the syntax tree is still not the semantic model (although in some cases it may be) so a third pass, a tree parser, is required. By further increasing the abstraction, it is possible to avoid manually developing the tree parser as well. Upon agreeing on the metamodel of the semantic model, it is possible to construct tools that directly generate a parser, that can map the input language to the semantic model. This entails that the grammar language has to be extended to include additional information about the methods for mapping language constructs, to model elements and their properties. This way, we can generate all components needed to parse the language and build the required semantic model.

3 Pattern Catalog

The different approaches for the parsing process that have been presented in Section 2, can be described as architectural design patterns. This section provides a catalog of them using a format similar to [4]. Similarly, because of their higher-level nature, these patterns do not have such a specific intent as general design patterns and therefore, the intent section has been renamed to *Description*. Furthermore, the sections on alternative names and related patterns have also been removed. In *Description,* the main idea of the discussed architectural structure is explained. *Motivation* describes the main factors for choosing the pattern. *Applicability* enumerates the criteria required for the pattern to be relevant when applied. In *Structure*, the composition and collaboration of the parser components are explained and represented with a summarizing figure. The *Consequences* section highlights the deliverables and warns about potential disadvantages of the pattern. In particular, the following aspects are examined: (1) the intermediate data structures used in the pattern and their memory consumption; (2) the clarity of the resulting component structure and the ease of modifications and extensions; (3) the level of expressiveness in the language that the pattern allows; (4) the reusability; (5) the extent of required compiler-specific knowledge; (6) the amount of code to be hand-written and the development time required and (7) the effort required to build and integrate the components in the system under construction. *Implementation* provides some guidelines or best practices to consider when employing the architecture. Last but not least are the *Known Uses* section, it presents an example and provides references, so that the application and implementation of the pattern can be grasped and later studied more efficiently.

Table 1 can be consulted for a short summary of the actors in the field of computer languages and their motivation in using this pattern catalog.

The figures included in the pattern descriptions use a loosely formalized, but intuitive graphical notation that explains the component structure and the data flow among components. We have not found a standard notation for this purpose that was intuitive enough. Our notation uses the following conventions: Program components are represented with rounded rectangles that include a “meshed gear or cogwheel” icon. Components supplied by third-party vendors have a double border. Generated components have a dashed border. Components that have to be hand-written have a single border. Input and output artifacts and intermediate data structures are represented by an arbitrary icon and are explained in the caption. Arrows show the information flow between components. Arrows with the gear icon denote that a component generates another.

In the following, these patterns will be discussed:

1. Ad-hoc Parser
2. Delimiter-Directed Parser

3. Multiple Pass Parser
4. Common Carrier Syntax
5. Parser Generator
6. Semantic Mapper Generator

Table 1
Motivations of actors in using the pattern catalog

Role	Focus	Expectations	Motivation
User	Software product	The specified requirements should be satisfied by the final software product.	Choosing the right architectural design can facilitate satisfying the requirements.
Domain Specialist	Input and output models	The expressiveness of the textual domain-specific language used in the system is high enough to properly model domain-specific artifacts and the syntax is intuitive and easy to use. Output models may have to meet similar criteria.	Architectural patterns influence the expressiveness of the language and the way they can be processed.
Developer	Code and component structure	The software can be developed in an easy and quick way. The code is easy to understand, to extend and to maintain.	The architectural pattern influences complexity and maintainability.
Tool Developer	Reusable tools	Providing market-ready tools that can be reused in real-life software products and can facilitate rapid software development.	Several pattern explained here are based on increasing abstraction by reuse. A good tool should leverage the advantages of these patterns while mitigating the weaknesses.

3.1 Ad-hoc Parser

Description The parser is a single monolithic unit. There is no explicit notion of grammar nor are there consecutive subtasks.

Motivation The complexity of the language does not require a higher-level pattern and it is desirable to avoid the development overhead of that.

This solution is often applied, if the performance of the system is so critical that higher-level patterns cannot be used because of their additional runtime overhead.

Applicability This kind of parser is only applicable with simple languages. If the language is such that it can be executed on-the-fly, we can keep memory usage low. On-the-fly processing means that the fragments of the script can be processed immediately, as they are read, and there is no need to store significant information about the context.

Structure The parser itself is a single unit that reads the input and processes it. It does not contain any common structural units. Figure 2 depicts an ad-hoc parser.

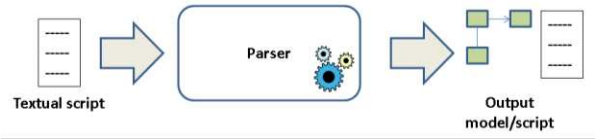

Figure 2
An ad-hoc parser

Consequences Because the parser is a single unit, there is no need for communication among components or building intermediate data structures. This reduces memory consumption and execution time.

Because of the lack of inner structures, the parser code may be difficult to understand, maintain and extend. If the language is likely to change in the future, the maintenance cost of monolithic parsers drastically increases.

The lack of inner structures and a systematic engineering process also implies that only low-complexity systems can be developed in this way. This greatly limits the expressiveness of the language.

The parser does not have reusable components but the low complexity leads to less time spent on its development.

Building an ad-hoc parser does not require specific knowledge in language theory or compiler engineering.

Implementation Because of the ad-hoc nature of the solution there is no general implementation structure. The specifics of the processed language must be checked in order to realize a practical implementation.

Known Uses In [9] Brian Kernighan demonstrates a simple implementation of the grep command-line utility. The grep utility expects a regular expression and looks for matching lines in the given input. The implementation explained by Brian Kernighan uses a limited subset of standard POSIX regular expressions but solves the matching problem on the fly with a minimal memory footprint. The code is apparently easy to understand because of the low complexity of the problem but once more advanced regular expression features are required, extension becomes a difficult task.

3.2 Delimiter-Directed Translation

Description The parser searches for separator symbols that separate the tokens of the input language script. The type of each token is then inferred by its position. The parser may build a semantic model in the memory, but it may also be possible to execute the language script on the fly.

Motivation The simple structure of the language does not warrant building a full-fledged parser that creates a substantial syntax tree in the memory. This can save memory and reduce execution time. The development overhead of syntax-directed parsers is also avoided.

Applicability The language can easily be split into tokens by looking for separator symbols and tokens can easily be interpreted by their position.

Structure The parser remains a major component, but it may also build a semantic model and pass it to an execution component. Figure 3 shows the structure of a delimiter-directed parser.

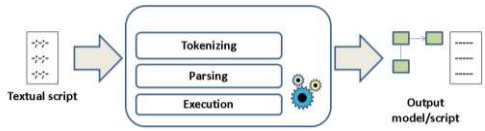

Figure 3
A delimiter-directed parser

Consequences The parser is fast, simple and has a minimal memory footprint because the lack of separate components avoids communication overhead and creating intermediate data structures.

Its code is somewhat easier to maintain, extend and understand when compared to ad-hoc parser since there is already a stream of clearly distinguished tokens, which are usually reflected in the code as array indexes. Although most languages use several different delimiters, if the syntax is more complex, it is not really easy to capture it with the delimiter-driven approach and the code also becomes difficult to read and modify. This limits the expressiveness of the language under design.

The parser does not have significantly reusable components but the low complexity leads to less time spent on coding. If structured well, the tokenizer may be reused.

Building a delimiter-directed parser does not require specific knowledge in language theory or compiler engineering.

Implementation Delimiter-directed parsers are frequently coded with a loop that reads statements one by one. This usually means reading the input line by line. Then, within a loop, the lines are split into tokens that are practically stored in an array or a list structure. Most programming languages also provide tokenizer functions. This may be followed either by populating a semantic model or a direct function call that processes the tokenized information.

Known Uses Comma-separated values (CSV) is a common file format that enumerates properties of entities. Each entity is described by its own line and the property values follow a specific order and are separated by commas or semicolons. Such a file can easily be processed by a delimiter-directed parser.

3.3 Multiple Pass Parser (Syntax-Directed Translation)

Description The notion of grammar is used to systematically create the parser that attempts to derive the input word from the production rules. The parser is usually divided into different logical components that prepare and perform this derivation and then map the resulting syntax tree to the semantic model. The number of the components may vary from parser to parser.

The development of the parser is driven by the grammar of the language but it is possible that the resulting code does not explicitly express the grammar.

Motivation The language is too complex, and parsing it with an ad-hoc parser or a delimiter-directed parser would be challenging.

Facilities for better maintenance and extensibility are required.

Applicability The pattern is always applicable; nevertheless the specific parsing algorithms have different limitations regarding the type of grammars they can handle. In general, a large subset of context-free grammars can be handled by choosing the appropriate algorithm. Parsing algorithms have different attributes with regard to the generality of the grammar, performance and memory consumption.

Structure The parser is composed of several components, and the following three are the most common: (1) the lexical analyzer, (2) the syntactic analyzer and the (3) tree parser.

A lexical analyzer provides a token stream for a syntactic analyzer, which in turn, builds a syntax tree. The syntax tree is quite a low-level construct that reflects the structure of the language itself but usually not the semantic meaning of the model. A third component may be used to map the syntax tree to the semantic model. Most often, a semantic model is provided although in some cases, the syntax tree may function as a semantic model as well. In Figure 4, we can see the workflow between the components of a multiple-pass parser.

Consequences Implementing the parser requires knowledge in compiler development.

Based on the chosen algorithm, the code may not explicitly reflect the grammar.

The parser can handle a wide subset of context-free grammars, the concrete limitations of which depend on the particular algorithm.

Based on the theory of formal languages, the parser can be algorithmically efficient. However, there are intermediate data structures used between the consecutive passes, which means that building them requires computational time and they increase the memory footprint.

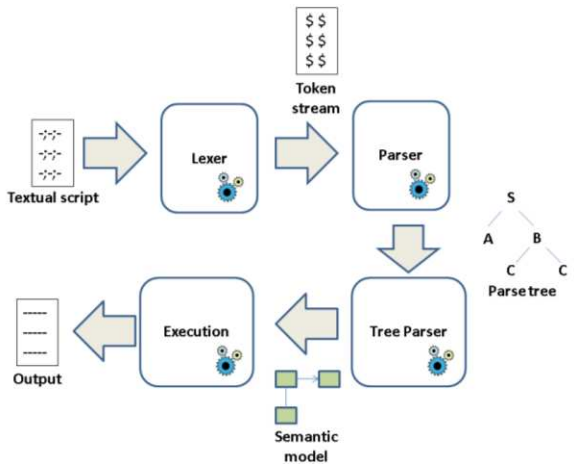

Figure 4
A multiple pass parser

Because of the systematic construction facilitated by the notion of grammar, the code is easier to maintain, to extend and to understand. The code may not always explicitly reflect the grammar, so the cost increases with future changes.

The separation of concerns achieved by the decomposition of the parser requires a lot of coding efforts and these components are only moderately reusable.

Implementation The lexical tokens are usually described by a regular language, which has limited expressiveness but this still increases abstraction and thus facilitates the implementation of the syntactic analyzer. The syntactic analyzer works with context-free languages and therefore can capture more aspects of the language than the lexical analyzer. In automata theory, context-free languages are recognized by push-down automata. It is not surprising that many implementations therefore use a stack data structure. A large set of algorithms uses a table-driven approach that requires a parsing table, which determines the action to take by examining the topmost stack symbol and the current input token. Other algorithms use recursive calls to capture a LIFO (Last In First Out) behavior, such as the recursive descent parser or the recursive ascent parser [10] [11].

Known Uses Most hand-written parsers of complex languages use multiple passes to simplify parsing and parser generators usually generate code using this abstraction.

3.4 Common Carrier Syntax (Syntax-Directed Translation)

Description The language syntax is composed of a limited set of language constructs, which makes it possible to reuse an existing parser. The available language constructs have a general nature so that a wide range of domain-specific languages can be expressed with it. An optional grammar description can further limit the syntax. In this context, such optional grammar will be referred to as vocabulary or schema. The parser then may have two inputs: the script to be processed, and its schema description.

Motivation The reuse of the fixed set of language constructs also makes the toolchain heavily reusable.

Using more uniform syntaxes among different languages facilitates standardization of the syntax and lowers the learning curve for new users.

The limited set of language constructs can be defined in such a way that facilitates efficient parsing.

Applicability The syntax of the language under design fits into the syntax that available common carrier syntaxes provide. This is usually the case when the language is read more often than modified. In this case, conciseness, in which these syntaxes usually fail, is not such an important aspect.

Identical or similar carrier syntax is used for other domain-specific languages in the environment where the language under construction is being developed. End users of the language are already familiar with the carrier syntax, which lowers the learning curve of the new language and the existing toolchain can be reused when it comes to processing scripts of a new language.

Structure From an architectural viewpoint, the inner design of the parser is irrelevant. It can be considered as a black box that has one or two inputs: the optional schema and the language script to parse. Depending on the intent of the tool, it may provide rich functionality of processing and transformations or simply the minimum required to transform the script into a syntax tree or any other language-independent data structure that will reflect how the elements of the language script relate to each other. Figure 5 shows how common carrier syntaxes are used to process textual scripts.

Consequences Implementing a language in common carrier syntax is easy; it consists of specifying how the previously defined syntax will be used to express model elements. This can be done with an informal description or with a schema language that places further limitations on the syntax, depending on the functionality provided by the underlying common carrier syntax.

Common carrier syntaxes may sometimes be too verbose, since the fixed elements of the syntax add some syntactic noise. This also has a negative effect on the readability by humans. The extent of this depends greatly upon the actual common

carrier syntax. This is often unwanted and a more concise and intuitive syntax is preferred despite the advantages of using a common carrier syntax.

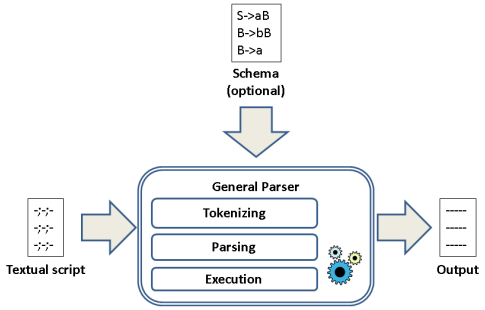

Figure 5
A parser of a common carrier syntax

Languages implemented in common carrier syntaxes are very easy to extend by modifying the (implicit or explicit) schema.

Using a common carrier syntax allows heavily reusing the parser and other tools used for language processing. Depending on our choice of the common carrier syntax, there may be numerous free and commercial implementations of parsing and processing tools. Because of the generality and constant development, these tools tend to be quite mature and efficient. Nevertheless, different processing libraries may have different APIs and different tools may be invoked with different options. This can make it practical to use a build management tool to integrate components. If there are good third-party tools available, coding may be required only for integration.

The standardization lowers the learning curve for each actor involved in the development and use of the software product under construction.

Implementation One well-known standard for common carrier syntaxes is the eXtensible Markup Language (XML) [12]. It has several schema languages available to define the vocabulary of our domain-specific languages, although not all of them are supported in each parser. It has a high number of related standards that assist in the transformation and processing of XML documents: XSLT [13], XPath [14], XQuery [15], and so on. XML is frequently criticized because of its verbose syntax, which is not the most convenient to write or read manually without specific tooling. On the other hand, its broad support and rich functionality make it a stable foundation for domain-specific languages.

Two possible alternatives to XML are YAML [16] and JSON [17]. Their syntax is more concise and they are also standardized. However, they lack the accompanying transformation and processing standards, and that highly reduces their functionality. They also lack standard means of specifying a schema, although there are third-party solutions to define constraints.

Known Uses MathML [18] is an application of XML to create a language that can describe mathematical formulae. The language itself is defined using the XML Document Type Definition (DTD) schema language. Browsers and rendering software that support MathML leverage existing XML parser libraries. Although the syntax of MathML is quite verbose, the XML nature of it makes it possible to simply embed formulae into web pages or to process them with XML tools.

3.5 Parser Generator (Syntax-Directed Translation)

Description A parser generator software is used to generate a multiple pass parser from the grammar description. The grammar is specified within the own notation of the parser generator and this description is used to generate a parser using a widely applicable parsing algorithm. Production rules in the grammar can usually contain the so-called semantic action routines that are code fragments written in the target programming language. These code fragments are generated into the output code and are run when a particular language element is recognized. It makes possible for the programmer to build a syntax tree or to populate a semantic model.

Motivation The language is complex enough to warrant a syntax-directed parser; however, either the development team is not skilled in writing parsers or the parser does not need to be highly optimized or customized. Using a parser generator, the development time of the parser is usually low.

Applicability The language can be parsed with the available general parsing algorithms and the performance of such a solution will suffice. Also, there are available parser generators that suit the requirements or building such is affordable.

Structure The parser generator takes the grammar description, which may contain additional information about generation parameters, for example, target programming language in which the parser is implemented, the package name in case of Java code, and so on. The generator then outputs one or more software components that are used to parse scripts and build a syntax tree or a semantic model. In Figure 6, we can see a system that uses a parser generator.

Consequences The build process of the parser is more complex because of the code generation step.

The programmer must write the grammar that provides a higher-level view of the language and does not have to deal too much with the lower-level code. One exception is writing the semantic action routines if the default parse tree built by the generated parser needs to be customized. This lowers the learning curve, limits hand-written code and allows for the rapid development of parsers.

Semantic action routines are foreign code in the grammar description. Since they are factored out from their context, they cannot be properly validated. Besides, scattering also makes these code pieces difficult to understand. The overall effect of them may not be easily recognized, which can make the development process more error-prone and the debug process more difficult.

The generated code is usually a multiple-pass parser, which means that the memory footprint will be high because of the large data structures used in the parsing process.

The parser generator tool is highly reusable.

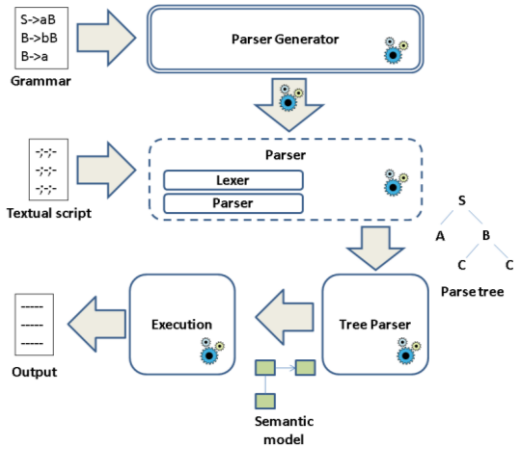

Figure 6

A parser system using a parser generator

Implementation There is a vast diversity among parser generators. They differ in the target language(s) they generate, in the grammar notation used to specify the syntax and in the particular parsing algorithm they use (which also implies different limitations on the syntax). They may generate a lexer or may also support the use of a hand-written lexer. Some parser generators generate table-driven code and fill in parsing tables according to the specified grammar while others may generate a recursive algorithm. Some parser generators may also support so-called syntactic predicates [19] which are additional notations intermixed with the grammar and can control certain parsing-time behavior that cannot be inferred from the production rules of the grammar.

Known Uses ANTLR [20] [21] [22] is one of the most popular parser generator tools, which is implemented in Java but can generate parsers in several target languages. It generates an LL(*) [23] parser, which is a top-down parser with arbitrary look-ahead length, then implements it with a recursive descent approach. It handles a wide subset of context-free grammars, although, because of the top-down nature, it cannot handle left-recursion.

3.6 Semantic Mapper Generator (Syntax-directed Translation)

Description Suppose that we already have an appropriate metamodel and we want to use a parser generator because of the advantages discussed earlier. Since the metamodel is fixed, it is possible to build such a parser generator that also generates a tree parser, not just a syntactical analyzer. The grammar has to be extended with additional mapping notation that specifies how language constructs are mapped to elements of the semantic model. This solution allows us to define this mapping at a higher level and to generate code instead of manually developing the tree parser.

Motivation Having a parser that directly outputs a semantic model increases abstraction and reduces hand-written code by leveraging generative programming [2].

Semantic action routines used in parser generators (see Section 3.5) lead to scattered code, which is difficult to read and the overall effect is not obvious; therefore this is an error-prone technique. Generating a parser that directly populates the semantic model overcomes this.

Applicability The metamodel of the semantic model is known, and there exists a tool that can map the language elements directly to the semantic model or, if this is not possible, the development of such a tool is an affordable option.

Structure The semantic mapper generator takes a grammar with semantic mapping information. It generates a semantic mapper that goes through the parsing process and builds an in-memory semantic model. This model is an instance of the used metamodel and also reflects the model information stored in the language script. The generated semantic mapper may be a monolithic unit or may be implemented as consecutive passes of parsing, like lexical analysis, syntactical analysis and tree parsing. The architecture that uses a semantic mapper generator is depicted in Figure 7.

Consequences The build process of the parser is more complex due to the code generation step.

Since the semantic model is built by the generated semantic mapper, there is no need for extra programming, such as using semantic action routines. This lowers the learning curve, eliminates hand-written code in the parsing phase and allows for rapid development of language parsers.

The generated high-level code may impede customizing finer-grained, inner behavior and thus may have an average performance or memory footprint.

The metamodel used by existing semantic mapper generators may be limiting and the alternative, developing a new semantic mapper generator for a custom metamodel may lead to (significantly) higher costs.

The generated code is usually a multiple-pass parser, resulting in a larger memory footprint for the data structures required for parsing.

The semantic mapper generator tool is highly reusable.

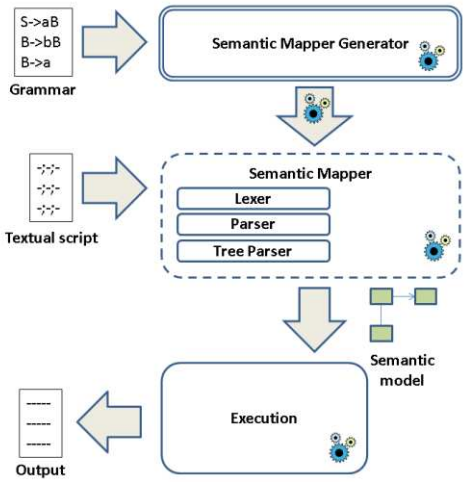

Figure 7
A parser system using a semantic mapper generator

Implementation Most consequences listed in Section 3.5 also apply to semantic mapper generator. Moreover, the grammar must be extended with extra notations that define how language constructs are mapped to the semantic model. Since general parsing algorithms build a syntax tree, designing such a notation has to practically account for the structure of the parse tree. An intuitive implementation idea is used by the Eclipse Xtext [24] project; it maps non-terminals at the left-hand side of parser rules to entities and uses assignment operators, inside the same rules, to assign certain parts of the right-hand side of the rule to properties of the same entity. When these assignments refer to a terminal substitution, a property with a primitive data type will be inferred or when referring to a non-terminal substitution, an association is assumed.

Known Uses The Eclipse Xtext project can be used to create languages. When the language scripts are parsed, it either populates an existing EMF[2] [25] model or infers a new one. This existing or inferred model will be populated with modeling information obtained from the language script. In this case, the known metamodel is EMF; all of the entities, properties and associations are mapped to EMF constructs, which can later be processed with a wide range of tools that work with EMF models.

[2] EMF is a metamodeling framework for the Eclipse platform.

Conclusions

In this paper, we have provided a catalog of architectural-level design patterns that can be used to create parsers of computer languages. This catalog summarizes the most important characteristics, motivations and consequences, which can facilitate the engineering work with these kinds of software products. The focus has been limited to the field of parsing, which is a small but important subset of language- and model-processing. Consequently, only architectural-level patterns have been included into the pattern catalog. Table 2 summarizes the most important characteristics of the discussed patterns. We have also shown actors in the industry that are involved in parser development, what their motivations are, and how this pattern catalog can help them to achieve their goals. We believe that the pattern catalog can greatly assist those involved in the industry. Nevertheless, we are also aware that these patterns only help in commencing to design a parser, and do not provide information regarding the more specific details concerning implementation. Potential future work on design patterns for language parsing and modeling could include lower-level best practices in the field of parsing and other common subtasks of model-processing.

Table 2

A summary of the characteristics of the discussed patterns

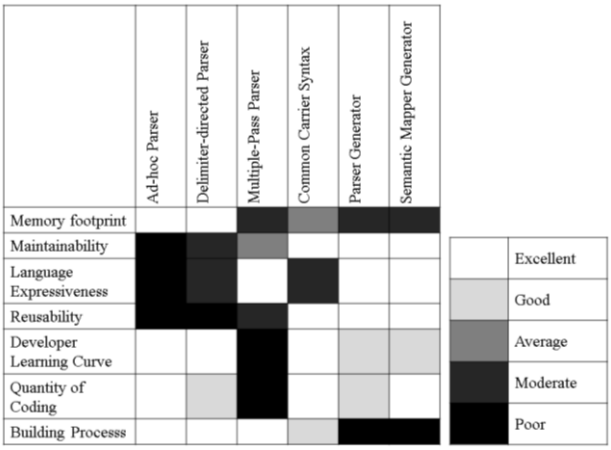

Acknowledgement

This work was partially supported by the European Union and the European Social Fund through project FuturICT.hu (grant no.: TAMOP-4.2.2.C-11/1/KONV-2012-0013) organized by VIKING Zrt. Balatonfüred.

References

[1] Fowler, M.: Domain-Specific Languages. Addison-Wesley (2010)

[2] Kelly, S., Tolvanen, J. Domain-Specific Modeling: Enabling Full Code Generation. Wiley - IEEE Computer Society Publications (2008)

[3] van Deursen, A., P. Klint, J. Visser. Domain-specific Languages: an Annotated Bibliography. ACM SIGPLAN Notices. June, 2000

[4] Gamma, E., Helm, R., Johnson, R., Vlissides, J.: Design Patterns: Elements of Reusable Object-Oriented Software. Addison-Wesley (1995)

[5] Nguyen, D., Ricken, M., Wong, S.: Design Patterns for Parsing. In: 36th SIGCSE Technical Symposium on Computer Science Education, pp. 477-481, ACM New York (2005)

[6] Schreiner, A. T., Heliotis, J. E.: Design Patterns in Parsing. In: 10th IEEE International Symposium on High Performance Distributed Computing, pp. 181-184, IEEE Press, New York (2001)

[7] Hopcroft, J. E., Motwani, R., Ullman, J. D.: Introduction to Automata Theory, Languages and Computation. Addison-Wesley (2001)

[8] Aho, A. V., Lam, M. S., Sethi, R., Ullman, J. D.: Compilers: Principles, Techniques, & Tools, Second Edition, Addison-Wesley (2007)

[9] Oram, A., Wilson, G.: Beautiful Code: Leading Programmers Explain How They Think. O'Reilly (2007)

[10] Morell, L., Middleton, D.: Recursive-ascent Parsing. Journal of Computing Sciences in Colleges, Volume 18 Issue 6, June 2003, pp 186-201

[11] Roberts, G. H.: Recursive Ascent: an LR Analog to Recursive Descent. ACM SIGPLAN Notices. New York (1988)

[12] Extensible Markup Language (XML) 1.0, http://www.w3.org/TR/xml/

[13] XSL Transformations (XSLT) Version 1.0, http://www.w3.org/TR/xslt

[14] XML Path Language (XPath) Version 1.0, http://www.w3.org/TR/xpath/

[15] XQuery 1.0: An XML Query Language, http://www.w3.org/TR/xquery/

[16] YAML Ain't Markup Language Version 1.2, http://www.yaml.org/spec/1.2/spec.html

[17] Introducing JSON, http://www.json.org/

[18] Mathematical Markup Language (MathML) Version 3.0, http://www.w3.org/TR/MathML3/

[19] Parr, T. J., Quong, R. W.: Adding Semantic and Syntactic Predicates To LL(k): pred-LL(k). CC '94 Proceedings of the 5th International Conference on Compiler Construction. London (1994)

[20] Parr, T. J., Quong, R. W.: ANTLR: a Predicated-LL(k) Parser Generator. Software—Practice & Experience. Volume 25 Issue 7, July 1995, pp. 789-810

[21] Terence, P.: The Definitive ANTLR 4 Reference. Second Revised Edition. Pragmatic Bookshelf (2013)

[22] ANTLR, http://www.antlr.org/

[23] Parr, T., Fisher, K.: LL(*): the Foundation of the ANTLR Parser Generator. PLDI '11 Proceedings of the 32nd ACM SIGPLAN Conference on Programming Language Design and Implementation. New York (2011)

[24] Eclipse Xtext, http://www.eclipse.org/Xtext/

[25] Eclipse EMF, http://www.eclipse.org/modeling/emf/

Review of Development Stages in the Conceptual Design of an Electro-Hydrostatic Actuator for Robotics

Velibor Karanović, Mitar Jocanović

University of Novi Sad
Faculty of Technical Sciences
Trg Dositeja Obradovića 6, 21000 Novi Sad, Serbia
e-mail: velja_82@uns.ac.rs; mitarj@uns.ac.rs

Vukica Jovanović

Old Dominion University
Mechanical Engineering Technology
111-D Kaufman Hall
Norfolk, VA 23529, USA
e-mail: v2jovano@odu.edu

Abstract: The design of modern robotic devices faces numerous requirements and limitations which are related to optimization and robustness. Consequently, these stringent requirements have caused improvements in many engineering areas and lead to development of new optimization methods which better handle new complex products designed for application in industrial robots. One of the newly developed methods used in industrial robotics is the concept of a self-contained power device, an Electro-Hydrostatic Actuator (EHA). EHA devices were designed with a central idea, to avoid the possible drawbacks which were present in other types of actuators that are currently used in robotic systems. This paper is a review of the development phases of an EHA device for robotic applications. An overview of the advantages and disadvantages related to current EHA designs are presented, and finally possible ideas for future developments are suggested.

Keywords: electro-hydrostatic actuator; hydraulics; robotics

1 Introduction

As a scientific area, robotics and its application have achieved a very high level of development and are present in almost all human activities. The intention of mankind, to assign precise, heavy and dangerous routine and non-routine jobs to

machines, has prompted the development of science and engineering, robotics included [1-6]. Application of robotics has allowed accurate, precise and highly efficient performance of such work tasks, with or without human interference.

With the aim of performing the designated tasks with utmost efficiency, robotic applications should have following characteristics: functional design, optimized control unit and adequate power drive unit (an aggregate). Functional design pertains to design solutions which allow simple robot control for the most efficient realization of tasks (functions). Control units should provide reliable, adjustable and efficient control of a robot in any situation. Finally, power a drive unit, using one or a combination of energy sources (electric, pneumatic, and hydraulic), is tailored to match the given task and operating conditions. In order to achieve maximum working performance and avoid drawbacks of classical drive units, various authors have contributed to research and development of combined robotic drive units [7-13]. One such example is the development of the combined electro-hydrostatic drive (EHA – Electro-Hydrostatic Actuator).

As a self-contained power device [14] the Electro-Hydraulic/Hydrostatic Actuator (EHA), was first developed and patented in 1950s to actuate landing gears, wing flaps or other movable parts of an aircraft. Generally, the EHA device was designed to suit applications in which smaller size and weight-to-power ratio are required (for example hand and leg prosthesis, exoskeletons, etc.). Considering the advantages and drawbacks of EHA, scientists and engineers have subsequently investigated various possibilities to adapt EHA for different applications.

The goal of this paper is to present an overview of those research papers which deal with the application of combined electro-hydrostatic actuators in robotics. The combination of various drive types is aimed towards achieving the best possible task performance, as well as some other benefits which are difficult to attain using conventional drives. The second section of this paper provides an overview of important contributions in this area. In the third section presents a critical review of the advantages and disadvantages of EHA devices previously discussed in the paper and in the last chapter, the conclusions and possibilities of further development of EHA units are discussed.

2 A Review of EHA Development

Design problems related to current drive systems in robotics are very frequently a research focus in the advancement of energy consumption efficiency. Hydraulic drives are usually used in a robust robotic applications which perform tasks under heavy workloads. However, thanks to the improvements in advanced manufacturing technology, the use of hydraulic drives in miniature robotic systems is increasing. These new, miniaturized solutions are developed for the purpose of maximum efficiency and better exploitation of available resources (materials, size, energy, etc.).

Power-by-Wire technology was developed for aerospace industry [15] and further refined and improved to adapt EHA devices for industrial applications in robotics. The integration of hydraulic components which work with electrical components that control the hydraulic system, resulted in a number of advantages. Some of these were related to improved flexibility during operation, decreased energy use, smaller size, higher power-to-mass ratio and improved continuous control of operating parameters under high external payloads. Significant technological advances in manufacture of hydraulic components along with improved integration of embedded systems, lead to new applications of hydraulics in robotics. New materials and new manufacturing technologies allowed manufacture of miniature hydraulic components, thus saving space and decreasing loads on the structure, while designed to sustain large enough forces to perform tasks. Beside their tighter tolerances, the miniature components also had a minimum oil leakage, provided that assembly was well completed and that maintenance was timely.

Hydraulic system designs, similar to EHA, are used in large and massive robots. One such application is the vehicle with adaptive suspension [16-18], which is the result of a military scientific project conducted at the University of Ohio during the eighties of the twentieth century. Some time later, Bobrow published his paper on the development of a hydraulic drive for robotic applications [19]. The paper was an attempt to solve the problem which occurs when trying to control high torques using a combination of electric motor and gear train transmission. This problem was basically caused by friction and backlash [20] (due to present clearance between meshed teeth), which is inherent to gear transmission. In case when gear train transmission is not present, the torque has to be controlled directly by electric motor, with high accuracy. However, high torques are not possible without the use of electric motors and power amplifiers (which leads to an increased overall dimensions and higher mass) [19]. Moreover, electric motors and power amplifiers have unstable efficiency rates in case of short bursts of maximum electric motor power. The mentioned friction between gear teeth causes not only energy losses, but also material wear. The material wear further causes changes in component geometry which has influence on gap increase, decreasing the positioning accuracy and precision.

According to Pastrakuljić [21], power transmission in a hydrostatic system can be realized in two ways: by using distribution valves or a variable displacement pump. Control by distribution valves is often used in industry but has limited flexibility. Pastrakuljić also points out drawback while using single and double-acting cylinders. The difference in piston surface areas which are under pressure, results in the difference in piston rod forces and extension or retraction speeds. This problem can be partially solved using a differential distribution valve, whose ratio between the cross section areas of branches is proportional to the cross section areas ratio of piston with the single-action piston rod [21]. However, differential distribution valve solves the problem of piston rod extension or

retraction speed, but has no effect on the force. This can be remedied using a double piston cylinder, bearing in mind that this solution is not always applicable due to spatial restrictions. Another type of power transmission control in a hydrostatic system is based on a pump which performs two roles: generates flow and controls operation of a hydraulic cylinder or motor. This principle lies behind the EHA concept. Simplified, EHA system represents a closed hydraulic circuit where the pump is directly connected with the hydraulic cylinder or motor. Within such concept, actuator can be controlled in several ways. Fig. 1a) shows the most simple type of closed hydrostatic circuit with the installed pump and hydraulic motor of constant displacement, with no control of work speed. Figure 1b) shows a system with variable displacement hydraulic motor. Therefore, it allows control of work speed by varying the displacement of hydraulic motor work chambers which is performed by a mechanism installed within the hydraulic motor. Illustrated in Fig. 1c) is the case which is most frequently used in practice – it features a variable displacement pump and a constant displacement hydraulic motor. Fig. 1d) illustrates a system with variable displacement pump and hydraulic motor, which provides optimal system adjustment with minimum losses. However, the system is very complex to control and therefore rarely used in practice.

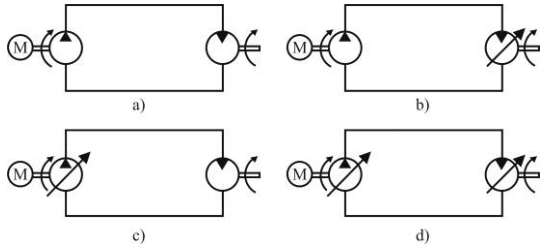

Figure 1
Types of hydraulic power transmission in a closed circuit [21]

An EHA design is based on a closed hydraulic circuit with a built-in bidirectional variable-displacement hydraulic pump, powered by an electric motor, and a bidirectional constant-displacement hydraulic actuator (cylinder or motor). There are two ways to control the pump displacement. The first, standard way of control, is to use the pump capable of regulating the volume of work chambers (servo pump), such as the axial piston pump with the swash-plate or vane pump and radial piston pump with variable eccentricity (distance between rotor and stator axes). Another way to control pump displacement is to adjust the number of revolutions using drive electric motor (servo motor) [15] (Fig. 2).

Linear, electrically actuated pump control was used in laboratory tests of EHA device, performed by Pastrakuljić [21], Habibi and Goldenberg [22, 23] (Fig. 3). The downside of such approach to control is the dead-band which occurs during the inversion of electric motor rotation [22].

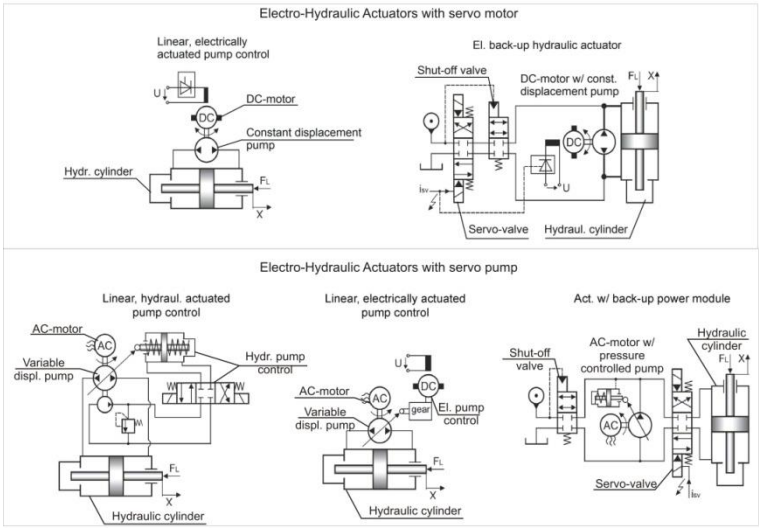

Figure 2
Control configuration of EHA system [15]

The dead-band represents magnitude of voltage or current values, for which the electric motor gives no response, and can be compared to backlash of gear transmission. In order to alleviate this effect, an adequate electric motor control system has been developed. For use in EHA system, Habibi proposes a gear pump which, compared to piston pumps, provides a more even flow at the discharge duct.

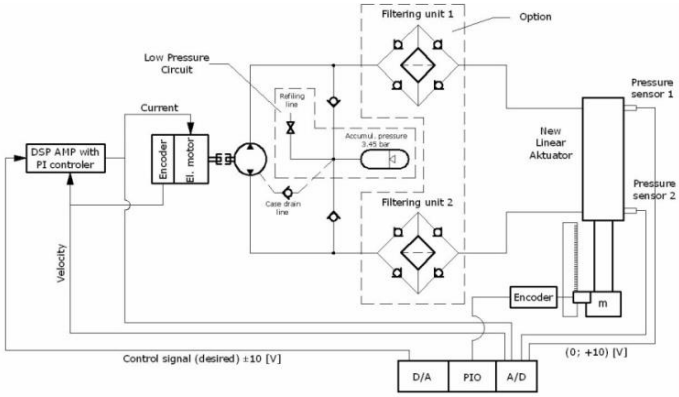

Figure 3
Scheme of EHA system [21]

Contribution to the development of EHA concept design for robots, has been made by Alfayad et al. [24-26]. His proposal is an answer to the already mentioned basic drawbacks of electromechanical, and also hydraulic drives. He

points out the drawback which pertains to the lack of centralized supply of hydraulic energy. An example of centralized energy supply is CB (Computational Brain) humanoid robot [27] or Big Dog, the quadruped robot developed by Boston Dynamics [28]. The basic flaw of the centralized system is that it has to satisfy the maximum load requirements of all the hydraulic actuators installed in a robot. Even with optimized design solutions of centralized hydraulic aggregates it often happens that their overall dimensions and mass are significant. It should be noted that control valves for hydraulic actuators also contribute to the increase of mass and overall dimensions of design solution. Bearing in mind that the actuators are located in robot joints - where they provide required element movements – it is necessary to connect them to the central aggregate by pipe line and/or hose line. This, in turn, increases the chances of hydraulic losses due to oil leaks or oil flow through the pipe line/hose line and the connectors. These unwanted effects are further exacerbated when using hydraulic hoses which run through the joints to connect actuators with the aggregate [25]. However, their use is required if the actuator is at some distance from power unit, and fixed to the element which performs movement during robot operation. The discussed flaws have prompted the research and development of the novel Integrated Electro-Hydraulic Actuator (IEHA) [25, 26]. The idea behind IEHA concept is based on two fundamental requirements. The first is to integrate hydraulic components (pump, reservoir, electric motor, pressure and position sensors) into a device which occupies small space and have bigger ratio power to weight, while the other is to simplify device control.

It has always been the problem to integrate robust and massive hydraulic components into sophisticated devices of miniature dimensions. Of course, such task can be realized at a high price. Nowadays, thanks to high technological development, miniature hydraulic components are a part of standard offer on the market, which has significantly reduced component prices. Thus, hydraulic components and systems are becoming attractive and are increasingly studied and researched within the area of robotics.

Small-space integration of IEHA components represents the realization of the decentralization principle. Owing to decentralization, each joint has its own IEHA installed, becoming an autonomous unit controlled by a centralized control system. The advantage is in avoiding the use of pipe lines and hose line to connect actuators and the aggregate which cancels the leak losses due to flow of work fluid through pipes/hoses. Also worth noting is the fact that each IEHA is sized according to host joint requirements. This significantly increases the aggregate efficiency rate of the system.

Another important characteristic of the IEHA concept is the simplified control process. In contrast to Habibi, Alfayad et al. propose pump displacement control by means of a mechanical–hydraulic regulation components built into the pump [24]. Evidently, the pump design must be adjusted to accommodate regulation components. This significantly simplifies the control of electrical motor drive,

considering that the rotor maintains constant number of revolutions. In the discussed case, a radial piston pump was used which – using certain (fixed) values of eccentricity – achieved flow and output pressure whose relation is shown on the diagram (Fig. 4).

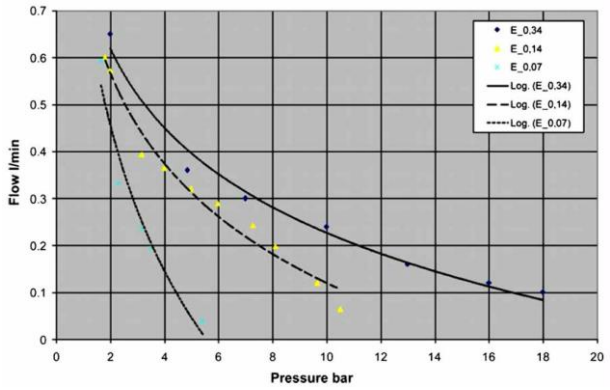

Figure 4

Relation of output flow and pressure values of IEHA for three eccentricity values (*E = 0.34; 0.14; 0.07 mm*) [25]

Experimental test of IEHA includes the lifting of 25 and 38 kg weights at 20 mm/s, where the cylinder piston is 20 mm in diameter and length of the piston rod is 120 mm. The same speed was obtained with both tests [25]. These results show potential capabilities of IEHA in terms of power-to-mass, and power-to-volume ratio. The specifications and real parameters of the manufactured IEHA prototype are given in Table 1.

Table 1

IEHA specifications [24]

Parameter	Value	Unit
Size LxWxP	80x40x40	mm
Weight	1000	g
Eccentricity	± 0.5	mm
Number of pistons (N)	20	-
Rotation speed (ω)	3000	RPM
Piston radius (R_p)	1.5	mm
Flow (Q)	± 500	cm^3/min
Pressure (P)	50 - 100	bar

In order to advance robot interaction with humans and environment, Kargov et al. designed a robotic hand prosthesis with hydraulic drive [29, 30]. Although based on the use of a centralized hydraulic system, their investigation emphasizes the need to miniaturize hydraulic components and points out their efficiency (Fig. 5).

In this paper, miniature components were made, enabling the hydraulic system - consisting of the pump, reservoir, control valves, electric motor drive and control unit - to be built into the natural-size robotic hand prosthesis. Moreover, its compact size and functionality allowed maximum performance.

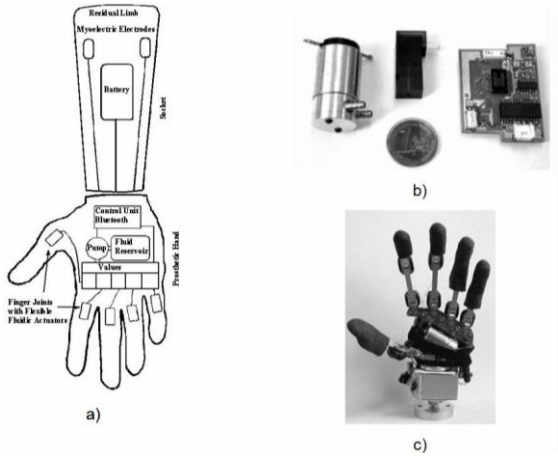

Figure 5

a) Schematic view of Kargov prosthetic hand; b) Size comparison of hydraulic pump (left); micro-valve (middle) and microcontroller (right) with a coin; c) Look of prosthetic hand [30]

Parallel to Kargov's work, Kaminaga et al. experimented with the application of electro-hydrostatic actuator on knee-joints and a robotic hand for a humanoid robot [31, 32]. The goal of this investigation was to achieve certain degree of adaptability of the mechanisms which generate robot movements, in situations when the robot interacts with humans or objects within its environment. In order to achieve the desired degree of adaptability, which allow the robot to simulate human-like reactions, when facing an obstacle. The built-in mechanisms generate human movements, with a convenient degree of back-drivability. Failing this requirement is liable to cause errors such as the displacement or breakage of the encountered object (obstacle), damage to the robot, positioning error, etc. The very ability of back-drivability gives the advantage to hydrostatic systems compared to their electric counterparts, since they are able to control the direction, sense and speed of movement under significant payloads. In confirmation of this claim, Fig. 6, shows a comparison between electro- and hydrostatic systems, relating their reaction speed, i.e., achievement of power unit per time unit. Additionally, the reliability of EHA device could be improved by use of vibrotactile force feedback strategy [33].

Beside the back-drivability, the paper [31] also points out the principle of modularity which facilitates assembly and disassembly of the system, thus improving maintenance.

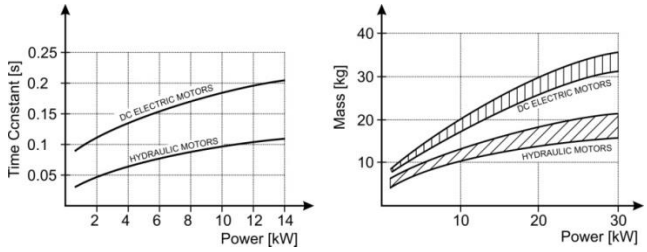

Figure 6
Time/Power and Mass/Power relationship for electrical and hydraulic motors [34]

Beside the back-drivability, the paper [31] also points out the principle of modularity which facilitates assembly and disassembly of the system, thus improving maintenance. Specially emphasized, as the advantage of hydraulic systems, is the fact, that a pressure increase leads to size reduction of hydraulic components, thus, contributing to diminished mass of the overall robot design. However, for the design solution proposed in this paper, pressure increase is limited due to use of hydraulic hoses. Hydraulic hoses are a flexible connection and are used to provide mobility of the hydraulic motor. At the same time, hydraulic hoses are a drawback for two primary reasons. Firstly, they are not fixed and are therefore potential obstacle to the movable elements during robot operation, and secondly, due to work pressure fluctuations, they are susceptible to breakage, which results in fluid leakage and pressure drop. Shown in Fig. 7, is a scheme of hydraulic system used to motorize robotic hand designed by Kaminaga. The hydraulic system of the anthropomorphic robotic hand is fairly simple. It is a closed hydraulic circle, which consists of a bidirectional trochoidal pump and constant displacement vane motors, one for each finger. To prevent oil deficiency and pump cavitations, due to leakage in components, additional oil supply is provided by the charge (or fill-in) pump.

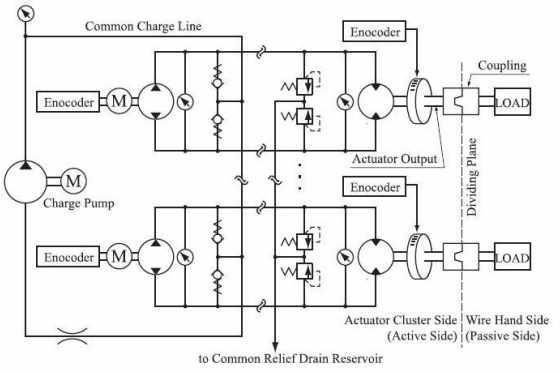

Figure 7
Anthropomorphic hand hydraulic scheme [31]

In addition to pumps and motors, each closed hydraulic circuit has two pressure limiting valves (security valves). These valves react to unexpected work load (pressure) spikes in the discharge duct, which occur, for example, when a robot confronts an obstacle. According to practical experience, the pressure limiting valves are set to the value 10% higher than the maximum work pressure. Actuators' work speeds are controlled by a pump regulator device or drive electric motor whose direction and speed of rotation are adjusted to the pre-set and measured values of pressure, force and speed.

The similar design of electro-hydrostatic actuator, as shown in Fig. 7, was used for the knee power augmenting [35-37] to improve physical strength of a human, requiring less skills for effective operation (Fig. 8).

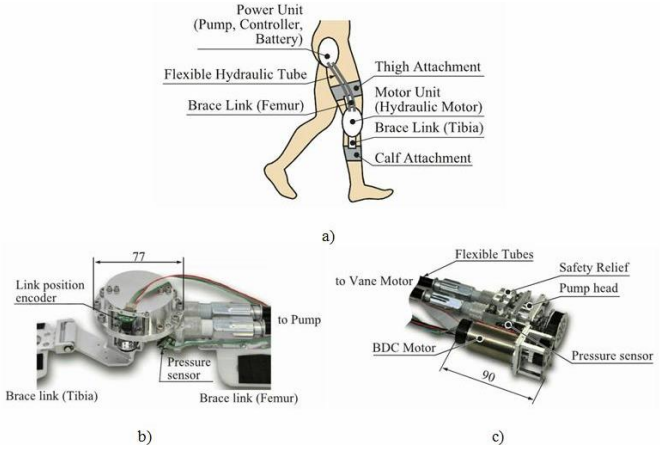

Figure 8

a) Knee power assist with EHA; b) Hydraulic motor; c) Hydraulic pump unit [35]

To decrease weight of device, instead of charge pump, in this installation was used pressurized accumulator to prevent oil deficiency and pump cavitation. Also in [36] was proposed use of developed low- impedance controller, which combines inertia scaling and disturbance observer based friction compensation. The controller have a task to compensate pump friction or pressure loss due to fluid friction that occurs in hoses. Specifications for actuator used in [35-37] are given in Table 2.

Table 2

EHA specifications [35]

Parameter	Value	Unit
Oil viscosity	100	cSt
Weight	1124	g
Pump displacement	0.36	cm^3/min
Motor displacement	24	cm^3/min

Maximum speed of motor (ω)	55	RPM
Maximum torque of motor (M)	30 at 10 rpm	Nm
Maximum operating pressure (p)	46	bar

Testing results of the power augmenting device show that the energy consumption of operator was reduced by 25% [36].

To improve back-drivability of an EHA and reduction of friction between sliding mechanical components of the pump, Kaminaga [38, 39] proposed use of viscous screw pump (Fig. 9), that transfers mechanical kinetic energy to fluid kinetic energy with viscous friction of the fluid. Screw pumps have some advantages over gear, vane and piston pumps such as small friction, high speed operation and very small pressure and flow pulsations. This is important in order to achieve smooth force control.

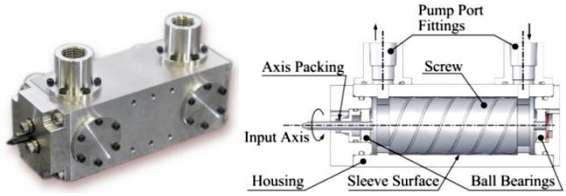

Figure 9

Outlook and cross section of developed screw pump design [38]

Evaluation of the developed screw pump performance is shown in Fig. 10. Linearity is present between the flow rate and pressure changes for each applied torque.

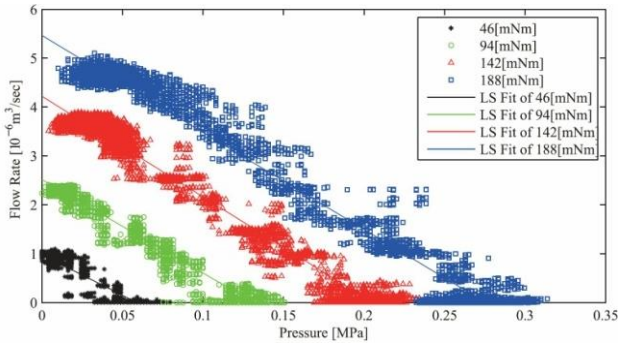

Figure 10

Result of pressure-flow rate characteristics evaluation. LS fit shows the lines fit with least-square method [38]

The presented mechanical design of the screw pump prototype achieved maximum discharge pressure of 12 bar and maximum flow rate of 3 cm^3/min. Also, the screw pump achieved 30% reduction of the pulsation against the trochoid pump in the worst case, while the total back-driving torque was one third

that of the case with the trochoid pump, which significantly improved efficacy and back-drivability of EHA. Design parameters of the screw pump are shown in Table 3.

Table 3
Screw pump specifications [38]

Parameter	Value	Unit
Oil viscosity	100	cSt
Axial screw length (l_t)	62	mm
Bore diameter (d_t)	28	mm
Groove width (w_c)	9	mm
Groove depth (h_c)	0.5	mm
Ridge width (w_b)	1	mm
Screw-sleeve gap (h_g)	15	μm
Number of helices (n_t)	3	-
Reduction before pump	2	-

Authors of this paper think that, implementation of condition monitoring in hydraulic systems, such as EHA/IEHA for robotics can significantly increase reliability and safety, and decrease maintenance costs. As the result of his investigation, Chinnah [40] developed an approach to monitoring relevant parameters using extended Kalman filter in order to increase reliability and efficiency of EHA devices. More precisely, he monitored two important parameters – bulk modulus and viscosity modulus, and their influence on EHA performance. The reduction of effective bulk modulus, as the result of the air in work fluid, significantly affects the response speed of EHA device, which reduces its stability in operation. On the other hand, the change in viscosity modulus indicates fluid contamination, sealant wear and/or wear of functional surfaces on components, which also impacts EHA operating efficiency. Sampson [41] also contributed to the development and improvement of EHA robot devices by investigating the possibility to achieve high positioning accuracy, which is measured on a nano scale. He employed fuzzy logic to provide control of positioning accuracy regardless of the magnitude of work forces and lengths of working strokes, taking into consideration Coulomb friction. The EHA control model was also advanced by contribution of Lin [42], who worked on the development of a controller which considers both the influence of friction and other non-linear parameters.

3 Advantages and disadvantages of EHA/IEHA units

From the presented research, summarized in this literature review, it is evident that researchers have put significant effort into investigation and development of novel actuator devices in robotic systems. A focus was placed on analysis of

previous research related to the development of a hybrid solution of actuator which yields high operating performance and meets numerous requirements of robotic systems users from various domains – robotic prosthesis for human limbs, humanoid robots, military applications, etc.

Although electric motors are reliable, compact and controllable, they suffer from deficiencies which render them incomplete despite the fact that they are the most frequently used actuators for robotic applications. Owing to their favorable features, hybrid (combined) electro-hydrostatic actuators can compensate for those deficiencies. Application of EHA/IEHA eliminate two important deficiencies: backlash (which are the result of tolerances of nominal dimensions and in-service wear of components used for power transmission – gear trains) and the small power-to-mass ratio.

EHA/IEHA unifies a number of characteristics which meet requirements of modern robotic systems. According to laboratory tests reported by previously mentioned authors, EHA/IEHA successfully meets requirements such as: accuracy, precision, simple control, ability to integrate, modularity, flexibility, compactness, energy efficiency, small mass, continuous control of rotation direction under high payloads, etc.

The concept of EHA/IEHA application requires that every joint or movable component has its own self-contained drive unit, which allows its independent operation even in case when some of the joints' drives fail (according to the principle of decentralization). This is not achievable with the centralized hydraulic aggregate, where, in case of its failure, the hydraulic system is out of service. Decentralization principle is also beneficial to maintenance. It is simpler and faster to replace a compact device installed within a joint, than to replace a complete central aggregate. One of the main drawbacks of the conventional hydraulic systems is that they rely on the central hydraulic aggregate. The central aggregate consists of one or more hydraulic pumps, which are actuated by one or several electric motors (or internal combustion engine, in case of a mobile application), and a spacious reservoir filled with hydraulic oil. The pump, electric motor and reservoir must be sized to meet requirements of all the actuators installed within robotic application. On the down side, this contributes to increase of robot design overall dimensions and mass.

The drawback of hydraulics, mentioned in reference [22], is variable pressure, which significantly affects accuracy and precision of robot operation. In addition to positioning accuracy, this phenomenon can affect the durability of individual components, e.g., hydraulic hoses. Pressure oscillations can lead to premature failure of hydraulic hoses. Such fluctuations can never be entirely eliminated, but certain contemporary solutions can greatly alleviate the problem. Available solutions include application of accumulator, Helmholz resonator, adaptive hydro-pneumatic pulsation damper, etc. [43-45].

One of the often considered drawbacks related to hydraulic components, are the internal and external fluid leaks. Internal fluid leak means oil flow from high- to low pressure zone (within components), while the external leak occurs outside the system, into environment. Increased presence of leaks affects total efficiency rate of individual hydraulic components, and the entire system. Hydraulic oil leaks increase either due to increase of the clearance between component work elements, or due to lower viscosity of hydraulic oil. Although modern seals are made of advanced materials - while the tolerances are ever tighter, either as the result of miniature hydraulic components, or increased accuracy and precision - friction is always present during operation as the result of the wear of contact surfaces. This increases clearances, and promotes oil leaks. The wear process, resulting in energy dissipation, depends on operating conditions, contact pairs materials, level of oil contamination, etc., but is certainly smaller than that in a case of mechanical transmission (gear train, friction pairs, levers, etc.).

An important detail also worth noting, in the authors' opinion, is that IEHA system [25] lacks a pressure limiting valve. The pressure limiting valve protects the system from overstepping the maximum allowed work pressure. Instead of pressure limiting valve, the system is equipped with sensors which define its operation, react to external influences, sending signals to control unit which decreases or increases pump capacity (indirectly regulating the pressure) by regulating eccentricity. This means that, when a disturbance in system operation occurs, the sensors should register pressure increase, and adequately regulate pump operation. Therefore, pressure increase and its regulation depend on the operation of sensors, central control unit, and pump. This is questionable in terms of control reliability, since it depends on more components than the solution which relies on the pressure limiting valve which directly regulates emerging disturbances.

The micro-pump for IEHA has complex design, especially if manufacturing tolerances are very tight, nearing those of the servo and proportional components (from 1 to 5 μm), which requires high quality surface finish and increases manufacturing costs. Complex design and high quality surface finish demand greater attention to component maintenance in general, with primary focus on the maintenance and conditioning of the energy medium, i.e., work fluid. Due to fluid contamination with particles, different wear mechanisms occur which most often contribute to failures of hydraulic systems. It is important to note that, due to the wear, system components become an internal source of fluid contamination. This contamination also leads to change in oil characteristics, especially the viscosity, which is crucial for hydraulic system operation. As a result of large amounts of contaminants present in the working fluid, there is another problem, which is the accumulation of impurities in the gaps between working elements of hydraulic components that causes failures in the form of three types of blockages - mechanical, physical-chemical, and thermal [46]. None of the reviewed papers provided the data on work fluids used by their systems. However, regardless of that, knowing that the clearances between movable and fixed work elements of

these micro components are on the same order of magnitude as servo-hydraulic components, one can recommend ISO 16/14/11 (NAS 6) oil purity class for EHA/IEHA, according to manufacturers of servo-hydraulic components [47]. This purity class requires built-in filters, which separate the mentioned impurities of external or internal origin from the fluid, thus maintaining the nominal service life of hydraulic components and fluid, while maintaining flawless system operation. It is also important to know the location of filter within the system, due to possible problem with cavitations and insufficient oil in-flow which can occur when the filter is placed at the suction branch.

In comparison to conventional hydraulic systems, the advantage of IEHA device lies in the fact that it is fixed on an actuator (i.e., joint), minimizing the unnecessary losses in fluid energy transfer through pipe lines and hose lines. Moreover, IEHA devices prevent potential hose line entanglement hazard during robot operation, which could otherwise lead to reduced hose cross section, resulting in pressure bursts and hydraulic surges. The use of EHA/IEHA also increases system's dynamic ability and reduces the number of potential locations where the external oil leaks are likely to appear. The application of EHA/IEHA in conjunction with symmetrical hydraulic cylinders and a bidirectional hydraulic motor, eliminates the need for flow valve or distributor valves, since flow direction and pump capacity are regulated by the integrated pump micro-valve. Another advantage of this device is the compact assembly of miniaturized hydraulic components with small overall dimensions and a very good ability of integration. Reduced overall dimensions contribute to space efficiency and lower mass of the resulting system in which EHA/IEHA is installed.

There are some additional proposals which are not directly related to the EHA problem, but could be used to improve functionality of EHA or IEHA. Precup et al., proposed a new design method for 2-DOF controllers that can be used to improve control simplicity at a low cost, particularly in industrial applications [48]. The development of controllers which take into account the dynamics of the entire robotic system, including interaction effects with environment such as slipping, rolling, resistance, etc. [49, 50] must also be considered. Heron and Huges [51] developed a novel contaminant monitoring scheme to examine the cleanliness level of fluid in a hydraulic system, for in the presence of solid contaminants in the fluid, the friction between working elements of hydraulic components increases and the system operates in the critical zone. Crowther et al. [52] built a neural network model for a hydraulic actuation system, investigating the lack of supply pressure, internal leakage in the actuator, and dynamic friction load. Skormin and Apone [53] developed a failure prediction procedure, detecting and utilizing trends exhibited by parameter estimation. The investigated faults included the leakage of the hydraulic pumps. Gaspar et al., proposed an observer-based prediction control [54] which can be used to predict critical values in advance using a short time interval. Petra et al. successfully implemented the neural network solution [55] which provide good accuracy and reduce the high demand for computational resources.

Conclusions

It is certain that the development of robotics is dependant upon the development of other related scientific and engineering areas. Hydraulics has definitely proven its worth in robotic applications, by yielding positive results in numerous laboratory experiments with EHA devices. These encouraging results further emphasize the need for constant research and development of hydraulic systems and components, and their modification to meet the requirements of various robotic applications.

As stated above, it can be noted that the EHA/IEHA devices have perspective in the field of robotics. As mentioned in Chapter 3, there are many ways to improve EHA/IEHA devices by implementing hardware and software solutions in order to: eliminate pulsations of pressure and flow, compensate positioning errors, simplify device installation, simplify equipment maintenance, improve accuracy, improve energy efficiency, etc.

Considering the application of hydraulics in robotics, it is certain that further research efforts shall be directed towards:

- Improving innovative design of hydraulic components used in the EHA and IEHA systems including miniaturization of hydraulic components and systems and developing ability to integrate hydraulic systems for robotic applications,
- Development of control systems for combined electro-hydraulic-mechanical actuators,
- Development of observer-based algorithms to predict critical parameters and improve time response of actuator,
- Development of procedures for the maintenance and preventive maintenance of miniature hydraulic systems,
- Development of power sources for electric motors in the form of miniature, large capacity batteries to enable long-term performance of EHA/IEHA systems in mobile applications.

References

[1] B. Batchelor, D. Hill, and H. Hodgson, "Automated Visual Inspection," 1985

[2] B. Davies, "A Review of Robotics in Surgery," *Proceedings of the Institution of Mechanical Engineers, Part H: Journal of Engineering in Medicine,* Vol. 214, pp. 129-140, 2000

[3] F. L. Lewis, C. T. Abdallah, and D. M. Dawson, *Control of Robot Manipulators,* Vol. 866: Macmillan Publishing Company New York, 1993

[4] L. Briones, P. Bustamante, and M. A. Serna, "Wall-Climbing Robot for Inspection in Nuclear Power Plants," in *Robotics and Automation, 1994. Proceedings, IEEE International Conference on*, 1994, pp. 1409-1414

[5] B. Preising, T. Hsia, and B. Mittelstadt, "A Literature Review: Robots in Medicine," *Engineering in Medicine and Biology Magazine, IEEE,* Vol. 10, pp. 13-22, 1991

[6] A. Iborra, J. A. Pastor, B. Alvarez, C. Fernandez, and J. M. F. Merono, "Robots in Radioactive Environments," *Robotics & Automation Magazine, IEEE,* Vol. 10, pp. 12-22, 2003

[7] A. Esser and H.-C. Skudelny, "A New Approach to Power Supplies for Robots," *Industry Applications, IEEE Transactions on,* Vol. 27, pp. 872-875, 1991

[8] K. Amundson, J. Raade, N. Harding, and H. Kazerooni, "Hybrid Hydraulic-Electric Power Unit for Field and Service Robots," in *Intelligent Robots and Systems, (IROS 2005) 2005 IEEE/RSJ International Conference on*, 2005, pp. 3453-3458

[9] E. P. Gels, "Electroactive Polymer (EAP) Actuators as Artificial Muscles: Reality, Potential, and Challenges," 2004

[10] T. Fukuda, H. Hosokai, H. Ohyama, H. Hashimoto, and F. Arai, "Giant Magnetostrictive Alloy (GMA) Applications to Micro Mobile Robot as a Micro Actuator without Power Supply Cables," in *Micro Electro Mechanical Systems, 1991, MEMS'91, Proceedings. An Investigation of Micro Structures, Sensors, Actuators, Machines and Robots. IEEE*, pp. 210-215

[11] H. Prahlad, R. Pelrine, S. Stanford, J. Marlow, and R. Kornbluh, "Electroadhesive Robots—Wall Climbing Robots Enabled by a Novel, Robust, and Electrically Controllable Adhesion Technology," in *Robotics and Automation, ICRA 2008, IEEE International Conference on*, pp. 3028-3033.

[12] N. G. Tsagarakis, M. Laffranchi, B. Vanderborght, and D. G. Caldwell, "A Compact Soft Actuator Unit for Small Scale Human Friendly Robots," in *Robotics and Automation, ICRA'09, IEEE International Conference on*, 2009, pp. 4356-4362

[13] S. Murata, E. Yoshida, A. Kamimura, H. Kurokawa, K. Tomita, and S. Kokaji, "M-TRAN: Self-Reconfigurable Modular Robotic System," *Mechatronics, IEEE/ASME Transactions on,* Vol. 7, pp. 431-441, 2002

[14] B. N. Ashton, "Self-contained Power Actuator," ed: Google Patents, 1954

[15] S. Frischemeier, "Electrohydrostatic Actuators for Aircraft Primary Flight Control-Types, Modelling and Evaluation," in *Proceedings of the Fifth Scandinavian International Conference on Fluid Power*, 1997, pp. 28-30

[16] K. Waldron and R. McGhee, "The Adaptive Suspension Vehicle," *Control Systems Magazine, IEEE,* Vol. 6, pp. 7-12, 1986

[17] S.-M. Song and K. J. Waldron, *Machines that Walk: the Adaptive Suspension Vehicle*: MIT press, 1988

[18] K. J. Waldron, V. J. Vohnout, A. Pery, and R. B. McGhee, "Configuration Design of the Adaptive Suspension Vehicle," *The International Journal of Robotics Research,* Vol. 3, pp. 37-48, 1984

[19] J. Bobrow and J. Desai, "Modeling and Analysis of a High-Torque, Hydrostatic Actuator for Robotic Applications," in *Experimental Robotics I*, 1990, pp. 215-228

[20] L. Walha, T. Fakhfakh, and M. Haddar, "Backlash Effect on Dynamic Analysis of a Two-Stage Spur Gear System," *Journal of Failure Analysis and Prevention,* Vol. 6, pp. 60-68, 2006

[21] V. Pastrakuljic, "Design and Modeling of a New Electro-Hydraulic Actuator," MSc, Department of Mechanical Engineering, University of Toronto, Toronto, Canada, 1995

[22] S. Habibi and A. Goldenberg, "Design of a New High Performance Electrohydraulic Actuator," in *Advanced Intelligent Mechatronics, 1999. Proceedings. 1999 IEEE/ASME International Conference on*, pp. 227-232

[23] S. Habibi, V. Pastrakujic, and A. Goldenberg, "Model Identification of a High Performance Hydrostatic Actuation System," *American Society of Mechanical Engineers, The Fluid Power and Systems Technology Division (Publication) FPST,* Vol. 7, pp. 113-119, 2000

[24] S. Alfayad, F. Ouezdou, F. Namoun, and G. Cheng, "Lightweight High Performance Integrated Actuator for Humanoid Robotic Applications: Modeling, Design & Realization," in *Robotics and Automation, 2009. ICRA'09. IEEE International Conference on*, 2009, pp. 562-567

[25] S. Alfayad, F. B. Ouezdou, F. Namoun, and G. Gheng, "High Performance Integrated Electro-Hydraulic Actuator for Robotics–Part I: Principle, Prototype Design and First Experiments," *Sensors and Actuators A: Physical,* Vol. 169, pp. 115-123, 2011

[26] S. Alfayad, F. B. Ouezdou, F. Namoun, and G. Gheng, "High Performance Integrated Electro-Hydraulic Actuator for Robotics. Part II: Theoretical Modelling, Simulation, Control & Comparison with Real Measurements," *Sensors and Actuators A: Physical,* Vol. 169, pp. 124-132, 2011

[27] G. Cheng, S.-H. Hyon, J. Morimoto, A. Ude, J. G. Hale, G. Colvin, W. Scroggin, and S. C. Jacobsen, "CB: A Humanoid Research Platform for Exploring Neuroscience," *Advanced Robotics,* Vol. 21, pp. 1097-1114, 2007

[28] M. Raibert, K. Blankespoor, G. Nelson, and R. Playter, "Bigdog, the Rough-Terrain Quadruped Robot," in *Proceedings of the 17th World Congress*, 2008, pp. 10823-10825

[29] A. Kargov, T. Asfour, C. Pylatiuk, R. Oberle, H. Klosek, S. Schulz, K. Regenstein, G. Bretthauer, and R. Dillmann, "Development of an Anthropomorphic Hand for a Mobile Assistive Robot," in *Rehabilitation Robotics, ICORR 2005, 9th International Conference on*, 2005, pp. 182-186

[30] A. Kargov, T. Werner, C. Pylatiuk, and S. Schulz, "Development of a Miniaturised Hydraulic Actuation System for Artificial Hands," *Sensors and Actuators A: Physical,* Vol. 141, pp. 548-557, 2008

[31] H. Kaminaga, J. Ono, Y. Shimoyama, T. Amari, Y. Katayama, and Y. Nakamura, "Anthropomorphic Robot Hand with Hydrostatic Cluster Actuator and Detachable Passive Wire Mechanism," in *Humanoid Robots, Humanoids 2009, 9th IEEE-RAS International Conference on*, 2009, pp. 1-6

[32] H. Kaminaga, J. Ono, Y. Nakashima, and Y. Nakamura, "Development of Backdrivable Hydraulic Joint Mechanism for Knee Joint of Humanoid Robots," in *Robotics and Automation, 2009, ICRA'09, IEEE International Conference on*, pp. 1577-1582

[33] P. Galambos, "Vibrotactile Feedback for Haptics and Telemanipulation: Survey, Concept and Experiment," *Acta Polytechnica Hungarica,* Vol. 9, pp. 41-65, 2012

[34] R. Abduli and P. Cener, *Electrohydraulic Servo Systems*. Belgrade: Military Press Center, 1986

[35] H. Kaminaga, T. Amari, Y. Niwa, and Y. Nakamura, "Electro-Hydrostatic Actuators with Series Dissipative Property and Their Application to Power Assist Devices," in *Biomedical Robotics and Biomechatronics (BioRob), 2010 3rd IEEE RAS and EMBS International Conference on*, pp. 76-81

[36] H. Kaminaga, H. Tanaka, and Y. Nakamura, "Mechanism and Control of Knee Power Augmenting Device with Backdrivable Electro-Hydrostatic Actuator," in *Proc. of 13th World Congress in Mechanism and Machine Science*, 2011, p. 534

[37] H. Kaminaga, T. Amari, Y. Niwa, and Y. Nakamura, "Development of Knee Power Assist using Backdrivable Electro-Hydrostatic Actuator," in *Intelligent Robots and Systems (IROS), 2010 IEEE/RSJ International Conference on*, 2010, pp. 5517-5524

[38] H. Kaminaga, H. Tanaka, K. Yasuda, and Y. Nakamura, "Screw Pump for Electro-Hydrostatic Actuator that Enhances Backdrivability," in *Humanoid Robots (Humanoids), 2011 11th IEEE-RAS International Conference on*, pp. 434-439

[39] H. Kaminaga, H. Tanaka, K. Yasuda, and Y. Nakamura, "Viscous Pump for Highly Backdrivable Electro-Hydrostatic Actuator," in *Robotics and Automation (ICRA), 2012 IEEE International Conference on*, pp. 3751-3756

[40] Y. A. Chinniah, "Fault Detection in the Electrohydraulic Actuator using Extended Kalman Filter," PhD, Department of Mechanical Engineering, University of Saskatchewan, Saskatoon, Canada, 2004

[41] E. B. Sampson, "Fuzzy Control of the Electrohydraulic Actuator," PhD, Department of Mechanical Engineering, University of Saskatchewan, Saskatoon, Canada, 2005

[42] Y. Lin, "Controller Design for Hydraulic Position Control Systems," PhD, Department of Mechanical Engineering, University of Saskatchewan, Saskatoon, Canada, 2011

[43] M. Ijas, "Damping of Low Frequency Pressure Oscillation," *Tampereen teknillinen yliopisto. Julkaisu-Tampere University of Technology. Publication; 656,* 2007

[44] W. Becke, J. Esser, H. Bublitz, U. Kooths, and O. Trecker, "Adaptive Hydropneumatic Pulsation Damper," ed: Google Patents, 1998

[45] S. Washio, S. Takahashi, M. K., and S. Yamaguchi, "Oil Hydraulic Pulsation Filters of Helmholtz Resonator Type," *Hydraulics & Pneumatics,* Vol. 24, pp. 729-735, 1993

[46] M. Jocanović, "Determination and Researching of Calculation Model for Solid Particle Flow with Oil Mass through Gaps, Depending on Constructional and Working Parameters of Hydraulic Components," PhD Doctoral, University of Novi Sad, Novi Sad, 2010

[47] M. Jocanović and V. Karanović, "Appendix to Researching Criteria for Defining Needful Grade of Clearness of Hydraulics Fluids in Accordance with Hydraulics Components and System Requirements," in *8th International Conference on Accomplishments in Electrical, Mechanical and Informatic Engineering DEMI*, Banja Luka, 2007, pp. 869-876

[48] R.-E. Precup, S. Preitl, E. M. Petriu, J. K. Tar, M. L. Tomescu, and C. Pozna, "Generic Two-Degree-of-Freedom Linear and Fuzzy Controllers for Integral Processes," *Journal of the Franklin Institute,* Vol. 346, pp. 980-1003, 2009

[49] A. Rodic and Gy. Mester, "Sensor-based Navigation and Integrated Control of Ambient Intelligent Wheeled Robots with Tire-Ground Interaction Uncertainties," *Acta Polytechnica Hungarica,* Vol. 10, 2013

[50] A. Widyotriatmo, A. K. Pamosoaji, and K.-S. Hong, "Control Architecture of an Autonomous Material Handling Vehicle," *International Journal of Artificial Intelligence,* Vol. 10, pp. 139-153, 2013

[51] R. Heron and M. Huges, "A Contaminant Monitor for Fluid Power Applications," in *International Conference on Condition Monitoring, Brighton, UK*, 1986, pp. 57-71

[52] W. Crowther, K. Edge, C. Burrows, R. Atkinson, and D. Woollons, "Fault Diagnosis of a Hydraulic Actuator Circuit using Neural Networks—an Output Vector Space Classification Approach," *Proceedings of the Institution of Mechanical Engineers, Part I: Journal of Systems and Control Engineering,* Vol. 212, pp. 57-68, 1998

[53] V. A. Skormin and J. Apone, "On-Line Diagnostics of a Variable Displacement Pump of a Flight Actuation System," in *Aerospace and Electronics Conference, NAECON 1995, Proceedings of the IEEE 1995 National*, pp. 503-510

[54] P. Gaspar, I. Szaszi, and J. Bokor, "The Design of a Combined Control Structure to Prevent the Rollover of Heavy Vehicles," *European Journal of Control,* Vol. 10, pp. 148-162, 2004

[55] M. I. Petra and L. C. DeSilva, "Implementation of Folding Architecture Neural Networks into an FPGA for an Optimized Inverse Kinematics Solution of a Six-Legged Robot," *International Journal of Artificial Intelligence,* Vol. 10, pp. 123-138, 2013

New Method for Evaluating the Visibility of Coronary Stents

János Dobránszky[1], György Ring[2], Eszter Bognár[3], Róbert Kovács[4], Enikő Bitay[5]

[1] MTA–BME Research Group for Composite Science and Technology, Műegyetem rakpart 3, H-1111 Budapest, Hungary dobranszky.janos@eik.bme.hu

[2] BME Faculty of Mechanical Engineering, Department of Materials Science and Engineering, Műegyetem rakpart 3, H-1111 Budapest, Hungary dobi@eik.bme.hu

[3] BME Faculty of Mechanical Engineering, Department of Materials Science and Engineering, Műegyetem rakpart 3, H-1111 Budapest, Hungary, eszter@eik.bme.hu

[4] BME Department of Electronics Technology, Műegyetem rakpart 3, H-1111 Budapest, Hungary, kovacs@ett.bme.hu

[5] Sapientia Hungarian University of Transylvania, Târgu-Mureş - Corunca, Aleea Sighişoarei 1C. Romania, bitay.eniko@eme.ro

Hommage à professor László Gillemot, the first engineer who applied X-ray in the Hungarian industry.

Abstract: In invasive radiology, X-ray imaging is used in both tracking the delivery system and assisting in correct positioning of stents. Until now there has been no objective and quantitative scale of X-ray visibility which is also known as radiopacity. There is a clear need from the part of interventional cardiologists for a quantitative in vitro evaluation method with which X-ray visibility can be graded repeatably, objectively, in a validated form across a wide range of fields. Therefore the development of the presented quantitative evaluation approach was decided in order to unambiguously classify the radiopacity of given cardiovascular implants under given in vitro imaging conditions. In this work the relative X-ray visibility index (XV_R), which expresses the visibility of the stent compared to the background and the method for determining the value of this index, is introduced. The XV_R index is related to a simple quantification method based on image analysis of X-ray images of stents. Nevertheless, this stent radiopacity quantification method can also be used in a wide range of clinical contexts.

Keywords: stent; visibility; radiopacity; X-ray microscopy; image analysis

1 Introduction

Invasive coronary angiography and percutaneous coronary angioplasty are the most important clinical processes for the assessment and therapy of coronary artery stenoses. In the revascularization process a high-resolution X-ray fluoroscope helps the interventional cardiologists to control the position of the stent. As biomedical product, stents have many important and strictly evaluated technical characteristics which form the basis of their comparison when choosing in the market. For these reasons the X-ray visibility is one of the most important functional properties of the stents [1, 2, 3].

Satisfactory X-ray visibility – which property is often called as "radiopacity" and sometimes as "radiovisibility" [4] or "radiodensity" – relies on a certain level of X-ray attenuation caused by the material of the stent. As a simple definition, radiopacity of a medical device or implant is the ability to absorb X-rays or reduce their permeation [5]. The attribute "radiopaque" is used to describe the ability of a substance to absorb X-rays and appear opaque (white) on radiographs [6]. Without a satisfactory visibility, the interventional cardiologists cannot oversee the location of the stent and its positioning into the stenosed artery precisely on the display of X-ray fluoroscope.

Whereas a standard exists [7] proposing a method for determination of the visibility of catheters, the ISO 25539-2:2008 standard [8] for vascular stents does not specify the precise test protocol. Because of this, assessment tests for classifying the visibility are carried out in numerous ways, but both stent producers and end-users use nowadays generally a subjective classification such as "good", "very good", "excellent", "average", "poor", "low", "high", etc. [9, 10]. An often used method is to characterize X-ray images by their average greyscale level on a 256 level scale. A stent or stent system is evaluated by the difference between the greyscale value of the stent and that of the surrounding area in the picture. [11, 12]. Another evaluation of stents or stent markers is possible by using a "graphic depiction" of marking on the radiograph [13] even more automatically in the fluoroscopy images [14, 15].

Elements that have high density and high atomic number, such as Pt, Ir, Ta, Nb, Pd, W, Mo strongly enhance the radiopacity compared to Fe, Cr, Ni, Co. This effect is used for example in case of Taxus Element Stent (37Fe-33Pt-18Cr-9Ni-2,6Mo), whiches thinner struts do not cause a reduction in stent visibility. Similarly, an excellent radiographic visibility characterizes the Wallstent; it consists of round wire struts of Co-Cr alloy but the composite wire has an inner core of Pt [16].

Comparing titanium, Ti–50Ta, Ti–45Ta–5Ir [17] and Nb-based alloys [18, 19] were found much more radiopaque. The producer of the ZoMaxx Stent developed a layered composite, in which the inner tantalum layer significantly improves radiopacity of the thin stent struts [20]. In order to improve the radiopacity the ends

of some stents are coated with gold markers [21] and dysprosium markers for visualizing the catheters [22].

There are many other works in which the authors evaluate the visibility of stents produced of Nitinol [23, 24, 25, 26], Co-Cr, Co-Pt, 316L [27, 28] and magnesium [29] but not having a clear quantitative method, the results remain inaccurate.

Some research is based on multi-slice computer tomography [30, 31]. The aim of these studies in the beginning was to investigate the stent expansion process, [32] afterwards to define the "stent lumen visibility" at *in vitro* conditions [33] or after the insertion of the stent [34, 35, 36, 37, 38]. CT scans were valued on a four or five-degree scale from "excellent" to "not gradable", etc. [39]. The drawback of this type of classification is that removal of subjective elements from the evaluation is not possible.

More different interpretations of term visibility have appeared applied in connection with invasive radiology: "stent visibility rate" was defined as the proportion of visible and the total length of the stent at the CT imaging [40], and "visibility-index" was generated from geometric data coming from quantitative coronary analysis (QCA) and IVUS-data [41]. A formula was described to provide a quantitative measure of the contrast between an object and the surrounding background. Different aspects of the imaging of a coronary stent were analyzed and it was stated that the general condition for X-ray visibility an object must fulfill, is to provide a level of contrast within the area where it is projected which is sufficient to be detected above the noise level of the image [42]. All these above summarized research could not result in such method, neither for the producers and nor for the end-users, which makes quantitative determination of stent visibility possible similarly to other functional parameters of stents (i.e. recoil, radial strength, metallic surface area, etc.).

There is a clear need for a quantitative evaluation method to grade X-ray visibility of stents, and to compare the different types quantitatively. It should be easily replicable, defined on an objective numerical scale, usable in a wide range of fields, and standardized to the point where it can be routinely applied in measuring X-ray visibility. The objective of this work was the elaboration of an *in vitro* method which meets each of the following conditions among the needs: objectively characterizes X-ray visibility, gives a quantitative result and permits comparing different sizes, materials and types of stents.

2 Method for Imaging the Stent

The new in vitro method for quantification of the visibility will be presented in the followings through the example of two coronary stents. One of them is a CoStar (2.5×18 mm) stent, the other one is a PRO-Kinetic (3.0×15 mm) stent; both are made of ASTM F 90 standard specified L-605 type Co-Cr alloy.

The first step of the *in vitro* quantification method is to obtain an X-ray microscopy (XRM) image of the stent preferably with the same voltage and cathode heating parameters as in clinical practice. For this a Dage XiDAT XD6600 type X-ray microscope was used. The three test values of cathode heating were 800, 1000 and 1200 mW, but the accelerating voltage was fixed at 90 kV in each case.

Using these X-ray imaging parameters, images were obtained in which the contrast and middle-tone values differ; two XRM images are shown in *Fig. 1* taken after balloon expansion of stents. It is also noticeable that in XRM images there are perceptibly different tones at image points in the background.

The X-ray detector renders the cylindrical, lattice-like structure of the implant as a flat projection. The XRM images obtained in this way vary apparently along different imaging parameters applied, or locate the metallic strut of the stent in a random position as *Fig. 2* shows. In the nine XRM images the same section of one stent is visible rotated into three distinct random orientations around its axis.

These effects will be discussed in a further paper based on the work of a corresponding PhD thesis [43], because it is obvious that all different positions and different cathode-heating levels can strongly increase the error of subjective evaluation. Therefore it is needed for a long time to find a solution for the quantitative determination of visibility without errors caused by subjective evaluation.

Apart from the XRM images of the stent, it is necessary for further analysis to have an XRM image of the empty background which image is obtained with absolutely identical parameters.

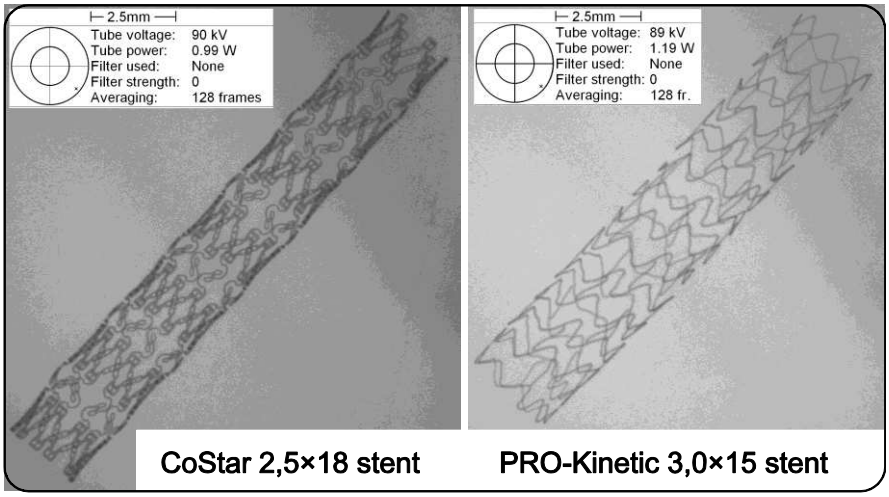

Figure 1

X-ray microscopic image of the examined CoStar stent (a) and PRO-Kinetic stent (b);
(as an example; the imaging parameters are intentionally different)

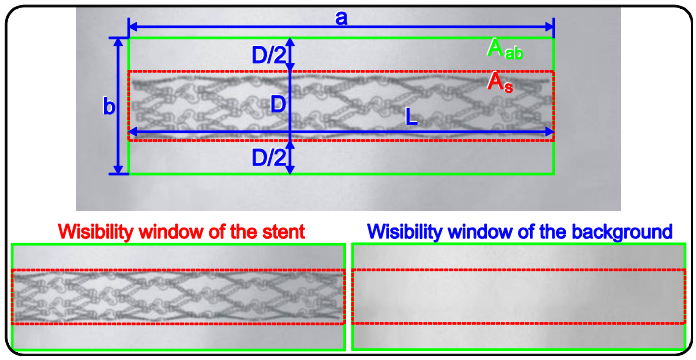

Figure 2

Visibility window on the stent XRM image is defined as the rectangle, which has one side the length of the stent and the other side twice the width (diameter) of the stent; the centred stent is enclosed by the dotted rectangle; these image were taken at 90 kV tube voltage and 1200 mW cathode heating

3 Method for Evaluating the XRM Images

In order to overlay the two XRM images – the one with the stent and the other image of only the background – an equally dimensioned and identically positioned so-called *visibility window* must be defined to line up and match the two images precisely. The image elements in terms of visibility will be interpreted in this window. When setting the dimensions of the visibility window medical experience and to the fact that visibility in every case strongly depends on the surrounding area and background must be taken into consideration. *Fig. 3* helps to survey the definition and construction of visibility window for the CoStar stent.

The visibility window is defined by sides a and b hence for the area A_{ab} equations (1), (2), and (3) have the following values:

$$a = L \tag{1}$$

$$b = D + 2\frac{D}{2} \tag{2}$$

$$2A_S \cong A_{ab} \tag{3}$$

where L is the length and D is the diameter of the stent in its expanded state, A_S is the surrounded area of the projection of the stent, and A_{ab} is the area of the visibility window. In the next step the visibility windows must be analyzed as an 8-bit, grayscale image since this is the picture format the interventional cardiologists see in practice.

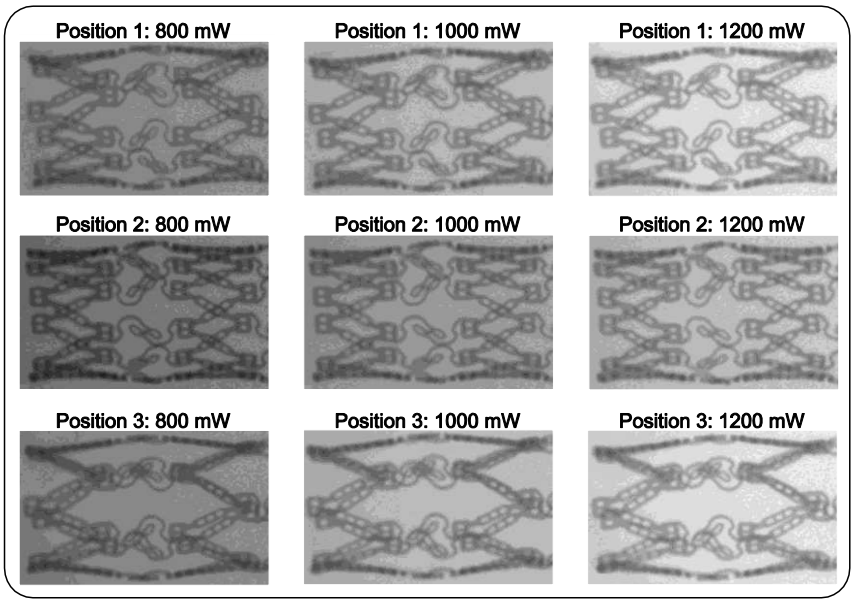

Figure 3
XRM images of two rings of a complete CoStar stent in three random rotated orientations, and three levels of cathode heating (at 90 kV tube voltages)

4 Results: Properties of the Visibility Windows

In the interests of defining a quantitative visibility parameter the distribution of *number of pixels* (N) of the visibility window must be analyzed according to the grayscale level (G). The values G = 0 and G = 255 correspond to the black and white color respectively. *Fig. 4* and *Fig. 5* show the *grayscale histograms* of visibility windows; that for the data points when the image contains the stent, $N_S(G)$, and that for the data points when the image does not contain it, $N_B(G)$.

The grayscale histogram of the stent-containing visibility window always shows a large interval in the dark pixels' region; the dark pixels' interval $G < G_{B_{MIN}}$ is started at the darkest point of the background's grayscale histogram ($G_{B_{MIN}}$ = 168 in Fig. 4 and Fig. 5). The area under the curve is proportional to the X-ray absorption of the stent, thus to the visibility, so it would be practical to define a visibility parameter which clearly reflects this simple regularity. Moreover, similar grey-scale image based segmentation method was elaborated for analysis of the captured images of printed, folded-gathered substrates or spectrograms [44, 45].

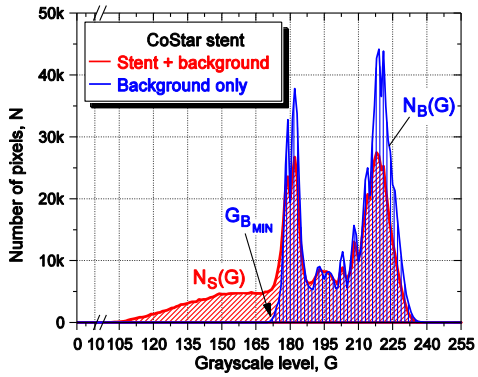

Figure 4
Grayscale histograms (distribution of the pixels) of XRM images of the visibility windows for CoStar stent

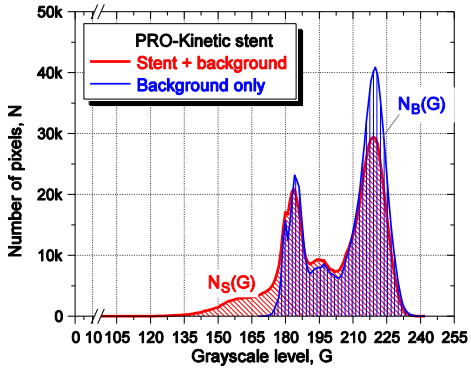

Figure 5
X-ray microscopic image of the examined CoStar stent (a) and PRO-Kinetic stent (b)

Let $U_S(G)$ and $U_B(G)$ be the *visibility functions* obtained by integration of the histogram of the stent containing and the empty visibility window, $N_S(G)$ and $N_B(G)$. The integrals of the grayscale histograms match the shaded areas under the two respective curves. The two integrals are given in equations (4) and (5), and the integral functions for the two examined stents are shown in *Fig. 6* and *Fig. 7*.

$$U_S(G) = \int_{G_L}^{G_H} N_S(G)\mathrm{d}G \tag{4}$$

$$U_B(G) = \int_{G_L}^{G_H} N_B(G)\mathrm{d}G \tag{5}$$

Where $N_S(G)$ is the grayscale histogram function of the visibility window containing the stent, $N_B(G)$ is the same of the background. $U_S(G)$ and $U_B(G)$ respectively are the two integrals, so-called *visibility functions*. The limits $G_L = 0$ and $G_H = 255$ are the respective boundary conditions, according to the extreme values of grayscale level.

In the first developing phase of this visibility quantification method, the grayscale histograms were produced by using the image analyzer software, Image-Pro Plus, and the numerical integrations were carried out by using the software Microcal Origin. Parallel to the validation, improvement and large-scale application of this method, customized software was also developed which ensures to evaluate even a huge number of XRM images easily and quickly.

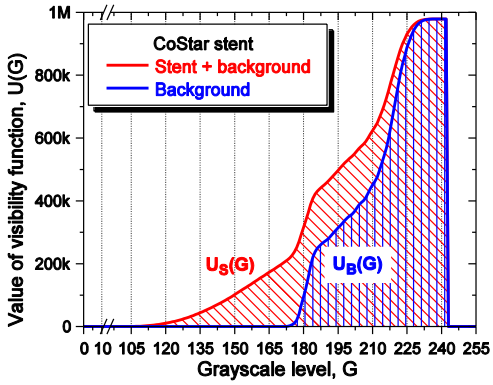

Figure 6

Visibility functions and areas under the curve of the stent-containing and the wide visibility window for CoStar stent

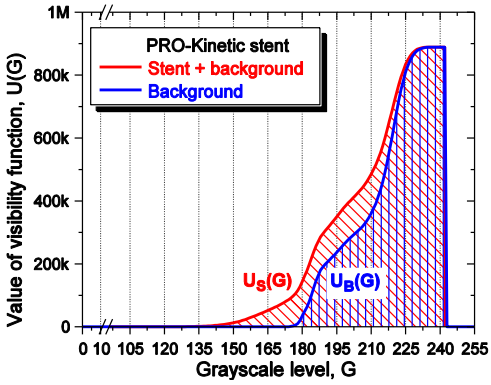

Figure 7

Visibility functions and areas under the curve of the stent-containing and the wide visibility window for PRO-Kinetic stent

5 Discussion: Computing the X-Ray Visibility

Figure 6 shows the two visibility functions: one for data from the visibility window containing only the background (empty), the other for data from the visibility window containing the background and the stent. The two visibility windows contain some image points with identical numerical values, and in fact the maximums of the two visibility functions are necessarily identical.

As a dimensionless index, let us introduce, the *relative X-ray visibility index*, XV_R, which expresses the visibility of the stent in comparison to the background within the visibility window. This is a proportional measure expressing the visibility of the stent as a percentage of the visibility of the background. From the ratio between the areas under the curve of the two visibility functions, the relative visibility index, XV_R, is defined by the following equation (6):

$$XV_R = \left(\frac{\int_{G_L}^{G_H} U_S(G)\mathrm{d}G}{\int_{G_L}^{G_H} U_B(G)\mathrm{d}G} - 1 \right) = \left(\frac{\int_{G_L}^{G_H} \int N_S(G)\mathrm{d}G}{\int_{G_L}^{G_H} \int N_B(G)\mathrm{d}G} - 1 \right) = \left(\frac{\psi_S}{\psi_B} - 1 \right) \tag{6}$$

where ψ_S and ψ_B express the *visibility number*, respectively for the stent containing and for the empty visibility window, on the basis of the 8-bit, grayscale XRM image. Equation (6) above derives these two terms from an expression for the double integral of the grayscale histogram of the XRM image.

The XV_R index defined this way characterizes the X-ray visibility of the stent itself under given X-ray microscopy imaging conditions. This parameter is suitable for quantitative evaluation and comparison of the visibility of different stents – which differ in type, material, diameter or length – in which identical scanning conditions must be ensured. For the two stents which were shown as examples, the following XV_R values were determined: 29.52% for the CoStar stent, and 20.15% for the PRO-Kinetic stent.

Between identical scanning conditions the relative visibility index excellently describes even quite small differences in visibility. In place of subjective evaluations or scales used earlier, a quantitative method and parameter which accurately ranks subtle deviations was developed based on objective measurements.

Conclusions

In the course of this study, a new *in vitro* method of measurement for the characterization of visibility (radiopacity) of stents was elaborated which objectively describes X-ray visibility providing quantitative results suitable for comparison of stents or catheters, guide-wires, markers and other cardiovascular devices. This objective, numerical index is suitable for routine use in evaluating radiopacity, as an *in vitro* method.

In clinical practice the elaborated method is suitable for assessing visibility parameters using 8-bit, grayscale X-ray microscopy (XRM) images.

The *relative X-ray visibility index*, XV_R, which characterizes the stent radiopacity under given X-ray microscopy conditions was introduced . This index is very effective for quantitative evaluation of the visibility of different stents – which differ in type, material, diameter or length – when identical scanning conditions are ensured.

Moreover, the principle and the calculation method of the relative X-ray visibility index are easily adaptable for the quantitative evaluation of X-ray angiograms and their improving algorithms.

Instead of the previously mentioned subjective evaluations or scales, the elaborated method has defined a quantitative feature which is based on objective data; consequently it permits precise ranking of subtle deviations.

Acknowledgements

This research was supported by the European Union and the State of Hungary, co-financed by the European Social Fund in the framework of TÁMOP 4.2.4. A/-11-1-2012-0001 'National Excellence Program'.

References

[1] Serruys PW (1997) *Handbook of Coronary Stents.* Martin Dunitz, London

[2] Serruys PW, Kutryk MJB, Ong ATL (2006) *Coronary-Artery Stents.* N Engl J Med. DOI: 10.1056/NEJMra051091

[3] Kutryk MJB, Serruys PW (1998) *Coronary Stenting.* Informa Healthcare, London

[4] Briguori C, Sarais C, Pagnotta P, Liistro F, Montorfano M, Chieffo A, Sgura F, Corvaja N, Albiero R, Stankovic G, Toutoutzas C, Bonizzoni E, Di Mario C, Colombo C (2002) In-Stent Restenosis in Small Coronary Arteries. Impact of Strut Thickness. J Am Coll Cardiol. DOI: 10.1016/S0735-1097(02)01989-7

[5] *Mosby's Medical Dictionary*, 8th edition (2009) Elsevier

[6] Hunter TB, Taljanovic MS (2003) Glossary of Medical Devices and Procedures: Abbreviations, Acronyms, and Definitions. RadioGraphics. DOI: 10.1148/rg.231025136

[7] Standard No. DIN 13273-7:2003-08; Catheters for Medical Use, Part 7, Determination of the X-Ray Attenuation of Catheters; Requirements and Testing (2003)

[8] Standard No. ISO 25539-2:2008; Cardiovascular Implants - Endovascular Devices - Part 2: Vascular Stents (2008)

[9] Wiskirchen J, Kraemer K, König C, Kramer U, Trübenbach J, Wersebe A, Tepe G, Dietz K, Claussen C, Duda S (2004) Radiopacity of Current Endovascular Stents: Evaluation in a Multiple Reader Phantom Study. J Vasc Intervent Radiol. DOI: 10.1097/01.RVI.0000136985.06722.AD

[10] Chan WA, Bini TB, Venkatraman SS, Boey FYC (2006) Effect of Radiopaque Filler on Biodegradable Stent Properties. J Biomed Mater Res A. DOI: 10.1002/jbm.a.30714

[11] Duda S, Wiskirchen J, Tepe G, Bitzer M, Kaulich TW, Stoeckel D, Claussen DC (2000) Physical Properties of Endovascular Stents: an Experimental Comparison. J Vasc Intervent Radiol 11:645-654. DOI: 10.1016/S1051-0443(07)61620-0

[12] Dyet JF, Watts WG, Ettles DF, Nicholson AA (2000) Mechanical Properties of Metallic Stents: How do These Properties Influence the Choice of Stent for Specific Lesions? Cardiovasc lntervent Radiol 23:47-54. DOI: 10.1007/s002709910007

[13] Miura S, Yoshioka T, Furuichi K, Tanaka T, Kichikawa K, Ohishi H (2003) Mechanical Properties of Biliary Metallic Stents: an Experimental Comparison. Nippon Acta Radiologica, 63:201–209. PMID: 12822444

[14] Courboulay V, Ménard M, Eboueya M, Courtellemont P, Vaillant R, Coisne D (2002) A Fuzzy Multi-Local Method to Detect Specific Shapes. In: *FUZZ-IEEE'02. Proceedings of the 2002 IEEE International Conference on Fuzzy Systems*, Université de La Rochelle, pp. 2:920-925

[15] Courboulay V, Desfieux J, Ménard M, Eboueya M, Courtellemont P, Vaillant R, Coisne D (2003) Localisation et détection de stents sur des images rayons-X bas contraste. Stent detection and localisation on low contrast X-ray images. ITBM-RBM 24:28–43. DOI: 10.1016/S1297-9562(03)00004-4

[16] von Birgelen C, Airiian SG, de Feyter PJ, Foley DP, van der Giessen WJ, Serruys PW (1998) Coronary Wallstents Show Significant Late, Postprocedural Expansion Despite Implantation with Adjunct High-Pressure Balloon Inflations. Am J Cardiol 82(2):129–134. PII: S0002-9149(98)00317-8

[17] O'Brien B, Stinson J, Carroll W (2008) Initial Exploration of Ti–Ta, Ti–Ta–Ir and Ti–Ir alloys: Candidate Materials for Coronary Stents. Acta Biomaterialia 4:1553–1559. DOI: http://dx.doi.org/10.1016/j.actbio.2008.03.002

[18] Beier F, Gyöngyösi M, Raeder T, v. Eckardstein-Thumb E, Sperker W, Albrecht P, Spes C, Glogar D, Mudra H (2006) First In-Human Randomized Comparison of an Anodized Niobium Stent Versus a Standard Stainless Steel Stent. An Intravascular Ultrasound and Angiographic Two-Center

Study: The VELA Study. Clin Res Cardiol 95:455–460. DOI: 10.1007/s00392-006-0406-7

[19] O'Brien B, Stinson J, Carroll W (2008) Development of a New Niobium-based Alloy for Vascular Stent Applications. J Mech Behav Biomed Mater 1:303–312. DOI: 10.1016/j.jmbbm.2007.11.003

[20] Abizaid A, Lansky AJ, Fitzgerald PJ, Tanajura LF, Feres F, Staico R, Mattos L, Abizaid A, Chaves A, Centemero M, Sousa AGMR, Sousa JE, Zaugg MJ, Schwartz LB (2007) Percutaneous Coronary Revascularization Using a Trilayer Metal Phosphorylcholine-coated Zotarolimus-Eluting Stent. Am J Cardiol 99:1403–1408. doi:10.1016/j.amjcard.2006.12.064

[21] Biehl V, Wack T, Winter S, Seyfert UT, Breme J (2002) Evaluation of the Haemocompatibility of Titanium-based Biomaterials. Biomolecular Engineering 19:97–101. DOI:http://dx.doi.org/10.1016/j.bbr.2011.03.031

[22] Saeed M, Hetts SW, English J, Wilson M (2012) MR Fluoroscopy in Vascular and Cardiac Interventions (review). Int J Cardiovasc Imaging 28:117–137. DOI: 10.1007/s10554-010-9774-1

[23] Nelson BD (2001) Expandable Metal Stents: Physical Properties and Tissue Responses. Techniques in Gastrointestinal Endoscopy 3:70–74. DOI: 10.1053/tgie.2001.22152

[24] Cheng Y, Cai W, Li HT, Zheng YF (2006) Surface Modification of NiTi Alloy with Tantalum to Improve its Biocompatibility and Radiopacity. J Mater Sci 41(15):4961–4964. DOI: 10.1007/s10853-006-0096-6

[25] Gutiérrez-Chico JL, Serruys PW, Girasis C, Garg S, Onuma Y, Brugaletta S, García-García H, van Es G-A, Regar E (2012) Quantitative Multi-Modality Imaging Analysis of a Fully Bioresorbable Stent: a Head-to-Head Comparison between QCA, IVUS and OCT. Int J Cardiovasc Imaging 28(3):467–478. DOI: 10.1007/s10554-011-9829-y

[26] Steegmüller R, Strobel M, Flaxmeier E, Schuessler A (2006) Micro-Welding for Improved Radiopacity of Nitinol-Stents. ADMEDES SchuesslerGmbH. ttp://www.admedes.com/sites/files/admedes/files/Micro-Welding_for_Improved_Radiopacity_of_Nitinol-Stents.pdf (2013-06-30)

[27] Kereiakes DJ, Cox DA, Hermiller JB, Midei MG, Bachinsky WB, Nukta ED, Leon MB, Fink S, Marin L, Lansky AJ (2003) Usefulness of a Cobalt Chromium Coronary Stent Alloy. Am J Cardiol 92:463–466. DOI:10.1016/S0002-9149(03)00669-6

[28] Kereiakes DJ, Cannon LA, Feldman RL, Popma JJ, Magorien R, Whitbourn R, Dauber IM, Rabinowitz AC, Ball MW, Bertolet B, Kabour A, Foster MC, Wang JC, Underwood P, Dawkins KD (2010) Clinical and Angiographic Outcomes after Treatment of de Novo Coronary Stenoses with a Novel Platinum Chromium Thin-Strut Stent. J Am Coll Cardiol 56:264–71. DOI:10.1016/j.jacc.2010.04.011

[29] Siekmeyer G, Steegmüller R, Schrader B, Hegel A, Strobel M, Schuessler A (2005) Novel Microjoining Techniques to Improve Stent Radiopacity. ADMEDES Schuessler GmbH. http://www.admedes.com/sites/files/admedes/files/Novel_MicroJoining_Techniques_to_Improve_Stent_Radiopacity.pdf (2013-06-30)

[30] Cademartiri F, Mollet NR, Runza G, Belgrano M, Malagutti P, Meijboom BW, Midiri M, de Feyter PJ, Krestin GP (2006) Diagnostic Accuracy of Multislice-computed Tomography Coronary Angiography is Improved at Low Heart Rates. The International Journal of Cardiovascular Imaging 22(1):101–105. DOI: 10.1007/s10554-005-9010-6

[31] La Grutta L, Runza G, Galia M, Maffei E, Lo Re G, Grassedonio E, Tedeschi C, Cademartiri F, Midiri M (2012) Atherosclerotic Pattern of Coronary Myocardial Bridging Assessed with CT Coronary Angiography. Int J Cardiovasc Imaging 28(2):405–414. DOI: 10.1007/s10554-011-9817-2

[32] Connolley T, Nash D, Buffiere JY, Sharif F, McHugh PE: X-Ray Micro-Tomography of a Coronary Stent Deployed in a Model Artery. Medical Engineering & Physics 29 (2007) 1132–1141. DOI:10.1016/j.medengphy.2006.10.016

[33] Maintz D, Gride M, Fallenberg EM, Heindel W, Fischbach R (2003) Assessment of Coronary Arterial Stents by Multislice-ct Angiography. Acta Radiologica 44:597–603. DOI:10.1080/02841850312331287719

[34] Kong L, Jin Z, Zhang S, Zhang Z, Wang Y, Song L, Zhang X: Assessment of Coronary Stents by 64-Slice-computed Tomography: In-Stent Lumen Visibility and Patency. Chin Med Sci J. 24 (2009) 156–160. PMID: 19848316

[35] Rist C, Nikolaou K, Flohr T, Wintersperger BJ, Johnson TR, Reiser MF, Becker CR (2006) Ultra-High-Resolution Mode for the Assessment of Coronary Artery Stents – ex vivo Imaging with 64-Slice-computed Tomography. Academic Radiology 13(9):1165-1167. DOI:10.1016/j.acra.2006.06.006

[36] Ehara M, Kawai M, Surmely J-F, Matsubara T, Terashima M, Tsuchikane E, Kinoshita Y, Ito T, Takeda Y, Nasu K, Tanaka N, Murata A, Fujita H, Sato K, Kodama A, Katoh O, Suzuki T (2007) Diagnostic Accuracy of Coronary In-Stent Restenosis using 64-Slice-computed Tomography: Comparison with Invasive Coronary Angiography. Journal of the American College of Cardiology 49(9):951–959. DOI: http://dx.doi.org/10.1016/j.jacc.2006.10.065

[37] Das KM, El-Menyar AA, Salam AM, Singh R, Dabdoob WAK, Albinali HA, Suwaidi JA (2007) Contrast-enhanced 64-Section Coronary Multidetector ct Angiography versus Conventional Coronary Angiography for Stent Assessment. Radiology 245(2):424–432. DOI: 10.1148/radiol.2452061389

[38] Rist C, Nikolaou K, Flohr T, Wintersperger BJ, Reiser MF, Becker CR (2006) High-Resolution ex vivo Imaging of Coronary Artery Stents using 64-Slice-computed Tomography – Initial Experience. Eur Radiol 16:1564–1569. DOI: 10.1007/s00330-006-0186-5

[39] de Heer LM, Habets J, Kluin J, Stella PR, Mali WP, van Herwerden LA, Budde RP (2012) Assessment of a Transcatheter Heart Valve Prosthesis with Multidetector-computed Tomography: *in vitro* and in vivo Imaging Characteristics. Int J Cardiovas Imag. DOI: 10.1007/s10554-012-0111-8

[40] Clarençon F, Piotin M, Pistocchi S, Babic D, Blanc R (2012) Evaluation of Stent Visibility by Flat Panel Detector CT in Patients Treated for Intracranial Aneurysms. Neuroradiology 54:1121–1125. DOI: 10.1007/s00234-011-1002-8

[41] Hagemeister J, Baer FM, Schwinger RHG, Höpp HW (2005) Compliance of a Cobalt Chromium Coronary Stent Alloy – the COVIS Trial. Current Controlled Trials in Cardiovascular Medicine 6:17 DOI: 10.1186/1468-6708-6-17

[42] Schmiedl R, Schaldach M: X-Ray Imaging of Coronary Stents (2000) Progress in Biomedical Research 5(3):184–196. http://progress.biomed.uni-erlangen.de/documents/200005030184.pdf (Accessed 30 December 2012)

[43] Ring György (2010) Pre-Clinical Evaluation of Coronary Stents and other Endoprotheses. PhD thesis, BME Faculty of Mechanical Engineering

[44] Apró M, Novaković D, Pál Sz, Dedijer S, Milić N (2013) Colour Space Selection for Entropy-based Image Segmentation of Folded Substrate Images. Acta Polytechnica Hungarica 10(1):43-62. DOI: 10.12700/APH.10.01.2013.1.3.

[45] Perović A, Đorđević Z, Paskota M, Takači A, Jovanović A (2013) Automatic Recognition of Features in Spectrograms Based on some Image Analysis Methods. Acta Polytechnica Hungarica 10(2):153–172. DOI: 10.12700/APH.10.02.2013.2.11

Application of Taguchi Methods for the Optimization of Factors Affecting Engine Performance and Emission of Exhaust Gas Recirculation in Steam-injected Diesel Engines

Görkem Kökkülünk, Adnan Parlak, Eyup Bağci, Zafer Aydin

Yildiz Technical University, Naval Arhitecture and Maritime Faculty, Marine Engineering Department, Istanbul, Turkey
gorkemk@yildiz.edu.tr, aparlak@yildiz.edu.tr, eyupbagci@yildiz.edu.tr, zaydin@yildiz.edu.tr

Abstract: In this study, optimal engine performance and pollutant emission conditions are investigated by using Taguchi Design Methods. Orthogonal arrays of Taguchi, the signal-to-noise (S/N) ratio and the analysis of variance (ANOVA) were employed to find the optimal levels and to analyze the effect of the operation conditions on performance and emission values. The parameters and their levels are engine speeds at 1200, 1600, 2000 and 2400 rpm, steam ratios of 0, 10, 20 and 30% and EGR ratios of 0, 10, 20 and 30%. Confirmation tests with the optimal levels of engine parameters were carried out in order to illustrate the effectiveness of the Taguchi optimization method. While steam and EGR ratios are found effective on emission parameters, significance levels for these parameters have been found low for effective power and torque. It was thus shown that the Taguchi method is suitable to solve the problems of performance and emissions for diesel engines.

Keywords: Taguchi Method; Diesel Engine; Pollutant Emissions; EGR; Steam

1 Introduction

With the growing awareness of environmental hazards, one of the most stringent problems that engineers and engine designers have encountered, in the process of diesel engine development, is the control and reduction of pollutant emissions to acceptable levels, as limited by relevant regulations. The emission rights applying to the relevant period are distributed amongst the actors of this market, keeping in mind that the permitted emission level should be gradually decreased from period to period by each actor [1]. Thus, ongoing developments in diesel emission control technologies are required to meet future emission regulations.

There are various methods for controlling NOx emissions in the open literature. Nowadays, the topics touching on water injection have become widely used methods to reduce NOx emissions [2-5]. Water can be supplied to the engine as a direct injection, water/fuel emulsification [6], hot water fumigation and steam injection. Alahmer et al. investigated the effect of emulsified diesel fuel and found that while improving NOx emissions, specific fuel consumption (SFC) increases [7]. Tauzi et al. analyzed the water injection into inlet manifold and observed that NOx emissions reduce significantly while increasing CO emissions with the raise of dilution ratio and SFC [8]. Ishida et al. investigated port water injection (fumigation) into diesel engine and observed that NOx emissions reduce about 50% [9]. Parlak et al. studied water injection in the form of steam phase into intake manifold and revealed that NOx emissions and SFC reduce effective power and torque increase with electronically controlled steam injection system [10].

EGR is another method for NOx reduction [11-15]. Haşimoğlu et al. examined the effects of EGR on diesel engine and found that although NOx emissions reduced considerably, smoke emissions and SFC deteriorated [16]. Mani et al. investigated the effect of cooled EGR using 100% waste plastic oil on diesel engine and observed that NOx, CO, CO_2 and smoke emissions decrease with the increase of EGR rate [17].

Although the NOx reduction rate with steam injection is reached up to 33% at full load condition, NOx can be decreased further by using EGR+steam injection combination. Kökkülünk [18] studied the effects of steam injected diesel engine with EGR on performance and emission parameters. However, there is a need to optimize the parameters considering engine performance and pollutant emissions. In this study, Taguchi methods are used in optimization of the factors affecting engine performance and emissions of EGR application on steam-injected diesel engine. In the experimental design; torque, effective power, SFC and emissions (NOx, CO, CO_2 and HC) are chosen as parameters and engine speed, EGR and steam ratio as factors. The conditions which maximize the torque and effective power and minimize the SFC and emissions were investigated.

2 Materials and Methods

2.1 Experimental Details

The experiments were carried out with a single cylinder, naturally aspirated, four-stroke Diesel engine. The engine specifications and experimental set-up are shown in Table 1 and Figure 1, respectively [19, 20].

Table 1
Engine specifications

Engine Type	Super Star
Bore [mm]	108
Stroke [mm]	100
Cylinder Number	1
Stroke Volume [dm^3]	0.92
Power, 1500 rpm, [kW]	13
Injection pressure [bar]	175
Injection timing [Crank Angle]	35
Compression ratio	17:1
Maximum speed [rpm]	2500
Cooling	Water
Injection	Direct Injection

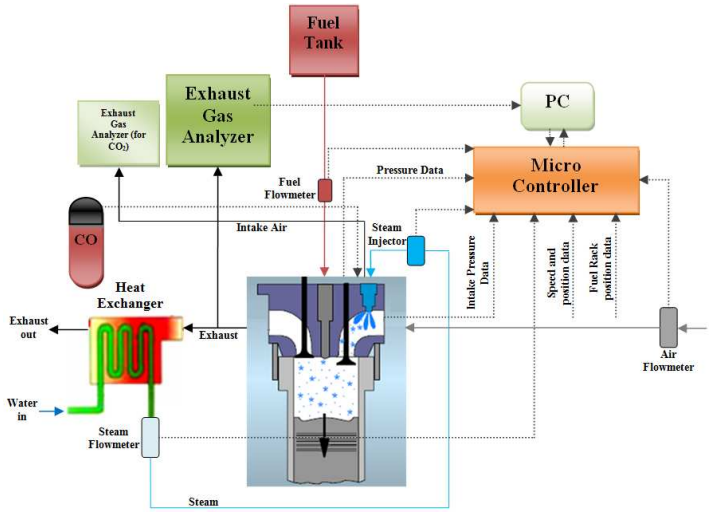

Figure 1
Experimental set-up

In order to measure brake torque, the engine is coupled with a hydraulic type dynamometer of 50 kW absorbing capacity using an "S" type load cell with the precision of 0.1 N. MRU Spectra 1600 L type and Bilsa Mod gas analyzers were used so as to measure exhaust gases [19, 20].

99% purity Linde Gas brand CO_2 gas was used for EGR application so as to the most compound in exhaust gases and to calibrate EGR ratio. Method of Needham et al. [21] was used in order to determine the amount of CO_2 gas. EGR percentage is:

$$EGR(\%) = \frac{CO_{2(intake\_manifold)} - CO_{2(surroundings)}}{CO_{2(exhaust\_manifold)}} x100 \quad (1)$$

Where $CO_{2(surroundings)}$ is the reference CO_2 percentage in surroundings. In this study, this value was neglected owing to being 0.03% in the literature [22]. EGR ratios were determined with a volume ratio of CO_2 value.

Experiments were done at the variable speeds 1200, 1600, 2000, and 2400 rpm at full load conditions. In the experiments, 0, 10, 20 and 30% steam and EGR ratios were carried out. The experiments were repeated for each steam and EGR ratio while performance and emission values were compared with those of a standard diesel.

2.2 Taguchi Design Method

In the literature, various studies have been conducted for optimizing parameters with Taguchi Design Method. Among them, Saravanan et al. investigated the effects of EGR rate, fuel injection timing and pressure in controlling NOx emission of diesel engine and experiments were designed as per Taguchi's L9 orthogonal array [23]. Ganapathy et al. analyzed thermodynamic model of Jatropha biodiesel fuelled engine by means of Taguchi method to assess the optimum engine design and operating parameters [24]. Parlak et al. studied the factors affecting emissions of a diesel engine fuelled tobacco oil seed methyl ester with Taguchi approach [25]. Win et al. investigated the effects of static injection timing, nozzle/valve opening pressure, nozzle tip protrusion, number of holes, plunger diameter, load torque, nozzle hole diameter, and engine speed on engine noise, combustion noise, smoke level, fuel economy, and exhaust emissions of a diesel engine [26]. Sivaramakrishnan et al. used Taguchi methods to optimize the diesel engine in regard to brake power, fuel economy and emissions [27].

The above studies, conducted by researchers, show that Taguchi methods provides effective solutions for investigating the effect of parameters on the performance and emissions of diesel engine. In the present study, experiments were designed to apply the Taguchi's methods to establish the effects of four (4) engine speed, steam and EGR ratios for the purpose of determining optimal conditions of performance and exhaust emissions. Three design factors and their levels are given in Table 2.

Table 2
Design factors and levels

Symbols	Factors	Level 1	Level 2	Level 3	Level 4
A	Engine Speed (rpm)	1200	1600	2000	2400
B	Steam Ratio (%)	0	10	20	30
C	EGR Ratio (%)	0	10	20	30

In Taguchi methods, the signal-noise (S/N) ratio is used to represent a performance characteristic and there are three types of S/N ratios; the lower-the better, the higher-the better and the more nominal-the better [27]. In this study, the lower-the better was used for SFC, NOx, CO, CO_2 and HC emissions and the

higher-the better for torque and effective power. These three different S/N ratios are expressed in Table 3, where n and Y is the number of repeated experiment and the measured value of the response variable, respectively.

Table 3
S/N Ratios Formulations

The lower-The better	$S/N = -10\log(\sum Y^2/n)$
The higher-The better	$S/N = -10\log(\sum(1/Y^2)/n)$
The more nominal-The better	$S/N = 10\log(\sum \bar{Y}^2/S^2)$

The orthogonal array mixed L_{16} selected as shown in Table 4, which has 16 rows corresponding to the number of tests with all columns at four levels and the factors and the interactions are assigned to the columns [28].

Table 4
Experimental Plan of L_{16}

Experiments No.	Designation	Factors		
		(A)	(B)	(C)
1	$A_1B_1C_1$	1	1	1
2	$A_1B_2C_2$	1	2	2
3	$A_1B_3C_3$	1	3	3
4	$A_1B_4C_4$	1	4	4
5	$A_2B_1C_2$	2	1	2
6	$A_2B_2C_1$	2	2	1
7	$A_2B_3C_4$	2	3	4
8	$A_2B_4C_3$	2	4	3
9	$A_3B_1C_3$	3	1	3
10	$A_3B_2C_4$	3	2	4
11	$A_3B_3C_1$	3	3	1
12	$A_3B_4C_2$	3	4	2
13	$A_4B_1C_4$	4	1	4
14	$A_4B_2C_3$	4	2	3
15	$A_4B_3C_2$	4	3	2
16	$A_4B_4C_1$	4	4	1

3 Results and Discussion

The measurement of the effective performance of motor vehicles takes place by means of bench tests [29]. In this study, the optimum values of the factors (engine speed, steam and EGR ratios) affecting engine performance and emissions of EGR application on steam injected diesel engine were determined by using Taguchi methods.

Table 5 shows the analysis of variance of experimental data. Effective power, torque, SFC, CO, CO_2, NOx and HC are determined between 96.5% and 99% confidence levels.

Table 5
ANOVA results

Factors		Sum of squares (SS)	Degree of Freedom (v)	Variance, VT	F_{factor}
Torque*	[A] Engine	174.49	3	58.16	60.49
	[B] Steam ratio	0.83	3	0.28	0.29
	[C] EGR ratio	9.29	3	3.10	3.22
	Error	5.77	6	0.96	
	Total	190.39	15	12.69	
Effective Power***	[A] Engine	72.49	3	24.16	546.53
	[B] Steam ratio	0.08	3	0.03	0.59
	[C] EGR ratio	0.39	3	0.13	2.92
	Error	0.27	6	0.05	
	Total	73.23	15	4.88	
SFC***	[A] Engine	6390.38	3	2130.13	288.96
	[B] Steam ratio	258.37	3	86.12	11.68
	[C] EGR ratio	1156.86	3	385.62	52.31
	Error	44.23	6	7.37	
	Total	7849.85	15	523.32	
NOx**	[A] Engine	41148	3	13716	14.97
	[B] Steam ratio	8346	3	2782	3.04
	[C] EGR ratio	384774	3	128258	139.95
	Error	5499	6	916.5	
	Total	439767	15	29317.8	
CO***	[A] Engine	3.08	3	1.03	123.35
	[B] Steam ratio	0.09	3	0.03	3.94
	[C] EGR ratio	2.15	3	0.72	86.02
	Error	0.05	6	0.01	
	Total	5.38	15	0.36	
CO_2***	[A] Engine	23.76	3	7.92	40.87
	[B] Steam ratio	7.12	3	2.37	12.25
	[C] EGR ratio	88.37	3	29.46	151.99
	Error	1.16	6	0.19	
	Total	120.41	15	8.03	
HC*	[A] Engine	2639.99	3	880	24.07
	[B] Steam ratio	367.70	3	122.57	3.35
	[C] EGR ratio	3385.70	3	1128.57	30.87
	Error	219.39	6	36.57	
	Total	6612.77	15	440.85	

**** At least 99% confidence*

*** At least 98.5% confidence*

** At least 96.5% confidence*

3.1 Exhaust Emissions

S/N values of factor levels of HC, NOx, CO and CO_2 emissions for engine speed, steam and EGR ratios are shown in Figure 2. As a result of study, by using the Taguchi approach, it is shown that engine speed and EGR ratios have been found to be significant in exhaust emissions. However, steam ratio has affected the exhaust emission in a different level.

After confirmation tests were carried out, the optimum design conditions were found as $A_4B_4C_1$ (2400 rpm, 30% steam ratio, 0% EGR) for CO and $A_1B_4C_1$ (1200 rpm, 30% steam ratio, 0% EGR) for CO_2. As can be seen from the Figure 2a, the effect of steam on CO_2 emissions have been found meaningful for only 10% steam ratio in 99% confidence level. On the other hand, CO has been found significant up to 20% steam ratios tested (Figure 2b).

As can be seen from Figure 2c and Figure 2d, after confirmations test carried out in 96.5% confidence level, the optimum design parameter combination were found as $A_4B_3C_1$ (2400 rpm, 20% steam, 0% EGR) for HC emissions and $A_4B_2C_4$ (2400 rpm, 10% steam, 30% EGR) for NOx with the 98.5% confidence level. However, there is not a meaningful change except for the 10% steam ratio for the NOx emissions.

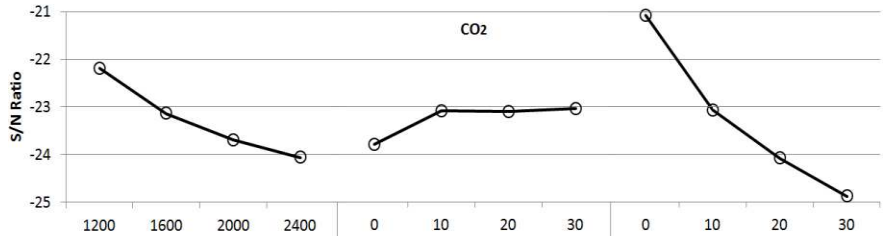

Figure 2 (a)
S/N values of factor levels for CO_2

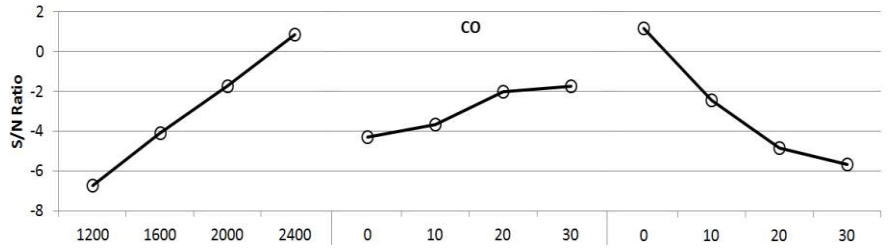

Figure 2 (b)
S/N values of factor levels for CO

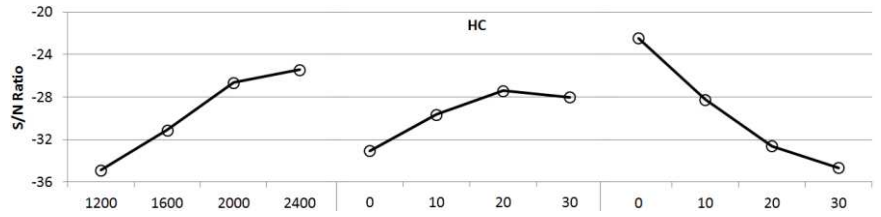

Figure 2 (c)
S/N values of factor levels for HC

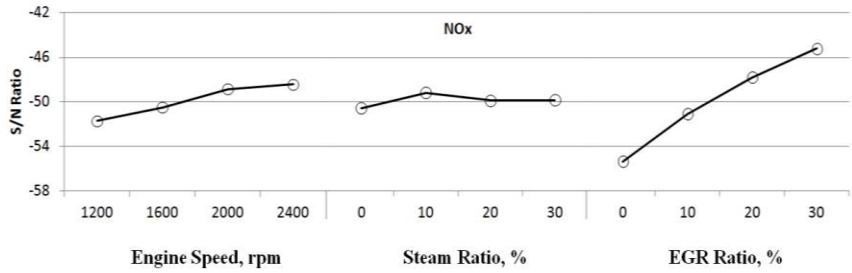

Figure 2 (d)
S/N values of factor levels for NOx

In conclusion, EGR has a distinct effect on NOx, in comparison to steam injection. But, when considering the negative effects of EGR on performance parameters, EGR could not be evaluated individually, as a method for reducing NOx emissions. Furthermore, when evaluating all exhaust emissions, steam injection become more significant, up to 20%.

3.2 Performance Parameters

S/N values of factor levels of SFC, effective power and torque for engine speed, steam and EGR ratios are shown in Figure 3. As a result of study by using the Taguchi approach, it is shown that engine speed has been found to be significant on performance parameters. However, steam and EGR ratios have affected exhaust emissions in a different level.

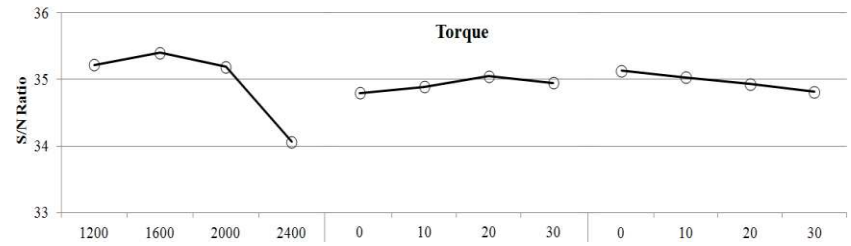

Figure 3 (a)
S/N values of factor levels for Torque

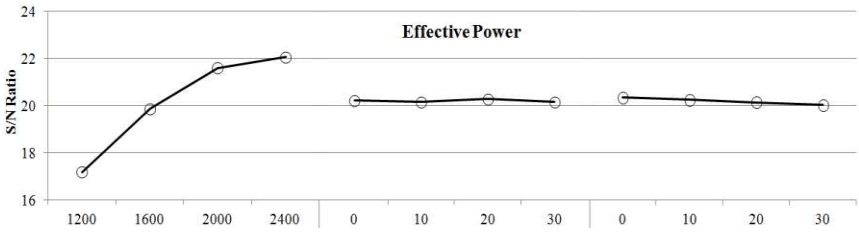

Figure 3 (b)
S/N values of factor levels for Effective Power

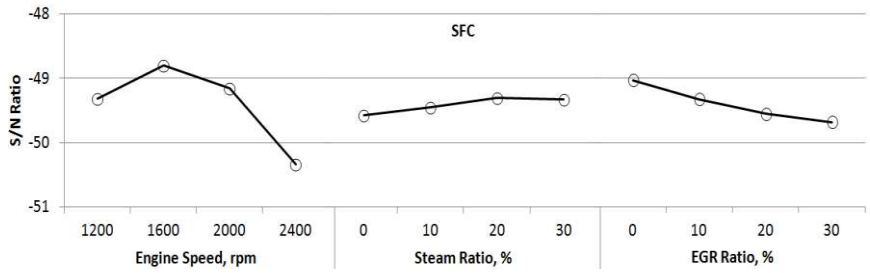

Figure 3 (c)
S/N values of factor levels for SFC

After confirmation tests carried out at a 99% confidence level, the optimum design parameter combination were found as $A_2B_3C_1$ (1600 rpm, 20% steam, 0% EGR) for SFC, $A_4B_3C_1$ (2400 rpm, 20% steam, 0% EGR) for effective power and with 96.5% confidence level, $A_2B_3C_1$ (1600 rpm, 20% steam, 0% EGR) for torque.

As can be seen from Figure 2d, $A_4B_2C_4$ is the optimum design parameter for NOx emissions. However, the optimum steam ratio is 10% for NOx, 20% for SFC. In addition, with regards to SFC, the minimum fuel consumption is found with a 0% EGR ratio.

Moreover, the effect of steam and EGR ratios, for effective power, become meaningful comparing with standard diesel and in the case of steam injection, there is not significant change between 10%-30%.

When considering both effective power and torque values, there is not a significant change in effective power and torque with the increase in EGR ratios. The reason of the limited reduces in effective power with the increase of EGR ratios could be derived from steam injection.

Table 6 and Table 7 show the comparison with experimental data and S/N ratios of calculated values for exhaust emissions.

Table 6
Experimental values and S/N ratios for exhaust emissions

Exp. No.	NOx		CO		CO_2		HC	
	Exp. val.	S/N	Exp. val.	S/N	Exp. val.	S/N	Exp. val.	S/N
1	697.30	-56.87	1.82	-5.23	10.35	-20.29	37.60	-31.50
2	448.00	-53.03	2.03	-6.15	12.20	-21.72	52.41	-34.38
3	316.14	-49.99	2.29	-7.19	14.20	-23.04	62.86	-35.96
4	220.15	-46.85	2.62	-8.38	15.30	-23.69	76.40	-37.66
5	426.20	-52.59	1.60	-4.08	15.16	-23.61	41.50	-32.36
6	588.35	-55.39	1.16	-1.29	11.06	-20.87	16.76	-24.48
7	191.12	-45.63	1.99	-6.01	16.55	-24.37	53.05	-34.49
8	261.61	-48.35	1.80	-5.11	15.28	-23.68	45.09	-33.08
9	228.60	-47.18	1.76	-4.91	17.55	-24.88	50.80	-34.11

10	135.35	-42.63	1.82	-5.20	17.97	-25.09	40.87	-32.22
11	587.62	-55.38	0.64	3.88	11.73	-21.38	6.68	-16.49
12	324.15	-50.21	1.10	-0.83	14.77	-23.38	15.42	-23.76
13	192.18	-45.67	1.42	-3.08	20.82	-26.36	51.40	-34.21
14	191.93	-45.66	1.28	-2.14	17.16	-24.69	23.43	-27.39
15	265.23	-48.47	0.87	1.21	14.95	-23.49	13.53	-22.62
16	494.58	-53.88	0.43	7.33	12.16	-21.69	7.530	-17.53

Table 7
Experimental values and S/N ratios for performance parameters

Exp.	Torque		Effective Power		SFC	
No	Exp. val.	S/N	Exp. val.	S/N	Exp. val.	S/N
1	57.64	35.21	7.24	17.19	284.64	-49.08
2	58.72	35.37	7.37	17.35	289.37	-49.22
3	57.29	35.16	7.19	17.14	296.07	-49.42
4	56.93	35.10	7.15	17.08	298.47	-49.49
5	59.79	35.53	10.01	20.01	277.56	-48.86
6	59.43	35.48	9.95	19.96	268.07	-48.56
7	58.00	35.26	9.71	19.74	279.62	-48.93
8	58.36	35.32	9.77	19.80	277.09	-48.85
9	58.01	35.26	12.14	21.68	298.00	-49.48
10	55.50	34.88	11.61	21.30	298.18	-49.48
11	58.72	35.37	12.29	21.79	270.08	-48.62
12	57.64	35.21	12.06	21.63	282.97	-49.03
13	49.77	33.93	12.50	21.93	347.62	-50.82
14	49.77	33.93	12.50	21.93	334.13	-50.47
15	49.77	33.93	12.50	21.93	322.63	-50.17
16	52.63	34.42	13.22	22.42	311.70	-49.87

In Taguchi methods, verification experiments should be done to determine optimum conditions and compared with experimental values. In this study, all values are within confidence levels, as a result of the verification experiments.

Conclusion

In this study, the effects of the factors (engine speed, steam and EGR ratios) on engine performance and emissions of an EGR application, with a steam injected diesel engine have been investigated using the Taguchi approach. Verification experiments were performed to compare with the Taguchi results and have a good agreement with the experimental data.

It is observed from the results, that effective power, SFC, CO and CO_2 are determined at least 99%, NOx at least 98.5% and torque, HC at least 96.5% confidence levels.

The optimum design parameter combinations have been found as $A_4B_4C_1$ (2400 rpm, 30% steam, 0% EGR), $A_1B_4C_1$ (1200 rpm, 30% steam, 0% EGR) for CO and CO_2, respectively and $A_4B_3C_1$ (2400 rpm, 20% steam, 0% EGR) and $A_4B_2C_4$ (2400 rpm, 10% steam, 30% EGR) for HC and NOx emissions, respectively.

For the performance parameters, the optimum design parameter combinations have been found as $A_2B_3C_1$ (1600 rpm, 20% steam, 0% EGR) for SFC, $A_4B_3C_1$ (2400 rpm, 20% steam, 0% EGR) for effective power and $A_2B_3C_1$ (1600 rpm, 20% steam, 0% EGR) for torque.

The optimum steam ratio is 10% for NOx and 20% for SFC. On the contrary, with regards to SFC, the minimum fuel consumption has been found with a 0% EGR ratio. For effective power and torque values, there is not considerable change in effective power and torque with an increase in EGR ratios. The reason of a limited reduction in effective power with the increase of EGR ratios could be explained due to steam injection.

Acknowledgement

This study was supported by TUBITAK 1001 Project (project no. 111M065) and Yildiz Technical University (YTU) Scientific Research Project Coor. (BAPK) (Project no. 2011-10-02-KAP02). Thanks to TUBITAK and YTU BAPK for the financial support.

References

[1] E. Karai, M. Barany: Towards Convergence of Accounting for Emission Rights, Acta Polytechnica Hungarica, Vol. 10, No. 1, 2013, pp. 177-196

[2] F. Bedford, C. Rutland, P. Dittrich, A. Raab, F. Wirbelit: Effects of direct water injection on DI Diesel Engine Combustion, SAE paper 2000-01-2938

[3] O. Armas, R. Ballesteros, F.J. Martos, J.R. Agudelo: Characterization of Light Duty Diesel Engine Pollutant Emissions Using Water-emulsified Fuel, Fuel, Vol. 84, 2005, pp. 1011-1018

[4] F. L. Dryer: Water Addition to Practical Combustion Systems - Concepts and Applications. Symposium (International) on Combustion, Vol. 16, 1997, pp. 279-295

[5] C. Y. Lin, K. H. Wang: Diesel Engine Performance and Emission Characteristics Using Three-Phase Emulsions as Fuel, Fuel Vol. 83, 2004, pp. 537-545

[6] G. Kökkülünk, E. Akdoğan, V. Ayhan: Prediction of Emissions and Exhaust Temperature for Direct Injection Diesel Engine with Emulsified Fuel using ANN, Turkish Journal of Electrical Engineering and Computer Sciences, Vol. 21, No:2, 2013, pp. 2141-2152

[7] A. Alahmer, J. Yamin, A. Sakhrieh, M. A. Hamdan: Engine Performance using Emulsified Diesel Fuel, Energy Conversion and Management, Vol. 51, 2010, pp. 1708-1713

[8] X. Tauzia, A. Maiboom, S. R. Shah: Experimental Study of Inlet Manifold Water Injection on Combustion and Emissions of an Automotive Direct Injection Diesel Engine, Energy, Vol. 35, 2010, pp. 3628-3639

[9] M. Ishida, H. Ueki, D. Sakaguchi: Prediction of NOx Reduction Rate Due to Port Water Injection in a DI Diesel Engine. SAE Technical Paper, 1997, 972961

[10] A. Parlak, V. Ayhan, Y. Üst, B. Şahin, İ. Cesur, B. Boru, G. Kökkülünk: New Method to Reduce NOx Emissions of Diesel Engines: Electronically Controlled Steam Injection System, Journal of Energy Institute, Vol. 85, 2012, pp. 135-139

[11] J. W. Heffel: NOx Emission Reduction in a Hydrogen fuelled Internal Combustion Engine at 1500 rpm using Exhaust Gas Recirculation, International Journal of Hydrogen Energy, Vol. 28, 2003, pp. 901-908

[12] M. Zheng, G. T. Reader, J. G. Hawley: Diesel Engine Exhaust Gas Recirculation-a review on advanced and novel concept. Energy Conversion and Management, Vol. 45, 2004, pp. 883-900

[13] H. E. Saleh: Experimental Study on Diesel Engine Nitrogen Oxide Reduction Running with Jojoba Methyl Ester by Exhaust Gas Recirculation, Fuel, Vol. 88, 2009, pp. 1357-1364

[14] A. Maiboom, X. Tauzia, J. F. Hetet: Experimental Study of Various Effects of Exhaust Gas Recirculation (EGR) on Combustion and Emissions of an Automotive Direct Injection Diesel Engine, Energy, Vol. 33, 2008, pp. 22-34

[15] L. Shi, Y. Cui, K. Deng, H. Peng, Y. Chen: Study of Low Emission Homogeneous Charge Compression Ignition (HCCI) Engine Using Combined Internal and External Exhaust Gas Recirculation (EGR), Energy, Vol. 31, 2006, pp. 2665-2676

[16] C. Haşimoğlu, Y. İçingür, H. Öğüt: Dizel Motorlarında Egzoz Gazları Resirkülasyonunun (EGR) Motor Performansı ve Egzoz Emisyonlarına Etkisinin Deneysel Analizi, Turkish Journal of Engineering Environmental Science, Vol. 26, 2002, pp. 127-135 (in Turkish)

[17] M. Mani, G. Nagarajan, S. Sampath: An Experimental Investigation on a DI Diesel Engine using Waste Plastic Oil with Exhaust Gas Recirculation, Fuel, Vol. 89, 2010, pp. 1826-1832

[18] G. Kökkülünk, A. Parlak, V. Ayhan, İ. Cesur: Investigation of Steam Injection with Exhaust Gas Recirculation (EGR) on a Diesel Engine. 3rd International Conference on Urban Sustainability, Cultural Sustainability, Green Development, Green Structures and Clean Cars (USCUDAR \'12), Barcelona, 2012, pp. 41-46

[19] G. Kökkülünk, G. Gonca, A. Parlak: The Effects of Design Parameters on Performance and NO Emissions of Steam-injected Diesel Engine with Exhaust Gas Recirculation, Arabian Journal for Science and Engineering, Vol. 39, No. 5, 2014, pp. 4119-4129

[20] G. Kökkülünk, G. Gonca, V. Ayhan, İ. Cesur, A. Parlak: Theoretical and Experimental Investigation of Diesel Engine with Steam Injection System on Performance and Emission Parameters, Applied Thermal Engineering, Vol. 54, No. 1, 2013, pp. 161-170

[21] J. R. Needham, A. J. Nicol, C. H. Such: Low Emission Heavy Duty Diesel Engine for Europe. SAE Paper, 1993-620-631

[22] S. Çetinkaya: Termodinamik, Nobel Yayınları, 1999, Ankara (in Turkish)

[23] S. Saravanan, G. Nagarajan, S. Sampath: Multi Response Optimization of NOx Emission of a Stationary Diesel Engine, Fuel, Vol. 89, 2010, pp. 3235-3240

[24] T. Ganapathy, K. Murugesan, R. P. Gakkhar: Performance Optimization of Jatropha Biodiesel Engine Model using Taguchi Approach, Applied Energy, Vol. 86, 2009, pp. 2476-2486

[25] A. Parlak, H. Karabaş, İ. Özsert, V. Ayhan, İ. Cesur: Application of Taguchi's Methods to Investigate Factors Affecting Emissions of a Diesel Engine Running with Tobacco Oil Seed Methyl Ester. International Journal of Vehicle Design, Vol. 59, 2012, pp. 196-211

[26] Z. Win, R.P. Gakkhar, S. C. Jain, M. Bhattacharya: Investigation of Diesel Engine Operating and Injection System Parameters for Low Noise, Emissions, and Fuel Consumption using Taguchi Methods, Proceedings of the Institution of Mechanical Engineering Part D-Journal of Automobile Engineering, Vol. 219, 2005, pp. 1237-1251

[27] K. Sivaramakrishnan, P. Ravikumar: Performance Optimization of Karanja Biodiesel Engine using Taguchi Approach and Multiple Regressions, ARPN Journal of Engineering in Applied Science, Vol. 7, 2012, pp. 506-516

[28] M. Kapsiz, M. Durat, F. Ficici: Friction and Wear Studies between Cylinder Liner and Piston Ring Pair using Taguchi Design Method, Advances in Engineering Software, Vol. 42, 2011, pp. 595-603

[29] I. Lakatos: Diagnostic Measurement for the Effective Performance of Motor Vehicles, Acta Polytechnica Hungarica, Vol. 10, No. 3, 2013, pp. 239-249

Benefit Evaluation Model for Gamified Add-Ons in Business Software

Ferenc Erdős[1] and Gábor Kallós[2]

[1] Department of Information Technology, Faculty of Engineering Sciences, Széchenyi István University, Győr, Hungary, e-mail: erdosf@sze.hu

[2] Department of Mathematics and Computational Sciences, Faculty of Engineering Sciences, Széchenyi István University, Győr, Hungary, e-mail: kallos@sze.hu

Abstract: Return on IT investment analysis has become a fundamental task of the finance function at corporations, let it be large multinational organizations or small and medium businesses (SME). Besides the cost analysis, the benefit analysis is also an essential component of economic calculations and decisions. Due to complicated profit calculations and estimation methods, the benefit of IT investments is less easily forecast and hence less frequently calculated than their costs. This study focuses on a special innovative type of IT investments, the gamified extensions of business software. Gamification, which refers to the use of game design elements in a non-gaming context, can expect big development in the field of business applications in the near future. Gamification features of business software generally enhance user experience, enabling people to do otherwise boring tasks. In the following we attempt to propose a sophisticated benefit evaluation model based on the hedonic wage model (HWM) and technology acceptance model (TAM) for this special type of IT projects.

Keywords: gamification; business software; benefit; IT investment

1 Gamified Environment for Business Software

Almost everybody likes to play. It sounds a little bit common place, but in business life it has had an increasing role recently. According to Gartner's estimate by 2014 roughly 70% of the largest enterprises[1] will use different game techniques for at least one business process [11]. Today business processes are mostly supported by business software applications, hence, these types of software will be the main target of gamification projects. Gamification refers to the use of game design elements for a non-gaming context [8], [9].

[1] Forbes Global 2000: an annual ranking of the top 2000 public companies in the world by Forbes magazine

In the field of learning gamification is a well-tried and tested feature [16], [25], and well used since video games are frequent in the market [12], [19]. Employees interact and learn in a gamified environment, but they don't always know they are really learning. They collect scores, badges to get places on leaderboards while more knowledge is gained and shared. One of the best-known examples of gamified learning is Ribbon Hero from Microsoft to educate users of Microsoft Office 2007 and 2010 how to use the ribbon interface [32]. Using games, leisure and serious to enhance and support learning has become known as game-based learning [19].

The opportunities of gamification for businesses are great – from having more engaged customers, to enable innovation or to motivate employees in work. In this study we emphasize the last one in the field of business software and highlight personal productivity driving business results.

Economists and business theorists have been considering the case for years that companies would be much more prosperous if they allocated and influenced human resources within their organizations using different methods [22], [26]. One of these concepts is to increase personal satisfaction at work connected to human resources management, therefore, happy employees are more productive, more loyal and far more motivated to do extra efforts for their employer. Gamification of human resource can be interpreted as a new approach in this field.

2 Benefits of Gamification Features

Despite the promising opportunities of game elements' adoption into serious contexts such as business software, theoretical models for the financial analysis are missing. In the past few years there have been many studies available about the elements [8], [9], [17], [20], the steps [33] and the general benefits [18] of gamification projects. In the following we attempt to measure monetary benefits of gamification add-ons implemented in different business software.

Essential types of gamification features of business applications generally enhance user experience, enable people to do otherwise boring tasks so that there is a visual design and other incentive substance using game design techniques.

Despite their great potential to advance efficiency throughout the company, gamifying of business software requires grounded managerial thought and consideration before they are implemented within an organization. Besides the clear declaration of gamification project goals, an adequate cost-benefit analysis is necessary with a thorough cause-effect breakdown. In this study we intend to provide only an ex-ante benefit evaluation model, nevertheless a total cost of ownership (TCO) calculation is an essential task besides benefit estimation. After the implementation from time to time an ex-post analysis of the effectiveness of the gamification project is very important too.

The monetary measurement of such benefits is very complicated because this feature raises efficiency by intangible qualitative factors. The incidental improvement of employee's performance is very hard to anticipate and measure, so the yields of such projects are vague.

Working from the principle that enhanced user experience shifts user activities towards higher value added activity, we provide a sophisticated procedure, which is a modification of Sassone's Hedonic Wage Model (HWM) [23].

3 HWM-based Evaluation

The hedonistic model, or labor value procedure can be interpreted as a TSTS (Time Savings Times Salary) model's extension [15], although the related basic idea of the method was applied in connection with the change in price research already in the 1930's [13]. HWM is based on the statement that labor resources of a company can be allocated with certain economic criteria. Every employee carries out different types of work related tasks, and these activities bring different values for the enterprise [24].

The original basis of this methodology is the hedonic equation in which the prices of different product models are the dependent variables and the characteristics of the product types are the independent variables. The basic conceptual model is to determine the price of goods that can be offered only in different composite shopping baskets. In this situation consumers have to consider the benefits of each individual good before they buy. [13]

For the use of the HVM evaluation model for gamification features in business software it is necessary to record and evaluate the relevant changes within the spectrum of the work processes owing to the gamification add-ons. The essence of our methodology is to identify all users where gamification features will be used, categorize tasks of these users and determine the proportion of time spent with these tasks as a percentage of total working hours.

At first, we have to determine the user groups ($i = 1, ..., I$) with the same activities, and the number of user group members (L_i, in i^{th} group) which are affected by the new gamified interface. If the intended application of gamification elements is optional for the users, the proportion that will use this feature (P_i, in i^{th} group) has to be estimated for every user group. In our estimation the obligatory usage of gamification could be unproductive for a part of users.

Then we have to establish the different activities ($j = 1, ..., J$) of the users. Furthermore, we have to determine for all user groups the time spent with each activity in proportion to total working time calculated. Based on these, the data analyzed can be presented in a so-called activity-profile matrix, which is denoted by $M = (m_{ij})$. Accordingly, m_{ij} denotes the office hours of activity "j" in proportion

to the total working hours by user group "*i*". In addition, the average hourly wages of each user group (C_i) need to be taken into account.

3.1 Maximizing Problem

For the solution of the maximizing problem we use the Lagrange method as Sassone did in his original hedonic wage model [23].

Assuming that the interested Reader is familiar with the Lagrange method for solving conditional extremum problems, we omit here the detailed presentation.

We note shortly that in practical economics, the modification of the classic extremum problem in the following way, is a common exercise: the domain of the original function (*f*) is restricted/constrained to special places (given by a function *g*).

The formal goal of the procedure is to determine the local extremum with function *L* – which no longer has outside conditions – defined by the equation

$$L(x_1, x_2, \dots, x_n, \lambda_1, \lambda_2, \dots, \lambda_m) = f(x_1, x_2, \dots, x_n) + \\ + \sum_{j=1}^{m} \lambda_j \, g_j(x_1, x_2, \dots, x_n). \quad (1)$$

If from the setting of the problem the existence of the extremum follows, the equation system

$$\frac{\partial}{\partial x_i}\left(f + \sum_{j=1}^{m} \lambda_j \, g_j \right)(\underline{a}) = 0 \quad \text{and} \quad g_j(\underline{a}) = 0 \quad (2)$$

(with $i \in \{1, 2, \dots, n\}$, $j \in \{1, 2, \dots, m\}$) consists of $n + m$ equations and $n + m$ unknown variables $x_1, x_2, \dots, x_n, \lambda_1, \lambda_2, \dots, \lambda_m$ and this system has only one solution, then its place is given by the first n components of the solution (the unknown variables $\lambda_1, \lambda_2, \dots, \lambda_m$ can be eliminated from the equation system without determining their values [4], [21]).

3.2 The Proposed Gamified Model

The economic criterion is to maximize the profit of the company under the circumstances of technical and economic constraints. The profit of the company (π) is the difference between revenues and costs, that is $\pi = R - C$.

Let's consider the short-run profit-maximization problem when inputs are fixed at some level, so we cannot change the amount of factors of production. In other words, there is a budget constraint for the wage costs of the affected employees in short term:

$$B \geq \sum_{i=1}^{I} C_i \cdot L_i \cdot P_i \tag{3}$$

To project the economic criterion for this problem, we have to maximize the profit from the work of the users, who use gamification features of a business application:

$$R\left(\sum_{i=1}^{I} m_{i1} \cdot L_i \cdot P_i, \ldots, \sum_{i=1}^{I} m_{iJ} \cdot L_i \cdot P_i\right) - \sum_{i=1}^{I} C_i \cdot L_i \cdot P_i \;\rightarrow \max \tag{4}$$

From (3) we can create the following constraint equation for the maximizing problem (4), in the form required for the Lagrange method:

$$\sum_{i=1}^{I} C_i \cdot L_i \cdot P_i - B = 0 \tag{5}$$

For the simplicity we introduce variable LP_i, which is the number of users in user group "*i*", which is intended to use the gamification software mechanics.

$$LP_i = L_i \cdot P_i \tag{6}$$

From parts (4) and (5) we can build the Lagrange function (*Lf*):

$$Lf(LP_1, \ldots, LP_I, \lambda) = R\left(\sum_{i=1}^{I} m_{i1} \cdot LP_i, \ldots, \sum_{i=1}^{I} m_{iJ} \cdot LP_i\right) - \left(\sum_{i=1}^{I} C_i \cdot LP_i\right) + \\ + \lambda \cdot \left(B - \sum_{i=1}^{I} C_i \cdot LP_i\right) \tag{7}$$

$$Lf(LP_1, \ldots, LP_I, \lambda) = R\left(\sum_{i=1}^{I} m_{i1} \cdot LP_i, \ldots, \sum_{i=1}^{I} m_{iJ} \cdot LP_i\right) - \\ - (1+\lambda)\left(\sum_{i=1}^{I} C_i \cdot LP_i\right) + \lambda \cdot B \tag{8}$$

From the Lagrange function (7) we can build the i^{th} piece partial derivative equations.

$$\frac{\partial LF}{\partial LP_i} = \sum_{j=1}^{J} \frac{\partial R}{\partial LP_i} \cdot m_{ij} - (1+\lambda) \cdot C_i = 0 \qquad \text{for } i = 1 \text{ to } I \tag{9}$$

$$\sum_{j=1}^{J} VMPA_j \cdot m_{ij} = (1+\lambda) \cdot C_i \qquad \text{for } i = 1 \text{ to } I \tag{10}$$

$VMPA_j$ describes the value of marginal product of the activity "*j*" of the employees from different groups, which are involved in the use of gamification features.

Every "*i*" (10) equation described on the left side is the weighted sum of the marginal product of the actual user groups' activities. On the right the average labor cost of the user group "*i*" is based on the assumption that the Lagrange multiplier is zero ($\lambda = 0$), so the marginal opportunity costs for the employment of user group "*i*" members are equal to the direct costs of the user group "*i*". According to this statement, the actual number of gamification users in different groups is optimal within the organization.

The "*i*" (10) equations build up a system of linear equations with *J* unknown marginal values. Starting from the fact that one of the *J* activities is an unproductive activity, which has zero marginal value ($VMPA_J = 0$), $J - 1$ equations (user groups) are needed to solve the system of linear equations. These values of marginal product of activities (from $VMPA_1$ to $VMPA_J$) represent the implicit unit labor cost for each activity.

4 TAM-based Prediction

The technology acceptance model, originally proposed by Davis [5], is a model to explain and predict the use of a system. The model is based on the theory of reasoned action (TRA) by Ajzen and Fishbein [1]. According to this model the use of an IT system can be explained or predicted by user's motivation, which is directly influenced by the features of system. Perceived usefulness and perceived ease of use are supposed to influence attitudes toward new technology and mediate the relationship between external variables and attitude [7].

As stated by Davis, perceived usefulness is the degree to which an individual believes that using a particular system would enhance his or her job performance and perceived ease of use is the degree to which an individual believes that using a particular system would be free of physical and mental effort [5].

Latter versions of TAM realized that behavioral intention as a further variable would be directly influenced by the perceived usefulness ant the perceived ease of use of a system [6], [27]. Davis and Venkatesh [28] have extended the model to TAM2 and introduced three interrelated social factors: subjective norm, voluntariness and image.

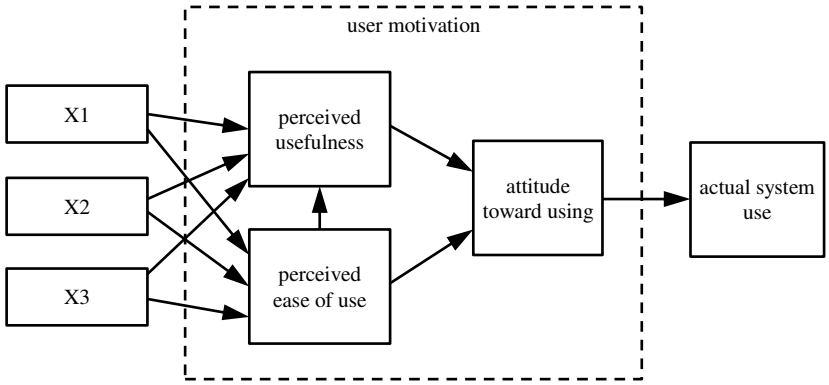

Figure 1
Original conceptual model for technology acceptance (Davis, 1986, p. 24)

The main goal of different technology acceptance models is to study how individual user perceptions affect the intentions to use information technology and further the actual usage as illustrated in Figure 2.

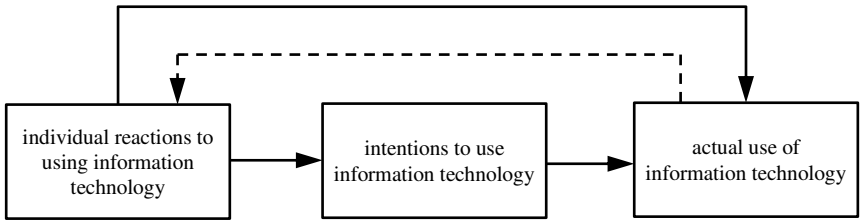

Figure 2
Basic concept of different technology acceptance models (Venkatesh et al., 2003)

To evaluate gamification add-ons in different business software we have combined the original TAM with other user acceptance research approaches and extended it with special factors. In the following we intend to use this model to forecast user acceptance of gamified business applications. We propose some external variables to predict the behavioral intention as a consequence of gamified software environment. The main goal is to forecast the changes within the spectrum of the work processes.

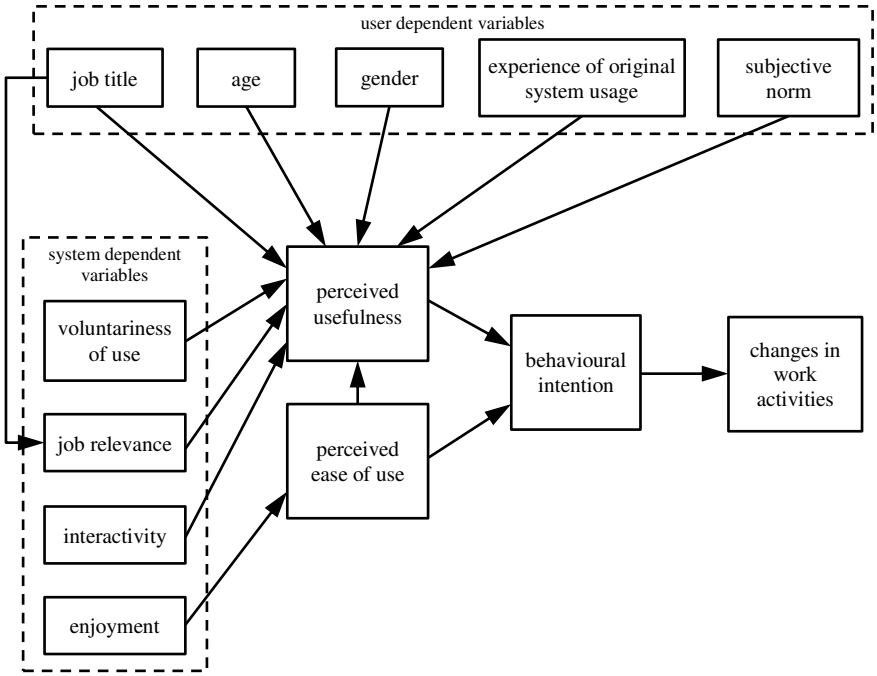

Figure 3
Model of gamification features use in business applications based on the technology acceptance model

The above described model assumes that functionality is identical between the original GUI and gamified solution. According to our theory it is necessary to estimate the relevance of different variables regarding to perceived usefulness and perceived easy to use. To evolve measurement scales for these two main motivation factors psychometric scales used in psychology can be used. The relevance of each variable is different due to the distinctive gamification solution and user characteristics. The significance analyses before implementation should be studied with real users and actual usage situations. The user sample has to contain employees from different user groups and has to be representative. The aim is to find significant factors that influence behavioral intention and the changes in work activities. Different descriptive statistical methods (such as mean, standard deviation, frequency and correlation) are available to determine significance of factors based on user's responses.

If a user regards the perceived usefulness or the perceived ease of use of the gamified software interface worse than the original GUI, it is necessary to enable the usage of the original one to avoid ineffectiveness and unproductiveness.

The next step is to estimate the new activity-profile matrix ($N = (n_{ij})$) with the help of TAM as a result of the gamification implementation. It is necessary to forecast for all user groups the modified time spent with each "j" activity in

proportion to total working time. According to our model, the increased user experience shifts the user activities towards higher value added activities in different degree, according to the variables of TAM. So we have to consider these factors for every employees of the user group and estimate the average new proportion of different activities, which can be used to estimate benefits extracted after applying gamification add-ons. The modified activity-profile matrix must reflect the increased efficiency as a result of gamified software environment.

The final step is to compare the original ($M = (m_{ij})$) and the new ($N = (n_{ij})$) activity-profile matrices and the activity increases or decreases have to be calculated for every user group. Using the values of marginal product of different "j" activities ($VMPA_j$) and the shift of activities ($N - M = (n_{ij} - m_{ij})$), financial benefit can be calculated for an employee of every user group and for an optional time period. The total benefit of gamification ownership (*TBGO*) is the summarized value of these calculations multiplied with the total of working hours of different user groups (t_i) projected for the whole investigated period and for the number of users in user group "i", which intended to use the gamification software elements (LP_i).

$$TBGO = \sum_{i=1}^{I} \left(\sum_{j=1}^{J} \left(VMPA_j \cdot (n_{ij} - m_{ij}) \cdot t_i \right) \cdot LP_i \right) \qquad (11)$$

For instance on the basis of a 40-hour work week and 48-week active work year for user group "i", a 3-year horizon calculation "t_i" equals 5,760 office hours.

4 Application Example

In the following – based on the work of Sassone [23] – we present a possible application of our model. During the building up of the application example our goal was to endow several systems working in the academic sphere (management information systems – MIS, document management system, education system and other office systems) with gamification features and to report of the achieved financial benefit of efficiency grows. To the creation of the activity profile matrix the data source was our workplace, Széchenyi István University.

The activities (scopes of the duties) were selected in a way that in the daily routine substantial differences should exist among the categories. We have distinguished one leader (head/full professor), one senior lecturer (associate professor, professor assistant), one demonstrator and one administrator position (4 groups). We took interviews with some colleagues in the groups, and averaging the answers an activity net was worked up (with common activities for the groups). During the configuration we used some reasonable simplifications in order to have a not too complicated descriptive matrix.

The leaders/full professors e.g. gave the following main activities: management or control/leadership (projects, industrial connections, discussions, meetings, coordination of department or institute), correspondence (with other leaders, professors, researchers), study and research (conferences, reading and writing papers), lessons and their preparation, administration (document management, mailing, education administration). We divided these complicated scopes of activities into 4 main parts according to the possible application for the other user groups. However, it is clear that the meaning of "study and research" can be very different for an administrator or for a lecturer. Since the different activity groups can have intersections, too (e.g. mailing – correspondence), we made "fine-tuning" among the categories. Moreover, for all employee types it can be detected that a part of the working time is useless (non-productive). It was added as a separate activity. So, for our case e.g. the activity profile of a leader/full professor is as follows: management – 36%, study and research – 19%, lessons and preparation – 15%, mailing and administration – 20%. Table 1 shows the recorded activity profile of all user groups.

After it we gave an estimation for the cost of the employment of the workers (hourly rate; here besides the wages we have planed the fringe benefits and additional costs). The value of the Lagrange-multiplicator was chosen to 0 (which means in the practice that there is no unnecessary capacity). The costs in our example are 24, 20.5, 18 and 14 monetary units, respectively.

Table 1

Recorded activity profile of users before the application of gamification techniques

		Activities					Hourly rate
		Manage/ Project	Study/ Research	Lessons/ Prep.	Admin.	Non-prod.	
User Groups	Head/ Professor	0.36	0.19	0.15	0.2	0.1	24
	Assoc./ Assist.Prof.	0.15	0.25	0.25	0.24	0.11	20.5
	Demonstrator	0.02	0.18	0.51	0.15	0.14	18
	Administrator	0.07	0.02	0	0.74	0.17	14

Omitting the non-productive activities we get a square matrix (activities and duties/profiles; here: our goal was to search a unique solution). In the next step we solve the equation system with the inverse matrix method, so we get the pure marginal value of the different activities (produced value in 1 hour; in our example: 36.5, 25.3, 20.6 and 14.8 monetary units, respectively).

The unit value of each activity – as written above – is, of course, an over-simplification of the real situation. The value of study/research in many cases cannot be measured directly – how can we calculate e.g. the research impasse? The experience can be very valuable… The result, however, correlates well with

the practical expectations, on average, the most valuable "unit price" of the management work e.g. can conveniently justify with the great obtainable benefit.

For the time being we could only estimate the change available with the introduction of the gamification add-ons, since the gamification-TAM model presented in Figure 3 was not yet validated. There are here several such uncertainties which can be built up correctly only with a longer tracking – among them immediately the one, that how many percent of the staff will be susceptible to the new structure.

The goal is clear – with the increase of the employee's satisfaction and acceptance – increased efficiency, which means partly the quicker/faster completion of a given task, on the other hand the possible execution of more value added tasks during a specific period of time, so we expect that the activities of the workers shift towards the most valuable activity categories.

If, for example, we can make the time spent with monotonic administration friendlier with a simultaneous running of a gamification application (e.g. kinder user interface, amusing effects, funny praises, collecting points and badges, setting goals), then the given task can be done partly more efficiently, partly in a less tiring (more amusing) way. The time saved (or a part of it) can be used for study/research, or so the colleague can undertake a greater "slice" from the project works.

Taking into account all of these factors we can estimate the financial yield of the increased efficiency.

We recorded the original profile and the calculated/estimated profile of a given employee-group (in our case now: associate professor/professor assistant; columns B and D in Table 2.). Assuming 40 hour working time (weekly) we determined the time required (weekly) for each activity (columns C and E). The efficiency-grow (in percent) is mostly an estimation (column F). After it we calculated the new performance of the colleague working with larger efficiency which now exceeds 40 hours (in our example: 41.15 hours; column G). Finally, we calculated the annual benefit (column J), based on the unit price of the activities, taking into account 45 working weeks annually. Concerning one associate professor/professor assistant, we have annually 2058 monetary units benefit.

Table 2

Benefit calculation for associate professors and professor assistants

	B	C	D	E	F	G	H	I	K
19	Benefit for Assoc/Assist Prof								
20	Activity	Init profile	Init hours	Final profile	Final hours	Proj increase	Equiv hours	Orig marg values	Annual new values
21	Manage/project	0.15	6	0.16	6.4	2	6.53	36.52	867.62
22	Study/research	0.25	10	0.27	10.8	1	10.91	25.32	1034.75
23	Lessons/prep	0.25	10	0.25	10	3	10.3	20.58	277.79
24	Admin	0.24	9.6	0.22	8.8	7	9.42	14.78	-122.38
25	Non-prod	0.11	4.4	0.1	4	0	4	0	0
26	Total	1.00	40.00	1.00	40.00		41.15		2057.8

We can observe that there will be such an activity where the objective function results negative values (here: administration), this naturally, does not diminish the benefit in total.

Similarly, we made this tabular for all worker groups (so we had 4 intermediate objective/cost functions). Finally, we recorded the data of a specific department (the number of the employees in each group) and the 4 intermediate cost functions –weighted properly– were combined in a final objective function (here: cell H45).

Table 3

Total benefit calculation of gamified software environment

H45 | fx | =D45*J16+F45*J25+D46*J34+F46*J43

	A	B	C	D	E	F	G	H
44								
45	Number of colleagues		Head/Prof	2	Assoc/Assist Prof	5	Objective function	42559
46			Demonstrator	14	Administrator	2		(Benefit)
47								

In the following, our goal was to examine the summarized financial effect of the gamification features with a probability forecast. To the forecast we used a Monte-Carlo simulation. This simulation technique is a generally accepted scientific tool to handle the risks resulting in uncertainty, the point of which is that based on the probability distribution assigned to each uncertainty factor we choose randomly values which are used in the experiments of the simulation [30].

The formal goal is to determine the expected value

$$\psi = E_{\varphi}[f(X)] = \int f(x)\varphi(x)dx \tag{12}$$

where X is a real-valued random variable with probability density φ, and f is a real-valued function. Since density φ is common unknown or too complicated, we estimate Ψ using randomly chosen $f(x_i)$ points. (The empirical mean obtained this way tends to the real integral value indeed in closed intervals.)

In our case

$$\psi = E_{\varphi}[TBGO(X)] = \int TBGO(x)\varphi(x)dx \tag{13}$$

and

$$\widehat{\psi} = \frac{1}{n}\big(TBGO(x_1) + TBGO(x_2) + \cdots + TBGO(x_n)\big), \tag{14}$$

where n is the number of experiments (n is large). Thus, increasing the number of experiments the distribution of total benefit of gamification ownership function arbitrary accuracy can be specified [14], [31].

In the gamification model to be analyzed, we fixed the estimated changed activity profile matrix as influential variables, and their possible intervals, respectively. In the probability distribution of the influential variables we used normal

distribution, but the value of the deviation was defined so that about 90% of the data should fit in the interval [mean – deviation, mean + deviation], not 68%, as usual. During the simulation, the values of the variables (in given intervals and with given distribution) were produced by a random number generator. Altogether we made 10000 experiments with computer aided Monte-Carlo simulation.

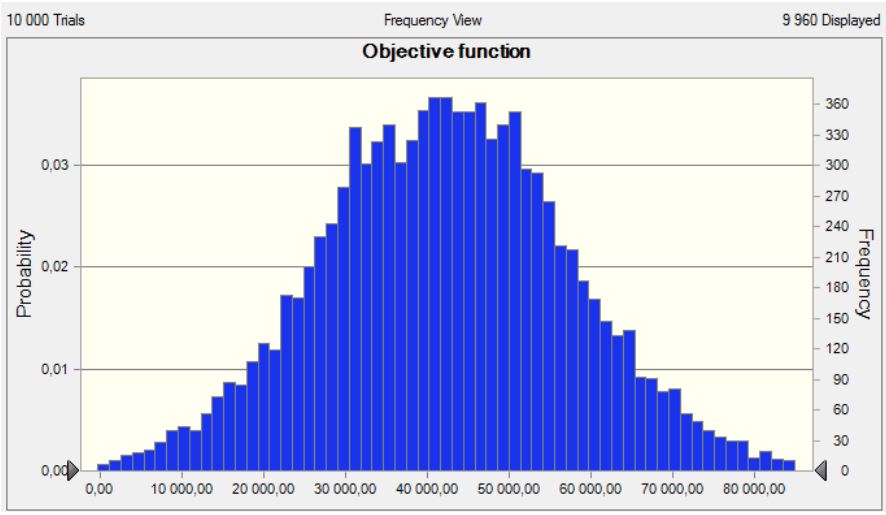

Figure 4
Probability forecast of gamification's total financial effect

Running the simulation we got the histogram (Figure 4) which suits "value by weight" well our prior expectations. The expected benefit falls with a very large probability in the interval [25000, 60000] monetary units. The chart serves with a little surprise anyway: our matrix is very sensitive even for small changes, so in several places the curve seems to be oddly deficient. We see too, that several extreme cases were not shown by the program (40 cases from the 10000).

Conclusions

In this study we proposed a complete procedure that facilitates the benefit calculations of gamification projects in the field of business applications. Based on the hedonic wage model and technology acceptance model, we defined a set of methods that allowed us to quantify the ex-ante, mid-term and ex-post financial measurement of such investments projects. The practical application of our framework needs significant and thorough estimation, examination and calculation efforts to get an adequate and real yield analysis.

References

[1] Ajzen, I., Fishbein, M.: Understanding Attitudes and Predicting Social Behaviour, Prentice Hall, Englewood Cliffs, NJ, p. 278 (1980)

[2] Aparicio, A. F., Vela, F. L. G., Sánchez, J. L. G., Montes, J. L. I.: INTERACCION '12: Proceedings of the 13th International Conference on Interacción Persona-Ordenador, Article No. 17 (2012)

[3] Bernhaupt, R.: Evaluating User Experience in Games: Concepts and methods, Springer, London, p. 286 (2010)

[4] Bertsekas, D. P.: Nonlinear Programming (Second Ed.), Athena Scientific Publ., Cambridge, MA, p. 777 (1999)

[5] Davis, F. D.: A Technology Acceptance Model for Empirically Testing New End-User Information Systems: Theory and Results, Doctoral dissertation, MIT Sloan School of Management, Cambridge, MA, p. 291 (1985)

[6] Davis, F. D., Bagozzi, R. P., Warshaw, P. R.: User Acceptance of Computer Technology: a Comparison of Two Theoretical Models, Management Science 35(8), pp. 982-1003 (1989)

[7] Davis, F. D., Venkatesh, V.: A Critical Assessment of Potential Measurement Biases in the Technology Acceptance Model: Three Experiments. International Journal of Human-Computer Studies, 45(1), pp. 19-45 (1986)

[8] Deterding, S., Dixon, D., Khaled, R., Nacke, L.: From Game Design Elements to Gamefulness: Defining "Gamification". Proceedings from MindTrek'11 (ACM), Tampere, Finland, pp. 9-15 (2011)

[9] Deterding, S., Sicart, M., Nacke, L., O'Hara, K., Dixon, D.: Gamification: Using Game Design Elements in Non-Gaming Contexts, Paper presented at CHI 2011, Vancouver, Canada, pp. 2425-2428 (2011)

[10] Erdős, F.: Different Techniques to Quantify the Yield of IT Projects, SEFBIS Journal 7, pp. 11-17 (2012)

[11] Gartner: Gartner Enterprise Architecture Summit 2011 – Press Release, Egham, UK, April 12, 2011, http://www.gartner.com/newsroom/id/1629214 Retrieved 3 March 2013

[12] Gee, J. P.: What Video Games Have to Teach US about Learning and Literacy, Palgrave Macmillan, New York, p. 225 (2003)

[13] Janko, W. H.: Informationswirtschaft 2 – Informationswirtschaft im Unternehmen, Wirtschaftsuniversität Wien, Wien, p. 571 (2010)

[14] Jorgensen, E.: Monte Carlo simulation models: Sampling from the Joint Distribution of "State of Nature"-Parameters, Proceedings of the Symposium on "Economic modelling of Animal Health and Farm Management", Farm Management Group, Dept. of Social Sciences, Wageningen University, pp. 73-84 (2000)

[15] Kesten, R., Schröder, H., Wozniak, A.: Konzept zur Nutzenbewertung von IT Investitionen. Arbeitspapiere der Nordakademie 3. Nordakademie, Elmshorn, p. 39 (2006)

[16] Lee, J. J., Hammer, J.: Gamification in Education: What, How, Why Bother? Academic Exchange Quarterly, 15(2) pp. 1-5 (2011)

[17] Liu, Y., Alexandrova, T., Nakajima, T.: Gamifying Intelligent Environments, Proceedings of the 2011 international ACM workshop on Ubiquitous meta user interfaces, pp. 7-12 (2011)

[18] Pankajakshan, V., Nair, S.: When Work Becomes Play: Gamification of HR, Proceedings of Tenth AIMS International Conference on Management, pp. 1327-1333 (2013)

[19] Prensky, M.: Digital Game-based Learning, USA, McGraw-Hill, New York, p. 442 (2007)

[20] Reeves, B., Read, J. L.: Total Engagement: Using Games and Virtual Worlds to Change the Way People Work and Businesses Compete. Harvard Business Press, Boston, p. 274 (2009)

[21] Reinhard, F., Soeder, H.: Dtv-Atlas zur Mathematik, Deutscher Taschenbuch Verlag, München, p. 272 (1974)

[22] Robins, J. A.: Organizational Considerations in the Evaluation of Capital Assets: Toward a Resource-based View of Strategic Investment by Firms, Organization Science 3(4), pp. 522-536 (1992)

[23] Sassone, P. G.: Cost-Benefit Methodology for Office Systems, ACM Transactions on Office Systems 5(3), pp. 273-289 (1987)

[24] Sassone, P. G., Schwartz, A. P.: Office Information Systems Cost Justification, IEEE Aerospace and Electronic Systems Magazine, 1(8), pp. 21-26 (1986)

[25] Simões, J., Redondo, R. D., Vilas, A. F.: A Social Gamification Framework for a K-6 Learning Platform. Computers in Human Behavior, 29(2), pp. 345-353 (2013)

[26] Suen, W., Chan, W.: Labour Market in a Dynamic Economy, Hong Kong Economic Policy Studies Series, City University of Hong Kong Press, Hong Kong (1997)

[27] Venkatesh, V., Davis, F. D.: A Model of the Antecedents of Perceived Ease of Use: Development and Test. Decision Sciences, 27(3), pp. 451-481 (1996)

[28] Venkatesh, V., Davis, F. D.: Theoretical Extension of the Technology Acceptance Model: Four longitudinal field studies, Management Science, 46(2), pp. 186-204 (2000)

[29] Venkatesh, V., Morris, M. G., Davis, G. B., Davis, F. D.: User Acceptance of Information Technology: Toward a Unified View, MIS Quarterly, 27(3), pp. 425-478 (2003)

[30] Vose, D.: Risk Analysis, John Wiley & Sons Ltd.: New York, p. 418 (2006)

[31] Watson, H.: Computer Simulation in Business. Whiley, New York, p. 358 (1981)

[32] Welinske, J.: Ribbon Hero – User Assistance Masquerading as a Game, Writer's UA, (2010), http://www.writersua.com/articles/ribbon_hero Retrieved 3 March 2013

[33] Werbach, K., Hunter, D.: For The Win: How Game Thinking Can Revolutionize Your Business, Wharton Digital Press, Philadelphia, p. 146 (2012)

Robust PID Controller Design for a Real Electromechanical Actuator

Rafik Salloum

Control Department, Electrical Engineering Faculty
School of Railway Engineering, Iran University of Science and Technology
Malek-Ashtar University of Technology
Lavizan, Shahid Babaee, 15875-1774 Tehran, Iran
E-mail: rafsal@mut.ac.ir; rafsal@mail.iust.ac.ir

Bijan Moaveni

School of Railway Engineering, Iran University of Science and Technology
Narmak, 16846-13114 Tehran, Iran; E-mail: b_moaveni@iust.ac.ir

Mohammad Reza Arvan

Control Department, Electrical Engineering Faculty
Malek-Ashtar University of Technology
Lavizan, Shahid Babaee, 15875-1774 Tehran, Iran; E-mail: arvan@mut.ac.ir

Abstract: Electromechanical actuators (EMA's) are of interest for applications that require easy control and high dynamics. In this paper, we design a robust PID controller for position control of a real electromechanical actuator. An EMA is modeled as a linear system with parametric uncertainty by using its experimental input-output data. PID controllers are designed by graphical findings of the regions of stability with pre-specified margins and bandwidth requirements and by applying the complex Kharitonov's theorem. This novel method enables designers to make the convenient trade-off between stability and performance by choosing the proper margins and bandwidth specifications. The EMA control system is passed to the Bialas' test, and validated on the basis of meeting a desired set of specifications. The effects of parameter variations on the system's stability and performance are analyzed and the simulation and test results show that the EMA with the new controller, in addition to robustness to parametric uncertainties, has better performance compared to the original EMA control system. The simulation and test results prove the superiority of the performance of the new EMA over the original EMA control system pertaining to its robustness to parametric uncertainties.

Keywords: electromechanical actuator (EMA); robust PID controller; Kharitonov theorem

1 Introduction

In recent years, electromechanical actuators (EMA's) are in high demand in robotics and aerospace science industries. An EMA has attractive characteristics such as simplicity, reliability, low cost, high dynamic characteristics, and easy control [1-3]. However, EMA modeling is subject to uncertainty due to several reasons, including operating point changes, parametric variations due to temperature changes, non-modeled dynamics, and asymmetric behavior. Consequently, the desired EMA's performance will be unachievable and, in some cases, its stability may be lost. Usually, based on experience, this problem will not be solved by using the conventional controllers; instead robust controllers are needed to obtain the desired performance and stabilization demands in dealing with dynamic uncertainties [4-6].

The primary motivation for designing the EMA was to access the ameliorated and favorable robustness to meet the application requirements. Robust controllers were designed to achieve robust stability, good tracking, and disturbance attenuation using the Lyapunov-based synthesis concept in [7, 8]. A genetic optimized PID controller was designed in [9], in order to improve the EMA system transient state behavior. A robust H_∞ controller for an EMA, was designed and tested to achieve a faster and more accurate system in [10].

There is a wide range of applications for PID controllers in industry due to their simplicity and effectiveness. However, the tuning process, whereby, the proper values for the controller parameters are obtained is a critical challenge. Also, the traditional PID controller lacks robustness against large system parameter uncertainties, the reason lies in the insufficient number of parameters to deal with the independent specifications of time-domain response, such as, settling time and overshooting [11]. Much effort is involved in designing robust PI, PD, or PID controllers for uncertain systems, based on different robust design methods, known in literature as Kharitonov's Theorem, Small Gain Theorem, H_∞ and Edge Theorem [12-14]. A graphical design method of tuning the PI and PD controllers achieving gain and phase margins is developed in [15]. An approach to design PID controllers for systems without time delay was presented in [16].

In this paper, a novel approach to the design of a robust PID controller for an EMA system with time delay, is proposed and applied to a "motor with harmonic drive" subsystem of the EMA system. This approach is presented, based on the complex Kharitonov theorem for interval model with time delay. The applied method enables the designer to make the convenient trade-off between stability and performance by choosing the appropriate margins and bandwidth specifications. The closed loop EMA system and "motor with harmonic drive" subsystem is modeled as linear systems with parametric uncertainty. The modeling is accomplished, by identifying the EMA system and "motor with harmonic drive" subsystem using experimental input-output data in different

operating points. Bialas' test based on edge theorem is also applied, to emphasize the robust controller validity.

The robust controller design procedure is then studied under simulation conditions, and its effectiveness is proven by comparing the closed loop performance identified through test data with that achieved by using the robust PID controller.

After presenting this introduction, we discuss the following: The EMA uncertain model and experimental set-up as described in Section 2. In Section 3, the robust PID computations by Kharitonov's theorem with bandwidth, phase and gain margins constraints are explained. In Section 4, the design validation is carried out and finally, conclusion are drawn.

2 Experimental Set-up and Uncertainty Modeling

EMA mainly consists of a DC motor driven by PWM driver, a harmonic drive reducer, a potentiometer position sensor, and a controller as shown in Figure 1. In this figure, r is the setpoint voltage, v is the PWM output, and δ is the output angle.

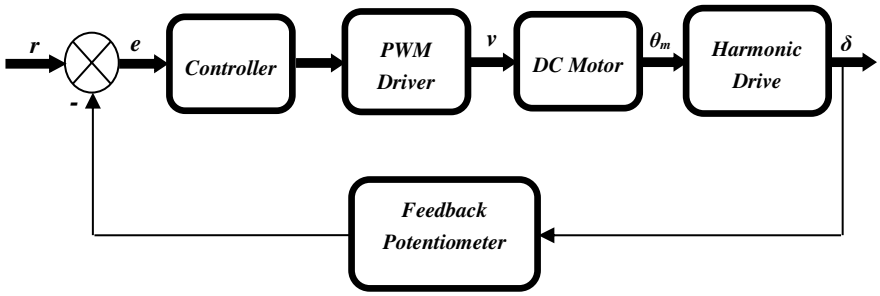

Figure 1
EMA block diagram

The experimental set-up consists of a permanent magnet DC motor with integrated harmonic drive gearing with 300:1 reduction ratio. The motor is driven by a PWM driver. The actual shaft position is recorded by a potentiometer fixed on the output shaft. A data acquisition card, which is connected to a PC, records the readings from the potentiometer.

The model of the DC motor and position control is well known in the literature [17, 18]. The model of the subsystem under consideration (motor with harmonic drive reducer) is:

$$\frac{\delta(s)}{v(s)} = \frac{K_m/N}{s(LJ_m s^2 + (Lb + RJ_m)s + Rb + K_m^2)} \tag{1}$$

where K_m (N.m/A) is the motor's torque constant, L (H) and R (Ohm) are the inductance and resistance of motor control coil respectively, b (N.m/rad/sec) is the viscous damping coefficient, N is the harmonic drive gear ratio, and J_m (Kg.m^2) is the rotor's moment of inertia.

Hence, considering that the change of armature current in time is negligible, we can use engineering judgment to neglect L. In addition, the viscous damping can be neglected. So, the EMA model can be represented as follows:

$$\frac{\delta(s)}{r(s)} = \frac{K}{s^3 + \frac{s^2}{\tau_m} + K.K_f} \tag{2}$$

Where K is a constant corresponds to the open loop gain, controller, and motor constants. K_f is the potentiometer coefficient in *v/deg*, and

$$\tau_m = \frac{RJ_m}{K_m^2}$$

In this phase, we planned to verify best fitting. To achieve this goal, a method of classic identification was used to establish the EMA's model from the test data, by minimizing the mean square error (MSE). While applying this method, five working points for the EMA system were used for model identification. The final output was the extraction of the uncertain model. For example, the test results of the studied EMA system in one working point are shown in Figure 2, whose model is:

$$G_1(s) = \frac{\delta(s)}{r(s)} = \frac{1}{\left(\frac{s}{148} + 1\right)\left(\frac{s^2}{105^2} + 2 * 0.89 * \frac{s}{105} + 1\right)}$$

Similarly, the models corresponding to the other working points were identified, and the nominal model of the EMA system is:

$$G_{EMA.nom}(s) = \frac{\delta(s)}{r(s)} = \frac{1}{\left(\frac{s}{140} + 1\right)\left(\frac{s^2}{119^2} + 2 * 0.831 * \frac{s}{119} + 1\right)} \tag{3}$$

Figure 3 shows the actual response curve and the identified model response.

It can be seen from Figure 4 that the frequency response of the model and the actual response of the EMA, are basically, identical. Therefore, the transfer function model described in (3), is recognized to approximately describe the original EMA system.

Next, the model of the "motor with harmonic drive" subsystem was identified for five working points. For instance, the test results in one working point of the studied EMA system are shown in Figure 4 and its model has the following form:

$$G_{HDMotor1}(s) = \frac{\delta(s)}{v(s)} = \frac{787.3e^{-0.0027\,s}}{(s^2 + 140.4s + 75.7)}$$

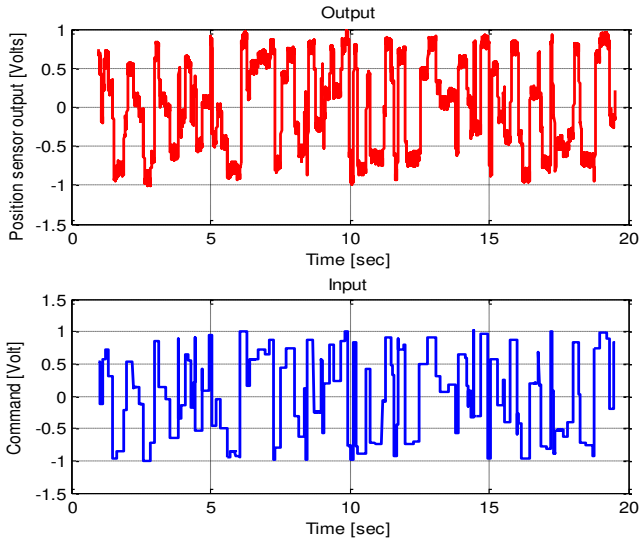

Figure 2
Input and output data captured from EMA

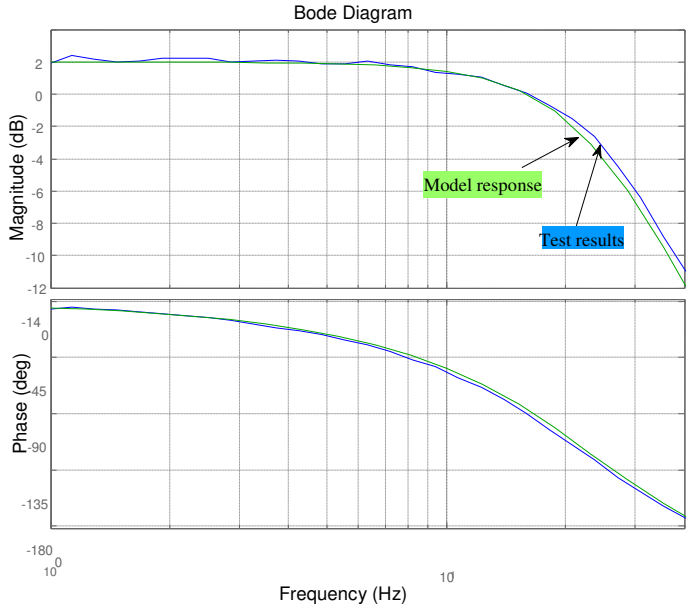

Figure 3
Frequency responses of the EMA's model and its test results

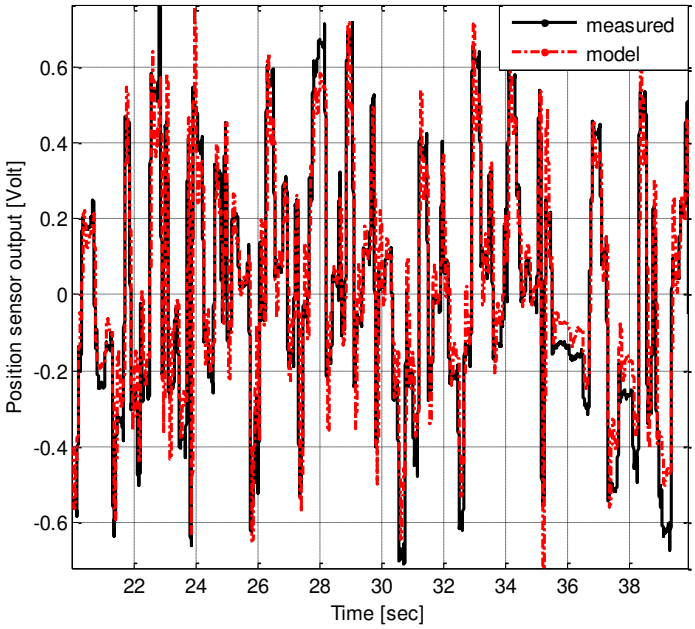

Figure 4
Outputs of "Motor and harmonic drive" subsystem and its model

The parametric uncertain model, with time delay, was built to be used in the robust controller design.

$$G_{HDMotor}(s) = \frac{K}{(s^2 + q_1 s + q_2)}\, e^{-T_d s} \tag{4}$$

The uncertain parameters of the model and their intervals are:

- $K \in [512.3\ ,\ 949.7]$; $K_{nominal} = 750.4$
- $q_1 \in [90.4\ , 197.6]$; $q_{1.nominal} = 144.2$
- $q_2 \in [35\ ,\ 90.5]$; $q_{2.nominal} = 70.5$
- $T_d \in [1.7\ ,\ 3.5]$; $T_{d.nominal} = 2.55\ msec$

3 Robust Controller Design by Kharitonov Theorem

In this section, the Kharitonov's theorem will be briefly presented, and it will be applied to design a robust controller for the EMA system under consideration. The studied system with gain-phase margin tester is illustrated in Figure 5.

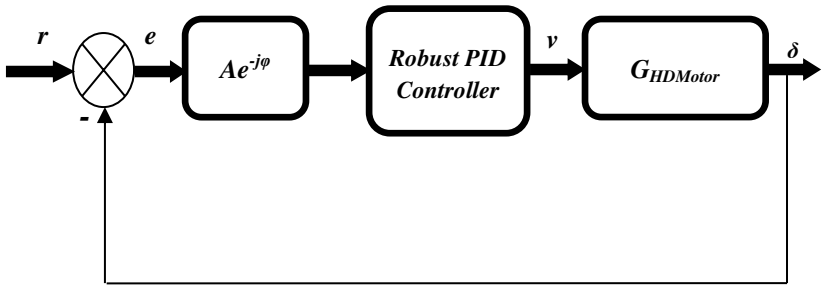

Figure 5
The studied control system with gain-phase margin tester

3.1 Kharitonov's Theorem and Kharitonov's Rectangles

Kharitonov's theorem deals with the stability of a system with closed-loop characteristic polynomial. Consider $I^*(s)$ to be the set of closed-loop characteristic polynomials of degree n for the interval systems of the form:

$$P(s) = p_0 + p_1 s + p_2 s^2 + \cdots + p_n s^n \tag{5}$$

Where$p_i$is a complex presented as: $p_i = a_i + jb_i;\ a_i \in \left[\underline{a_i}, \overline{a_i}\right]$ and $b_i \in \left[\underline{b_i}, \overline{b_i}\right]$ for $i=0,1,\ldots,n$. The degree is assumed to be invariant over the polynomials family. The necessary and sufficient condition for the stability of the entire family is formulated, in the following theorems. In such a case, the set of Kharitonov systems is as follows:

$$G_K(s) = \left\{ \frac{K_B^i(s)}{K_A^j(s)} : i,j = 1,2,3,4 \right\} \tag{6}$$

Where $K_B^i(s), i = 1,2,3,4$ and $K_A^j(s), j = 1,2,3,4$ denote the Kharitonov's polynomials associated with numerators and denumerators of the interval system respectively.

Theorem 1: Kharitonov's Theorem

Every polynomial in the family $I^*(s)$ is Hurwitz if and only if the following eight extreme polynomials are Hurwitz: [19]

$$\begin{aligned}
K^1(s) &= \left(\underline{a_0} + j\underline{b_0}\right) + \left(\underline{a_0} + j\overline{b_0}\right)s + \left(\overline{a_0} + j\overline{b_0}\right)s^2 + \left(\overline{a_0} + j\underline{b_0}\right)s^3 + \cdots \\
K^2(s) &= \left(\overline{a_0} + j\overline{b_0}\right) + \left(\overline{a_0} + j\underline{b_0}\right)s + \left(\underline{a_0} + j\underline{b_0}\right)s^2 + \left(\underline{a_0} + j\overline{b_0}\right)s^3 + \cdots \\
K^3(s) &= \left(\overline{a_0} + j\underline{b_0}\right) + \left(\underline{a_0} + j\underline{b_0}\right)s + \left(\underline{a_0} + j\overline{b_0}\right)s^2 + \left(\overline{a_0} + j\overline{b_0}\right)s^3 + \cdots \\
K^4(s) &= \left(\underline{a_0} + j\overline{b_0}\right) + \left(\overline{a_0} + j\overline{b_0}\right)s + \left(\overline{a_0} + j\underline{b_0}\right)s^2 + \left(\underline{a_0} + j\underline{b_0}\right)s^3 + \cdots
\end{aligned} \tag{7}$$

$$K^5(s) = \left(\underline{a_0} + j\underline{b_0}\right) + \left(\overline{a_0} + j\underline{b_0}\right)s + \left(\overline{a_0} + j\overline{b_0}\right)s^2 + \left(\underline{a_0} + j\overline{b_0}\right)s^3 + \cdots$$

$$K^6(s) = \left(\overline{a_0} + j\overline{b_0}\right) + \left(\underline{a_0} + j\overline{b_0}\right)s + \left(\underline{a_0} + j\underline{b_0}\right)s^2 + \left(\overline{a_0} + j\underline{b_0}\right)s^3 + \cdots$$

$$K^7(s) = \left(\overline{a_0} + j\underline{b_0}\right) + \left(\overline{a_0} + j\overline{b_0}\right)s + \left(\underline{a_0} + j\overline{b_0}\right)s^2 + \left(\underline{a_0} + j\underline{b_0}\right)s^3 + \cdots$$

$$K^8(s) = \left(\underline{a_0} + j\overline{b_0}\right) + \left(\underline{a_0} + j\underline{b_0}\right)s + \left(\overline{a_0} + j\underline{b_0}\right)s^2 + \left(\overline{a_0} + j\overline{b_0}\right)s^3 + \cdots$$

Theorem 2

The closed loop system containing the interval plant **G**(s) is robustly stable if and only if each of the Kharitonov systems in $G_K(s)$ is stable. [19]

Definition: Kharitonov Rectangle

Evaluating the four Kharitonov polynomials $K^1(s)$, $K^2(s)$, $K^3(s)$, and $K^4(s)$ at $s = j\omega_0$, the four vertices of Kharitonov's rectangle will be obtained. Therefore, given an interval polynomial family $P(s,\boldsymbol{q})$ and a fixed frequency $\omega = \omega_0$, the value $P(j\omega_0,\boldsymbol{q})$ is a rectangle whose vertices are given by $K_i(j\omega_0)$ for $i = 1,2,3,4$. [19]

Theorem 3: Origin Exclusion for Interval Families

An interval polynomial family $P(s,\boldsymbol{q})$ has invariant degree and at least one stable member $P(s,q^*)$ is robustly stable, if and only if, the origin of the complex plan is excluded from the Kharitonov's rectangle at all nonnegative frequencies, i.e. $0 \notin P(j\omega_0,\boldsymbol{q})$ for all frequencies. Practically, it is enough to check the zero exclusion for all $\omega \leq \omega_c$, i.e. for frequencies that are less than the crossover frequency. [19]

3.2 Controller Design

In this subsection, we design a robust PID controller, which robustly stabilizes the uncertain system, and guarantees the desired performance of closed loop system.

The required response of the EMA system to be designed, is a deadbeat response as shown in Table 1.

Table 1

System performance requirements

Parameter	Value
Rise time	t_r < 40 msec
Settling time	t_s < 60 msec
Steady-state position error	0
Overshoot	< 1%

Bandwidth	$10\ Hz \leq BW \leq 40\ Hz$
Gain margin	$G_m \geq 7\ dB$
Phase margin	$P_m \geq 40°$

Since the studied system has a time delay and gain-phase margin tester, the complex Kharitonov system will be used. The closed-loop characteristic polynomial of EMA system in Figure 5 is:

$$P(s) = [s^3 + q_1 s^2 + q_2 s] + A.K.(K_d s^2 + K_p s + K_i)(cos\omega T_d - jsin\omega T_d)(cos\varphi - jsin\varphi) \quad (8)$$

where K_p, K_i, and K_d are the coefficients of the PID controller. It is clear from (8) that the polynomial has invariant degree. The coefficients of PID controller K_p, and K_i can be expressed as functions of uncertainties, frequency, and K_d as follows:

$$K_p = f(\omega, K_d, a_i, b_i);\ K_i = g(\omega, K_d, a_i, b_i) \text{ for } \omega \in [0, \infty] \quad (9)$$

By varying the frequency, it is possible to draw the stability boundary in K_p-K_i plan for certain K_d.

The effect of the time delay T_d on the stabilizing region will be verified. The margins and K_d are assigned to be as follows: $A=1$, $\varphi = 0°$ and $K_d = 0.08$. The edge polynomial $K^6(s)$, which has the smallest stabilizing area, is illustrated in Figure 6.

The effect of the coefficient K_d is also considered. The larger K_d results in larger stability region as it is shown in Figure 7 for the first Kharitonov polynomial.

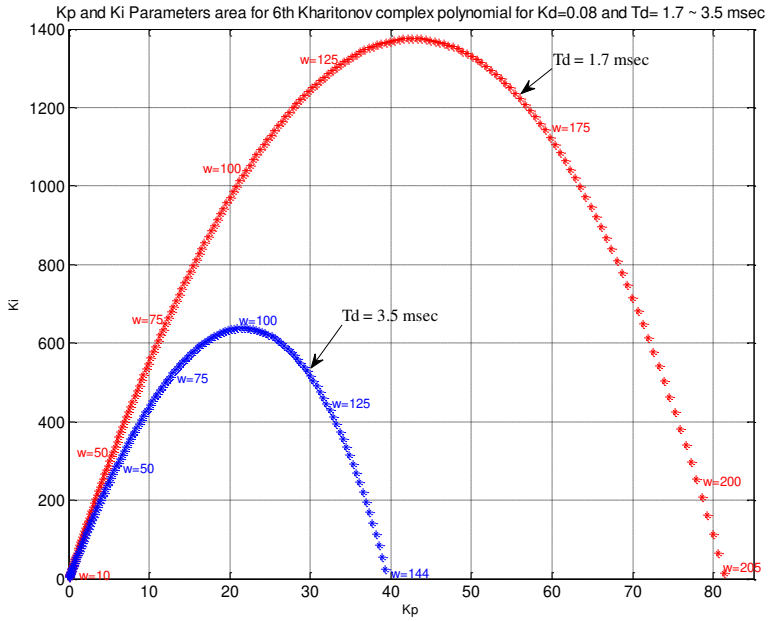

Figure 6

The effect of time delay on the stabilizing area

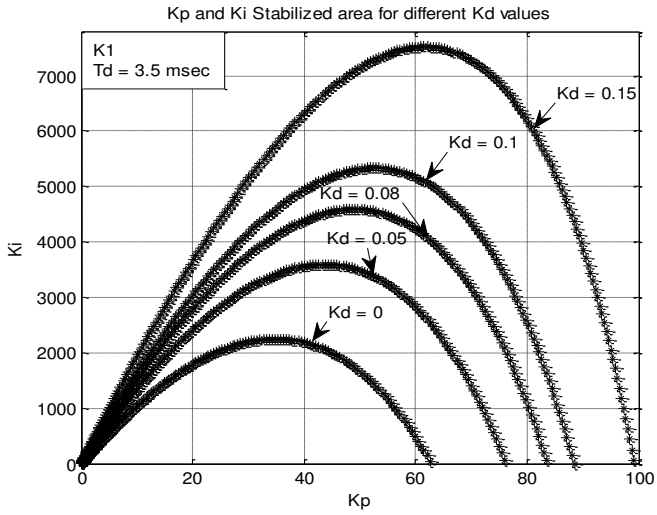

Figure 7

K^I for different values of K_d

Subsequently, the phase margin constraint is the issue of consideration, $P_m \geq 40°$. In this case, all eight Kharitonov's polynomials are plotted in Figure 8, and the stabilized area is that restricted under K^6 and K^8 polynomials.

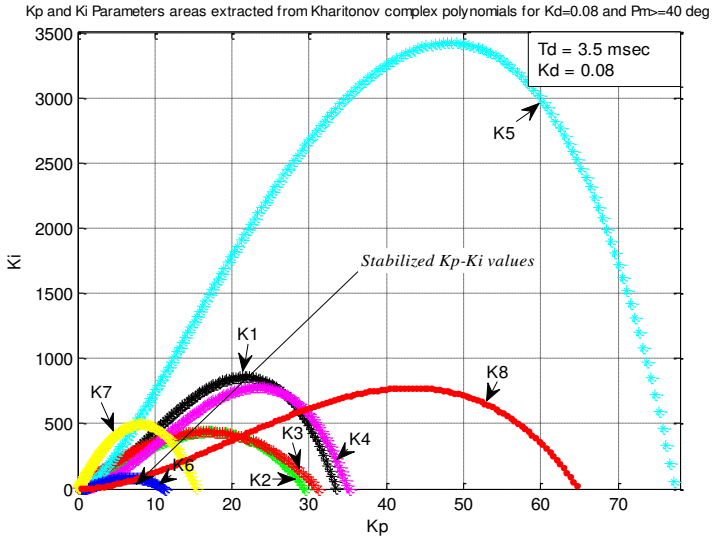

Figure 8

The stabilized lapped area for $P_m \geq 40°$

The next step, in addition to the phase margin constraint, the gain margin constraint will be added $G_m \geq 7\ dB$. The first four Kharitonov's polynomials are separately plotted in Figure 9. The lapped region under the two margins curves is the stabilizing region where the margins constraints are achieved.

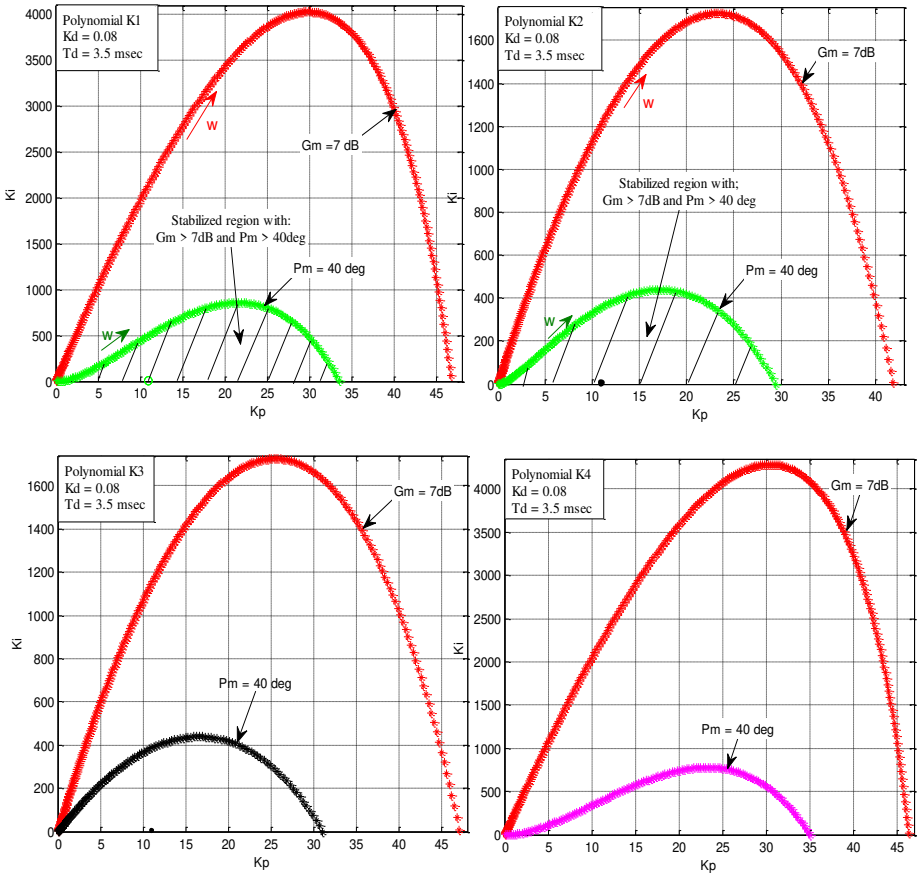

Figure 9

The stabilized lapped areas for the 4 first polynomials with $P_m \geq 40°$ and $G_m \geq 7dB$

Following, the bandwidth condition with upper and lower limits will lead to the restricted area shown in Figure 10 for bandwidth between 10 and 40 Hz.

Thus, all controller's coefficients situated in the common lapped region, shown in Figure 11, robustly stabilize the closed loop EMA system over all the uncertainties under consideration, and ensure the performance margins and bandwidth conditions.

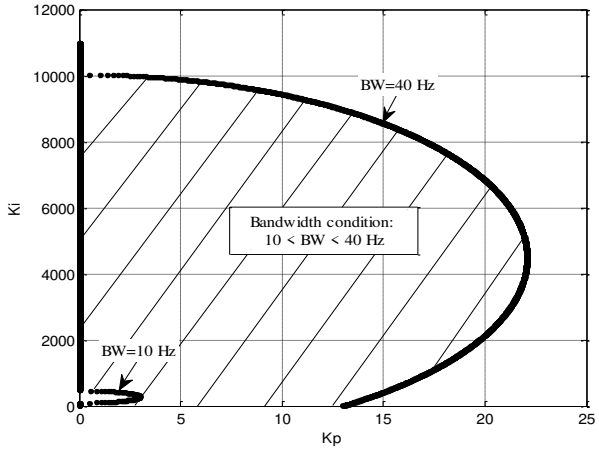

Figure 10
The stabilized area for *10<BW<40 Hz*

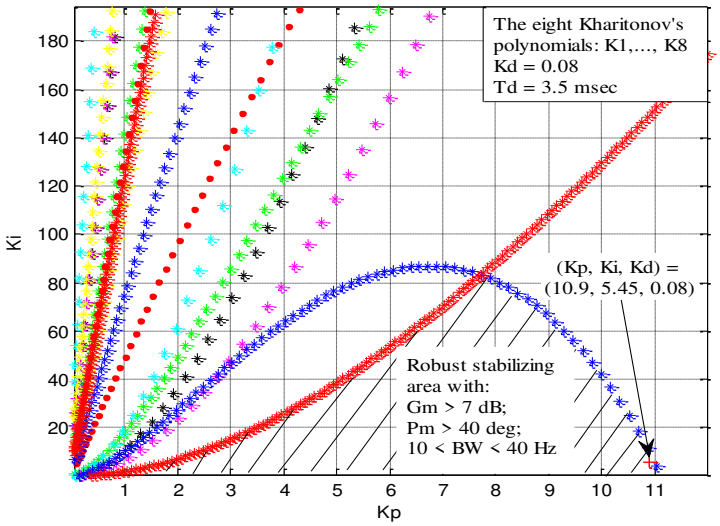

Figure 11
The stabilized lapped area for $P_m \geq 40°$, $G_m \geq 7dB$, *and 10<BW<40 Hz*

The PID controller coefficients should be selected from the stabilized area shown in Figure 11, so that the desired performance requirements of the EMA system are attained.

The selected PID controller is: (K_p, K_i, K_d) = (10.9, 5.45, 0.08). To affirm the method validation, the gain and phase margins for the polynomials family with the designed controller for all the edges uncertainties were extracted and tabulated in Table 2. It is noted that the constraint of required margins $P_m \geq 40°$ and $G_m \geq 7dB$ is verified.

Table 2

Margins for polynomials family with controller (10.9, 5.45, 0.08)

K	q_1	q_2	G_m (dB)	P_m (deg)
949.7	**197.6**	**90.5**	**16.4**	**85.5**
		35	**16.4**	**85.2**
	90.4	**90.5**	**14.6**	**59.2**
		35	**14.6**	**59.1**
512.3	**197.6**	**90.5**	**21.7**	**87.8**
		35	**21.7**	**87.3**
	90.4	**90.5**	**20**	**69.4**
		35	**20**	**69**

3.3 Stability and Performance Robustness Analysis

Figure 12 is the vivid illustration of the nominal closed-loop system analysis with maximum time delay, which indicates its high robustness with *17.6 dB* gain margin and *79.7 deg* of phase margin with bandwidth *12.9 Hz*.

The worst-case analysis (peak-over-frequency type) shows a degradation of the gain and phase margins to a mere *10 dB* and *54.9 deg*, which takes place at frequency *24.5 Hz*. However, the margins are still acceptable compared to the system's requirements. In addition, the frequency at which the worst-case takes place (*24.5 Hz)* is somewhat larger than the system's bandwidth.

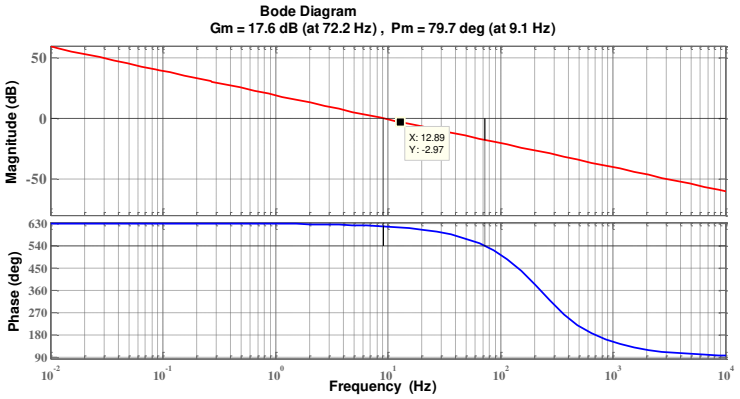

Figure 12

Bode diagram of nominal system with controller (10.9, 5.45, 0.08)

The sensitivity function is a measure of closed-loop performance for the EMA feedback control system. In the time domain, the sensitivity function indicates how well a step disturbance can be rejected. The uncertain sensitivity function S was calculated and the Bode magnitude plots for the nominal and worst-case values of the sensitivity function were compared, as shown in Figure 13.

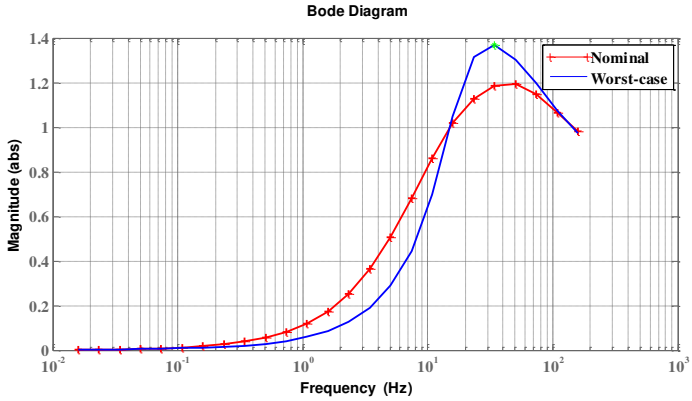

Figure 13

Bode magnitude plot of the nominal and worst-case sensitivity

It is observed that the sensitivity magnitude exceeds one at (15.1 Hz) which is more than the bandwidth of EMA system with the designed controller (12.9 Hz). The critical value of frequency at which maximum gain occurs (34 Hz) as shown in Figure13, with Lower bound 2.714 dB and Upper bound 2.722 dB. The sensitivity function step response, is plotted to observe the variability in disturbance rejection characteristics, as illustrated in Figure 14.

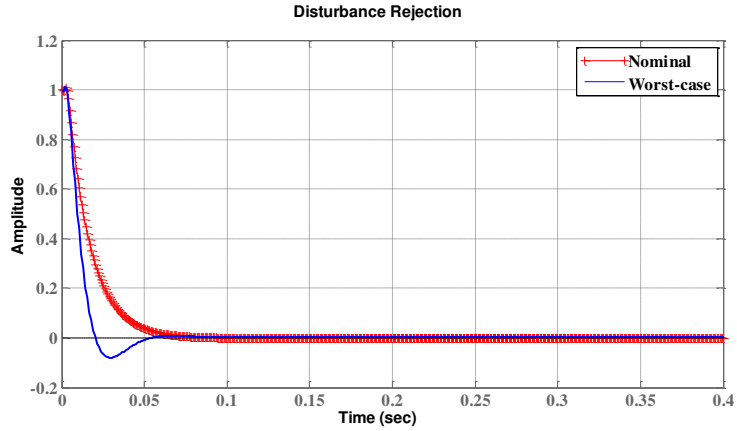

Figure 14

Step response of the nominal and worst-case sensitivity

Since it is enough to test the origin exclusion for $\omega \leq \omega_c$ (the crossover frequency which is less than *100 rad/sec* in the studied system), the rectangles were plotted for frequencies $\omega < 200$ *rad/sec* in Figure 15.

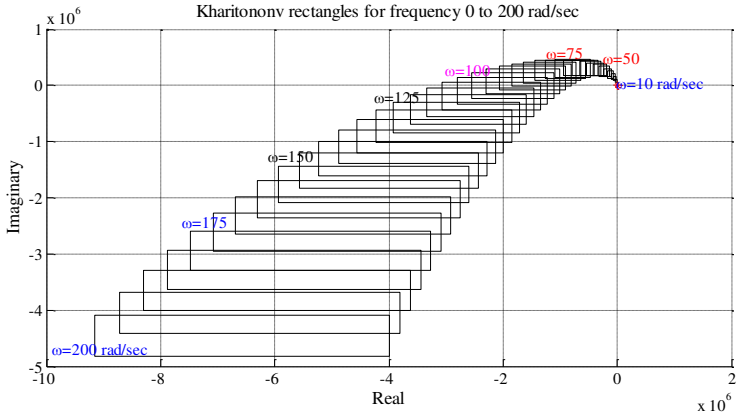

Figure 15

Kharitonov rectangles for the EMA system

As shown in Figure 15, the origin is excluded from the Kharitonov's rectangles, which affirms that the EMA closed loop system is robustly stable.

4 Robust Controller Validation

The EMA system, with the new robust controller, will be validated by Bials's test and by comparing its performance with the original EMA performance.

4.1 Validation by Bialas' Test

Suppose that the polynomials p_1 and p_2 are strictly Hurwitz with their leading coefficient nonnegative and the remaining coefficients positive. Let P_1 and P_2 be their Hurwitz matrices, and define the matrix:

$$W = -P_1 P_2^{-1} \tag{10}$$

Then each of polynomials

$$p = \lambda p_1 + (1-\lambda)p_2, \lambda \in [0,1] \tag{11}$$

is strictly Hurwitz *iff* the real eigenvalues of *W* all are strictly negative.

Remark: the Hurwitz matrix *Q,* for the polynomial *q(s),* is defined as follows

$$q(s) = q_0 s^n + q_1 s^{n-1} + q_2 s^{n-2} \ldots + q_n Q = \begin{bmatrix} q_1 & q_3 & q_5 & \cdots & \cdots & \cdots \\ q_0 & q_2 & q_4 & \cdots & \cdots & \cdots \\ 0 & q_1 & q_3 & q_5 & \cdots & \cdots \\ 0 & q_0 & q_2 & q_4 & \cdots & \cdots \\ 0 & 0 & q_1 & q_3 & q_5 & \cdots \\ \ldots & \cdots & \cdots & \ldots & \cdots & \cdots \end{bmatrix}$$

The designed controller by Kharitonov's theorem should be submitted to the Bialas' test at its 12 exposed edges.

For the first exposed edge: the two polynomials after numerical substitution are

$p_{11}(s) = 2s^3 + 262.78s^2 + 11239s + 5584.3,$

$p_{12}(s) = 2s^3 + 262.78s^2 + 11349s + 5584.3$

Which are both Hurwitz . The Hurwiz matrices of these two polynomials are:

$$P_{11} = \begin{bmatrix} 262.78 & 5584.3 & 0 \\ 2 & 11239 & 0 \\ 0 & 262.78 & 5584.3 \end{bmatrix}, \quad P_{12} = \begin{bmatrix} 262.78 & 5584.3 & 0 \\ 2 & 11349 & 0 \\ 0 & 262.78 & 5584.3 \end{bmatrix}$$

The eigenvalues of $W_1 = -P_{11}P_{12}^{-1}$ are -1, -0.9903, and -1. They are all real and negative. Hence, by Bials' test, the EMA system is stable on the first edge.

Similarly, the other 11 were checked and the eigenvalues of W_i for *i =2… 12* are all real negative. Another example, the eigenvalues of $W_{12} = -P_{121}P_{122}^{-1}$ are -0.5394, -0.5410, and -0.8718. So, by the edge theorem, the system is robustly stable for the uncertainties under consideration.

4.2 Performance Validation

Finally, the step responses of the EMA system with the designed robust controller and the identified original one were plotted (as illustrated in Figure 16).

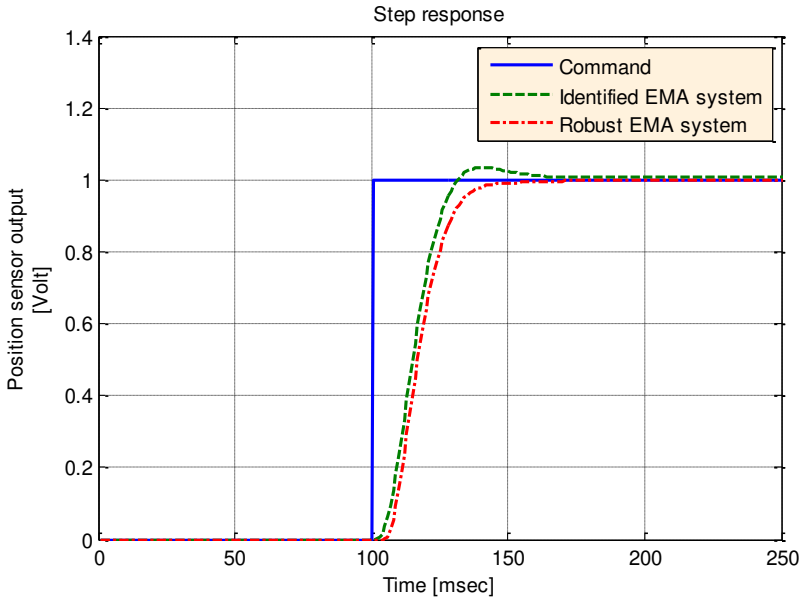

Figure 16

Step responses for EMA systems

The main characteristics of the EMA systems are shown in Table 3. The new designed EMA system, in addition to its robustness to parametric uncertainties and margins achievement, has no overshoot. In addition, in spite of small degradation in rise and settling times, they are still within the acceptable ranges.

Table 3

Characteristics of original and robust EMA systems

Model	$t_{r\ (0\sim90\%)}$ (msec)	t_s (msec)	t_p (msec)	Overshoot (%)
Identified original EMA	25	46	39.5	2.6
Robust EMA	30	48	--	0

A low pass filter (LPF) is added to the derivative path of the PID controller in order to pass only low frequency gain and attenuate the high frequency one.

$$LPF(s) = \frac{1}{0.001\ s + 1}$$

To attain the last results, the EMA system with the designed robust controller secures the robust stability over the uncertainties intervals and attains the required margins ($P_m \geq 40°$, $G_m \geq 7dB$) with an acceptable bandwidth. In time domain, it has no overshoots and no steady-state errors. Therefore, all the required specifications shown in Table 1 are accomplished.

Conclusions

A novel approach was proposed, to graphically design a robust PID controller, for a parametric uncertain system with time delay constrained with gain and phase margins conditions. It was then applied to an EMA system, the designed controller ensured robust stability, while shaping the performance in a desired fashion. Finally, in order to validate its practicality, the robust EMA system was compared with the identified EMA system. In addition, to its robustness, the robust EMA system proved better dynamic characteristics than the original.

References

[1] C. Gerada, and K. J. Bradley: Integrated PM Machine Design for an Aircraft EMA, IEEE Transactions on Industrial Electronics, Vol. 55, No. 9, 2008, pp. 3300-3306

[2] D. Howe: Magnetic Actuators, Sensors and Actuators, Vol. 81, 2000, pp. 268-274

[3] J. Liscouët, J.-C. Maré, and M. Budinger: An Integrated Methodology for the Preliminary Design of Highly Reliable Electromechanical Actuators: Search for Architecture Solutions, Aerospace Science and Technology, Vol. 22, 2012, pp. 9-18

[4] E. N. Gonçalves, R. M. Palhares, and R. H. C. Takahashi: H_2/H_∞ Robust PID Synthesis for Uncertain Systems, Proceedings of the 45th IEEE conference on Decision & Control, San Diego, CA, USA, December 13-15, 2006, pp. 4375-4380

[5] T. Yamamoto, T. Ueda, H. Shimegi, T. Sugie, S. Tujio, and T. Ono: A Design Method of Robust Controller and Its Application to Positioning Servo, JSME International Journal, Series III, Vol. 33, No. 4, 1990, pp. 649-654

[6] H. Lu, Y. Li, and C. Zhu: Robust Synthesized Control of Electromechanical Actuator for Thrust Vector System in Spacecraft, J. Computers and Mathematics with Applications, Vol. 64, Issue 5, 2012, pp. 699-708

[7] S. E. Lyshevski, R. D. Colgren, and V. A. Skormin: High Performance Electromechanical Direct-Drive Actuators for Flight Vehicles, Proceedings of the American Control Conference, Arlington, VA, June 25-27, 2001, pp. 1345-1350

[8] S. E. Lyshevski: Electromechanical Flight Actuators for Advanced Flight Vehicles, IEEE Transactions on Aerospace and Electronic Systems Journal, Vol. 35, No. 2, 1999, pp. 511-518

[9] M. Ristanović, Ž. Ćojbašić, and D. Lazić: Intelligent Control of DC Motor Driven Electromechanical Fin Actuator, J. Control Engineering Practice, Vol. 20, 2012, pp. 610-617

[10] C. Yoo, Y. Lee, and S. Lee: A Robust Controller for an Electro-Mechanical Fin Actuator, Proceeding of the American Control Conference, Boston, Massachusetts, June 30-July 2, 2004, pp. 4010-4015

[11] J. Dawes, L. Ng, R. Dorf, and C. Tam: Design of Deadbeat Robust Systems, Glasgow, UK, 1994, pp. 1597-1598

[12] R. Toscano: A Simple Robust PI/PID Controller Design via Numerical Optimization Approach, J. of Process Control, Vol. 15, 2005, pp. 81-88

[13] D. Valério, J. Costa: Tuning of Fractional Controllers Minimising H2 and H_∞ Norms, Acta Polytechnica Hungarica, Vol. 3, No. 4, 2006, pp. 55-70

[14] R. Bréda, T. Lazar, R. Andoga, and L. Madarász: Robust Controller in the Structure of Lateral Control of Maneuvering Aircraft, Acta Polytechnica Hungarica, Vol. 10, No. 5, 2013, pp. 101-124

[15] N. Tan: Computation of Stabilizing PI-PD Controllers, International Journal of Control, Automation, and Systems, 7(2), 2009, pp. 175-184

[16] Y. J. Huang and Y. J. Wang: Robust PID Tuning Strategy for Uncertain Plants Based on the Kharitonov Theorem, ISA Transactions, Vol. 39, 2000, pp. 419-431

[17] P. C. Krause, O. Wasynczuk, and S. D. Sundhoff: Analysis of Electric Machinery and Drive Systems, IEEE press, 2002

[18] K.-K. Shyu, and Y.-Y. Lee: Identification of Electro-Mechanical Actuators within Limited Stroke, Journal of Vibration and Control, Vol. 16(12), 2010, pp. 1737-1761

[19] S. P. Bhattacharyya, H. Chapellat, and L. H. Keel: Robust Control: The Parametric Approach, Prentice Hall, 1995

Parameter Influence on the Harmonically Excited Duffing Oscillator

Livija Cveticanin[1], Gyula Mester[2] and Istvan Biro[2]

[1] Faculty of Technical Sciences, Trg D. Obradovica 6, 21000 Novi Sad, Serbia
cveticanin@uns.ac.rs

[2] University of Szeged, Faculty of Engineering, Mars tér 7, H-6724 Szeged, Hungary; gmester@inf.u-szeged.hu; biro-i@mk.u-szeged.hu

Abstract: In this paper the influence of the initial conditions and the interaction of the parameters on the motion of the strong nonlinear Duffing oscillator are investigated. The initial conditions are arbitrary and need not be zero. An analytical procedure for solving the strong nonlinear differential equation with excitation term is developed. The obtained solutions give the physical explanation of the excited vibrations caused by the excitation force and non-zero initial conditions. The analytical results are compared with numerical results and show good agreement.

Keywords: Duffing oscillator; harmonic excitation; non-zero initial conditions; jump effect

1 Introduction

Vibration data, obtained by repeated measurement in a forced system (for example, motor-support system), represent a spectra of different values, in spite of the fact, that the measuring position and conditions, as well as, the excitation of the system has not changed. Using the theoretical consideration of the excited vibration of non-linear systems, it is to be expected that the obtained results have to be highly repeatable and to satisfy certain rules (see [1]-[13] and References mentioned in them). For all of the aforementioned analytical investigations, it is common to assume that the motion is steady state, with non-zero initial conditions. Namely, it is stated that the initial conditions have nothing to do with the long term motion properties and need not to be taken into account. The discrepancy between the experimental and analytical values gives us an idea to investigate nonlinear excited vibrations by including the initial conditions. In the paper [14], the vibrations of a harmonically excited pure nonlinear oscillator (the linear displacement term fails) with non-zero initial conditions is analyzed. It has been noticed that in spite of long term motion, the influence on the initial conditions on the motion remains. The intention of this paper is to analyze the

effect of the initial conditions on the motion of an excited nonlinear oscillator of Duffing type. For this model the linear displacement force is also taken into consideration. The model of the system is a strong nonlinear second order differential equation with an excitation term

$$\ddot{y} + \alpha y + \gamma y^3 = F_0 \cos(\Omega t), \tag{1}$$

and arbitrary initial conditions

$$y(0) = y_0, \quad \dot{y}(0) = \dot{y}_0, \tag{2}$$

where α and γ are the coefficients of the linear and cubic terms, F_0 and Ω are the excitation amplitude and frequency, y_0 and $\dot{y}_0$ are the initial displacement and velocity, respectively. The solution of (1) is assumed in the form which is usual for the linear vibration model. Using the harmonic balance method the coefficients of the solution are determined. For the special group of parameter values the jump-up and jump-down phenomena are investigated with special attention to the influence of the initial values. The interaction between the oscillator parameters and arbitrary initial conditions on the vibration are also analyzed. For certain numerical values the analytically obtained results are compared with numerical results. They are in good agreement.

2 Analytical Solving Procedure

Let us assume the solution of (1) as a sum of trigonometric functions

$$y = A\cos(\Omega t) + B\cos(\omega t) + C\sin(\omega_1 t), \tag{3}$$

where A, B, C and also ω and ω_1 are unknown values. This form corresponds to the usual solution of the harmonically excited linear oscillator. Substituting (3) and its first and second time derivative into (1) we obtain

$$\begin{aligned} &F_0\cos(\Omega t) = (\alpha - \Omega^2)A\cos(\Omega t) + (\alpha - \omega^2)B\cos(\omega t) + (\alpha - \omega_1^2)C\sin(\omega_1 t) \\ &+ \gamma(A\cos(\Omega t) + B\cos(\omega t) + C\sin(\omega_1 t))^3. \end{aligned} \tag{4}$$

Separating the terms with the first order trigonometric functions $\cos(\Omega t)$, $\cos(\omega t)$ and $\sin(\omega_1 t)$ in (4), the following system of three algebraic equations is obtained

$$\begin{aligned} &\cos(\Omega t): \quad (\alpha - \Omega^2)A + \frac{3}{4}\gamma A(A^2 + 2B^2 + 2C^2) = F_0, \\ &\cos(\omega t): \quad (\alpha - \omega^2) + \frac{3}{4}\gamma(2A^2 + B^2 + 2C^2) = 0, \\ &\sin(\omega_1 t): \quad (\alpha - \omega_1^2) + \frac{3}{4}\gamma(2A^2 + 2B^2 + C^2) = 0. \end{aligned} \tag{5}$$

The initial conditions (2) with (3) give two additional algebraic equations

$$B = y_0 - A, \quad \omega_1 = \dot{y}_0 / C. \tag{6}$$

Substituting (6) into $(5)_3$ the parameter C as the function of A follows

$$C^2 = \frac{2}{3\gamma}\left[\alpha + \frac{3\gamma(A^2 + (y_0 - A)^2)}{2}\right]\left[\sqrt{1 + \frac{3\gamma\dot{y}_0^2}{\left[\alpha + 3\gamma(A^2 + (y_0 - A)^2)/2\right]^2}} - 1\right]. \tag{7}$$

Using (6) and (7), the relations $(5)_1$ and $(5)_2$ transform into

$$F_0 = (\alpha - \Omega^2)A + \frac{3\gamma A}{4}\left(A^2 + 2(y_0 - A)^2\right) + \frac{4A}{3\gamma}\left(\sqrt{\left(\alpha + \frac{3}{2}(A^2 + (y_0 - A)^2)\right)^2 + 3\gamma\dot{y}_0^2} - \left(\alpha + \frac{3}{2}(A^2 + (y_0 - A)^2)\right)\right), \tag{8}$$

and

$$0 = (\alpha - \omega^2) + \frac{3\gamma}{4}\left(2A^2 + (y_0 - A)^2\right) + \frac{4}{3\gamma}\left(\sqrt{\left(\alpha + \frac{3}{2}(A^2 + (y_0 - A)^2)\right)^2 + 3\gamma\dot{y}_0^2} - \left(\alpha + \frac{3}{2}(A^2 + (y_0 - A)^2)\right)\right). \tag{9}$$

Eq. (8) is a sixth order algebraic equation for parameter A. The solution for A has to be substituted into (9) and the solution for ω.

3 Solution for Non-Zero Initial Displacement

For the case when the initial velocity is zero ($\dot{y}_0 = 0$) but the initial displacement is a non-zero one ($y_0 \neq 0$)

$$y(0) = y_0, \quad \dot{y}(0) = 0, \tag{10}$$

the aforementioned relations (7)-(9) transform into

$$(\alpha - \Omega^2)A + \frac{3}{4}\gamma A(A^2 + 2B^2) = F_0, \quad (\alpha - \omega^2) + \frac{3}{4}\gamma(2A^2 + B^2) = 0, \quad C = 0, \quad \omega_1 = 0, \quad B = y_0 - A. \tag{11}$$

The general solution (3) simplifies into

$$y = A\cos(\Omega t) + (y_0 - A)\cos(\omega t), \tag{12}$$

where A and ω are the solutions of the equations

$$\begin{aligned} &\frac{9}{4}\gamma A^3 - 3y_0\gamma A^2 + (\alpha - \Omega^2 + \frac{3}{2}\gamma y_0^2)A - F_0 = 0, \\ &\omega^2 = \alpha + \frac{3}{2}\gamma A^2 + \frac{3}{4}\gamma(y_0 - A)^2. \end{aligned} \tag{13}$$

The relation $(13)_2$ can be rewritten in the form

$$\omega^2 = \omega_f^2 - \frac{3}{2}\gamma A(y_0 - \frac{3}{2}A), \tag{14}$$

where $\omega_f = \sqrt{\alpha + 3\gamma y_0^2/4}$ is the approximate frequency of free vibration [15]. Eq. (14) represents the corrected frequency of vibration caused by harmonic excitation. The frequency depends not only on the initial amplitude, as in the case for free vibrations of cubic nonlinear oscillator, but also on the excitation properties. Introducing the new variable $A = Y + 4y_0/9$ into $(13)_1$, we have a cubic algebraic equation.

$$Y^3 + pY + q = 0 \tag{15}$$

where

$$p = \frac{12(\alpha - \Omega^2) + 2\gamma y_0^2}{27\gamma}, \quad q = Q - \frac{4F_0}{9\gamma}, \quad Q = \frac{144y_0(\alpha - \Omega^2 + 88\gamma y_0^3}{729\gamma}. \tag{16}$$

The number of real solutions of (15) depends on the relation between the parameters of the excitation force F_0 and Ω, ant the initial displacement y_0. As suggested by mathematicians the number of real solutions (one or three) depends on the sign of the discriminant $D = (q^2/4) + (p^3/27)$ which is according to (16)

$$D = \frac{1}{4}\left(Q - \frac{4F_0}{9\gamma}\right)^2 + \frac{p^3}{27}. \tag{17}$$

For $D>0$ the number of real solutions of (15) is one and for $D<0$ it is three. The boundary discriminant of $(13)_1$ is $D=0$, when two of the real solutions are equal and the third differs.

3.1 Discussion of the Domain of Solutions

For computational reasons, let us rewrite the relation (17) in the form more suitable for analysis

$$D = \left(\frac{2}{9\gamma}\right)^2 \left(F_0 - \frac{9\gamma Q}{4} - \frac{9\gamma}{2}\sqrt{\frac{|p|^3}{27}}\right)\left(F_0 - \frac{9\gamma Q}{4} + \frac{9\gamma}{2}\sqrt{\frac{|p|^3}{27}}\right), \tag{18}$$

where according to (16) the $\Omega(p)$ and $Q(p)$ functions are

$$\Omega = \sqrt{\alpha - \frac{1}{2}\left(27\gamma p - 2\gamma y_0^2\right)}, \quad Q = \frac{4py_0}{9} + \frac{64y_0^3}{729}. \tag{19}$$

The discriminant (18) is zero for (19) and

$$F_{01} = \frac{16\gamma}{81} y_0^3 + \gamma p y_0 - \frac{\gamma|p|}{2}\sqrt{3|p|}, \quad F_{01} = \frac{16\gamma}{81} y_0^3 + \gamma p y_0 + \frac{\gamma|p|}{2}\sqrt{3|p|}. \tag{20}$$

Substituting(19) into (20) the boundary F_0-Ω functions for various values of initial displacement y_0 are obtained as

$$\begin{aligned} F_{01} &= \frac{16\gamma y_0^3}{81} + \frac{\left|12\left(\alpha - \Omega^2\right) + 2\gamma y_0^2\right|}{27}\left(y_0 - \frac{1}{2}\sqrt{\frac{\left|12\left(\alpha - \Omega^2\right) + 2\gamma y_0^2\right|}{9\gamma}}\right), \\ F_{01} &= \frac{16\gamma y_0^3}{81} + \frac{\left|12\left(\alpha - \Omega^2\right) + 2\gamma y_0^2\right|}{27}\left(y_0 + \frac{1}{2}\sqrt{\frac{\left|12\left(\alpha - \Omega^2\right) + 2\gamma y_0^2\right|}{9\gamma}}\right). \end{aligned} \tag{21}$$

Analyzing the relations (19) and (21) it is obvious that for

$$p = \frac{16y_0^2}{27}, \quad i.e., \quad \Omega = \sqrt{\alpha + \frac{3}{2}\gamma y_0^2}, \tag{22}$$

the excitation amplitude is minimal and has the value $F_{0\min}$=0.

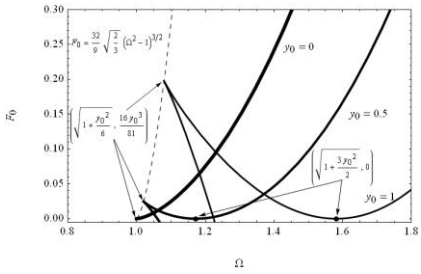

Figure 1
F_0-Ω curves with characteristic points for α=γ=1 and various initial displacements

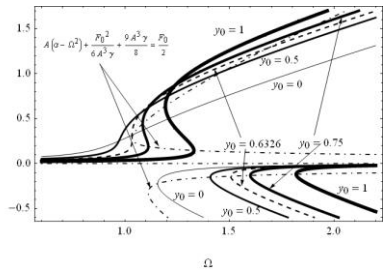

Figure 2
A-Ω curves with characteristic points α=γ=1, F_0 =0.05 and various initial displacements

In addition, if the discriminant is zero, it follows

$$\Omega = \sqrt{\alpha + \frac{\gamma y_0^2}{6}}, \quad F_0 = \frac{16\gamma y_0^3}{81}, \tag{23}$$

as the value of p is zero. The values (22) and (23) correspond to two characteristic points in the F_0-Ω plane. In Fig. 1 the F_0-Ω curves (21) for several values of initial

displacements (y_0=0;0.5;1) are plotted. The parameters of the system are α=1 and γ=1. The excitation amplitude is positive, i.e., F_0>0. It can be seen that for y_0=0 the F_0-Ω curve is single-valued. Namely, the relations (21) transform into only one and give a curve which separates the F_0-Ω plane into two regions: left from the limit curve where the discriminant D is positive and right of the curve where the discriminant is not positive ($D\geq 0$). For y_0>0, the F_0-Ω curves are multi-valued. The two curves (21) give in the F_0-Ω plane an additional region where $D\geq 0$. The obtained region is larger for higher values of initial displacement. The Ω and F_0 coordinates for the peak points of the region are $(\sqrt{1+y_0^2/6}, 16y_0^3/81)$ and $(\sqrt{1+3y_0^2/2}, 0)$ according to (22) and (23). The higher the value of y_0 the peak values move toward higher values of Ω and F_0. For F_0 higher than the peak value only one jump frequency is evident for which the discriminant changes the sign. For the 'jump frequency' there is the transition from the region where D>0 to the region where D<0.

3.2 Analytical Expression of Solutions

As it was previously mentioned the number of real solutions of $(13)_1$ depends on the sign of the discriminant D.

a) For D=0 three real solutions of $(13)_1$ exist, where two of them are equal

$$A_1 = \frac{4y_0}{9} + 2\sqrt[3]{-\frac{Q}{2} + \frac{2F_0}{9\gamma}}, \quad A_{2,3} = \frac{4y_0}{9} + \sqrt[3]{\frac{Q}{2} - \frac{2F_0}{9\gamma}}. \tag{24}$$

b) For the values of excitation F_0 and Ω which are inside the area (21) the discriminant is negative and three real solutions are

$$A_1 = \frac{4y_0}{9} + K\cos\frac{\varphi}{3}, \quad A_2 = \frac{4y_0}{9} + K\cos\frac{\varphi+2\pi}{3}, \quad A_3 = \frac{4y_0}{9} + K\cos\frac{\varphi+\pi}{3}, \tag{25}$$

where

$$K = 2\sqrt{-\frac{p}{3}}, \quad \cos\varphi = -\frac{Q}{2} + \frac{2F_0}{9\gamma}\left(-\frac{p}{3}\right)^{-3/2} \tag{26}$$

c) Outside the region (21), where the discriminant D of $(13)_1$ is positive, only one real solution exists

$$A = \frac{4y_0}{9} + \sqrt[3]{-\frac{Q}{2} + \frac{2F_0}{9\gamma} + \sqrt{D}} + \sqrt[3]{-\frac{Q}{2} + \frac{2F_0}{9\gamma} - \sqrt{D}} \tag{27}$$

The result (27) is valid for all values of F_0 and for the excitation frequency which satisfies the relation

$$\Omega < \sqrt{\alpha + \frac{1}{6}\gamma y_0^2} \tag{28}$$

where the parameter p and the discriminant are always positive.

In Fig. 2 according to (23)-(27) the response amplitude A as a function of the excitation frequency Ω for several initial displacements (y_0=0;0.5;0.6326;0.75;1) is shown. The excitation amplitude is F_0=0.05 and the parameters of the oscillator are α=γ=1. We note that, depending on the value of y_0, some of the curves are multi-valued while others are single-valued. It is of special interest to determine the characteristic points in A-Ω curves where the bifurcation of the solution appears.

3.3 Characteristic Points

Let us rewrite the relation $(13)_1$ into the form

$$\Omega = \sqrt{\frac{9\gamma A^2}{4} - 3y_0\gamma A - \frac{F_0}{A} + \frac{3\gamma y_0^2}{2} + \alpha} \tag{29}$$

To obtain the characteristic peak values in the aformentioned A-Ω curves, the first derivative of (29) for Ω as a function of the amplitude A has to be equated with zero

$$\frac{9}{2}\gamma A^3 - 3y_0\gamma A^2 + F_0 = 0 \tag{30}$$

The cubic algebraic equation has one or three real solutions dependent on the sign of the discriminant

$$D_1 = \frac{F_0}{81\gamma^2}\left(F_0 - \frac{16\gamma y_0^3}{81}\right) \tag{31}$$

For D_1>0, when $F_0 > 16\gamma y_0^3/81$, only one real solution for A exists

$$A_m = \frac{2y_0}{9} + \sqrt[3]{\frac{1}{9}\left(-\frac{F_0}{\gamma} + \frac{8y_0^3}{81}\right) + \sqrt{D_1}} + \sqrt[3]{\frac{1}{9}\left(-\frac{F_0}{\gamma} + \frac{8y_0^3}{81}\right) - \sqrt{D_1}} \tag{32}$$

For D_1=0, i.e., $F_0 = 16\gamma y_0^3/81$ two real solutions exist

$$A_{m1} = -\frac{2y_0}{9}, \quad A_{m2,m3} = \frac{4y_0}{9} \tag{33}$$

For $D_1<0$, i.e., $0 < F_0 < 16\gamma y_0^3/81$ three real solutions exist

$$A_{m1} = \frac{2y_0}{9}\left(1+2\cos\frac{\psi}{3}\right), \quad A_{m2} = \frac{2y_0}{9}\left(1+2\cos\frac{\psi+2\pi}{3}\right),$$
$$A_{m2} = \frac{2y_0}{9}\left(1+2\cos\frac{\psi+4\pi}{3}\right) \tag{34}$$

where

$$\cos\psi = 1 - \frac{81F_0}{8y_0^3\gamma} \tag{35}$$

Analyzing the relation (30) the initial displacement as the function of the response and excitation amplitude is expressed

$$\frac{1}{3\gamma A^2}\left(\frac{9}{2}\gamma A^3 + F_0\right) = y_0 \tag{36}$$

Substituting (36) into $(13)_1$ we eliminate the initial displacement and we have the $A(\Omega)$ function for various values of F_0

$$(\alpha - \Omega^2)A + \frac{9}{8}\gamma A^3 - \frac{F_0}{2} + \frac{F_0^2}{6\gamma A^3} = 0 \tag{37}$$

Substituting the values of the amplitudes A_m (32)-(34) into (37) the frequencies Ω_m are obtained

$$\Omega_{mi} = \sqrt{\alpha + \frac{9}{8}\gamma A_{mi}^2 - \frac{F_0}{2A_{mi}} + \frac{F_0^2}{6\gamma A_{mi}^4}} \tag{38}$$

where i=1,2,3. The values (A_m,Ω_m) correspond to certain constant value of F_0 and initial displacement y_0.

In Table 1, the characteristic amplitudes and frequencies for the oscillator with parameter values F_0=0.05, α=γ=1 and various initial conditions y_0 are calculated.

It can be concluded that for y_0<0.6326 one solution exists, while for $y_0 \geq 0.6326$ number of solutions is three. Comparing the values in Table 1 with the characteristic points in Fig. 2, it can be seen that they are in good agreement.

Table 1
Characteristic amplitudes and frequencies for various initial conditions

Y_0	A_1	Ω_1	A_2	Ω_2	A_3	Ω_3
0	-0.22314	1.1559				
0.5	-0.15140	1.4085				
0.63257	-0.14057	1.5057	0.28114	1.0328	0.28114	1.0328
0.75	-0.13254	1.5996	0.18902	1.1110	0.44351	1.0843
1	-0.11893	1.8191	0.14610	1.3295	0.63950	1.1931

3.4 Explanation of the Solution

Based on the approximate analytical solution (12), and results given in the previous Section, the physical phenomena and vibration of the harmonically excited Duffing oscillator with non-zero initial displacement are discussed. The parameters α and γ and also the initial displacement y_0 are treated as constant values. For the constant values of excitation amplitude F_0 the excitation frequency Ω is increased from zero to infinity.

1) For the excitation frequency $\Omega \approx \varepsilon > 0$, where ε is a small positive value, the parameter A is positive and satisfies the relation $A < y_0$ (see Eq. $(13)_1$). The approximate solution (12) for vibration simplifies into

$$y \approx A + (y_0 - A)\cos(\omega t) \tag{39}$$

where

$$\omega \approx \omega_f \sqrt{1 - \frac{3\gamma A y_0}{2\omega_f^2}} \tag{40}$$

The harmonic vibration with amplitude (y_0-A) and frequency ω (40) is around the position A. If the calculated parameter A is small, i.e. $A << y_0$, the relation (39) simplifies into

$$y = y_0 \cos(\omega t) \tag{41}$$

The frequency of excited vibration ω is smaller than the frequency of free vibration ω_f. The period of excited vibration is longer than for free vibration of the system. Comparing the excited frequency ω with the excitation frequency Ω it has been concluded that the second is significantly smaller than the first one.

2) For the excitation frequency

$$\Omega^* = \sqrt{\left(\alpha + \frac{3}{4}\gamma y_0^2\right) - \frac{F_0}{y_0}} = \omega_f \sqrt{1 - \frac{F_0}{y_0 \omega_f^2}} \tag{42}$$

we have $A=y_0$. The solution (12) simplifies into

$$y = y_0 \cos(\Omega^* t) \tag{43}$$

The vibration is harmonic in nature, with amplitude y_0 and frequency Ω^* which represents the corrected value of the frequency of free vibration of the system ω_f. The correction parameter depends on the excitation amplitude and the initial displacement. The higher the amplitude of excitation, the more significant is the variation of the frequency to that of free vibration. The period of excited vibration is longer than for free vibration. The relation (42) is valid only for $F_0/(y_0\omega_f^2) \le 1$.

3) For $\Omega>\Omega_{m1}$, where Ω_{m1} is the jump down frequency (37) in A-Ω diagram (see Table 1), the calculated parameter A becomes negative with absolute value $|A|<<y_0$. The oscillations are approximately periodical (39) with frequency

$$\omega \approx \omega_f \sqrt{1+\frac{3\gamma|A|y_0}{2\omega_f^2}} \tag{44}$$

Due to (44) it is evident that the frequency of excited vibration ω is higher than for free vibration ω_f and the period of excited vibration is shorter than for free vibration. For $\Omega>>\omega_f$ the value $|A|$ tends to zero and the frequency of vibration is close to ω_f. The effect of excitation disappears.

4) According to $(13)_1$ it is evident that for $\Omega<\Omega^*$ the parameter A satisfies the relation $A<y_0$. As the difference between the excited and excitation frequency is a small positive value ε, i.e. $\omega-\Omega=\varepsilon>0$, it is convenient to rewrite the solution (12) into the form

$$y = y_0 \cos\Omega t - 2(y_0 - A)\sin(\frac{\omega-\Omega}{2}t)\sin(\frac{\omega+\Omega}{2}t) \tag{45}$$

which is suitable for analysis. The second term in the relation (45) describes trembling with negative amplitude and period $T=2\pi/(\omega-\Omega)$. The period of trembling is lengthened by decreasing the difference between the frequencies ω and Ω. The period is longest for the minimal value of the difference $(\omega-\Omega)$.

5) For $\Omega^*<\Omega<\Omega_{m1}$ the parameter A satisfies the relation $A>y_0$ and according to (13) the difference between the excited and excitation frequencies is positive. The relation transforms into

$$y = y_0 \cos(\Omega t) + 2(A - y_0)\sin(\frac{\omega-\Omega}{2}t)\sin(\frac{\omega+\Omega}{2}t) \tag{46}$$

For the small difference between frequencies ω and Ω the trembling effect is added to the harmonic vibration. The smaller the frequency difference is the higher the trembling period.

4 Examples

Here three numerical examples are considered in an oscillator: 1. The excitation frequency is varied, 2. The excitation amplitude is varied and 3. The initial displacement is varied.Consider the vibrations of an oscillator with values $\alpha=\gamma=1$ and initial displacement $y_0=1$.

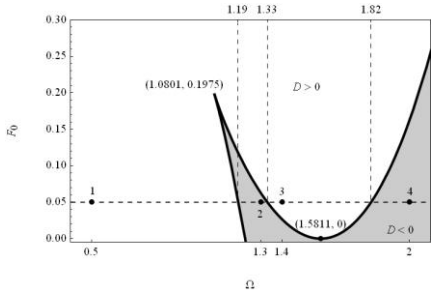

Figure 3
F_0-Ω curve with characteristic points for $\alpha=\gamma=1$ initial displacement $y_0=1\alpha=\gamma=1$

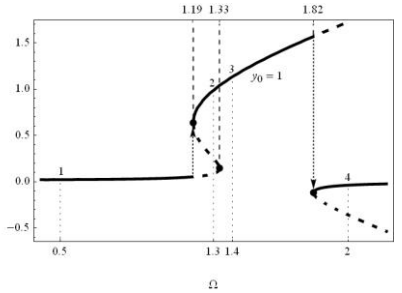

Figure 4
A-Ω curve with characteristic points for and $F_0=0.05$ and initial displacement $y_0=1$

In Fig. 3 the F_0-Ω curve is plotted. The F_0-Ω curve separates the region where $D>0$ and the region where $D\leq 0$ (shaded area). Four (Ω, F_0) sets of excitation parameters are selected: point 1 (0.5, 0.05) for $D>0$, point 2 (1.3, 0.05) for $D<0$, point 3 (1.4, 0.05) for $D>0$, and (2, 0.05) for $D<0$. In Fig. 3 the characteristic points calculated in Table 1 for $y_0=1$ and also the peak values of F_0-Ω are given.

In Fig. 4 the A-Ω curve for $F_0=0.05$ is plotted. The points 1-4 are plotted and the numeric values of the characteristic points are signed. In Fig. 5 the y-t diagrams obtained analytically and numerically for the four mentioned parameter values are plotted.

From the Figures the following is evident:

For the parameter values $\alpha=\gamma=1$, initial displacement $y_0=1$, and excitation values $F_0=0.05$ and $\Omega=0.5$ (point 1) the mathematical model of the system is $\ddot{y}+y+y^3=0.05\cos(0.5t)$. According to the previous consideration the approximate analytical solution is $y=0.02291\cos(0.5t)+0.97709\cos(1.3103t)$. Point 1 is in the region $\Omega<\Omega_1=1.1931$, where only one solution for A exists (see Fig. 4).

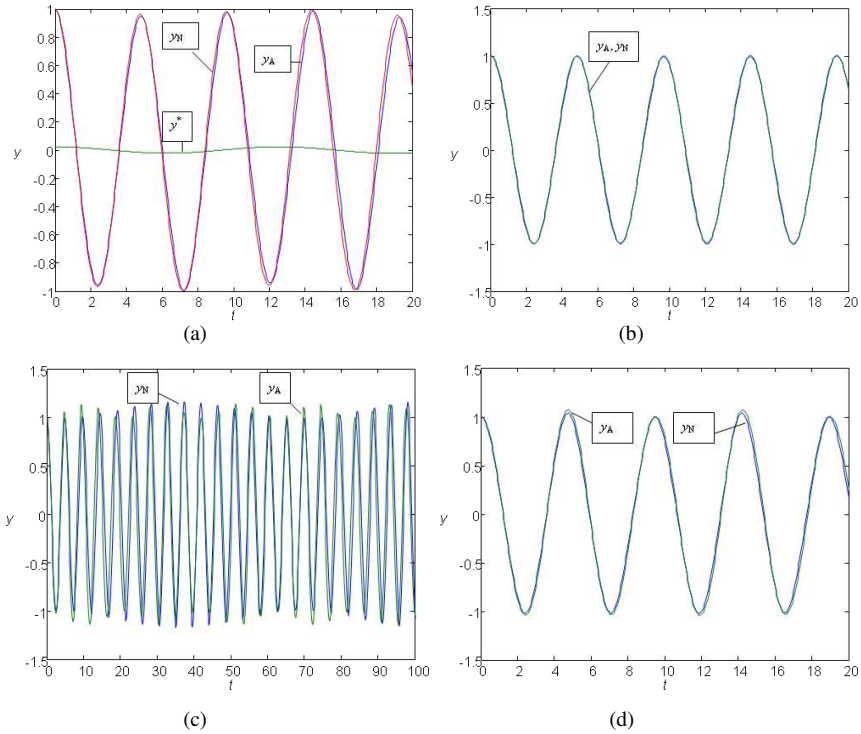

Figure 5

Time history diagrams obtained analytically (y_A), numerically (y_N) and the 'carrying curve' y^* for y_0=1, α=γ=1, F_0=0.05 and:a) Ω=0.5, b) Ω=1.3, c) Ω=1.4 and d) Ω=2

In Fig. 5a the analytical and numerical solution are plotted. The difference between the time history diagrams y-t is negligible. The vibration has two terms: the first is with amplitude $A<<y_0$ and with period 4π, and the second vibration term is with frequency $\omega<\omega_0$. In Fig. 5a it has been shown that the first term in the analytical solution can be treated as the 'carrying vibration' and the second term is the 'carried vibration' which is along the first one. The total vibration is with maximal amplitude y_0.

Differential equation of motion for Ω=1.3 (point 2) is $\ddot{y} + y + y^3 = 0.05\cos(1.3)$. Point 2 is in the region Ω_1=1.1931<Ω<Ω_2=1.3295, where three real solutions for A exist (Fig. 3): A_1=0.25058, A_2=0.089264, A_3=0.99349. As for Ω_1=1.1931 the jump phenomena for amplitude A occurs, (see Fig. 4), the biggest value A_3 is valid for further analytical calculation. The approximate analytical solution is y=0.9935cos(1.3t)+0.0065cos(1.575t). In Fig. 5b the analytical solution is compared with numerically obtained one by solving the differential equation. As the amplitude $A>>B$, the term with excitation frequency Ω is dominant. For this

case the term with excited frequency ω can be treated as a correction function. The approximate solution $y \approx 0.9935\cos(1.3t)$ is almost harmonic with amplitude close to y_0.

Point 3, with excitation frequency $\Omega=1.4$, is in the region $\Omega_2=1.3295<\Omega<\Omega_3=1.8191$ where only one real solution for A exists (Fig. 3). The calculated value is $A=1.0717$ and is higher than the initial value of the amplitude ($y_0=1$) while coefficient B is negative ($B=-0.0717$). For $\ddot{y}+y+y^3=0.05\cos(1.4)$ the approximate solution is $y=1.0717\cos(1.4t)-0.717\cos(1.6513t)$. In Fig. 5c the analytical and numerical solutions y-t are plotted. The obtained solutions are in good agreement. From the analytical solution it has been seen that the term with excitation *frequency* $\Omega=1.4$ is still the dominant one. Comparing the analytical solution by neglecting the second term as a small value, with the free vibration it has been concluded that the amplitude of vibration is higher and the period of vibration is shorter.

The excitation frequency $\Omega=2$ in point 4 is in the region $\Omega>\Omega_3=1.8191$ where three real solutions for A (see Fig. 4) can be calculated ($A_1=-3.5994\times10^{-2}$, $A_2=-0.35752$, $A_3=1.7268$). For $\Omega_3=1.8191$ there is a jump in the value of A and the smallest absolute value of A corresponds to the real vibrating system. Thus, for $\Omega=2$ (point 4) the solution is $y=1.03599\cos(1.3442t)-0.03599\cos(2t)$. In Fig. 5d the analytically obtained solution is compared with the numerical result, which is the solution of the differential equation $\ddot{y}+y+y^3=0.05\cos(2t)$. The second term in the approximate solution is negligible in comparison to the first term. Comparing the approximate solution $y \approx 1.03599\cos(1.3442t)$ with $y=1\cos(1.322t)$ for the free vibrations of the oscillator [15] described with $\ddot{y}+y+y^3=0$ it can be seen that the amplitude and frequency of vibration of the harmonically excited oscillator is smaller than for $\Omega=1.4$ and tends toward the properties of the free oscillator.

In Fig. 6 the time history diagram for $\alpha=\gamma=1$, $\Omega=1.3$, initial amplitude $y_0=1$ and excitation amplitude $F_0=0.25$ is plotted. There is only one real solution for A (see Fig. 3) which gives the approximate analytical solution $y=1.0976\cos(1.3t)-0.0976\cos(1.6776t)$, which in comparison with the numerical one shows good agreement. Comparing Fig. 6 with Fig. 5b the influence of increase of the excitation amplitude on the vibration properties of the oscillator is visible. For a higher value of F_0 the trembling effect is evident, while for smaller F_0 the motion with approximately constant amplitude occurs.

In Fig. 7 the time history diagrams for an oscillator with $\alpha=\gamma=1$, $\Omega=1.5$, $F_0=0.05$ and various initial conditions ($y_0=0.5$ and $y_0=1$) are plotted. It has been shown that the oscillating properties deeply depend on initial displacement.

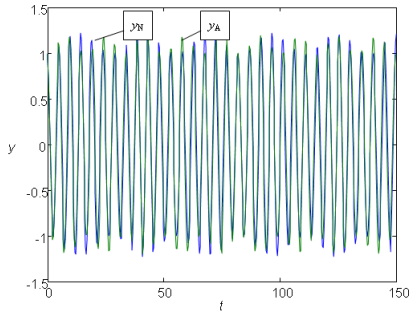

Figure 6
Analytical y_A-t and numerical y_A-t diagrams for Ω=1.3,α=γ=1,F_0=0.25 and y_0=1

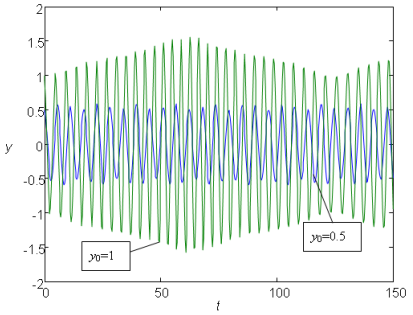

Figure 7
Time history diagrams for Ω=1.4,α=γ=1,F_0=0.05 and: y_0=0.5 and y_0=1

Conclusions

The following has been concluded:

1) The vibration of a non-linear undamped harmonically excited oscillator depends on initial conditions and their influence cannot be neglected independently on the value of the excitation parameters.

2) Upon analyzing the total vibration of the harmonically excited Duffing oscillator, it can be concluded that it contains two terms: first, a harmonic vibration with excitation frequency and second, a harmonic vibration with excited frequency. When varying the excitation frequency from zero to a higher values the vibration terms vary as follows:

a) For zero excitation frequency the first term is a constant value and the second term is a harmonic vibration. The sum of these two terms yields the vibration around the constant value and the maximal amplitude corresponds to initial displacement.

b) By increasing the excitation frequency the first term transforms into a harmonic function with a long vibration period: the period of vibration decreases and the amplitude of vibration decreases from the constant value by increasing the excitation frequency. For the second term, the period of vibration decreases and the amplitude increases when the excitation frequency increases. The total vibration represents the vibration of the second term, around the first one and the total amplitude is equal to the initial displacement.

c) By further increasing the excitation frequency, the relation between the frequencies of vibration of the first and the second term give the trembling effect, where the total vibration period decreases by increasing the excitation frequency and the amplitude remains equal to the value of the initial displacement.

d) For a further increase of excitation frequency, the second term becomes a dominant vibration with a longer period than that of the first term. The period of

trembling increases and the difference between the maximal and minimal amplitude decreases.

e) By further increase of the excitation frequency, up to a certain value, when the amplitude of the first term is equal to initial displacement and of the second term is zero, the total vibration is a pure harmonic, with an amplitude equal to initial displacement and with that certain excitation frequency. For such excitation force, the vibration response is independent on the elastic properties of the oscillator.

f) For an even further increase of excitation frequency, the trembling effect appears, but with a positive sign: the period of the first term decreases and its amplitude is higher than the initial displacement while the frequency of the second term increases and the amplitude is smaller than initial displacement. In spite of that, the total amplitude of vibration is higher than initial displacement. By further increase of excitation frequency the trembling in vibration of the excited oscillator disappears and the vibration tends to a periodical with an amplitude equal to initial displacement and frequency which tends to the frequency of free vibration of the oscillator.

g) For significantly high excitation frequency, the excitation force has only a marginal influence on the vibration of the oscillator. Namely, the amplitude of vibration and the frequency of the excited oscillator do not depend on the parameters of excitation. The vibration is almost harmonic in nature, with an amplitude equal to initial displacement and with frequency of a free vibration. Based on this conclusion, it is recommended to use an excitation force with a high excitation frequency.

3) The initial displacement has an influence on the excitation domain which gives one, two or three steady-state vibrations. The excitation amplitude - excitation frequency curve is single-valued, if the initial displacement is zero and it separates the domains of one and three steady state motions equally. For arbitrary initial displacement, the excitation curve is multi-valued: for excitation parameters inside the region of this curve, three steady-state motions exist, while outside this region the motion only one steady state amplitude exists. The obtained region is larger for higher values of initial displacement. The higher the value of initial displacement the peak values move toward higher values of excitation frequency and excitation amplitude.

4) The number of peak amplitudes, which define the position of jump phenomena, depend on initial displacement. If the initial displacement is zero, only one characteristic peak value in the excited undamped Duffing oscillator exists.

Acknowledgement

This work was partially supported by the Secretariat for Science and Technological Development, Autonomous Province of Vojvodina (Proj. No 114-451-2094/2011) and Ministry of Science of Serbia (Proj. No. ON 174028 and IT 41007).

References

[1] Burton, T. D.: A Perturbaion Method for Certain Non-Linear Oscilltors, International Journal of Non-Linear Mechanics, 19 (1984) 397-407

[2] Cheng, Y. K., Chen, S. H. and Lau, S. L.: A Lindstedt-Poincare Method for Certain Strongly Non-Linear Oscillators, International Journal of Non-Linear Mechanics, 26 (1991) 367-378

[3] Friswell, M. and Penny, J. E. T.: The Accuracy of Jump Frequencies in Series Solutions of the Response of a Duffing Oscillator, Journal of Sound and Vibration, 169 (1994) 261-269

[4] Worden, K.: On Jump Frequencies in the Response of the Duffing Oscillator, Journal of Sound and Vibration, 198 (1996) 522-525

[5] Qaisi, M. I.: Analytical Solution of the Forced Duffing's Oscillator, Journal of Sound and Vibration, 194 (1996) 513-520

[6] He, J-H.: Modified Lindstedt-Poincaré Methods for some Strongly Non-Linear Oscillations Part I: Expansion of a Constant, International Journal of Non-Linear Mechanics, 37 (2002) 309-314

[7] Amore, P. and Aranda, A.: Improved Lindstedt-Poincaré Method for the Solution of Nonlinear Problems, Journal of Sound and Vibration, 283 (2005) 1115-1136

[8] Patil, N. S. and Mallik, A. K.: Experimental Investigation of the Response of a Harmonically Excited Hard Duffing Oscillator, Pramana - Journal of Physics, 68 (2007) 99-104

[9] Kovacic, I. and Brennan, M. J.: On the Use of Two Classical Series Expansion Methods to Determine the Vibration of Harmonically Excited Pure Cubic Oscillators, Physics Letters A, 372 (2008) 4028-4032

[10] Brennan, M. J., Kovacic, I., Carrella, A. and Waters, T. P.: On the Jump-Up and Jump-Down Frequencies of the Duffing Oscillator, Journal of Sound and Vibration, 318 (2008) 1250-1261

[11] Mester, Gy.: Intelligent Mobile Robot Motion Control in Unstructured Environments, Acta Polytechnica Hungarica, 7 (2010) 153-165

[12] — : The Duffing Equation: Nonlinear Oscillators and their Behaviour, Eds: Kovacic, I. and Brennan, M. J. (2011) Wiley

[13] Vahidi, A. R., Babolian, E. and Asadi Cordshooli, Gh.: Numerical Solutions of Duffing's Oscillator Problem, Indian Journal of Physics, 86 (2012) 311-315

[14] Cveticanin, L.: Forced Pure Nonlinear Symmetrical Oscillators, Mathematical and Computer Modelling, 55 (2012) 1580-1593

[15] Cveticanin, L.: The Approximate Solving Methods for the Cubic Duffing Equation Based on the Jacobi Elliptic Functions, International Journal of Nonlinear Sciences and Numerical Simulation, 10 (2009) 1491-1516

Interaction between Periodic System of Rigid Inclusions and Rectilinear Cohesive Cracks in an Isotropic Medium under Transverse Shear

Vagif M. Mirsalimov, Fuad F. Hasanov

Azerbaijan Technical University
Baku, Azerbaijan
E-mail: mir-vagif@mail.ru, hff74@mail.ru

Abstract: We consider a plane problem of fracture mechanics for an isotropic medium with a periodic system of circular holes filled with absolutely rigid inclusions soldered along the contour and weakened by rectilinear cracks with interfacial bonds at the end zones collinear to the abscissa and ordinate axes of unequal length under transverse shear. The problem on equilibrium of isotropic composite medium with cohesive cracks is reduced to the solution of the system of nonlinear singular integro-differential equations with Cauchy type kernel. The tangential forces at the end zones of the cracks are found from the solution of this system of equations. The crack propagation condition is stated with regard to ultimate stretching of the material bonds.

Keywords: isotropic medium; periodic system of circular holes; cohesive forces; rigid inclusions; transverse shear; prefracture zone; cracks with interfacial bonds

1 Introduction

At present, technical means, in the form of perforated elements are used in many fields of engineering. Therefore, development of strength analysis methods of perforated elements of machines and constructions is of great value. Investigation of these problems is important in connection with development of power engineering, chemical industry and other branches of engineering and also with wide use of periodic structure materials.

By investigating the stress distribution in shear of the plane perpendicular to fibers (inclusions) orientation, one can get a good notion on typical stress distributions in the microstructure of reinforced materials. The solution of this problem opens new opportunities for mechanical properties forecasting of composite materials on given initial characteristics, for constituent components and in the form of microstructure. At the design stage of new machines and structures it is necessary to take into account the cases when, in components of the machines and/or

structures, there may appear cracks. A large amount of literature has been devoted to these problems (see review of the papers in [1, 2]). In a great majority of papers, the authors have considered only the Criffith's cracks, i.e. the cracks with not interacting edges. In structurally-inhomogeneous materials, in availability of violated structure zones near the crack, a considerable part of the crack is drawn into the failure process. In this case the fracture zone may be considered as some end-zone adjoining to the crack with a material with partially violated interparticle couplings. Among the investigations of the last years we can note the papers [3-11].

2 Formulation of the Problem

Begin with an isotropic medium weakened by a system of circular holes of radii λ $(\lambda < 1)$ and the centers at the points

$$P_m = m\omega \quad (m = 0, \pm 1, \pm 2, \ldots), \ \omega = 2$$

The circular holes of the medium are filled with absolutely rigid inclusions soldered along the contour. In [12] the investigations were limited to the consideration of Griffith's cracks. In the present study, the isotropic medium is weakened with two periodic systems of rectilinear cohesive cracks collinear to the abscissa and ordinate axes of unequal length (Fig. 1). The crack faces outside of the end zones are free from external loads. The plane under consideration is subjected to transverse shear by the forces τ_{xy}^{∞}. It is required to determine the stress strain state in the isotropic medium according to boundary conditions on non-availability of elastic displacements, along the contour of circular holes and the external loads on the faces of periodic system of cracks outside end zones.

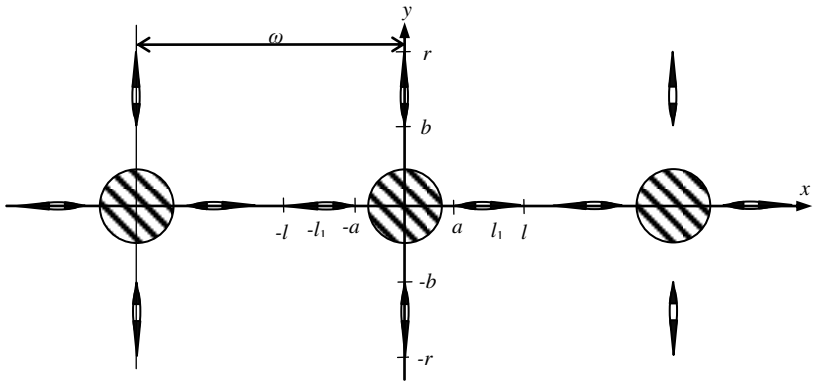

Figure 1
Calculation scheme of the problem on interaction of rigid inclusions and cohesive cracks

As the external load τ_{xy}^{∞} increases, there will arise concluding prefracture zones on the continuation of rectilinear cracks. The model bridged cracks at the end zones are used [13-21]. The crack's end zones are modeled by the areas with weakened interparticle bonds in the medium material. Interaction of faces of these zones are modeled by introducing bonds with the given deformation diagram between the prefracture zone faces. The physical nature of such bonds and the sizes of the prefracture zones depend on the form of the material.

When the external load τ_{xy}^{∞} acts on the composite body, in bonds connecting the faces of end prefracture zones, there arise tangential forces $q_x(x)$ and $q_y(y)$, respectively. These stresses are not known beforehand and should be defined.

Due to the symmetry of boundary conditions and geometry of the domain *D* occupied with the material, the stresses are periodic functions with the main period ω.

The boundary conditions of the problem have the form

$u+iv=0$ on the contours of circular holes (1)

And on the crack faces

$\sigma_y - i\tau_{xy} = 0$ collinear to the abscissa axis (2)

$\sigma_x - i\tau_{xy} = 0$ collinear to the ordinate axis

For the faces of end prefrature zones

$\sigma_y - i\tau_{xy} = -iq_x(x)$ collinear to the abscissa axis (3)

$\sigma_x - i\tau_{xy} = -iq_y(y)$ collinear to the ordinate axis

The basic relations of the stated problem should be complemented with the relationships connecting the shear of prefracture zone faces and forces in the bonds. Without loss of generality, we will represent these equations in the form

$$u^+(x,0) - u^-(x,0) = C(x,q_x(x))q_x(x) \quad (4)$$

$$v^+(0,y) - v^-(0,y) = C(y,q_y(y))q_y(y)$$

where the functions $C(x,q_x(x))$ and $C(y,q_y(y))$ are effective compliances of the bonds, $(u^+ - u^-)$ is the shear of the faces of end prefracture zones collinear to abscissa axes; $(v^+ - v^-)$ is the shear of the faces of end prefracture zones collinear to ordinate axis.

To determine the ultimate quantity of the external load under which the crack propagation occurs, the problem statement should be complemented with crack

propagation condition (criterion). In place of such a condition we take [22] a deformational fracture criterion (critical shear of prefracture zone faces) on the faces of end prefrature zones

$u^+ - u^- = \delta_{\text{IIc}}$ collinear to the abscissa axis (5)

$v^+ - v^- = \delta_{\text{IIc}}$ collinear to the ordinate axis

where δ_{IIc} is the crack resistance characteristics of the medium material.

3 The Method of the Boundary-Value Problem Solution

In order to solve the problem in a natural way we combine the method worked out by solving the periodic elastic problem [2] with the method [23] for constructing in the explicit form the Kolosov-Muskhelishvili potentials, corresponding to unknown tangential displacements along cracks with the end zones. We represent the stresses and displacements [24] by the Kolosov-Muskheleshvili potentials $\Phi(z)$ and $\Psi(z)$

$$\sigma_x + \sigma_y = 4\,\mathrm{Re}\,\Phi(z),\ \Phi(z) = \varphi'(z),\ \Psi(z) = \psi'(z)\ \ (z = x + iy) \tag{6}$$

$$\sigma_y - \sigma_x + 2i\tau_{xy} = 2\left[\bar{z}\Phi'(z) + \Psi(z)\right]$$

$$2\mu(u + iv) = \kappa\varphi(z) - z\overline{\Phi(z)} - \overline{\psi(z)}$$

where $\kappa = 3 - 4\nu$ for plane strain, $\kappa = (3-\nu)/(1+\nu)$ for plane stress state; μ and ν is a shear modulus and the Poisson's ratio, respectively. Based around formulas (6) and boundary conditions on the contours of circular holes and on the surfaces of cracks with end zones, the problem is reduced to definition of two analytic functions $\Phi(z)$ and $\Psi(z)$ in domain D from the boundary conditions (t and t_1 are the affices of the points of the crack surfaces with end zones collinear to abscissa and ordinate axes, respectively)

$$\varepsilon\overline{\Phi(\tau)} + \Phi(\tau) - \left[\bar{\tau}\Phi'(\tau) + \Psi(\tau)\right]e^{2i\theta} = 0 \tag{7}$$

$$\Phi(t) + \overline{\Phi(t)} + t\overline{\Phi'(t)} + \overline{\Psi(t)} = f_x(t) \tag{8}$$

$$\Phi(t_1) + \overline{\Phi(t_1)} + t_1\overline{\Phi'(t_1)} + \overline{\Psi(t_1)} = f_y(t_1)$$

where $\tau = \lambda e^{i\theta} + m\omega\ \ (m = 0, \pm 1, \pm 2, \ldots)$;

$$f_x(t)=\begin{cases}0 & \text{on free faces of cracks collinear to the abscissa } Ox \text{ axis}\\ -iq_x(t) & \text{on the faces of crack' s end zones}\end{cases}$$

$$f_y(t_1)=\begin{cases}0 & \text{on free faces of cracks collinear to the ordinate } Oy \text{ axis}\\ -iq_y(t_1) & \text{on the faces of crack' s end zones}\end{cases}$$

The problem statement simultaneously covers the cases of rigid inclusions ($\varepsilon=-\kappa$) and free holes ($\varepsilon=1$). We look for the solution of boundary value problem (7)-(8) in the form

$$\Phi(z)=\Phi_1(z)+\Phi_2(z)+\Phi_3(z),\ \Psi(z)=\Psi_1(z)+\Psi_2(z)+\Psi_3(z) \tag{9}$$

$$\Phi_1(z)=\frac{1}{2\omega}\int_{L_1} g(t)\cot\frac{\pi}{\omega}(t-z)dt \tag{10}$$

$$\Psi_1(z)=-\frac{\pi z}{2\omega^2}\int_{L_1} g(t)\sin^{-2}\frac{\pi}{\omega}(t-z)dt$$

$$\Phi_2(z)=\frac{i}{2\omega}\int_{L_2} g_1(t_1)\cot\frac{\pi}{\omega}(it_1-z)dt_1$$

$$\Psi_2(z)=-\frac{i}{2\omega}\int_{L_2} g_1(t_1)\left[2\cot\frac{\pi}{\omega}(it_1-z)+\frac{\pi}{\omega}(2t_1+iz)\sin^2\frac{\pi}{\omega}(it_1-z)\right]dt_1$$

$$\Phi_3(z)=i\tau_{xy}^{\infty}+i\sum_{k=0}^{\infty}\alpha_{2k+2}\frac{\lambda^{2k+2}\rho^{(2k)}(z)}{(2k+1)!} \tag{11}$$

$$\Phi_3(z)=i\tau_{xy}^{\infty}+i\sum_{k=0}^{\infty}\beta_{2k+2}\frac{\lambda^{2k+2}\rho^{(2k)}(z)}{(2k+1)!}-i\sum_{k=0}^{\infty}\alpha_{2k+2}\frac{\lambda^{2k+2}S^{(2k+1)}(z)}{(2k+1)!}$$

where $\rho(z)=\left(\frac{\pi}{\omega}\right)^2\sin^{-2}\left(\frac{\pi}{\omega}z\right)-\frac{1}{3}\left(\frac{\pi}{\omega}\right)^2$; $S(z)=\sum_m{}'\left[\frac{P_m}{(z-P_m)^2}-\frac{2z}{P_m}-\frac{1}{P_m}\right]$, the prime of the sum sign indicates that the subscript m=0 is excluded from the summation; the integrals in (10) are taken on the line $L_1=[-l,-a]\cup[a,l]$, $L_2=[-r,-b]\cup[b,r]$; $g(t)$ and $g(t_1)$ are the desired functions characterizing the shear of crack faces with end zones

$$g(x)=-\frac{2\mu i}{1+\kappa}\frac{d}{dx}\left[u^+(x,0)-u^-(x,0)\right]\quad \text{on } L_1 \tag{12}$$

$$g_1(y)=\frac{2\mu}{1+\kappa}\frac{d}{dy}\left[v^+(0,y)-v^-(0,y)\right]\quad \text{on } L_2$$

To relations (9)-(12) we should add additional conditions following from the physical sense of the problem

$$\int_{-l}^{-a} g(t)dt = 0\,, \quad \int_{a}^{l} g(t)dt = 0 \tag{13}$$

$$\int_{-r}^{-b} g_1(t_1)dt_1 = 0\,, \quad \int_{b}^{r} g_1(t_1)dt_1 = 0$$

Refer to the dependences to which the coefficients of equations (9)-(11) should satisfy. From the anti-symmetry conditions for the coordinate axes we find

$$\operatorname{Im}\alpha_k = 0\,, \quad \operatorname{Im}\beta_k = 0 \quad (k=1,2,...)$$

From the condition of constancy of the principal vector of all forces acting on the arch, connecting two congruent points in D it follows that

$$\alpha_0 = \frac{\pi^2}{24}\beta_2\lambda^2$$

It is easy to see that the functions (9)-(11) under condition (13) determine the class of problems with periodic distribution of stresses.

The unknown functions $g(x)$, $g_1(y)$ and the constants α_{2k} and β_{2k} should be defined from boundary conditions (7) and (8). Subject to the periodicity conditions, the system of boundary conditions (7) is replaced by one functional equation, for example on the contour $\tau = \lambda e^{i\theta}$, the system of conditions (8) by the boundary conditions on L_1 and L_2.

To compose the equations with respect to the coefficients α_{2k} and β_{2k} of the functions $\Phi_3(z)$ and $\Psi_3(z)$ we represent boundary conditions (7) in the form

$$\varepsilon\overline{\Phi_3(\tau)} + \Phi_3(\tau) - \left[\bar{\tau}\Phi_3'(\tau) + \Psi_3(\tau)\right]e^{2i\theta} = f_1(\theta) + if_2(\theta) + \varphi_1(\theta) + i\varphi_2(\theta) \tag{14}$$

$$f_1(\theta) + if_2(\theta) = -\varepsilon\overline{\Phi_1(\tau)} - \Phi_1(\tau) + \left[\bar{\tau}\Phi_1'(\tau) + \Psi_1(\tau)\right]e^{2i\theta} \tag{15}$$

$$\varphi_1(\theta) + i\varphi_2(\theta) = -\varepsilon\overline{\Phi_2(\tau)} - \Phi_2(\tau) + \left[\bar{\tau}\Phi_2'(\tau) + \Psi_2(\tau)\right]e^{2i\theta}$$

For the functions $f_1(\theta) + if_2(\theta)$ and $\varphi_1(\theta) + i\varphi_2(\theta)$ we will assume that they expand on $|\tau| = \lambda$ in Fourier series. By anti-symmetry, these series have the form

$$f_1(\theta) + if_2(\theta) = \sum_{k=-\infty}^{\infty} A_{2k}e^{2ik\theta}\,, \quad \operatorname{Re}A_{2k} = 0 \tag{16}$$

$$A_{2k} = \frac{1}{2\pi}\int_0^{2\pi}\left[f_1(\theta) + if_2(\theta)\right]e^{-2ik\theta}d\theta \quad (k = 0,\pm1,\pm2,\ldots)$$

$$\varphi_1(\theta)+i\varphi_2(\theta)=\sum_{k=-\infty}^{\infty}B_{2k}e^{2ik\theta}\,,\quad \operatorname{Re}B_{2k}=0$$

$$B_{2k}=\frac{1}{2\pi}\int_0^{2\pi}\left[\varphi_1(\theta)+i\varphi_2(\theta)\right]e^{-2ik\theta}d\theta\qquad (k=0,\pm1,\pm2,\ldots)$$

Substituting to these series relation (12) and changing the integration order, after calculation of integrals by means of residue we find

$$A_k=-\frac{1}{2\omega}\int_{L_1}g(t)f_{2k}(t)dt$$

$$f_0(t)=(1+\varepsilon)\gamma(t)\,,\quad \gamma(t)=\cot\frac{\pi}{\omega}t$$

$$f_2(t)=-\frac{\lambda^2}{2}\gamma^{(2)}(t)$$

$$f_{2k}(t)=-\frac{(2k-1)}{(2k)!}\lambda^{2k}\gamma^{(2k)}(t)+\frac{1}{(2k-3)!}\lambda^{2k-2}\gamma^{(2k-2)}(t)\qquad (k=2,3,\ldots)$$

$$f_{-2k}(t)=-\frac{\varepsilon}{(2k)!}\lambda^{2k}\gamma^{(2k)}(t)\qquad (k=1,2,\ldots)$$

$$B_{2k}=-\frac{i}{2\omega}\int_{L_2}g_1(t_1)\varphi_{2k}(it_1)dt_1$$

$$\varphi_0(it_1)=\frac{1}{2}(1+\varepsilon)\left[\delta(it_1)-\overline{\delta(it_1)}\right],\quad \delta(it_1)=\cot\frac{\pi}{\omega}(it_1)$$

$$\varphi_2(it_1)=-\frac{\lambda^2}{2}\delta^{(2)}(it_1)+2\left[\delta(it_1)-it_1\delta'(it_1)\right]$$

$$\varphi_{2k}(it_1)=\frac{(1-2k)\lambda^{2k}}{(2k)!}\delta^{(2k)}(it_1)+\frac{2\lambda^{2k-2}}{(2k-2)!}\left[k\delta^{(2k-2)}(it_1)-it_1\delta^{(2k-1)}(it_1)\right]\quad (k=1,2,\ldots)$$

$$\varphi_{-2k}(it_1)=-\frac{\varepsilon\lambda^2}{(2k)!}\delta^{(2k)}(it_1)\quad (k=1,2,\ldots)$$

Substituting to the left side of boundary condition (14) instead of $\Phi_3(\tau)$, $\overline{\Phi_3(\tau)}$, $\Phi_3'(\tau)$ and $\Psi_3(\tau)$ their expansion in Laurent series in the vicinity of $z=0$, and to the right side of (14) the Fourier series (16) and comparing the coefficients at the same degrees of $e^{i\theta}$ we get two infinite system of algebraic equations with respect to the coefficients α_{2k} and β_{2k}

$$i\alpha_{2j+2}=\sum_{k=0}^{\infty} ia_{j,k}\alpha_{2k+2}+b_j \quad (j=0,1,2,\ldots) \tag{17}$$

$$a_{j,k}=\frac{2j+1}{\varepsilon}\gamma_{j,k}\lambda^{2k+2j+2}$$

$$\gamma_{0,0}=\frac{3}{8}g_2\lambda^2+\varepsilon\sum_{k=1}^{\infty}\frac{(2j+1)g_{i+1}^2\lambda^{4i+2}}{2^{4i+4}}$$

$$\gamma_{j,k}=\frac{(2j+2k+2)!\,g_{j+k+1}}{(2j+1)!(2k+1)!2^{2i+2k+2}}+\frac{(2j+2k+4)!\,g_{j+k+2}\lambda^2}{(2j+2)!(2k+2)!2^{2i+2k+4}}+$$

$$+\frac{g_{j+1}g_{k+1}\lambda^2}{2^{2i+2k+4}}\left[1+\frac{(1+\varepsilon)^2K_2\lambda^2}{1-(1+\varepsilon)K_2\lambda^2}\right]+$$

$$+\varepsilon\sum_{i=0}^{\infty}\frac{(2j+2i+1)!(2k+2i+1)!\,g_{j+i+1}g_{k+i+1}\lambda^{4i+2}}{(2j+1)!(2k+1)!(2i+1)!(2i)!2^{2j+2k+4i+4}} \quad (j,k=1,2,\ldots)$$

$$\varepsilon b_0=A_2'-\sum_{k=0}^{\infty}\frac{g_{k+2}\lambda^{2k+4}}{2^{2k+4}}A_{-2k-2}'$$

$$\varepsilon b_j=A_{2j+2}'-\frac{(2j+1)g_{j+1}\lambda^{2j+4}}{(1-(1+\varepsilon)K_2\lambda^2)2^{2j+2}}A_0'-\sum_{k=0}^{\infty}\frac{(2j+2k+3)!\,g_{j+k+2}\lambda^{2j+2k+4}}{(2j)!(2k+3)!2^{2j+2k+4}}A_{-2k-2}'$$

$$g_j=2\sum_{m=1}^{\infty}\frac{1}{m^{2j}} \quad (j=1,2,\ldots), \quad K_2=\frac{\pi^2}{24}$$

$$A_0'=A_0+B_0-2i\tau_{xy}^{\infty}, \quad A_2'=A_2+B_2+i\tau_{xy}^{\infty}$$

$$A_{2k}'=A_{2k}+B_{2k} \quad (k=\pm1,\pm2,\ldots)$$

The coefficients β_{2k} are determined by the relation

$$i\beta_2=\frac{1}{1-(1+\varepsilon)K_2\lambda^2}\left[-A_0'+(1+\varepsilon)\sum_{k=1}^{\infty}\frac{g_{k+1}\lambda^{2k+2}i\alpha_{2k+2}}{2^{2k+2}}\right] \tag{18}$$

$$i\beta_{2j+4}=i(2j+3)\alpha_{2j+2}+\varepsilon\sum_{k=0}^{\infty}\frac{(2j+2k+3)!\,g_{j+k+2}\lambda^{2j+2k+2}}{(2j+2)!(2k+1)!2^{2j+2k+4}}i\alpha_{2k+2}-A_{-2j-2}'$$

Requiring that functions (9)-(11) should satisfy the boundary condition on the faces of the crack with end zone L_1, we get a singular integral equation with respect to $g(x)$

$$\frac{1}{\omega}\int_{L_1}g(t)\cot\frac{\pi}{\omega}(t-z)dt+H(x)=f_x(x) \tag{19}$$

$$H(x) = \Phi_s(x) + \overline{\Phi_s(x)} + x\overline{\Phi_s'(x)} + \overline{\Psi_s(x)}$$

$$\Phi_s(z) = \Phi_2(z) + \Phi_3(z)\,,\ \Psi_s(z) = \Psi_2(z) + \Psi_3(z)$$

Similarly, satisfying the boundary condition on the line L_2 after some transformations we get one more singular integral equation with respect to the desired function $g_1(y)$

$$-\frac{\pi}{\omega^2}\int_{L_1} g_1(t)\left[(t-y)\mathrm{sh}^{-2}\frac{\pi}{\omega}(t-y)\right]dt + N(y) = f_y(y) \tag{20}$$

$$N(y) = \Phi_0(iy) + \overline{\Phi_0(iy)} + iy\overline{\Phi_0'(iy)} + \overline{\Psi_0(iy)}$$

$$\Phi_0(z) = \Phi_1(z) + \Phi_3(z)\,,\ \Psi_0(z) = \Psi_1(z) + \Psi_3(z)$$

Systems (17) and (18) together with singular integral equations (19) and (20) are the main resolving equations of the problem and allow to define the functions $g(x)$, $g_1(y)$ and the coefficients α_{2k}, β_{2k}.

4 Method of Numerical Solution and Analysis

Using the expansion of the functions $\cot\frac{\pi}{\omega}z$, $\mathrm{sh}^{-2}\frac{\pi}{\omega}z$ in the main strip of periods, and also using the substitution of variables, after some transformations we will reduce the singular integral equations to the standard form. Using the quadrature formulas [23, 25], we reduce main resolving equations (17), (18), (19), (20) to the totality of two infinite system of linear algebraic equation and to two finite algebraic systems with respect to approximate values $p_k^0 = g(\eta_k)$ $(k = 1,2,\ldots,M)$, $R_\nu^0 = g_1(\eta_\nu)$ $(\nu = 1,2,\ldots,M)$ of the desired functions at the nodal points

$$\sum_{\nu=1}^{M} A_{m\nu}p_\nu^0 + \frac{1}{2}H_*(\eta_m) = f_x(\eta_m) \quad (m = 1,2,\ldots,M-1) \tag{21}$$

$$\sum_{\nu=1}^{M}\frac{p_\nu^0}{\sqrt{1/2\,(1-\lambda_1^2)(\tau_\nu+1)+\lambda_1^2}} = 0$$

$$\sum_{\nu=1}^{M} B_{m\nu}R_\nu^0 + \frac{1}{2}N_*(\eta_m) = f_y(\eta_m) \quad (m = 1,2,\ldots,M-1) \tag{22}$$

$$\sum_{\nu=1}^{M}\frac{R_\nu^0}{\sqrt{1/2\,(1-\lambda_2^2)(\tau_\nu+1)+\lambda_2^2}} = 0$$

Here $A_{m\nu}=\dfrac{1}{2M}\left[\dfrac{1}{\sin\theta_m}\cot\dfrac{\theta_m+(-1)^{|m-\nu|}\theta_\nu}{2}+B(\eta_m,\tau_\nu)\right]$,

$\theta_m=\dfrac{2m-1}{2M}\pi\quad(m=1,2,\ldots,M)$, $\tau_m=\cos\theta_m$, $\eta_m=\tau_m$, $\lambda_1=a/l$,

$$B(\eta,\tau)=-\frac{1-\lambda_1^2}{2}\sum_{j=0}^{\infty}g_{j+1}\left(\frac{l}{2}\right)^{2j+2}u_0^jA_j$$

$$A_j=(2j+1)+\frac{(2j+1)(2j)(2j-1)}{1\cdot2\cdot3}\left(\frac{u}{u_0}\right)+\ldots+$$

$$+\frac{(2j+1)(2j)(2j-1)..\left[(2j+1)-(2j+1-1)\right]}{1\cdot2\cdot\ldots\cdot(2j+1)}\left(\frac{u}{u_0}\right)^j$$

$$u=\frac{1-\lambda_1^2}{2}(\tau+1)+\lambda_1^2,\quad u_0=\frac{1-\lambda_1^2}{2}(\eta+1)+\lambda_1^2$$

$$B_{m\nu}=\frac{1}{2M}\left[\frac{1}{\sin\theta_m}\cot\frac{\theta_m+(-1)^{|m-\nu|}\theta_\nu}{2}+B_*(\eta_m,\tau_\nu)\right]$$

$$B_*(\eta,\tau)=-\frac{1-\lambda_2^2}{2}\sum_{j=0}^{\infty}(-1)^j(2j+1)g_{j+1}\left(\frac{r}{2}\right)^{2j+2}u_1^jA_j'$$

$$A_j'=(2j+1)+\frac{(2j+1)(2j)(2j-1)}{1\cdot2\cdot3}\left(\frac{u_1}{u_2}\right)+\ldots+\left(\frac{u_1}{u_2}\right)^j$$

$$u_1=\frac{1-\lambda_2^2}{2}(\tau+1)+\lambda_2^2,\quad u_2=\frac{1-\lambda_2^2}{2}(\eta+1)+\lambda_2^2,\quad \lambda_2=\frac{b}{r}$$

The right side of the obtained systems contains the unknown stresses $q_x(\eta_m)$ and $q_y(\eta_m)$ at the nodal points, belonging to prefracture zones. Using the obtained solution, we represent of equation (12) in the form

$$g(x)=-\frac{2\mu i}{1+\kappa}\frac{d}{dx}\left[C(x,q_x(x))q_x(x)\right] \tag{23}$$

$$g_1(y)=\frac{2\mu}{1+\kappa}\frac{d}{dy}\left[C(y,q_y(y))q_y(y)\right]$$

These equations help to determine the traction at the bonds of the end zones of cracks. For constructing missing equations conditions (23) should be fulfilled at the nodal points. We use the finite differences method. And as a result we get two more systems from M_1 and M_2 equations in order to determine approximate values

$q_x(\eta_{m_1})$ $(m_1 = 1,2,\ldots,M_1)$ and $q_y(\eta_{m_2})$ $(m_2 = 1,2,\ldots,M_2)$. Since, in the perforated body the stresses are finite, the solution of singular integral equations should be sought in the class of universally bounded functions. Consequently, to system (21)-(22) we should add the conditions of stress bounded environment at the crack vertices

$$\sum_{k=1}^{M}(-1)^{k+M} p_k^0 \tan\frac{\theta_k}{2} = 0, \quad \sum_{k=1}^{M}(-1)^k p_k^0 \cot\frac{\theta_k}{2} = 0 \tag{24}$$

$$\sum_{\nu=1}^{M}(-1)^{\nu+M} R_\nu^0 \tan\frac{\theta_\nu}{2} = 0, \quad \sum_{\nu=1}^{M}(-1)^{\nu} R_\nu^0 \cot\frac{\theta_\nu}{2} = 0$$

The obtained systems of equations (17), (18), (21)-(24) completely define the solution of the problem. For numerical realization of the stated method the calculations were performed. Each of the infinite system of equations were reduced to five equations. In numerical calculations $M = 30$ that corresponds to portioning of integration interval into 30 Chebyshev nodes. Since the sizes of the end zones are unknown, the resolving algebraic system of equations (17)-(18); (21)-(24) of the problem is nonlinear even for linear-elastic bonds. For its solution the sequential approximations method is used [25]. The essence of this method is solving the algebraic system for some definite values of end zones sizes with respect to the remaining unknowns. The remaining unknowns enter the resolving system linearly. The accepted values of the end zone sizes and the appropriate values of the remaining unknowns will not satisfy, generally speaking, the stress bounded conditions at the crack vertices. Therefore, choosing the values of end zone sizes, we will repeat calculations until the stress bounded conditions of (24) will be satisfied with the given accuracy. In the case of nonlinear law of deformation of bonds, for determination of tangential forces at the end prefracture zones, the iteration algorithm similar to the method of elastic solutions [26] was used. It is assumed that the law of deformation of inter-particle bonds at the end prefracture zone is linear for $(u^+ - u^-) \le u_*$ and $(v^+ - v^-) \le v_*$. The first step of iterative calculation process is to solve the systems of equations for linear-elastic bonds. The next iterations are fulfilled only in the case when the inequality $(u^+ - u^-) > u_*$ or $(v^+ - v^-) > v_*$ holds on the part of the end prefracture zone. For such iterations, the system of equations at each approximation is solved for quasi-linear bonds with effective compliance changing along the end zone forces and dependent on the quantity of forces in bonds that was calculated at the preceding step. Calculation of effective compliance is conducted as in definition of the secant modulus in the method of variables of elasticity parameters [27]. The sequential approximations process finishes when the forces along the end zone, obtained on two sequential iterations do not differ at all. The nonlinear part of the curve of bonds deformation was approximated by the nonlinear dependence whose ascending section corresponded to deformation of bonds $(0 < (u^+ - u^-) \le u_*)$ with their maximal traction of bonds. For $(u^+ - u^-) > u_*$ the

deformation law was described by nonlinear dependence determined by the points (u_*, τ_*) and (δ_c, τ_c), for $\tau_c \geq \tau_*$ an ascending linear dependence hold (linear strengthening corresponding to elastico-plastic deformation of bonds).

In order to determine the limit equilibrium state of the medium under which the crack propagates, we use condition (5). Using the obtained solution, by the conditions defining the ultimate external load we find the followings:

$$C(d, q_y(d))q_y(d) = \delta_{\text{IIc}} \tag{25}$$

$$C(d^*, q_x(d^*))q_x(d^*) = \delta_{\text{IIc}}$$

Here d and d^* are the coordinates of the points at the foundation of the end prefracture zones, respectively. The length of the end zone, tractions in bonds and shear of opposite faces of end prefracture zone from the loading parameter τ_{xy}^{∞} were found as a result of numerical calculation. The dependence of relative length of the end prefracture zone $l_* = (l - l_1)/\lambda$ on dimensionless value of the external load $\tau_{xy}^{\infty}/\tau_*$ for different values of the radius of holes (curves 1-4): 1 – $\lambda = 0{,}2$; 2 – $x = 0{,}3$; 3 – $\lambda = 0{,}4$; 4 – $\lambda = 0{,}5$ are represented in Fig. 2.

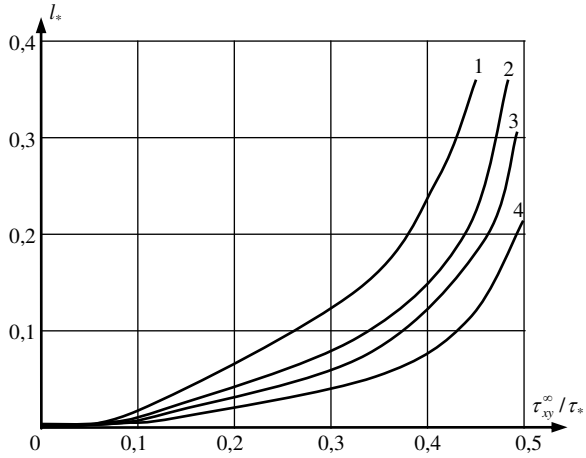

Figure 2

Dependence of relative length of the end prefracture zone $l_* = (l - l_1)/\lambda$ on dimensionless value of the external load $\tau_{xy}^{\infty}/\tau_*$ for different values of the radius of holes (curves 1-4): 1 – $\lambda = 0{,}2$; 2 – $\lambda = 0{,}3$; 3 – $\lambda = 0{,}4$; 4 – $\lambda = 0{,}5$

The dependence of tractions in the bonds q_x/τ_{xy}^{∞} in relative size of l_* for different values of the radius of holes; $\lambda = 0{,}2 \div 0{,}5$ (curves 1-4) are cited in Fig. 3.

The joint solution of the algebraic system and condition (25) enables (for the given characteristic of material crack resistance) to define the critical quantity of

the external load, the sizes of end zones of the cracks for the limit-equilibrium state under which the crack propagates.

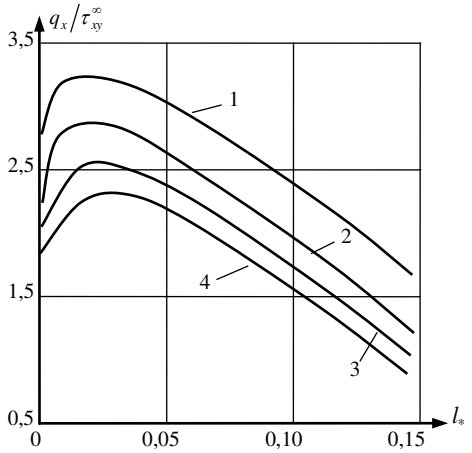

Figure 3

Traction distribution in bonds q_x/τ_{xy}^{∞} from the relative size l_* of the end zone for different values of the radius of the holes $\lambda = 0{,}2 \div 0{,}5$ (curves 1-4)

On the base of the obtained numerical results, the graphs of dependence of critical load $\tau^* = \tau_{xy}^{\infty}/\tau_*$ for the distance $a_* = a - \lambda$ for the both ends of cracks collinear to the abscissa axis (curve 1 corresponds to the left end) for $\lambda = 0.3$ are structured in Fig. 4.

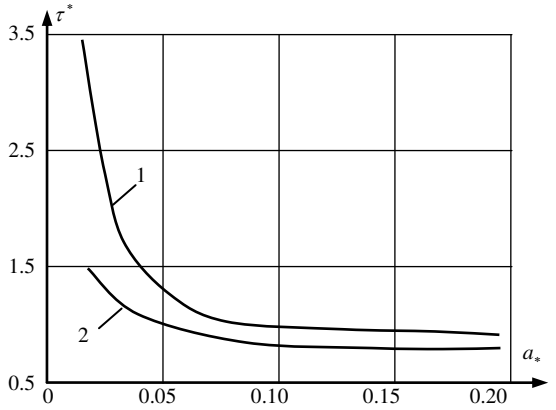

Figure 4

Dependence of critical load $\tau^* = \tau_{xy}^{\infty}/\tau_x$ on the distance $a_* = a - \lambda$ for the both ends of the cracks, collinear to the abscissa axis (curve 1 corresponds to the left end) for $\lambda = 0{,}3$

The dependence of critical load τ^{*a} when the crack length $l_* = l - a$ changes is represented in Fig. 5. For $\lambda = 0.3$, $a_* = 0.05$

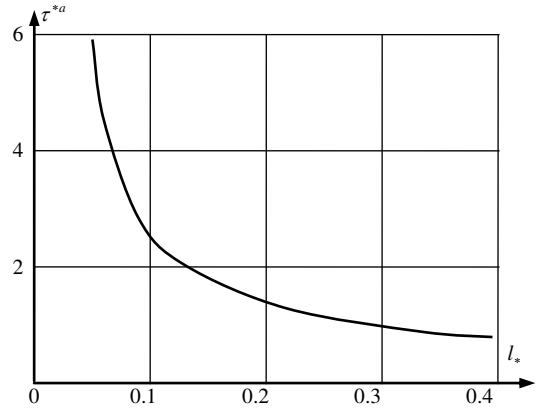

Figure 5

Dependence of critical load τ^{*a} when the crack's length $l_* = l - a$ changes, for $\lambda = 0.3$, $a_* = 0.05$

Conclusions

The analysis of the limit equilibrium state of a body with periodic system of rigid inclusions and rectilinear cracks, with interfacial bonds at the end zones under transverse shear, is reduced to a simultaneous parametric investigation of resolving algebraic system (17), (18), (21), (22)-(24) and deformation criterion of fracture (25) under different laws of deformations of interparticle bonds of the material, elastic constants and geometric characteristics of a perforated body. The traction in bonds and shear of the crack surfaces are determined directly from the solution of the obtained algebraic systems.

The model of the cohesive crack allows us to investigate the main regularities of traction distributions in bonds under different deformation laws; to analyze the limit equilibrium of the crack with end prefracture zone, with regard to deformational condition of fracture; to estimate the critical external load and material's crack resistance. The obtained relations enable to investigate the limit equilibrium state of the medium with a periodic system of circular holes filled with absolutely rigid inclusions soldered along the contour and weakened with bridged rectilinear cracks at the end zones collinear to abscissa and ordinate axes of unequal length under transverse shear.

References

[1] Savruk M. P.: 'Fracture Mechanics and Strength of Materials. Vol. 2: Stress Intensity Factors in Cracked Bodies'. Kiev, Naukova Dumka (1988) (in Russian)

[2] Mirsalimov V. M.: 'Fracture of Elasto - and Elastoplastic Bodies with Cracks'. Baku, Science, 1984 (in Russian)

[3] Elices M., Guinea G. V., Gómez J., Planas J.: 'The Cohesive Zone Model: Advantages, Limitations and Challenges', Engineering Fracture Mechanics, Vol. 69, Issue 2, pp. 137-163, 2002

[4] Yang Q., Cox B.: 'Cohesive Models for Damage Evolution in Laminated Composites International' Journal of Fracture, Vol. 133, Issue 2, pp 107-137, 2005

[5] Dong C. Y.: 'The Integral Equation Formulations of an Infinite Elastic Medium Containing Inclusions, Cracks and Rigid Lines', Engineering Fracture Mechanics, Vol. 75, Issue 13, pp. 3952-3965, 2008

[6] Ghannad M., Zamani Nejad M.: 'Elastic Analysis of Heterogeneous Thick Cylinders Subjected to Internal or External Pressure Using Shear Deformation Theory', Acta Polytechnica Hungarica, Vol. 9, No. 6, pp. 117-136, 2012

[7] Pasternak Ia. M., Vasil'ev K. V., Sulym H. T.: 'Antiplane Deformation by Concentrated Factors of Bounded Bodies with Cracks and Rigid Inclusions', Journal of Mathematical Sciences, Vol. 190, Issue 5, pp. 710-724, 2013

[8] Xiao J. H., Xu Y. L., Zhang F. C.: 'Interaction between Periodic Cracks and Periodic Rigid-Line Inclusions in Piezoelectric Materials', Acta Mechanica, Vol. 224, pp. 777-787, 2013

[9] Hasanov F. F.: 'Fracture of a Body Weakened with Periodic System of Circular Orifices at Transverse Shear', Materials. Technologies, Tools, Vol. 18, No. 1. pp. 17-23. 2013

[10] Caimmi F., Pavan A.: 'A Numerical Study of Crack–Fibre Interaction at Varying Fibre Orientation', Engineering Fracture Mechanics, Vol. 101, pp. 129-139, 2013

[11] Kun Zhou, Hsin Jen Hoh, Xu Wang, Leon M. Keer, John H. L. Pang, Bin Song, Q. Jane Wang: 'A Review of Recent Works on Inclusions', Mechanics of Materials, Vol. 60, pp. 144-158, 2013

[12] Mirsalimov V. M.: 'Interaction between a Periodic System of Elastic Inclusions and Rectilinear Cracks in an Isotropic Medium', Journal of Applied Mechanics and Technical Physics January–February, Vol. 19, Issue 1, pp. 136-145, 1978

[13] The special issue: Cohesive Models, Eng. Fract. Mech., Vol. 70, No. 14, pp. 1741-1987, 2003

[14] Mirsalimov V. M: 'Cracks with Bonding between the Lips in Bushings of Friction Couples', Materials Science, Vol. 42, Issue 2, pp 200-209, 2006

[15] Mir-Salim-zade M. V.: 'Crack Initiation in a Stiffened Plate', Journal of Applied Mechanics and Technical Physics, Vol. 48, Issue 4, pp. 562-570, 2007

[16] Mirsalimov V. M.: 'The Solution of a Problem in Contact Fracture Mechanics on the Nucleation and Development of a Bridged Crack in the Hub of a Friction Pair', Journal of Applied Mathematics and Mechanics, Vol. 71, Issue 1, pp. 120-136, 2007

[17] Mirsalimov V. M.: 'Nucleation of Cracks in a Perforated Fuel Cell', Journal of Applied Mechanics and Technical Physics, Vol. 48, Issue 5, pp. 723-733, 2007

[18] Mirsalimov V. M., B. E. Rustamov: 'Interaction of Prefracture Zones and Crack-Visible Cavity in a Burning Solid with Mixed Boundary Conditions', Acta Mechanica, Vol. 223, Issue 3, pp. 627-643, 2012

[19] Zolgharnein E., Mirsalimov V. M.: 'Nucleation of a Crack under Inner Compression of Cylindrical Bodies', Acta Polytechnica Hungarica, Vol. 9, No. 2, pp. 169-183, 2012

[20] Mirsalimov V. M., Zolgharnein E.: 'Cracks with Interfacial Bonds in the Hub of a Friction Pair', Meccanica, Vol. 47, No. 7, pp. 1591-1600, 2012

[21] Mirsalimov V. M., Rustamov B. E.: 'Effect of Damages on Crack-Visible of the Cavity Opening Displacement in Burning Solid Fuel', Inter. J. of Damage Mechanics, Vol. 21, No. 3, pp. 373-390, 2012

[22] Panasyuk V. V.: 'Deformation Criteria in Fracture Mechanics', Materials Science, Vol. 22, No. 1, pp. 7-17, 1986

[23] Panasyuk V. V., Savruk M. P., Datsyshyn A. P.: 'A General Method of Solution of Two-Dimensional Problems in the Theory of Cracks', Eng. Fract. Mech., No. 2, pp. 481-497, 1977

[24] Muskhelishvili N. I.: 'Some Basic Problems of Mathematical Theory Elasticity' Amsterdam, Kluwer, 1977

[25] Mirsalimov V. M.: 'Non-One-Dimensional Elastoplastic Problems' Nauka, Moscow, 1987 (in Russian)

[26] Il'yushin A. A.: 'Plasticity' Moscow and Leningrad, Gostexhizd, 1948 (in Russian)

[27] Birger I. A.: 'The Design of Structures Allowings for Plasticity and Creep', Izv. Akad. Nauk SSSR, Mekhanika, No. 2, pp. 113-119, 1965

An Artificial Neural Network Model for Road Accident Prediction: A Case Study of a Developing Country

Francisca Nonyelum Ogwueleka

Department of Computer Science, Federal University-Wukari
200 Katsina-AlaRoad, P.M.B.1020 Wukari, Taraba State, Nigeria
ogwuelekafn@fuwukari.edu.ng

Sanjay Misra

Department of Computer Engineering, Atilim University
Kizilcasar Mh., 06830 Ankara, Turkey; smisra@atilim.edu.tr

Toochukwu Chibueze Ogwueleka

Department of Civil Engineering, University of Abuja
Village Gwagwalada, Near Airport, Abuja, Nigeria
ogwueleka@futminna.edu.ng

L. Fernandez-Sanz

University of Alcala
Plaza de San Diego, s/n, 28801 Alcala de Henares, Madrid, Spain
luis.fernandezs@uah.es

Abstract: Road traffic accidents (RTA) are one of the major root causes of the unnatural loses of human beings all over the world. Although the rates of RTAs are decreasing in most developed countries, this is not the case in developing countries. The increase in the number of vehicles and inefficient drivers on the road, as well as to the poor conditions and maintenance of the roads, are responsible for this crisis in developing countries. In this paper, we produce a design of an Artificial Neural Network (ANN) model for the analysis and prediction of accident rates in a developing country. We apply the most recent (1998 to 2010) data to our model. In the design, the number of vehicles, accidents, and population were selected and used as model parameters. The sigmoid and linear functions were used as activation functions with the feed forward-back propagation algorithm. The

performance evaluation of the model signified that the ANN model is better than other statistical methods in use.

Keywords: Artificial neural network; road; accident; linear function; back propagation; vehicles

1 Introduction

Artificial Neural Network (ANN) systems have been applied in different information technology problems, such as traffic in communication and transportation engineering [1]. ANN has been widely applied in travel behavior, flow and management [2]. Artificial neural networks are employed for modeling the relationship that exist among driver injury severity and crash causes or factors that have to do with the driver, vehicle, roadway and the environment characteristics. The use of artificial neural networks can reveal the relationship that exists between vehicle, roadway and environment characteristics and driver injury severity [3]. Traffic forecasting problems involving complex interrelationships between variables of traffic system can be efficiently solved using ANN. They provide realistic and fast ways for developing models with enough data [4]. This study explains the use of neural networks in the modeling of the number of persons fatally injured in motor vehicle accidents in data sets of the states of the USA. The ANN models help us to compare the states' road safety performance by the number of motor vehicle fatalities.

Used in many fields, the application of ANNs has seen a lot of success in a number of different areas of specialization, including transportation engineering. Abdelwahab and Adel-Aty [3] researched the relationship that exists between driver injury severity and driver, vehicle, road, and environment characteristics, using two well-known neural network paradigms, the multilayer perceptron and the fuzzy adaptive resonance theory neural networks. Recently, ANN has been adopted for sequential forecasting of incident duration from the point of view of incident notification to the incident road clearance [5]. Prediction of the lane-change occurrence with respect to freeway crashes using the traffic surveillance data collected from a pair of dual loop detectors [6], and a study understanding the circumstances under which drivers and passengers are more likely to be killed or more severely injured in an automobile accident, can help to improve the overall driving safety situation [7].

The advantage of ANN over conventional programming depends on its ability to solve complex and non-algorithmic problems. ANN uses past experience to learn how to deal with the new and unexpected situations. The statistical distribution of the data does not need to be known when developing an ANN model. There is no need for prior knowledge about the relationships amongst the variables being

modeled. Hence, ANN has the ability to model complex, nonlinear relationships without previous assumptions of the nature of the relationship, like a black box [8]. The most important key element of ANN paradigm is the novel structure of the information processing system. The synapses associated with irrelevant variables readily show negligible weight values; relevant variables present significant synapse weight values. Neural networks, which are good at broad and flat transformation of data, are nonlinear, able to relate input with output, and are error tolerant. Another advantage of ANN analysis is that it allows the inclusion of a large number of variables.

Road traffic accidents (RTAs) play an important role in the economy of any country and especially such huge financial losses in developing countries affect very much the development of these nations. Due to RTAs, the financial loss in some developing countries like Nigeria is more than the GDP of 20 African countries (see Figure 2). In the next section, we will see how RTAs affect the economy of a developing country.

In this paper, the development an Artificial Neural Network (ANN) model was carried out for the examination and prediction of accidents rate using Nigeria as a case study. Our model was developed by considering data from 1998 to 2010 for prediction accuracy. In the design of the system, the number of vehicles, accidents, and population are selected and used as model parameters. We used the sigmoid and linear functions as activation functions with the feed forward-back propagation algorithm. By analyzing the performance evaluation of the model, we found that the ANN model is better than other statistical methods.

The paper is organized in the following chapters. We provide the detail of our case study, which in our case is Nigeria, in the next section. The related work is also discussed in the same section. In the next paragraph we have data of our case study.

2 Facts regarding RTAs in Nigeria: A Case Study under Consideration

Poor road structure and population growth have greatly led to an increase in accident rates. The establishment of the Federal Road Safety Corps (FRSC) by the government of the Federal Republic of Nigeria in 1988 (vides Decree 45 of 1988 as amended by Decree 35 of 1992, with effect from 18th February, 1988) was to reduce the accidents. The Commission was given the following responsibilities; policymaking, organization and administration of road safety in Nigeria. Mr. Osita Chidoka, the FRSC Corps Marshal and Chief Executive, estimated that Nigeria currently loses three billion naira every year to road crashes. Road crashes cost Nigeria 13% of her gross national product (GNP), which inhibits economic and

social development [9]. Nigeria loses about 3% of GDP from Road Traffic Crashes that is about 17% of current National reserves as shown in Figure 1.

Income lost from 2009 RTCs in Nigeria was more than the GDP of over 20 individual African countries. Nigerian income losses for 2009 vs. 2009 GDP select African Countries are shown in Figure 2.

The cause of traffic accidents can be a factor or combination of many factors. The basic factors which cause or increase the severity of probable accidents are driver's behavior, vehicle features, highway characteristics, environmental effects and traffic characteristics (Ozgan, 2003).

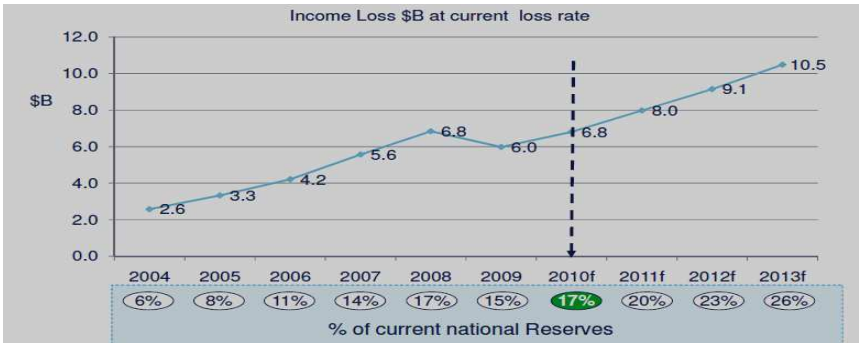

Source: Euromonitor, CBN, World Bank, PwC Analysis

Figure 1
Nigeria's current national reserves

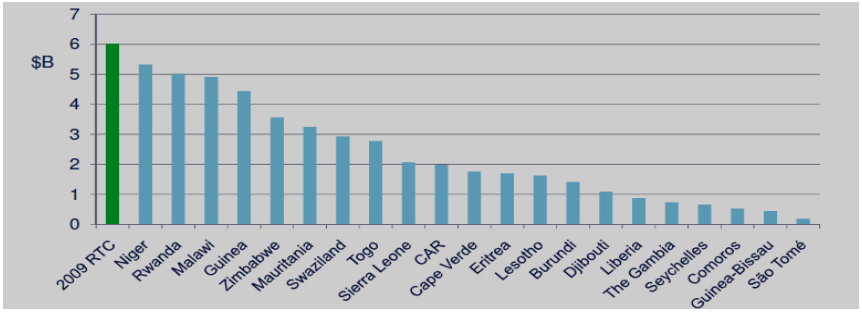

Source: IFC, PwC Analysis

Figure 2
Nigeria's 2009 vs. 2009 GDP of selected African countries

Traffic volumes in number of vehicles per day and road lengths in kilometers are the most important explanatory variables in an accident prediction model, both for road sections and intersections. The parameters of the model can vary significantly between road types and countries because road characteristics, user

behavior and vehicle types can differ. An accident prediction model is a mathematical formula describing the relation between the level of existing road safety, such as crashes, injuries, fatalities etc., and variables that explain this level, such as road length, width, and traffic volume.

In Nigeria, about 85% of the accounted causes of road accidents are believed to have been constituted by human factors [10]. Many researches carried out in Nigeria revealed that most accidents caused by human factors are the result of driving while drunk, drugs, inexperience or poor driving skills, health problems, psychological problems and temperament. These have been shown in different ways by drivers. It is also noted that these human factors are the greatest contribution to the increasing surge of traffic accidents in Nigeria [10]. The attitude towards road traffic accidents includes such behavioral elements of the drivers as: sleeping while driving and tiredness, inadequate preparation for a journey, not been familiar with the highway signs, cutting corners, driving after taking excess alcohol, driving with bad eye sight especially in the night, ignorance of the use seat belts, the incapability of handling unforeseen circumstances, wrong use of road signs and vehicle signaling, overtaking and incompetent maneuvering.

Osime et al. [11] observed in their study that about 285,699 cases of RTA occurred between 1970 and 1979 with 57,136 deaths, which amounts to 20%. Again, 188,012 cases of RTA occurred between 1990 and 1999, where about 76,870 deaths were recorded, amounting to 41%. Reasons for this include the oil explosion in Nigeria, which occurred in the 1970s. This empowered many Nigerians financially to afford cars of their choices. This also aided in the repair of roads and the construction of new roads in Nigeria. But given that people were not yet exposed to high traffic of cars in Nigeria roads, this led to many cases of RTAs. Also, due to the fact that people are new to the development, cases of speeding could still be assumed to be relatively small. With the availability of good roads and due to the fact that some drivers drive with reasonable speed, which amount to some cases of RTAs, the deaths that occurred were about 20%. However, there was a sharp change observed between 1990 and 1999. The mortality rate increased to 41%, while the number of RTAs decreased. This is the time economic recession was observed in Nigeria, which led to the inability of acquiring new cars by most people; instead there was an increase in the purchase of used cars, which in turn led to an increase in RTAs. The economic recession also affected most roads, which left them in a bad state, making it more likely to cause fatal accidents. The country equally experienced neglect in the health sector, with little attention paid to RTAs cases.

Research on the trends of accidents on Nigeria roads starting from 1960 to 1989 shows an increase in the number of fatal accidents that occurred. It was also discovered that about 18,000 deaths were recorded between 1960 and 1969 with respect to road accidents. This figure given here increased by five times between 1980 and 1989, with more than 92,000 deaths recorded [12]. The total amount of RTAs in Nigeria between 1960 and 2004 is 969,850 with 275,178 recorded deaths

and 843,691 recorded injuries within the same period. In 1988, the rate of RTAs reduced drastically, which is attributed to the effectiveness of the Federal Road Safety Commission in Nigeria, which assumed operation on 18th February 1988. The key responsibility of the Federal Road Safety Commission is to bring to sustainable minimum the rate of RTAs in Nigeria. The major strategies to achieve this as adopted by the commission to improve road safety in Nigeria are through awareness and enforcement.

The number of injured and killed people is currently increasing rapidly in Nigeria. If until 2020 the trends in RTAs continue, it will be considered as the second most noted cause of fatalities in the world. RTAs contribute greatly in huge economic overheads, extreme human distress and disaster. A long term sustainable road traffic system can be achieved if the traffic safety work is developed and intensified. Figure 3 shows Nigeria's position in RTAs.

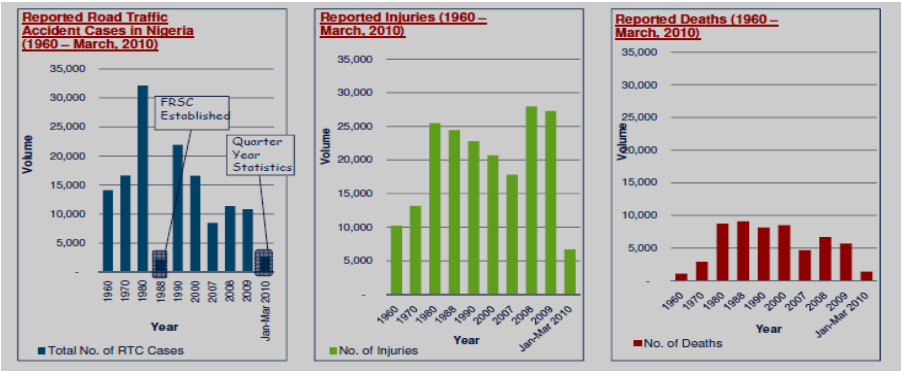

Source: FRSC, PwC Analysis

Figure 3
Nigeria's position in reported RTA causes, injuries and death

Records obtained from Federal Road Safety Corps (FRSC) in 2009 states that about 4,120 deaths were recorded, with 20,975 seriously injured persons in RTAs involving about 11,031 vehicles across Nigeria. In 2008, the commission stated that about 11,341 RTAs occurred, claiming a total number of 6,661 lives and with 27,980 injured persons. From January to June 2010, RTAs amounted to 5,560 cases, with 3,183 deaths and 14,349 injuries.

3 Related Studies

The issue of Road traffic accident (RTA) has been seen to be dreadful all over the world. The rate of RTAs has reduced in some developed countries, while it still on the increase in some developing countries [13]. It has been observed that RTA is

prevalent in Nigeria, with seasonal epidemics [14]. It has been reported by the police force that a total of 98,168 deaths occurred between 1980 and 1989, and 244,864 persons were injured in RTAs [15]. This brings an average of 10,000 persons being killed and 25,000 persons being injured annually. A document has stated that one third and one ninth of the whole of Nigerians may be exposed to the risk being injured or killed, respectively, annually by RTAs [16]. Despite the struggle to reduce the rate of RTAs in Nigeria, it is still ranked high with respect to RTA in the world [17]. The most disturbing aspect is the economic back-bone of a nation, are the young adult group, who are the most affected by these RTAs [18], [19]. Oladehinde et al. [20] discussed the visual functions of commercial drivers in relation to road accidents in Nigeria and basically observed that it is one of the causes of road traffic accidents.

Most traffic accident prediction models are based on statistical regression techniques. In 1949, Smeed [21] studied the calculated number of fatally injured persons in the accidents and compared the accident rates in different countries. Thus, the first study concerning deaths in traffic accidents were executed by Smeed and the study became the initiator of many practical models [21]. He proposed to consider the trend of the accident rates in the USA and the economic cost of road accidents, and he analyzed the level of success of various accident prevention methods used.

Many practical models have been established on the basis of Smeed's work [21]. Leeming [22] proposed the Smeed's factors for different countries and different years. Pitsiava-Latinapoulou and Tsohos [23] analyzed a 14-year record concerning the relationship between fatal road accidents and the number of registered vehicles in Greece using statistical method and described a relationship that is at a fairly good degree of accuracy by Smeed's equation (SE). Adams [24] examined accident black spot treatment and seat belt legislation on behalf of vehicle safety regulations, benefitting from explanations of Smeed's Law. Broughton [25] validated the empirical relationship between SE (Sameed's equation) and other developed models on the basis of SE to provide common methods for predicting fatality and accident totals. Gharaybeh [26] researched the development of traffic safety in Jordan over the last two decades, using Smeed's Formula. Navin et al. [27] developed a road safety model that includes special cases of the Smeed's model.

Many communications traffic and transportation engineering problems have been solved using ANN methodology [28]. ANNs have been applied in travel behavior management and the flow of traffic [2]. Artificial neural networks were employed for modeling the factors that have to do with driver injury severity and causes of crash with respect to vehicles, drivers, roadway and environment features. The use of artificial neural networks can reveal the factors that relate to vehicle, roadway and environment features and driver injury severity [29]. Traffic forecasting problems involving complex interrelationships between variables of traffic system can be efficiently solved using ANN. They offer realistic and continual ways of

building models, thereby providing enough data [4]. This study explains the use of ANN in the designing of the number of persons fatally injured in motor vehicle accidents in data sets of the states of the US. The ANN models have assisted us to compare the safety of the states' roads by the number of motor vehicle fatalities.

The use of ANNs has been effective in a variety of areas which includes transportation engineering. Abdelwahab and Adel-Aty [29] researched the factors concerning driver injury strictness and driver, vehicle, road, and environment features by applying two popular ANN algorithms known as the multilayer perceptron algorithm and the fuzzy adaptive resonance theory ANN. Chronological forecasting of event duration from a point of view of event notification to the event road clearance has been carried out by ANN recently [5]. The occurrence of lane-change related freeway crashes has been predicted using the traffic inspection data composed from a pair of dual loop detectors [6], and the establishment of a study which will provide clear knowledge of how drivers and passengers can easily be killed or most likely be deeply injured RTAs will go a long way to way to advance the driving safety condition [7].

The advantage of ANN against normal programming languages is that it can be used to solve non algorithmic problems or provide solutions to complex problems. ANN can learn how to deal with the new and unexpected situations with the help of past experience. There is no need to establish the how the data are distributed when building an ANN models. Also there is no need to establish before-hand how the variables being used in the model relate to one another. It has the capability to model compound, non-linear factors without establishing before-hand the nature of the factors, like a black box [8]. The major component of an ANN algorithm is the original configuration of the information processing system. The synapses related to irrelevant variables shows very little function values; on the other hand, important variables give important synapse function values. Neural networks which are good at broad and flat transformation of data are nonlinear, able to relate input with output and are error tolerant. Another advantage of ANN analysis is that it allows the inclusion of a large number of variables.

4 Proposed Methodology

The road traffic accidents (RTA) data obtained from the FRSC and Nigerian Police was from 1998 to 2010 (Table 1). In 2003, there were 16,795 accounted cases of road traffic accidents; 28,215 person were injured with 8672 recorded deaths. The ratio of deaths to RTA was 1.93:1 in 2003.

Multi-layer perceptron ANN adopts different learning algorithms; and one the most well-known techniques is back propagation and it was used in this study.

Table 1
Data of road traffic accident cases, the injured persons with deaths

Year	Total cases reported	No. of persons killed	No. of persons injured
1998	17,117	6578	17,547
1999	12,503	5953	18,000
2000	12,325	6336	20,555
2001	15,621	7845	26,745
2002	16,452	8452	27,102
2003	16,795	8672	28,215
2004	14,279	5351	16, 897
2005	8962	4519	15,779
2006	9114	4944	17,390
2007	9132	4916	20,944
2008	11,341	6661	27,980
2009	11,031	4120	20,975
Jan-June 2010	5,560	3183	14, 349

The road accident was categorized using a self-organizing map (SOM) based clustering. The number of RTAs, vehicles, and populace were taken and used as model factors. Road types and country are also used as parameters. The input variables are the number of vehicles per day and the road length in kilometers. The designed Multi-Layer Perceptron Neural Network (MLPNN) consists of the input layers, hidden layers and an output layer, as shown in Figure 4.

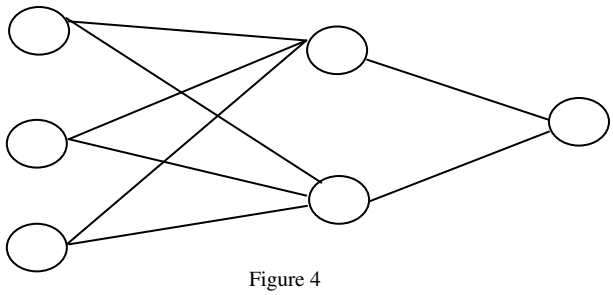

Figure 4
Neural Network

After clustering the entire datasets, (ANN) is used to get a model that is the best for predicting road traffic accident, as ANN always learns from past experience after it completes its first training, and so it becomes an appropriate methodology for prediction. The ANN technique shows some tolerance to a good extent over errors that may exist within the training set. It has the ability to show the veiled and dependencies that are not linear and still learn from its past experience after completing its first training, and this makes it appropriate method that is suitable

for prediction. The Multi-Layer Perceptron Neural Network (MLPNN), which is also called the multilayer feed-forward neural network, was chosen and used in this study. Figure 5 is a graphical representation of the overall architecture of the proposed system.

The data that is present in the databases are obtained from Federal Road Safety Commission, Abuja-Nigeria. The data are preprocessed by removing the duplicates and providing the values that are missing. The data were first formatted to an acceptable form for clustering; this is because data that have similar factors are clustered together, while data that have less peculiar factors are clustered differently through a methodology called unsupervised grouping of similar datasets into a predefined groups. To prepare the data that is best for mapping out the process, there is need to change data consequently. The formatted data are further preprocessed in order to put the data in the form best for clustering. Clustering was performed with a k-means algorithm. SOM was used as the basis for clustering of data items. The method proposed uses k-means measurement, which is used to measure distance or differences that exist between the sampled data, because it is the major factor for cluster scrutiny. After clustering all the datasets, with self-organizing map techniques, ANNs are used to obtained best pair of road accidents for the specified type of accident characteristics. The prediction was done using Multilayer Perceptron Neural Networks (MLPNN).

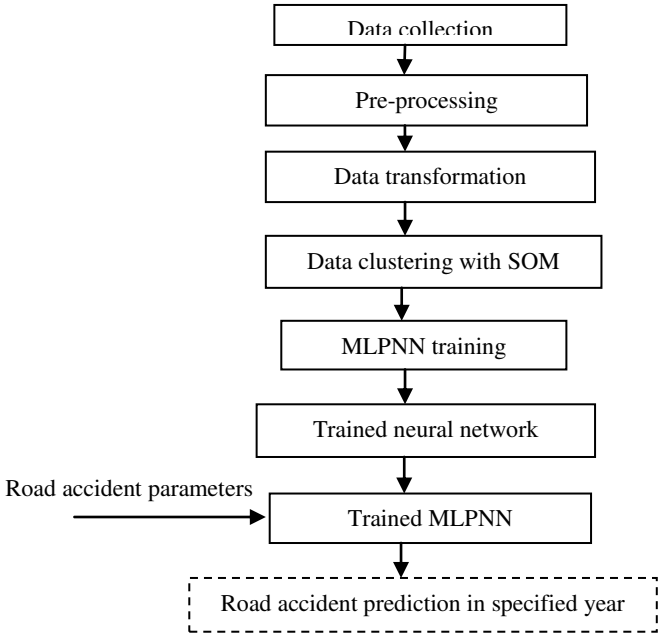

Figure 5
The training architecture

One of the simple algorithms used in this research is:

```
Initialize map
For r from 0 to I                    (where r is the weight vector)
        Randomly select a sample
        Get best matching unit
        Scale neighbours
Increase r with small amount
        End for
```

Initialization of weight vectors is step one in building up of the SOM, after which a vector among the samples is selected randomly and SOM searched for weight vectors that best represent the sample. Each weight vector has a location, with neighboring weights very close to it. The chosen weight is compensated as it is more likely to be the randomly chosen sample vector. Also, the neighbors of that weight are also rewarded, as it is likely to be the selected sample vector. Here, r is increased a little with respect to amount of neighbors, and to what extent will each weight can learn to decrease with time. The steps are repeated a good number of times.

The major aim for carrying out training in a multilayer feed-forward network is to obtain what will make ANN output weight values to match the actual target values very closely. To design and train multilayer perceptron network involves several challenges, which include determining the number of hidden layers to be used in the network, determining the number of neurons to be used in each hidden layer, establishing a general acceptable solution that avoids local minima, converging to an optimal solution as and when due or in good time, and validating the neural network to test for over fitting.

Though there exist errors and noise in the training set, ANN still possesses the capability to find the dependencies that are hidden and are not linear, and it also learns from past experience as it completes its training. ANN is still the best prediction tool.

One of the best training ANN algorithm for prediction is Back propagation (BP). During prediction using BP, errors found in the network are propagated backward to the appropriate nodes. BP carries out is process by adjusting the weight values along with the bias values in order to increase the square sum of the difference that exist among the given output and output values that is generated by the network.

The back propagation technique was used efficiently by these steps [30]:

1) A sample for training was presented to the ANN.
2) The output of the ANN was compared with required output and the calculation of error in each output neuron is done.

3) The calculation of the local error, which is estimated from each neuron by establishing what the output should have been with a scaling factor and to what extent either low or high the output, must be adjusted in order to match the needed output.

4) Lowering the local error by adjusting of the weights of each neuron.

5) Fault is assigned to neurons for the local error found at the previous level; this assigns a higher task to neurons that are strongly connected by weights.

6) Iterate algorithm starting from step 3 using neurons found at the previous level; use each neuron fault as its error.

In this study, the adjustment of the weight value was carried out using conjugated gradient algorithm with help of gradient during backward propagation of errors in the network. The conjugate gradients algorithm uses more paths that are direct to best group of weight values when compared with the gradient descent. It is also faster and more robust. It does not require explicit specification of learning rate and momentum factors.

The steps [30] in the proposed approach are given as follows;

1) Calculate the amount of data in the dataset

2) Generate a group of clusters and establish the centroid of the clusters.

3) Establish the Euclidean distance for each data using the centroids the existing groups of clusters.

4) Allocate data to the group of clusters using minimum distance

5) Iterate steps three and step four until all changes in the clusters disappears.

6) This step deals with the generation of the standard deviation for the group of clusters that are formed. Put aside all the clusters with generated standard deviation that are less than 0.

7) The above steps are repeated until the generated standard deviation for the whole clusters attains a value that is less than 0.

The following pseudo-code shows the algorithm for clustering:

Set N_C, N_o (where $N_C = 1$ and $N_o = 1$)
Calculate N_C (where $N_C = N_C - N_o + 1$
Form C_{if} clusters of N_C size
compute centroid
Iterate
For every value starting from one to N and N_C
Compute the Euclidean distance
Find the list distance

Apply data to a group of cluster until all no change is found in the clusters
For every cluster value which is equal from one to N_C
Compute the standard deviation
If standard deviation is less than Φ
Remove C_r from C_{if} where $C_r \in C_{if}$ and add to C_a
Find the rest of the clusters until its values reaches zero

Where

N = Amount of data in the dataset, N_C = Amount or a group of clusters

N_o = Amount or a group of clusters that has zero standard deviation

C_a = Original clusters, C_{if} = Intermediately formed clusters

C_r = Cluster that will be removed.

Figure 6 is the flow chart diagram depicting the process of clustering T. The first value for $N_C = 1$ and $N_o = 0$. The minimum distance among the clusters is obtained by after computing the centroid and Euclidean distance of the data items.

5 Results

The designed MLPNN contains three input layers with two hidden layers and one output layer. The output layer carries out the prediction of the RTA rate when presented with the factors.

Comparing 2004 and 2005 RTA summary from Table 2, there is an observed 37% reduction in total RTA cases; the amount of persons killed was reduced by 16%; and the amount of persons injured was reduced by 7%.

Table 2
Summary of 2004 and 2005 RTA

Year	**2004**	**2005**	**Remarks**
Total reported RTA cases	14279	8962	37% reduction in RTA
Persons killed	5351	4519	16% reduction in the number of persons killed
Persons injured	16897	15779	7% reduction in the number of persons injured

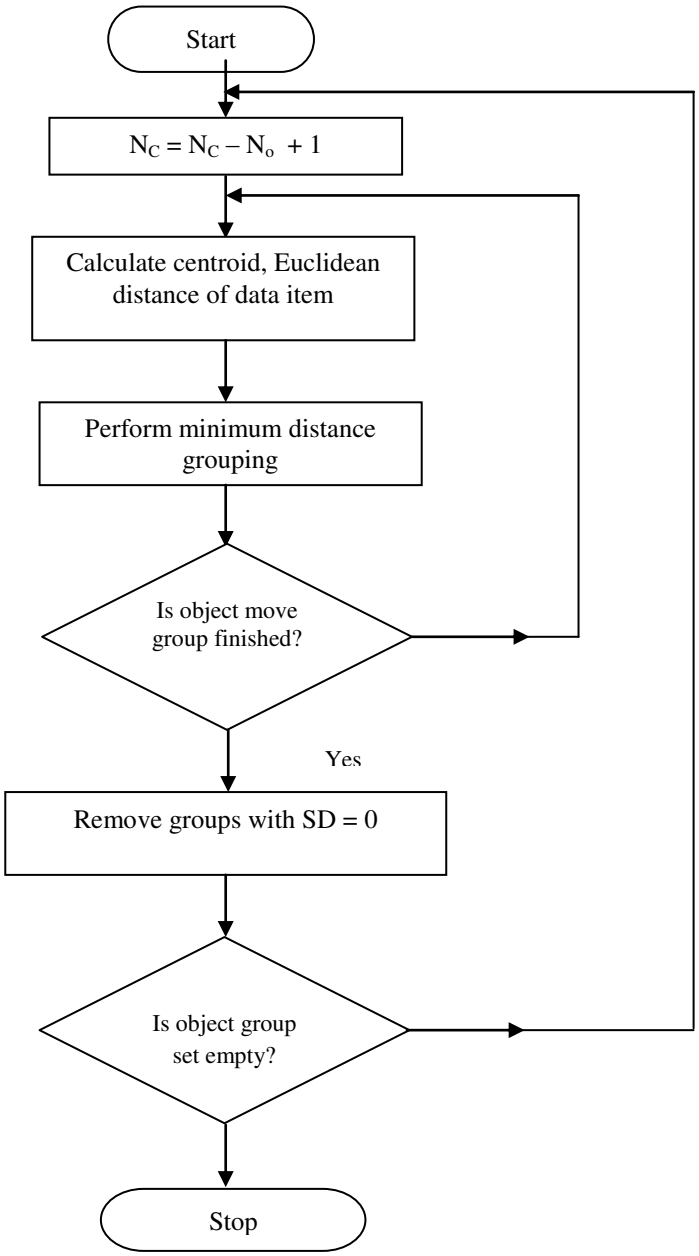

Figure 6
Clustering process flowchart

The road traffic accident summary of 2004 and 2005 are shown in Figures 7 and 8, respectively.

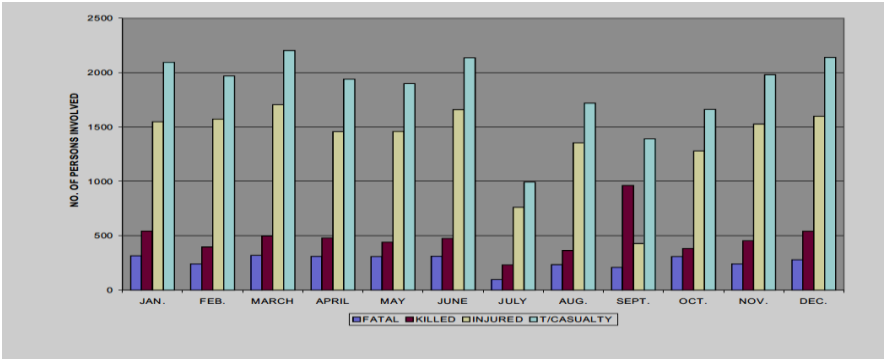

Figure 7
Road Traffic Accident summary 2004

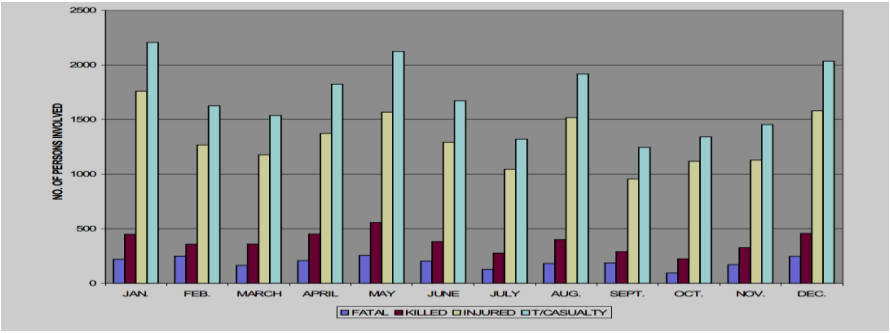

Figure 8
Road Traffic Accident summary 2005

Tables 3(a) and 3(b) are the data of RTA year summary of cases reported, total persons killed and persons injured for 2005 and 2004 respectively.

Table 3(a): 2005 RTA summary

Month	**Total cases reported**	**Persons killed**	**Persons injured**
Jan	980	447	1760
Feb	1040	358	1267
March	591	359	1178
April	679	450	1373
May	1118	556	1567
June	841	381	1291

Table 3(b): 2004 RTA summary

Month	**Total cases reported**	**Persons killed**	**Persons injured**
Jan	1333	544	1550
Feb	1039	397	1572
March	1312	498	1705
April	1498	481	1458
May	1206	440	1459
June	1144	476	1661

July	438	276	1045	July	487	233	761
Aug	956	399	1518	Aug	1136	365	1354
Sept	630	289	955	Sept	829	963	428
Oct	376	224	1117	Oct	1925	383	1279
Nov	624	325	1128	Nov	1036	455	1526
Dec	689	455	1580	Dec	1104	542	1598
Total	**8962**	**4519**	**15779**	**Total**	**14049**	**5777**	**16351**

From the comparison of 2004 and 2005, it was observed that 2004 has the higher reported RTA cases, number of persons killed and also number of persons injured.

Figure 9 shows the drift in RTAs starting from the year 2000 to the year 2007. The amount of RTAs in the year 2007 equals to 12,038, which implies an increase of 3.2% greater that of the year 2006 and another increase of 2.8% greater than that of the year 2000.

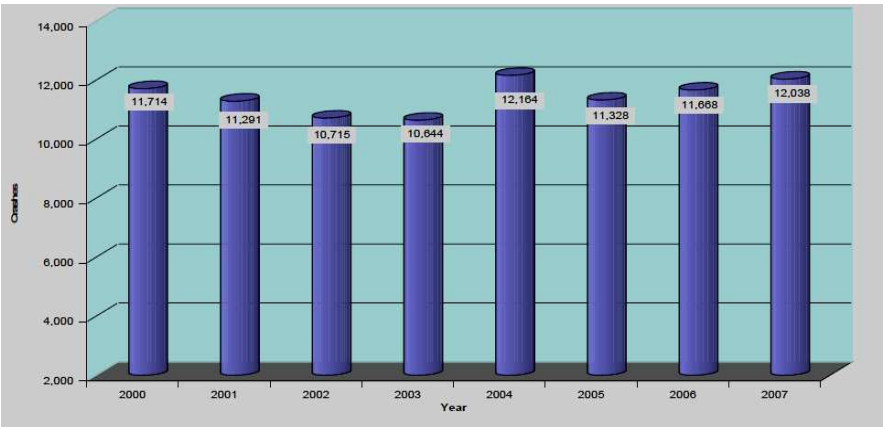

Figure 9
RTA 2000 – 2007

From the analysis of 2004 against 2005 and also from 2000 to 2007, the RTA target verses actual from 2001-2015 were obtained through prediction from collected data. Figure 10 shows the predicted RTA for 2010 to 2015.

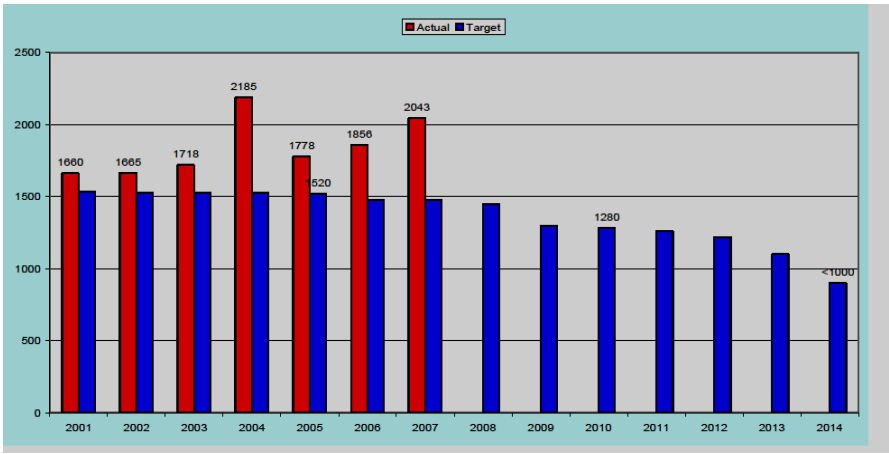

Figure 10
RTA fatalities target vs. actual 2001-2015

6 Discussion

The comparative analysis of 2004 against 2005 and 2000 to 2007 made the prediction of RTA for 2010 to 2015 using primary source collected data capable of allowing an accurate and good data model. The multilayer feed-forward neural network with its learning technique worked through the output value comparison with the accurate answer and also performed the computation of the already established error function. The error is inputted back to the ANN algorithm and it adjusts the weight values of every connection to bring down the values of the error function to minimal.

Hungary has an area of 93 030 km^2, and inhabitants of 10 174 853 (2002), a road network of 158 798 km (2000) and passenger car ratio of 273 per 1 000 inhabitants (2003). The adoption of Hungarian National Transport Safety Program (NKP) by the government took place in 1993 with the primary aim being to bring to a minimal the amount of fatalities and seriously injured persons to 20 to 30 percent when compared to 1992 figure. Efficient transport safety programs were to be submitted and for adoption in 2005 for a duration between 2010 and 2015. The national road network makes up 19% of the total road network. 52% of the accidents involving personal injuries and 77% of the fatal accidents took place on the national road network in 2003. The number of deaths per million vehicle kilometer varies between 30 and 32, which is one of the highest figures in the European Union [31].

Non-use of the seat belt, speeding, inefficient road bypass and inadequate police plan for road safety are the major challenges in Hungary with respect to road safety. In spite of this Hungary has succeeded to achieve a decrease in fatalities per 10 000 vehicles from 10.1 (1990) to 2.8 (2004). From CARE project data (http://europa.eu.int/comm/transport/ care/index_en.htm), it was noted that the amount of accidents, injuries and fatalities declined all through the time between 1991-2000. There were 1 200 deaths on Hungarian roads in 2000. The amount of accidents, injuries and fatalities increased again from 2000 to 2004. Recent fatality figures are however lower than in the mid-1990s.

The major cause of deaths within age range of 4 to 35 in North America has been revealed to be RTAs [32]. The long and far distances people drive in order to pay visit relatives, attend school and go to work across the state are the major causes of high rate of death and serious injuries. The effectiveness of safety measure in cars have brought down the amount of deaths due to RTAs by one out of three in Canada for the past twenty years, while rate of injuries still remain the same in recent years [33].

The major human factors the influence RTAs should be given higher priority by performing some tasks [34], such as carrying out full research in order to have a consistent foundation for determining the main human elements that contribute to road accidents with latest circumstances; these tasks includes checking, and modifying the local rules, disciplinary measures for correcting and filtering out the traffic offenders; putting in effective awareness for the drivers to enlighten and educate them; developing effective vehicle mechanics operation policies; developing hazard perception systems; danger assessment and decision making; giving adequate concern for further enlightenment and training; staging safety awareness with a focus on: change in human behavior, enhancing driving skills, and organizing a good level of traffic monitoring. These tasks helped in Hungarian RTA reduction and improved road safety and can be used for Nigeria case.

Conclusion

Some of these designed solutions will go a long way in reducing RTAs in Nigeria when implemented. The institution of a high level National Road Safety Council will complement the effort of FRSC, and also a special sub-group for road safety information and campaigns. Revisiting the activities and duties of all the bodies that are charged with the national responsibility for road safety management activities will equally go a long way to reduce RTAs in Nigeria; enhancing the collaboration among the Ministry of Works, FRSC, VIO, hospitals, transporters, NCDC, Army, Police Force, and insurance companies with respect to RTAs coming together to develop one inclusive and comprehensive annual national statistical yearbook on all RTAs; the development of strong a policy to regulate driving speed limits; an urgent plan to develop means for black spot management, and creating a special funding for black spots; and revisiting the rules for

commercial traffic, and fortify the full implementation of the rules, together with the rules governing the transportation of human beings, their luggage and goods.

ANN showed its advantage over conventional programming in this study. This is due to its capability to provide solutions to non-algorithmic problems and can learn how to deal with the new and unexpected situations by the help of past experience. Neural networks are able to relate input with output, allow large number of variables and are error tolerant.

References

[1] Ozgan, E. and Demirci. R. (2008) Neural Networks-based Modeling of Traffic Accidents In Interurban Rural Highways, Duzce Sampling. J. Applied Sci., 8, pp. 146-151

[2] Himanen, V. (1998) Neural Network in Transport Application. Ashgate Pub. Co., USA, pp. 311-340

[3] Abdelwahab, H. T. and Abdel-Aty, M. A. (2001) Development of ANN Models to Predict Driver Injury Severity in Traffic Accidents at Signalized Intersections, Transport. Res. Rec., 1746, pp. 6-13

[4] Riviere, C., Lauret, P., Manicom R., J. F., Page, Y., (2006) A Bayesian Neural Network Approach to Estimating the Energy Equivalent Speed. Accident Analysis and Prevention, 38, pp. 248-259

[5] Wei, C. H. and Lee, Y. (2007) Sequential Forecast of Incident Duration Using ANN Models. Accident Analysis and Prevention. 39(5), pp. 944-954

[6] Pande, A., and Abdel-Aty, M. (2006) Assessment of Freeway Traffic Parameters Leading To Lane-Change Related Collisions. Accident Analysis and Prevention. 38, pp. 936-948

[7] Delen, D., Sharda, R., and Bessonov, M. (2006) Identifying Significant Predictors of Injury Severity in Traffic Accidents Using A Series of Artificial Neural Networks Accident Analysis & Prevention. 38 (3), pp. 434–444

[8] Karayiannis, N. B. and Venetsanopoulos, A. N. (1993) ANNs: Learning Algorithms. Performance Evaluation and Applications. Kluwer Academic Publishers, Boston

[9] Ohakwe J., Iwueze, I. S., Chikezie, D. C. (2011) Analysis of Road Traffic Accidents in Nigeria: A Case study of Obinze/Nekede/Iheagwa Road in Imo State, southeastern, Nigeria. Asian Journal of applied Sciences, 4(2): pp. 166-175

[10] Odumosu, A. O., (2005) Demeanour Transposition as Strategy for Traffic Accident Reduction in Nigeria: Case Study of Niger State, Nigeria, Proc. 13th International Conference on Road Safety on Four Continents, Warsaw, Poland, p. 18

[11] Osime, O. C., Ehikhamenor, E., Oludiran, O. O., Iribhogbe, P. E., Ighedosa, S. E. and Elusoji, S. O. (2006) Road Traffic Accident Trends in Nigeria. International Journal of Injury Control and Safety Promotion, 13(4), pp. 251-253

[12] Adeolu J. O. (1993) Road Accident Trends in Nigeria. Accident Analysis and Prevention. 25(4), pp. 485-487

[13] Willette R. E. and Walsh J. M. (1983) Drugs, Driving and Traffic safety. WHO Offset Publication No. 78, World Health Organization: Geneva. pp. 1-10.

[14] Asogwa, S. E. (1978) Road Traffic Accidents: A Major Public Health Problem. Public Health 92, pp. 237-45

[15] The Nigeria Police Force Management Services and Research Department. Data on Establishment of Force. Force Headquarters Lagos, 1989, pp. 1-19

[16] Ezenwa A. O. (1986) Trend and Characteristic of RTA in Nigeria. J Roy Soc Health, 1, pp. 27-29

[17] Agunloye O. (1988) Road Danger in Nigeria- Truth and Consequences. J Fed Road Safety Commission, Nigeria. 1, pp. 11-16

[18] Oyemade A. (1973) Epidemiology of Road Traffic Accidents in Ibadan And Its Environs. Niger Med J. 3, pp. 174-177

[19] Asogwa S. E. (1980) Some Characteristics of Drivers and Riders Involved in Road Traffic Accidents in Nigeria East Africa. Med Journal. 57, pp. 399-404

[20] Oladehinde M. K, Adeoye A. O, Adegbehingbe B. O, and Onakoya A. O. (2007) Visual Functions of Commercial Drivers in Relation to Road Accidents in Nigeria. Indian J Occup Environ Med. 11, pp. 71-75

[21] Smeed, R. J., (1949) Some Statistical Aspects of Road Safety Research. Journal of Royal Statistical Society Series A 112, pp. 1-34

[22] Leeming, J. J. (1976) Comparing International Road Accident Deahts. AGARD Conference Proceedings, pp. 15-17

[23] Pitsiava-Latinopoulou M. and Tsohos, G. (1982) The Application of Smeed's Equation for Road Accidents in Greece. Accident Analysis and Prevention, 14(1), 1-6

[24] Adams, J. (1985) Smeed's Law, Seat Belts, and the Emperor's New Clothes. Human Behavior and Traffic Safety, pp. 193-257

[25] Broughton, J. (1988) Predictive Models of Road Accident Fatalities, Traffic Engineering & Control, 29(5), pp. 296-300

[26] Gharaybeh, F. A. (1994) Application of Smeed's Formula to Assess Development of Traffic Safety in Jordan, Accident Analysis and Prevention, 26(1), p. 113

[27] Navin, F. P. D., Bergan, A., and Zhang, G. (1996) Road Safety Model: Some Fundamental Ideas, in Transportation Research Record. 1563, pp. 48-57

[28] Ozgan, E. and R. Demirci. (2008) Neural Networks-based Modeling of Traffic Accidents in Interurban Rural Highways, duzce sampling. J. Applied Sci., 8: 146-151

[29] Abdelwahab, H. T. and M. A. Abdel-Aty (2002) Artificial Neural Networks and Logit Models for Traffic Safety Analysis of Toll Plazas. Transport. Res. Rec., 1784: pp. 115-125

[30] Ogwueleka, T. C and Ogwueleka, F. N. (2010) Prediction of Solid Waste Generation Using Self Organizing Map and Multilayer Perceptron Neural Networks. IUP University Journal of Science and Technology, Vol. 6, No. 1, pp. 39-50

[31] Road Safety Country Profile (2005) Magyarország, Hungary, pp. 1-2

[32] Subramanian, R., (2003) Motor Vehicle Traffic Crashes as a Leading Cause of Death in the United States, 2001. U.S. Department of Transportation, National Highway Traffic Safety Administration, document DOT HS 809 695

[33] Road Injuries and Fatalities - The Health Impacts of Urban Sprawl. An Information Series from Ontario College of Family Physician. Vo. 2. www.ocfp.on.ca

[34] http://www.itm.su.se/documents/poster/Road_sweepers_20120308.pdf(last accessed on 30.10.2012)

Predicting Academically At-Risk Engineering Students: A Soft Computing Application

Necdet Güner, Abdulkadir Yaldır, Gürhan Gündüz, Emre Çomak, Sezai Tokat, Serdar İplikçi

Pamukkale University, Department of Computer Engineering, Denizli, Turkey, nguner@pau.edu.tr; akyaldir@pau.edu.tr; ggunduz@pau.edu.tr; .ecomak@pau.edu.tr; stokat@pau.edu.tr; iplikci@pau.edu.tr

Abstract: This paper presents a study on predicting academically at-risk engineering students at the early stage of their education. For this purpose, some soft computing tools namely support vectors machines and artificial neural networks have been employed. The study population included all students enrolled in Pamukkale University, Faculty of Engineering at 2008-2009 and 2009-2010 academic years as freshmen. The data are retrieved from various institutions and questionnaires conducted on the students. Each input data point is of 38-dimension, which includes demographic and academic information about the students, while the output based on the first-year GPA of the students falls into either at-risk or not. The results of the study have shown that either support vector machine or artificial neural network methods can be used to predict first-year performance of a student in a priori manner. Thus, a proper course load and graduation schedule can be transcribed for the student to manage their graduation in a way that potential dropout risks are reduced. Moreover, an input sensitivity analysis has been conducted to determine the importance of each input used in the study.

Keywords: at-risk students; least-square support vector classification; radial basis functions neural network; support vector classification

1 Introduction

There have been many new universities established in Turkey in recent years. As a result, the number of students studying at Turkish universities is increasing, which allows students with diverse backgrounds attend the same classes. Many students are failing in their studies, as a result of having different learning levels. Engineering students, especially those without a sufficient background in math and science, are more likely to fail in courses [1] [2].

Some of the students cannot manage to graduate within the expected period, which leads to economical losses for both the family and the public. These losses

can be greatly reduced by taking necessary social and academic predictive measurements, if academically at-risk students can be identified in advance.

There are many studies on predicting the success of university students and the factors influencing their success. Some of this research has focused on the reasons for early withdrawal. For instance, Tinto [3] has observed that 73% of the withdrawals occur within the first two years. In addition, McGrath and Braunstein [4] have found that low grade point average (GPA) at the first year is the major factor causing the early withdrawal. Some scientific research revealed that one of the major factors assisting to predict the success of students is their first-year GPAs and that there is a direct correlation between the first-year GPAs and graduating successfully in time [4] [5].

Apart from these findings, it has been found that half of the engineering students in the United States withdraw within the first two years [6]. In Australia, it has been reported that only 20% of the students in Queensland University of Technology have managed to graduate within four years [7]. In addition, more than 25% of the students in Australia consider withdrawing seriously within the early years of their study [8]. Researchers have revealed that there is a strong relationship between the first year academic success and the continuation of a university education [5]. Therefore, it is of great importance to predict the first year success of students.

There have been numerous researchers investigating the factors that have influence the success of students. These studies can be divided into three groups, namely,

(i) Academic background of students [5] [9] [10] [11]

(ii) Social, economic, and educational levels of students' families [9] [12]

(iii) Physiological and individual properties of students [13] [14] [15] [16].

In the literature, there have been many research papers attempting to predict the GPAs of students by using data mining and Soft Computing (SC). For instance, in the study by Affendey et al. [17], the influencing factors contributing to the academic performance of the students have been ranked using the Bayesian Approach, Radial Basis Function Neural Networks (RBFNN). On the other hand, Vandamme et al. [18] have divided the students into three groups and then predicted the academic success of the students by using different methods such as discriminant analysis, neural networks, random forests, and decision trees. In another application, Oladokun et al. [19] have developed an artificial neural network model to predict the performance of the students who are entering universities through the National University Admission Examination in Nigeria. The model was able to correctly predict the performance of more than 70% of prospective students. Also, Huang [20] has used multiple regression and SC methods to obtain a validated set of mathematical models in order to predict academic performances of students in Engineering Dynamics Courses.

In this study, SC methodologies have been employed to predict the first-year engineering students who fall into an at-risk group. The at-risk is defined as the students who have a GPA less than 2.00 (out of 4.00). Therefore, it is important to predict first-year GPA's of the newly enrolled students. It has been known that academic performances of students can be improved through academic and other consultancy assistance by predicting their performances as early and accurate as possible [21] [22] [23].

Support Vector Classification (SVC) approaches are based on the Structural Risk Minimization and Statistical Learning Theory and handle the classification problem by converting it into either a quadratic programming problem in the conventional SVC case or a set of linear equations in the Least-Squares SVC case, respectively. The idea behind the use of SVC approaches in the prediction of the academic performances of the first-year university students is the fact that SVC models are simple to obtain and that they have higher generalization potential. The rest of this paper is organized as follows: In Section 2 the prediction problem is defined in detail, Section 3 describes the SC methods used herein, Section 4 outlines the Input-Sensitivity Analysis, Section 5 explains the obtained results and finally, the paper ends with the conclusions.

2 Problem Definition

This research was conducted among the students who have enrolled in the Faculty of Engineering at Pamukkale University, a public university in Denizli, which is located in the southwest part of Turkey. To determine the academically at-risk students, we have used Machine Learning methods based on the data containing information about the students who enrolled in Pamukkale University Faculty of Engineering departments in academic years 2008-2009 and 2009-2010. The data are retrieved from Pamukkale University Students' Registry (PUSR) and Turkish Students Selection and Placements Centre (SSPC), which is responsible for the execution of University Entrance Exam (UEE).

Data about the academic background of students comprise the following: type of high school graduated, high school GPA, individual scores obtained from each or combined subject at the UEE, and numbers of correct and wrong answers given in each or combined subject at the UEE. Demographic data include gender, age, and the department of students, their parents' educational and socio-economic levels, their hometown distance to Pamukkale University, and their willingness of working part-time at the university. A total of 38 different types of data were considered for the 1050 Faculty of Engineering students, who enrolled in academic years 2008-2009 and 2009-2010 and are tabulated in Table 1 given here in the appendix.

Table 1
Data Retrieved from Pusr and SSPC

1. Gender
2. Year of birth
3. Department
4. Day/evening studies
5. Type of high school
6. High school graduation year
7. High school GPA
8. Distance of hometown to university
9. Mother alive/dead
10. Father alive/dead
11. Mother and father living together
12. Total number of siblings
13. Number of siblings studying at university
14. Father's education
15. Socio-economical level of the family*
16. Mother's education
17. Willing to work at the university
18. Attended to English preparatory school in university
19. High school graduation rank
20. Verbal score of the high school
21. Quantitative score of the high school
22. Equally weighted score of the high school
23. Number of correct answers in Math-1 test of the UEE
24. Number of correct answers in Science-1 test of the UEE
25. Number of correct answers in Math-2 test of the UEE
26. Number of correct answers in Science-2 test of the UEE
27. Number of false answers in Math-1 test of the UEE
28. Number of false answers in Science-1 test of the UEE
29. Number of false answers in Math-2 test of the UEE
30. Number of false answers in Science-2 test of the UEE
31. Quantitative-1 score of the UEE
32. Verbal-1 score of the UEE
33. Equally weighted-1 score of the UEE
34. Quantitative-2 score of the UEE
35. Equally weighted-2 score of the UEE
36. Physics test score of the UEE
37. Number of correct answers to complex numbers, logarithms, and trigonometry questions in the Math-2 test of the UEE
38. Number of correct answers to limit, derivatives, and integral questions in the Math-2 test of the UEE
39. University first year GPA

** Socio-economic levels of the families have been calculated as a combination of ten different data about students and their families collected by PUSR at the registration.*

It should be noted that some of the data are in binary form (e.g., gender), some of them are integers (e.g., total number of siblings), and the remaining are real numbers (e.g., high school GPA). No matter what the forms of the answers are, they all have been normalized into the interval [0, 1] in this study. Therefore, 1050

normalized data points of 39 dimensions have been used to obtain proper prediction models. The first 38 rows of Table 1 are taken as inputs for the prediction models, while the output falls into either at-risk or not, based on the first-year GPA of the students taken from row 39 of Table 1.

3 Soft Computing Methods (SC)

For all of the SC tools employed in this study, it is assumed that the data set $\mathcal{D}$ is collected for obtaining optimal model and has the form given below:

$$\mathcal{D} = \{\mathbf{x}_k ; y_k\}_{k=1}^{k=N} \tag{1}$$

where $\mathbf{x}_k \in \mathbb{R}^n$ is n-dimensional k^{th} input vector, $y_k \in \{-1,+1\}$ is the corresponding binary output, and N is the total number of data, which is $N = 1050$ for this work. It is desired to find a model that represents the relationship between the input and output data points. Each SC tool used to obtain a proper model has its own modeling parameters, and different modeling parameters result in different models. Therefore, it is inevitable to search for the optimal modeling parameters in the parameter space. For this purpose, $\mathcal{D}$ is randomly divided into three parts: 600 for training, 200 for validation, and 250 for testing. Then, in order to find the best model for each SC tool, a grid search approach is adopted. In this approach, the modeling parameter space is divided by grids, and for each node (corresponding to specific parameter values) on the grid, a model is obtained using the training data set, and then, the model, which produces the least validation error based on the validation data set is chosen as the optimal model. Finally, optimal models for the SC tools are compared with each other by using the test data.

3.1 Support Vector Classification

The primal form of a SVC model is given by Equation (2), which is linear in a higher dimensional feature space F.

$$\hat{y}_i = \langle \mathbf{w}, \mathbf{\Phi}(\mathbf{x}_i) \rangle \tag{2}$$

where $\mathbf{w}$ is a vector in the feature space F, $\mathbf{\Phi}(.)$ is a mapping from the input space to the feature space, and $\langle . \rangle$ stands for the inner product operation in F. The SVC algorithms regard the classification problem as an optimization problem in dual space in which the model is given by Equation (3).

$$\hat{y}_i = \sum_{j=1}^{N_{Tr}} \alpha_j y_j K(\mathbf{x}_i, \mathbf{x}_j) \tag{3}$$

where N_{Tr} is the number of training data, α_j is the coefficient corresponding to the training data $\mathbf{x}_j$, and $K(\mathbf{x}_i, \mathbf{x}_j)$ is a Gaussian kernel function given by,

$$K(\mathbf{x}_i, \mathbf{x}_j) = \left\langle \mathbf{\Phi}(\mathbf{x}_i), \mathbf{\Phi}(\mathbf{x}_j) \right\rangle = e^{-\frac{\left\|\mathbf{x}_i - \mathbf{x}_j\right\|^2}{2\sigma^2}} = K_{ij} \tag{4}$$

The kernel function handles the inner product in the feature space, and thus, the explicit form of $\mathbf{\Phi}(\mathbf{x})$ does not need to be known. In the model given by Equation (3), a training point $\mathbf{x}_j$ corresponding to a non-zero α_j value is referred to as the support vector. The primal form of the classification problem is as follows:

$$\min_{\mathbf{w},b,\xi,\xi^*} P = \frac{1}{2}\|\mathbf{w}\|^2 + C\sum_{i=1}^{N_{Tr}} \xi_i \tag{5}$$

subject to the constraints,

$$y_i \left\langle \mathbf{w}, \mathbf{\Phi}(\mathbf{x}_i) \right\rangle \le 1 - \xi_i, \ i = 1, \ldots, N_{Tr} \tag{6a}$$

$$\xi_i \ge 0, \ i = 1, \ldots, N_{Tr} \tag{6b}$$

where ξ_i's are slack variables, $\|.\|$ is the Euclidean norm, and *C* is a regularization parameter. By adding the constraints to the primal form of the classification problem, the Lagrangian can be obtained as

$$L_P = \frac{1}{2}\|\mathbf{w}\|^2 + C\sum_{i=1}^{N_{Tr}} \xi_i - \sum_{i=1}^{N_{Tr}} \alpha_i \left(y_i \left\langle \mathbf{w}, \mathbf{\Phi}(\mathbf{x}_i) \right\rangle - 1 + \xi_i \right) - \sum_{i=1}^{N_{Tr}} \mu_i \xi_i \tag{7}$$

where α_i's and μ_i's are Lagrange multipliers. First-order conditions of the primal optimization problem are obtained by taking partial derivatives of L_P with respect to the design variables and then setting them to zero as follows:

$$\frac{\partial L_P}{\partial \mathbf{w}} = 0 \mapsto \mathbf{w} = \sum_{i=1}^{N_{Tr}} \alpha_i y_i \mathbf{\Phi}(\mathbf{x}_i) \tag{8}$$

$$\frac{\partial L_P}{\partial \xi_i} = 0 \mapsto C - \alpha_i - \mu_i = 0, \quad i = 1, \ldots, N_{Tr} \tag{9}$$

Now, the dual form of the optimization problem becomes a Quadratic Programming (QP) problem as:

$$\min_{\boldsymbol{\alpha}} D = \frac{1}{2}\sum_{i=1}^{N_{Tr}}\sum_{j=1}^{N_{Tr}}\alpha_i\alpha_j y_i y_j K_{ij} - \sum_{i=1}^{N_{Tr}}\alpha_i \tag{10}$$

subject to the constraints,

$$\sum_{i=1}^{N_{Tr}}\alpha_i y_i = 0 \text{ and } 0 \le \alpha_i \le C,\ i = 1,\ldots,N_{Tr} \tag{11}$$

Solution of the QP problem given by equations (10) and (11), yields the optimum values of α_i's [24]. Furthermore, when only the support vectors are considered, the model becomes as follows:

$$\hat{y}_i = \sum_{\substack{j=1 \\ j\in SV}}^{\#SV}\alpha_j y_j K(\mathbf{x}_i, \mathbf{x}_j) \tag{12}$$

where #SV stands for the number of support vectors in the model. The SVC model given by Equation (12) is sparse in the sense that the whole training data are represented by only support vectors. The parameters of SVC are the regularization parameter C and the kernel parameter σ.

3.2 Least-Square Support Vector Classification

Least-squares support vector classification (LSSVC) is a variety of SVC, which has almost the same level of capability in classification and regression as SVC [25] [26]. LSSVC finds optimal value of the cost function given in Equation (13) subject to equality constraints instead of inequality ones in the SVC case. Therefore, it is desired to minimize the following:

$$\frac{1}{2}\|\mathbf{w}\|^2 + \frac{C}{2}\sum_{i=1}^{N_{Tr}}\xi_i^2 \tag{13}$$

subject to

$$y_i\left(\langle \mathbf{w}, \boldsymbol{\Phi}(\mathbf{x}_i)\rangle + b\right) = 1 - \xi_i, i = 1,\ldots,N_{Tr} \tag{14}$$

Because the optimization problem is built on linear equations, computational burden of LSSVC is less than that of SVC. On the other hand, SVC is sparser than LSSVC in the sense that the former contains less number of support vectors in the model than the latter. However, both approaches exhibit similar classification performances. Yet, we have employed both approaches in this study for the sake of comparison. Equation (15) is obtained when Eqs. (13-14) are presented in dual optimization form with Lagrange multipliers.

$$L(\mathbf{w},b,\boldsymbol{\alpha},\boldsymbol{\xi}) = \frac{1}{2}\|\mathbf{w}\|^2 + \frac{C}{2}\sum_{i=1}^{N_{Tr}}\xi_i^2 - \sum_{i=1}^{N_{Tr}}\alpha_i\left[y_i\left(\left\langle \mathbf{w},\boldsymbol{\Phi}(\mathbf{x}_i)\right\rangle + b\right) - 1 + \xi\right] \tag{15}$$

where $\alpha_i \in \mathbb{R}^n$ are the Lagrange multipliers. The first-order conditions for optimality are as follows:

$$\frac{\partial L}{\partial \mathbf{w}} = 0 \rightarrow \mathbf{w} = \sum_{i=1}^{N_{Tr}}\alpha_i\boldsymbol{\Phi}(\mathbf{x}_i), \tag{16a}$$

$$\frac{\partial L}{\partial b} = 0 \rightarrow \sum_{i=1}^{N_{Tr}}\alpha_i = 0, \tag{16b}$$

$$\frac{\partial L}{\partial \xi_i} = 0 \rightarrow \alpha_i = -C\xi_i,\ i = 1,\ldots,N_{Tr}, \tag{16c}$$

$$\frac{\partial L}{\partial \alpha_i} = 0 \rightarrow y_i = \left\langle \mathbf{w},\boldsymbol{\Phi}(\mathbf{x}_i)\right\rangle + b + \xi_i,\ \ i = 1,\ldots,N_{Tr} \tag{16d}$$

With the elimination of $\mathbf{w}$ and ξ_i, a set of linear equations are obtained as given by Equation (17), the solution of which contains Lagrange multipliers and the bias term.

$$\begin{bmatrix} 0 & \mathbf{Y}^T \\ \mathbf{Y} & \mathbf{Z}\mathbf{Z}^T + C^{-1}I \end{bmatrix}\begin{bmatrix} b \\ \boldsymbol{\alpha} \end{bmatrix} = \begin{bmatrix} 0 \\ \mathbf{1} \end{bmatrix} \tag{17}$$

where the matrix is a $(N_{Tr}+1)\times(N_{Tr}+1)$ square matrix,

$$\mathbf{Z}^T = \left[\, y_1\boldsymbol{\Phi}(x_1),\ldots, y_N\boldsymbol{\Phi}(x_{N_{Tr}})\,\right] \tag{18a}$$

$$\mathbf{Y}^T = \left[\, y_1, y_2,\ldots,y_{N_{Tr}}\,\right] \tag{18b}$$

$$\boldsymbol{\alpha}^T = \left[\, \alpha_1,\alpha_2,\ldots\alpha_{N_{Tr}}\,\right] \tag{18c}$$

and C is a scalar parameter. Similar to SVC, the output value of LSSVC is computed by Equation (12) after Lagrange multipliers and bias values are found. In contrast to SVC, Lagrange multipliers in LSSVC might be positive or negative. It should be noted that the number of support vectors in the model is the same as the number of training data. The inner product $\left\langle \boldsymbol{\Phi}(\mathbf{x}_i),\boldsymbol{\Phi}(\mathbf{x}_j)\right\rangle$ is handled by the Gaussian kernel function as in the SVC case.

3.3 Radial Basis Function Neural Networks

Radial basis function neural networks (RBFNN) are special artificial neural network structures in which the hidden units are activated with respect to the distance between the input vector and a predefined centre vector. RBFNN can provide a nonlinear model for the target dataset with its simple and yet fast learning network structure [27], and therefore, it is a sensible alternative to use complex polynomials for function approximation.

In a RBFNN, there is only one hidden layer that uses neurons with radial basis function (RBF) activation functions. RBFs implement localised representations of functions, and they are real valued functions whose outputs depend on the distance of the input from the stored centre vector of each hidden unit [28]. Thus, it has its peak value at the centre and decreases in each direction along the centre. Different functions, such as multi-quadratics, inverse multi-quadratics, and bi-harmonics, could be used as RBF. A typical selection is a Gaussian function for which the output of the i^{th} hidden unit is written as

$$y = \sum_{i=1}^{\#HU} w_i \exp(-\left\|\mathbf{x}_k - \mathbf{v}_i\right\|^2 / 2\sigma_i^2),\ i = 1,\ldots,\#HU \tag{19}$$

where $v_i \in \mathbb{R}^n$ is n-dimensional centre vector of the RBF of the i^{th} hidden neuron, σ_i is the width of RBF of the i^{th} hidden neuron, *#HU* is the number of hidden units, and w_i is the weight of the i^{th} hidden unit. An RBFNN is completely determined by choosing the dimension of input-output data; number of RBFs; and values of v_i, σ_i and w_i. The function approximation or classification performance of RBFNN is obtained by defining all these parameters. The dimension of input-output data is problem dependent and defined clearly at the beginning. Choice of the number of RBFs plays a critical role and depends on the problem under investigation. For simplicity in calculations, σ_i values are all taken equal to σ. In this study, *#HU* and σ are grid searched to choose the best values for validation data. In the training phase, hidden unit neurons are added using an orthogonal least squares algorithm to reduce the output error of network until the sum-squared error goal is reached [29].

4 Input-Sensitivity Analysis

By input-sensitivity analysis, it can be determined to what extent the output of the SVC model is sensitive to each input of the model. In this respect, the partial derivative of the output $\hat{y}(\mathbf{x})$ with respect to each input is needed. Let us remember that the input-output relationship of the SVC model is

$$\hat{y}(\mathbf{x}) = \sum_{\substack{j=1 \\ j\in SV}}^{\#SV} \alpha_j y_j K(\mathbf{x}_i, \mathbf{x}_j) \tag{20}$$

where $\mathbf{x}_j$'s are the support vectors, $\mathbf{x} \in \mathbb{R}^n$ is n-dimensional input vector and $K(\mathbf{x}, \mathbf{x}_j)$ is a Gaussian kernel function given by

$$K(\mathbf{x}, \mathbf{x}_j) = e^{-\frac{\|\mathbf{x}-\mathbf{x}_j\|}{2\sigma^2}} = e^{-\frac{(x_1-x_{j1})^2+(x_2-x_{j2})^2+\ldots+(x_n-x_{jn})^2}{2\sigma^2}} \tag{21}$$

Then, the input-output relationship becomes

$$\hat{y}(\mathbf{x}) = \sum_{i\in S} \alpha_j y_j K(\mathbf{x}, \mathbf{x}_j) = \sum_{i\in S} \alpha_j y_j e^{-\frac{(x_1-x_{j1})^2+(x_2-x_{j2})^2+\ldots+(x_n-x_{jn})^2}{2\sigma^2}} \tag{22}$$

Now, the partial derivatives can be written by

$$\frac{\partial \hat{y}(\mathbf{x})}{\partial \mathbf{x}_k} = \frac{\partial \sum_{i\in S} \alpha_j y_j e^{-\frac{(x_1-x_{j1})^2+(x_2-x_{j2})^2+\ldots+(x_n-x_{jn})^2}{2\sigma^2}}}{\partial \mathbf{x}_k} \tag{23}$$

The derivative in Equation (23) can be calculated as

$$\begin{aligned}
\frac{\partial \hat{y}(\mathbf{x})}{\partial \mathbf{x}_k} &= \frac{\sum_{i\in S} \alpha_j y_j \partial e^{-\frac{(x_1-x_{j1})^2+(x_2-x_{j2})^2+\ldots+(x_n-x_{jn})^2}{2\sigma^2}}}{\partial \mathbf{x}_k} \\
&= \sum_{i\in S} \alpha_j y_j \frac{\partial e^{-\frac{(x_1-x_{j1})^2+(x_2-x_{j2})^2+\ldots+(x_n-x_{jn})^2}{2\sigma^2}}}{\partial \mathbf{x}_k} \\
&= \sum_{i\in S} \alpha_j y_j \frac{(x_{jk}-x_k)}{\sigma^2} e^{-\frac{(x_1-x_{j1})^2+(x_2-x_{j2})^2+\ldots+(x_n-x_{jn})^2}{2\sigma^2}} \\
&= \sum_{i\in S} \alpha_j y_j \frac{(x_{jk}-x_k)}{\sigma^2} K(\mathbf{x}, \mathbf{x}_j)
\end{aligned} \tag{24}$$

For a SVC model obtained by the data set $\{\mathbf{x}_i; y_i\}_{i=1}^{i=N}$, it is possible to build a sensitivity vector for the k^{th} input as

$$\mathbf{s}_k = \left[\frac{\partial \hat{y}(\mathbf{x}_1)}{\partial \mathbf{x}_k} \quad \frac{\partial \hat{y}(\mathbf{x}_2)}{\partial \mathbf{x}_k} \quad \ldots \quad \frac{\partial \hat{y}(\mathbf{x}_N)}{\partial \mathbf{x}_k} \right] \tag{25}$$

Thus, the norm $\|\mathbf{s}_k\|$ of the sensitivity vector can be regarded as a numerical measure that indicates the sensitivity of the output to the k^{th} input for the SVC model obtained by the data set $\{\mathbf{x}_i; y_i\}_{i=1}^{i=N}$. For large sensitivity of the output to the k^{th} input, we obtain relatively large $\|\mathbf{s}_k\|$ values and vice versa. That being $\|\mathbf{s}_k\| = 0$ means no sensitivity to the k^{th} input, *e.g.* no matter how much the k^{th} input is changed the output is not affected. By comparing the sensitivity vectors regarding to all inputs, it is possible to determine the relative sensitivities of the inputs. Moreover, some inputs having very small sensitivities can be discarded from the data set and then the SVC model can be re-obtained with the new data set.

Similar to the case given for SVC case, using RBFNN input output equation given in (19), the partial derivative of output variable $\hat{y}(\mathbf{x})$ with respect to each input vector $\mathbf{x}_k$ can be obtained as

$$\frac{\partial \hat{y}(\mathbf{x})}{\partial x_k} = \sum_{i=1}^{\#HU} w_i \frac{\left(x_k - v_i(k)\right)}{\sigma^2} e^{-\frac{\|\mathbf{x}-\mathbf{v}_i\|}{\sigma^2}} \tag{26}$$

The sensitivity analysis of input variables is made by using Equation (26). The last four inputs 35, 9, 32 and 34 can be pruned as they have relatively lower sensitivity than other inputs. In this study, as also highlighted in the literature [30], the sensitivity analysis is initially examined at first hand prior to the design of the classifier structures. But, as the pruning of the last 4 inputs does not change the results significantly, the pruning of the network structure is not conducted in order to see the whole effect of the questionnaire.

5 Results and Discussions

Each SC method used in this study has its own parameter set to be optimized. To find the optimal parameter set, a grid search approach is adopted, where the parameter space is divided into grids. A node in the grid corresponds to a parameter set. In the grid search, validation performances of the models for each nodes (parameter sets) are calculated, and then, the parameter set having the least validation error is determined as the optimal parameter set. Table 2 tabulates the optimal parameter sets found by grid search for each method employed in the study. The optimal parameter sets are given in the second column. The optimal parameter sets, training, validation and test performance for each method, can be seen in columns 3-5 in Table 2.

Table 2
Optimal Parameters and Obtained Results

Method	Parameters	Train %	Validation %	Test %
SVC	$C = 0.1,\ \sigma = 0.6$	98.66	73.50	68.80
LSSVC	$C = 1.6,\ \sigma = 121$	91.50	78.50	75.60
RBFNN	$\#HU = 67,\ \sigma = 1.3$	77.17	78.00	77.60

As can be seen in the table, all methods exhibit satisfactory validation and test performances almost over 70%. However, the LSSVC and RBFNN yield better results than SVC. It can also be seen that the validation and test results for LSSVC and RBFNN methods are close to each other. The reason for the SVC approach to give relatively weak performance can be attributed to the fact that the SVC model may go into over-fitting. This can be observed if the performances of the methods in Table 2 are examined. The less training error the method produces, the more over-fitting and the worse generalization it does.

As a result of sensitivity analysis performed for the three methods, normalized $\mathbf{s}_k$ results have been presented with a bar graph in Figure 1. Also, the actual $\mathbf{s}_k$ values and inputs according to sensitivity ranks are presented in Table 3.

It is assumed that any input k which has a normalized $\mathbf{s}_k$ value less than 0.33 can be regarded as having a low impact on the student's academic success in the first semester. These inputs are year of birth, high school graduation year, mother alive/dead, number of siblings studying at university, number of correct answers in math-1 test of the UEE, number of false answers in science-1 test of the UEE, number of false answers in science-2 test of the UEE, quantitative-1 score of the UEE, verbal-1 score of the UEE, equally weighted-1 score of the UEE, quantitative-2 score of the UEE and equally weighted-2 score of the UEE, and indicated with '*' in Figure 1. Based on this sensitivity analysis, it is observed that some inputs have less impact on the output than others and these inputs can be discarded in further applications.

Table 3
Sensitivity Analysis Results

	SVC		LSSVC		RBFNN	
Sensitivity Rank	Input k	$\mathbf{s}_k$	Input k	$\mathbf{s}_k$	Input k	$\mathbf{s}_k$
1	38	61.1627	25	53.87	1	134.0328
2	20	49.1408	26	46.748	17	121.1353
3	26	47.2159	36	43.451	4	114.5789
4	22	43.6456	37	34.691	11	101.6467
5	25	40.8373	24	32.603	10	100.3562
6	21	38.4838	19	30.843	38	98.3192
7	7	37.5234	1	27.208	18	94.1968
8	19	36.6386	38	26.353	26	87.8470
9	37	35.7801	20	25.487	14	81.8787
10	36	29.7689	3	20.379	3	81.6844
11	8	25.3821	7	20.233	20	79.4239
12	24	23.4596	22	19.637	7	74.7644
13	29	23.0989	21	14.656	8	72.6266
14	1	21.672	28	14.495	19	71.6740
15	27	20.2662	15	14.104	16	68.9167
16	6	17.6121	23	12.798	36	66.8006
17	34	17.4067	5	12.228	12	66.4493
18	3	16.3039	4	11.784	5	65.0252
19	14	15.1906	2	11.573	22	62.9082
20	31	13.9646	33	11.39	25	62.2902
21	28	13.2361	8	10.419	15	59.9410
22	33	12.0748	29	10.278	21	56.4296
23	15	10.8849	14	9.7945	24	55.4738
24	2	10.279	31	7.0194	37	54.6353
25	4	10.1053	32	6.5261	13	49.9793
26	30	9.9314	6	6.0264	23	47.3972
27	12	7.3607	10	5.3529	27	43.3737
28	23	5.7258	27	5.2585	30	42.4624
29	35	5.7243	34	4.7037	28	37.8810
30	16	4.2286	11	4.4312	31	37.4403
31	11	4.2085	30	3.6643	33	36.6683
32	17	3.4682	35	3.4183	29	35.8899
33	5	2.8061	17	2.7849	9	34.9133
34	10	2.8017	12	2.7604	2	29.9388
35	18	2.5429	16	1.7147	6	27.5962
36	32	2.4576	18	1.3411	35	26.2895
37	9	1.5825	9	0.97898	32	22.6935
38	13	1.5804	13	0.95468	34	20.8956

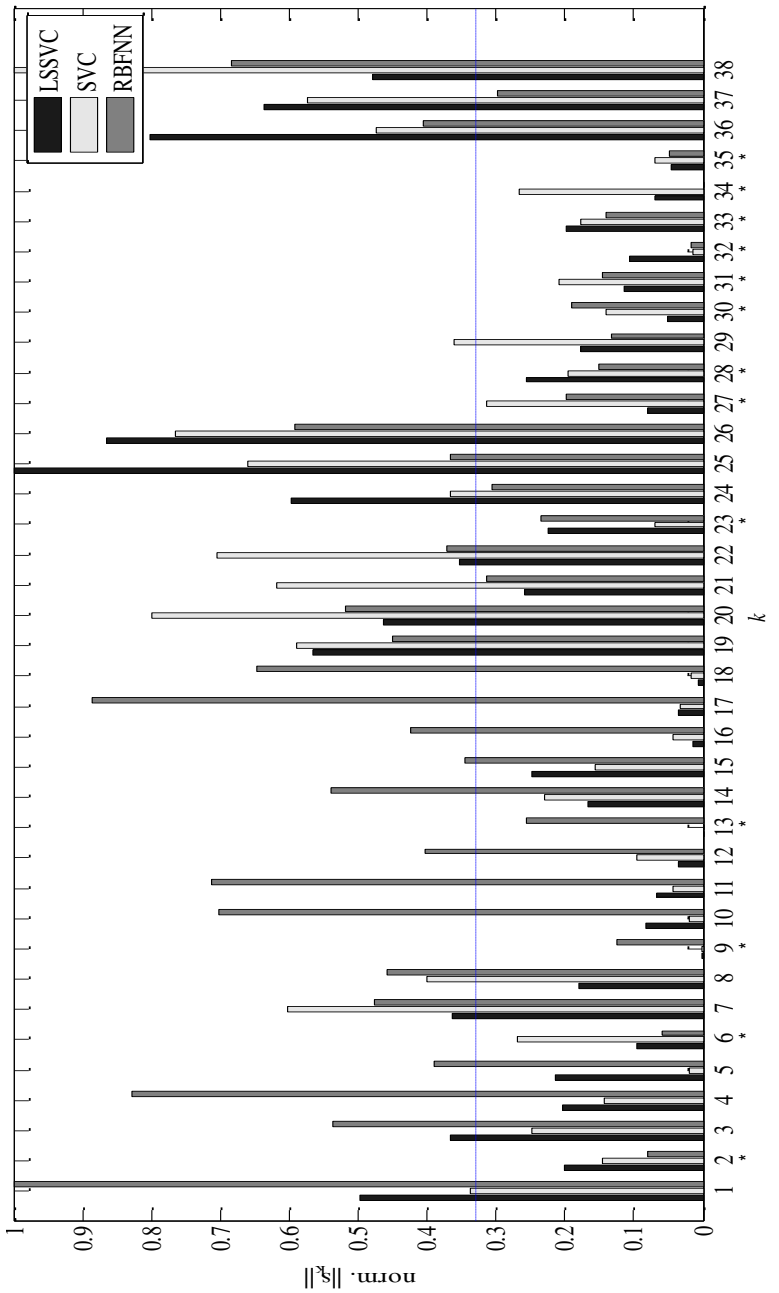

Figure 1
Input-Sensitivity Analysis Report

Conclusions

In this paper, a study on predicting academically at-risk engineering students newly enrolled to a university has been presented. For this purpose, some SC tools, namely, Support Vectors Machines and Artificial Neural Networks have been used, because of their high generalization capabilities. The data containing information 1050 students are retrieved from PUSR and SSPC, which are responsible for the execution of UEE. In the study, it has been assumed that the first-year success of an engineering student is mainly dependent on the performance in the centralized UEE, high school performance, and socio-economic and educational level of the family. Therefore, the data used in the study have been prepared accordingly. The results revealed that all the soft computing tools we have used yielded satisfactory prediction performances for both test and validation data. To be specific, both LSSVC and RBFNN provide more than 75% validation and test performance, whereas SVC provides 73.50% for validation and 68.80% for testing. The reason for the SVC method to give relatively weak performance can be explained by the fact that it makes more over-fitting than others as can be seen in Table 2.

Moreover, based on the obtained models a sensitivity analysis has been conducted, which has revealed that some inputs in the study can be ignored since the output is less sensitive to them than others. The results of this analysis can be used in similar applications in future.

Based on these SC approaches, a computer application may be developed to provide an academic counseling service for freshman engineering students, by means of which student advisors can predict the students' GPA scores at the end of the first semester by entering the required data into the application and can warn them when necessary. It is planned at the Engineering Faculty of Pamukkale University to apply such computer software to the freshman students who will enroll to the faculty in 2013-2014 academic year.

In conclusion, either support vector machine-based methods or RBFNN's can be used to predict first-year performance of a student based on a priori knowledge and data. Thus, a proper course load per semester and graduation schedule can be developed for a student to manage their graduation in a way that potential drop-off risks are reduced.

Acknowledgement

The authors gratefully acknowledge the help of the Pamukkale University Students' Registry and Turkish Students Selection and Placements Centre in Ankara for providing the necessary data.

References

[1] P. Broadbridge, S. Henderson, Mathematics Education for 21st Century Engineering Students - Final Report, Melbourne, Australian Mathematical Sciences Institute, 2008

[2] P. Kent, R. Noss, Mathematics in the University Education of Engineers, A Report to the Ove Arup Foundation, London, the Ove Arup Foundation, 2003

[3] V. Tinto, Leaving College; Rethinking the Causes and Cures of Student Attrition, Chicago, University of Chicago Press, 1994

[4] M. McGrath, A. Braunstein, "The Prediction of Freshmen Attrition", College Student Journal, Vol. 31, pp. 396-408, 1997

[5] S. M. DeBerard, D. J. Julka, G. I. Spielmans, "Predictors of Academic Achievement and Retention among College Freshmen: A Longitudinal Study", College Student Journal, Vol. 38, pp. 66-85, 2004

[6] M. Crawford, K. J. Schmidt, "Lessons Learned from a K-12 Project", Proceedings of the 2004. American Society for Engineering Education Annual Conference and Exposition, Washington, American Society for Engineering Education, pp. 1-13, 2004

[7] R. H.Cuthbert, H. L. MacGrillivray, "Investigation of Completion Rates of Engineering Students", In D'Arcy- A.L. Warmington, M. Victor, G. Oates, C. Varsavsky. (eds.) 6th Southern Hemisphere Conference on Mathematics and Statistics Teaching and learning (El Calafate DELTA' 07), 26-30 November 2007, El Calafate, Argentina, pp. 35-41, 2007

[8] K. L. Krause, "Serious Thoughts about Dropping Out in First Year: Trends, Patterns and Implications for Higher Education", Studies in Learning, Evaluation, Innovation and Development, Vol. 2, No. 3, pp. 55-68, 2005

[9] J. R. Betts, D. Morell, "The Determinants of Undergraduate Grade Point Average", The Journal of Human Resources, Vol. 34, No 2, pp. 268-293, 1999

[10] K. McKenzie, R. Schweitzer, "Who Succeeds at University? Factors Predicting Academic Performance in First Year Australian University Students", Higher Education Research and Development, Vol. 20, No. 1, pp. 21-33, 2001

[11] N. W. Burton, L. Ramist, Predicting Success in College: SAT Studies of Classes Graduating Since 1980, College Board Report No 2001-2. New York, College Entrance Examination Board, 2001

[12] S. M. R. Ting, "Predicting Academic Success of First-Year Engineering Students from Standardized Test Scores and Psychosocial Variables", International Journal of Engineering Education, Vol. 17, No. 1, pp. 75-80, 1998

[13] S. Museus, D. Hendel, "Test Scores, Self-Efficacy and the Educational Plans of First-Year College Students", Higher Education in Review, Vol. 2, pp. 63-88, 2005

[14] T. Farsides, R. Woodfield, "Individual Differences and Undergraduate Academic Success: the Roles of Personality, Intelligence and Application", Personality and Individual Differences, Vol. 34, pp.1225-1243, 2003

[15] J. D. A. Parker, L. J. Summerfeldt, J. Marjorie, M. J. Hogan, S. A. Majeski, "Emotional Intelligence and Academic Success: Examining the Transition from High School to University", Personality and Individual Differences, Vol. 36, pp. 163-172, 2004

[16] S. Trapmann, B. Hell, J .O. W. Hirn, H. Schuler, "Meta-Analysis of the Relationship between the Big Five and Academic Success at University", Zeithschrift für Psychologie, Vol. 215, No. 2, pp. 132-151, 2007

[17] L. S. Affendey, I. H. M. Paris, N. Mustapha, N. Sulaiman, Z. Muda, "Ranking of Influencing Factors in Predicting Students' Academic Performance," Information Technology Journal, Vol. 9, No. 4, pp. 832-837, 2010

[18] J. P. Vandamme, N. Meskens, J. F. Superby, "Predicting Academic Performance by Data Mining Methods", Education Economics, Vol. 15, No. 4, pp. 405-419, 2007

[19] V. O. Oladokun, A. T. Adebanjo, O. E. Charles-Owaba, "Predicting Students Academic Performance Using Artificial Neural Network: A Case Study of an Engineering Course", The Pacific Journal of Science and Technology, Vol. 9, No. 1, pp. 72-79, 2008

[20] S. Huang, "Predictive Modeling and Analysis of Student Academic Performance in an Engineering Dynamics Course", Doctoral Dissertation, Utah State University, Logan Utah, 2011

[21] J. M. Braxton, A. S. Hirschy, S. A. McCladon, Understanding and Reducing College Student Departure: ASHE-ERIC Higher Education Report. San Francisco, John Wiley and Sons Inc., 2004

[22] G. D. Kuh, J. Kinzie, J. H. Schuh, E. J. Witt, Student Success in College Creating Conditions That Matter, San Francisco, John Wiley and Sons Inc., 2010

[23] M. L. Upcraft, J. N. Gardner, B. O. Barefoot, Challenging and Supporting the First-Year Student. A Handbook for Improving the First Year of College, San Francisco, John Wiley and Sons Inc., 2005

[24] E. Alpaydın, Introduction to Machine Learning, Cambridge, The MIT Press, 2010

[25] J. A. K. Suykens, J. Vandewalle, "Least Squares Support Vector Machine Classifiers", Neural Processing Letters, Vol. 9, No. 3, pp. 293-300, 1999

[26] D. Tsujinishi, S. Abe, "Fuzzy Least Squares Support Vector Machines for Multi-Class Problems", Neural Networks, Vol. 16, pp. 785-792, 2003

[27] N. B. Karayiannis, S. Behnke, "New Radial Basis Neural Networks and Their Application in a Large-Scale Handwritten Digit Recognition Problem", In L. Jain, A. M. F. Fanelli (eds.) Recent Advances in Artificial Neural Networks: Design and Application. Florida, CRC Press, 2000

[28] R. J. Schilling, J. J. Carroll, A. F. Al-Ajlouni, "Approximation of Nonlinear Systems with Radial Basis Function Neural Networks", IEEE Transactions on Neural Networks, Vol. 12, No. 1, pp. 1-15, 2001

[29] S. Chen, C. F. N. Cowan, P. M. Grant, "Orthogonal Least Squares Learning Algorithm for Radial Basis Function Networks", IEEE Transactions on Neural Networks, Vol. 2, pp. 302-309, 1999

[30] D. S. Yeung, I. Cloete, D. Shi, W. W. Y. Ng, Sensitivity Analysis for Neural Networks, Natural Computing Series, Berlin Heidelberg, 2010

New Resonant Inverter Tuning for Three-Phase Current Source Parallel Resonant Inverters

Alireza Namadmalan[1], Javad Shokrollahi Moghani[2]

[1]Jundi-Shapur University of Technology, Dezful, Iran, namadmalan@jsu.ac.ir
[2]Amirkabir University of Technology, Tehran, Iran, moghani@aut.ac.ir

Abstract: This paper presents a new tuningloop for three-phase current source parallel resonant inverters. The switching frequency is tuned by using a phase-locked loop (PLL) circuit based on a new Phase Detector (PD). In practice, the resonant capacitors and inductors have tolerances that cause different resonant frequency for each phase. This paper shows that a conventional PDcauseshigher voltage stress over switches and DC-link inductor. In the proposed tuning loop, the PLL tracks the average value of the resonant frequencies that reduces the voltage stress. In addition, there is no feedback from the loadcurrents to detect the phase error, which is another advantage of the new method. A laboratory prototype of a three-phase current source parallel resonant half-bridge inverter was built to verify the advantages of the proposed tuning system with operating frequency of 22 kHz.

Keywords: resonant inverter tuning; three-phase current source parallel resonant inverters; phase-locked loop (PLL)

1 Introduction

Resonant Inverters are most commonly used because they provide sinusoidal waveforms with lower harmonics and less EMI problems. A large number of topologies have been developed in this area which can be divided into single-phase and multi-phase structures. Three-phase resonant inverters are widely used in industrial applications. Such applications include high power DC-DC converters, contact-less power transfer systems and multi-phase induction heating systems [1-13].

In comparison with single-phase resonant inverters, the three-phase inverters have a smaller input filter and higher power density. Moreover, the load currents and output voltages have less distortion due to third order harmonics elimination for three-wire structures. Hence, the three-phase resonant inverters have better sinusoidal waveforms in low quality factors (Q<5) which is important in traveling wave induction heating systems [9].

Three-phase current-fed parallel resonant inverters are widely utilized in high voltage and high power DC-DC converters; because they provide higher boosting ratio and they have no current sharing problems. The current source inverters have limited control methods but they are less affected by input voltage ripples and they have short-circuited protection capability [13-20]. Figure 1 shows two possible topologies for three-phase current source parallel resonant inverters with three-wire connection.

Conventionally, PDs measure the phase difference between the voltage and the current of a single resonant tank [21-25]. Hence, a conventional PLL is applicable when the three resonant tanks have a same resonant frequency. However, designing the three resonant tanks without tolerance and frequency deviation is practically impossible. This paper shows that the three-phase current source topologies are sensitive to the tolerances and the systems are unbalanced under no-load and light-load conditions. In addition, the switching losses, DC-link current ripples and voltage stress are increased. The proposed PD tracks the average value of the resonant frequencies that reduces the DC-link current ripples and voltage stress over the switches S_1-S_6.

In a conventional tuning loop, the current of resonant tank is measured for phase error detection. In the new PLL, voltages of the low-side switches are the inputs of the PD and there is no feedback from the output currents. Thus, there is no Current Transformer (CT) or Hall Effect sensor for current sensing, which makes the system simple, more reliable and cost effective. The dynamic behavior of the new tuning loop is simulated in steady state and transient conditions. The proposed PD has similar structure for the two topologies, as shown in Figure 1. For simplicity, the laboratory prototype is implemented based on the half-bridge inverter.

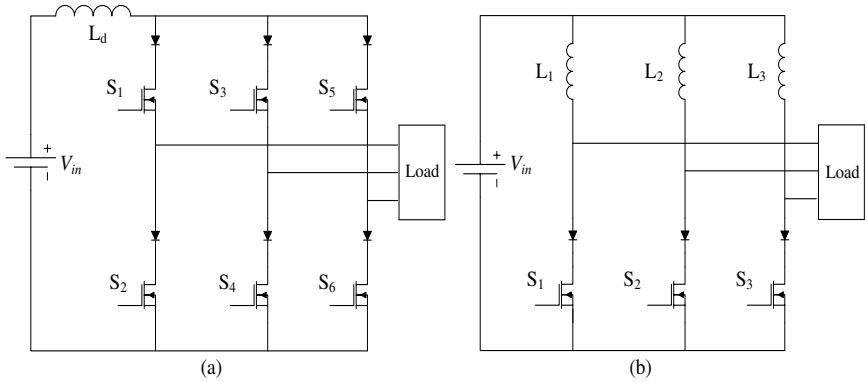

Figure 1

Three-phase current source parallel resonant topologies: (a) the full-bridge inverter; (b) the half-bridge inverter

2 System Description

Figure 2 shows the half-bridge topology with a star-connected resonant tank. The performance of the resonant inverter tuning is similar for the half-bridge and full-bridge inverters. In the both cases, each switch conducts 120 degrees to achieve Zero Voltage and Zero Current Switching (ZVZCS) at the resonant frequency. The half-bridge inverter has asymmetrical current injection while the full-bridge inverter has symmetrical current injection.

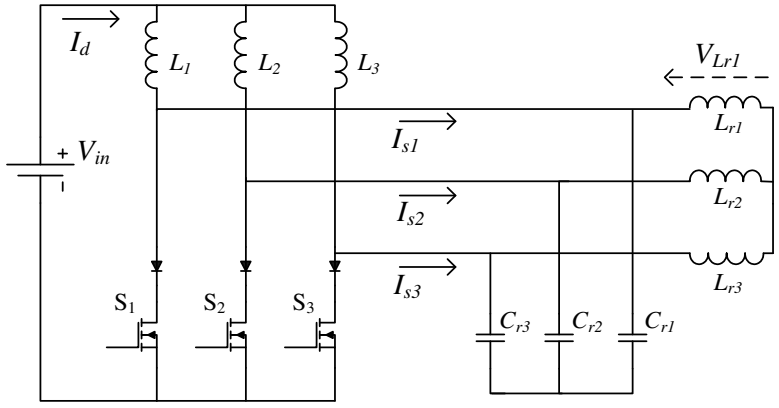

Figure 2
The half-bridge inverter with star-connected resonant tank

Figure 3 shows the three-step operation of the half-bridge inverter where each switch conducts for 120 degrees of the switching period. Each switch is connected in series with a blocking diode to prevent the internal body diode of the switches from short circuit. Operation of the inverters is investigated with and without the tolerances as follows:

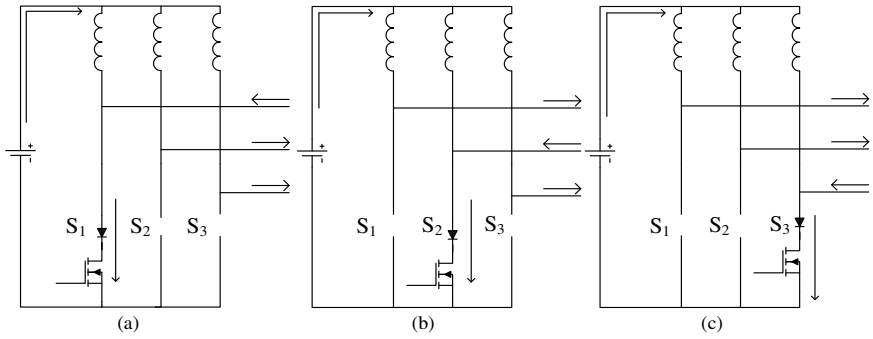

Figure 3
Three-step operation of the half bridge inverter

2.1 Operation without the Tolerances

In this section, the parameters of the inverter are considered with no tolerance. Hence, the three resonant tanks have a similar resonant frequency. The inductance of L_1, L_2 and L_3 (L_d for full-bridge inverter as seen from Figure 1) are much larger than the resonant inductors ($L_{r1} = L_{r2} = L_{r3} = L_r$), so under normal steady state operation the DC-link current, I_d, is approximately constant.

Regarding Figure 3, voltage of S_1 is derived by equation (1) for a switching period duration while the converter works at the resonant frequency. The ω_r, T_s, C_r and V_m are the angular resonant frequency, switching period, per-phase resonant capacitor and phase-phase voltage of the inverter.

$$\begin{aligned} &V_{S1} = 0, && 0 < t < \frac{T_s}{3} \\ &V_{S1} = V_m sin(\omega_r t - \frac{2\pi}{3}), && \frac{T_s}{3} < t < \frac{2T_s}{3} \quad , \ \omega_r = 2\pi f_r = \frac{1}{\sqrt{L_r C_r}} \\ &V_{S1} = -V_m sin(\omega_r t), && \frac{2T_s}{3} < t < T_s \end{aligned} \tag{1}$$

For the half-bridge inverters, the amplitude of the phase-phase voltage, V_m, is derived by employing the inductor volt-second balance principle on L_1, where V_{in} is the DC-link voltage. Similarly, V_m is derived by equation (3) for the full-bridge inverters by employing the inductor volt-second balance principle on L_d.

$$\int_0^{2\pi} V_{L1} d\theta = \int_0^{\frac{2\pi}{3}} V_{in} d\theta + \int_{\frac{2\pi}{3}}^{\frac{4\pi}{3}} [V_{in} - V_m sin(\theta - \frac{2\pi}{3})] d\theta + \int_{\frac{4\pi}{3}}^{2\pi} [V_{in} + V_m sin(\theta)] d\theta = 0 \tag{2}$$

$$\rightarrow V_m = \frac{2\pi}{3} V_{in}$$

$$V_m = \frac{\pi}{3} V_{in} \tag{3}$$

Figure 4 shows per-phase equivalent circuit of the resonant inverter and R is the per-phase load resistance. According to 120^0 conduction, the I_{s1} and voltage of S_1 are shown in Figure 5 for the full-bridge and half bridge topologies at the resonant frequency. For the both topologies, the peak voltage of the switches is the amplitude of the phase-phase voltage or V_m. The DC-link voltage, V_{in}, of the two topologies is 50 V. As seen from Figure 5(b), the injected current of the full-bridge inverter has no third order harmonics. Hence, the inverter have lower THD of current for low quality factor operations (Q<5), in comparison with single-phase topologies [14-20].

The quality factor of the parallel resonant load is derived by equation (4). For the half-bridge topology, the injected current has second order harmonics and is suitable for high quality factor operations. In addition, the half-bridge topology is useful for high boosting ratio converters, as shown in equation (2).

$$Q = \frac{R}{\omega_r L_r} \tag{4}$$

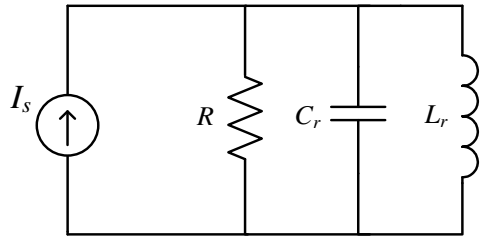

Figure 4

Single-phase equivalent circuit of the resonant tank and the inverter

Let's consider that the switching frequency of the inverter is greater (or smaller) than the resonant frequency. Hence, there is a phase difference, β, between the injected current, I_s, and voltage of the tank circuit. Figure 6 shows the phase plot of a parallel resonant tank with quality factor of10 and resonant frequency of 25 kHz. The phase plot represents the phase difference β between the injected current I_s and the resonant tank voltage for different switching frequencies.

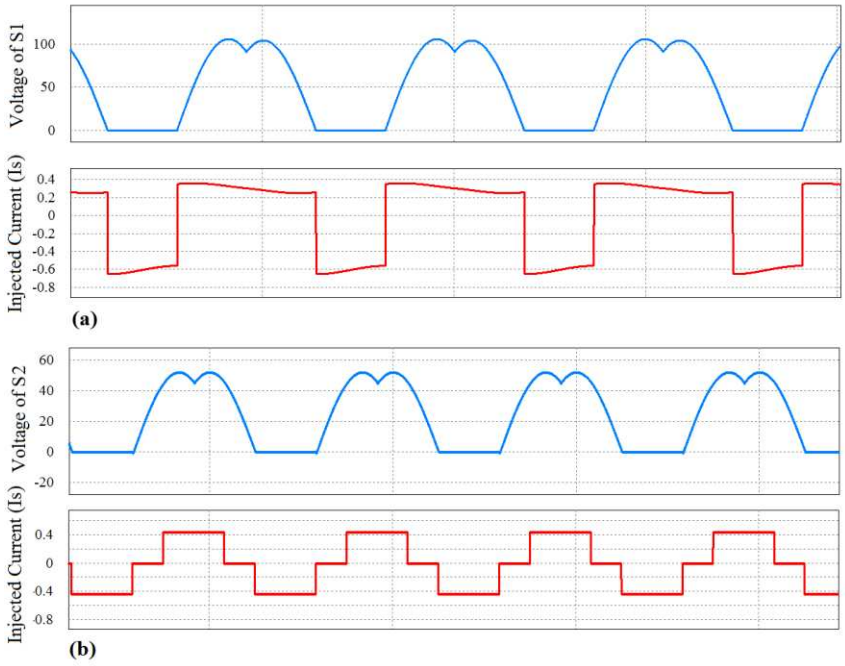

Figure 5

The voltage of S_1 and the injected current connected to S_1, I_{s1}: (a) for the half-bridge inverter; (b) voltage for the full-bridge inverter

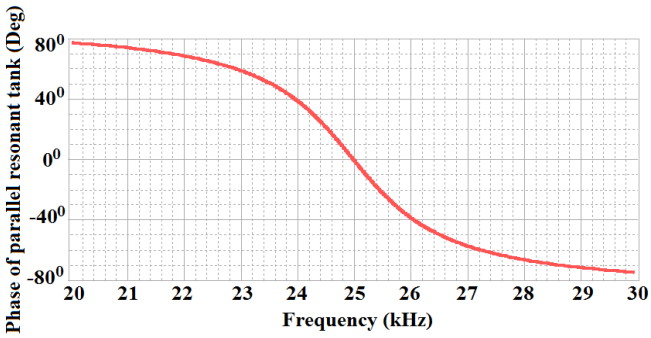

Figure 6

Phase plot of a parallel resonant tank with quality factor of 10

Figure 7 shows the voltage of S_1 and the phase difference β for two conditions (over and under the resonant frequency). Regarding equation (2), the peak value of the phase-phase voltage, V_m, is rewritten as follows:

$$\int_0^{2\pi} V_{L1}d\theta = \int_0^{\frac{2\pi}{3}} V_{in}d\theta + \int_{\frac{2\pi}{3}}^{\frac{4\pi}{3}} [V_{in} - V_m \sin(\theta - \frac{2\pi}{3} + \beta)]d\theta + \int_{\frac{4\pi}{3}}^{2\pi} [V_{in} + V_m \sin(\theta + \beta)]d\theta = 0 \qquad (5)$$

$$\rightarrow V_m = \frac{2\pi}{3\cos\beta} V_{in}$$

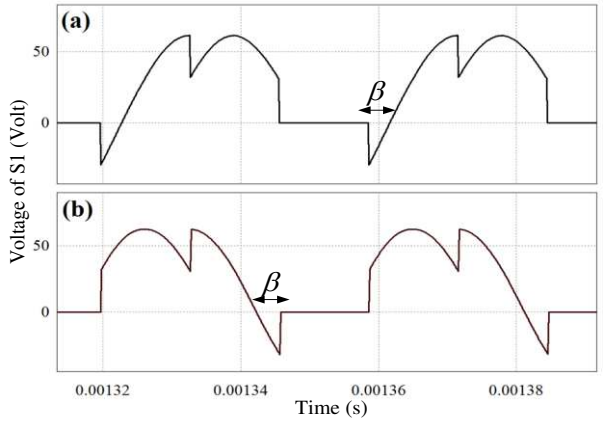

Figure 7

Voltage of S_1 at the two different conditions: (a) over the resonant frequency; (b) under the resonant frequency

Forthe full-bridge topology, the equation (5) is rewritten as follows:

$$\rightarrow V_m = \frac{\pi}{3\cos\beta} V_{in}$$

2.2 Operation with the Tolerances

Let's consider that each resonant tank has different parameters (different L_r and C_r). Hence, the frequency deviation Δf caused by the tolerances is derived as follows:

$$\Delta f = \frac{\partial f_r}{\partial L_r}\Delta L_r + \frac{\partial f_r}{\partial C_r}\Delta C_r = -\frac{1}{4\pi\sqrt{L_r C_r}}\left(\frac{\Delta L_r}{L_r} + \frac{\Delta C_r}{C_r}\right) \Rightarrow \Delta f = -\frac{f_r}{2}\left(\frac{\Delta L_r}{L_r} + \frac{\Delta C_r}{C_r}\right) \tag{6}$$

Figure 8(a) and Figure 8(b) show the phase plot of the three parallel resonant tanks with quality factors of 10 and 2, respectively. The frequency deviations for the resonant tanks1 to 3 are assumed to be 0%, +3% and -3%, respectively. The average value of the three resonant frequencies (f_{r1}, f_{r2} and f_{r3}) is 25 kHz.

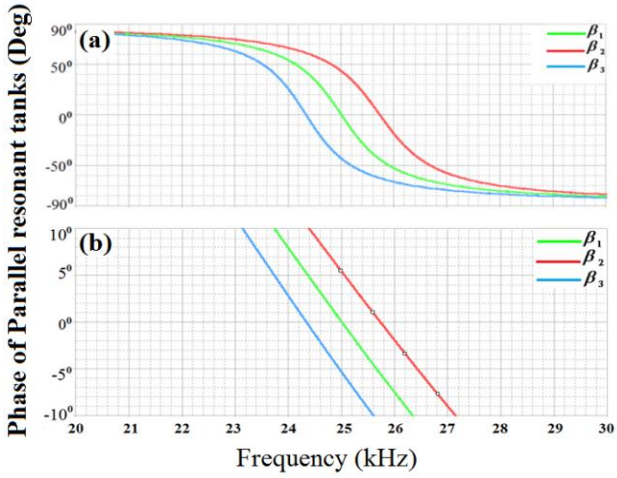

Figure 8

The phase plot of three parallel resonant tanks: (a) quality factor of 10; (b) quality factor of 2

According to equation (2), the phase-phase voltages of the resonant tanks are derived by solving the equations (7) through (9):

$$\int_0^{2\pi} V_{L1}d\theta = \int_0^{\frac{2\pi}{3}} V_{in}d\theta + \int_{\frac{2\pi}{3}}^{\frac{4\pi}{3}} [V_{in} - V_{m2}\sin(\theta - \frac{2\pi}{3} + \beta_2)]d\theta + \int_{\frac{4\pi}{3}}^{2\pi} [V_{in} + V_{m3}\sin(\theta + \beta_3)]d\theta = 0 \tag{7}$$

$$\int_0^{2\pi} V_{L2}d\theta = \int_0^{\frac{2\pi}{3}} V_{in}d\theta + \int_{\frac{2\pi}{3}}^{\frac{4\pi}{3}} [V_{in} - V_{m3}\sin(\theta - \frac{2\pi}{3} + \beta_3)]d\theta + \int_{\frac{4\pi}{3}}^{2\pi} [V_{in} + V_{m1}\sin(\theta + \beta_1)]d\theta = 0 \tag{8}$$

$$\int_0^{2\pi} V_{L3}d\theta = \int_0^{\frac{2\pi}{3}} V_{in}d\theta + \int_{\frac{2\pi}{3}}^{\frac{4\pi}{3}} [V_{in} - V_{m1}\sin(\theta - \frac{2\pi}{3} + \beta_1)]d\theta + \int_{\frac{4\pi}{3}}^{2\pi} [V_{in} + V_{m2}\sin(\theta + \beta_2)]d\theta = 0 \tag{9}$$

$$\rightarrow \begin{cases} V_{m2}\cos(\beta_2-\frac{\pi}{6})+V_{m3}\cos(\beta_3+\frac{\pi}{6})=\frac{2\pi}{\sqrt{3}}V_{in} \\ V_{m3}\cos(\beta_3-\frac{\pi}{6})+V_{m1}\cos(\beta_1+\frac{\pi}{6})=\frac{2\pi}{\sqrt{3}}V_{in} \\ V_{m1}\cos(\beta_1-\frac{\pi}{6})+V_{m2}\cos(\beta_2+\frac{\pi}{6})=\frac{2\pi}{\sqrt{3}}V_{in} \end{cases} \quad (10)$$

TheV_{L1}, $V_{L2}$and$V_{L3}$are voltage of the DC-link inductors (L_1, L_2 and L_3). According to Figure 2, the V_{m1}, V_{m2} and $V_{m3}$are equal to the following values:

$$\begin{cases} V_{m1}=V_{Lr1}-V_{Lr2} \\ V_{m2}=V_{Lr2}-V_{Lr3} \\ V_{m3}=V_{Lr3}-V_{Lr1} \end{cases} \quad (11)$$

V_{Lr1}, V_{Lr2} and V_{Lr3} are the voltage ofthe resonant inductors shown in Figure 2. By solving the equation set (10), the phase-phase voltages are derived as a function of β_1, β_2, β_3 and V_{in}. For the full-bridge inverter, the equation set (10) can be rewritten by employing the inductor volt-second balance principle on$L_d$and considering the following complex equation:

$$V_{m1}\,exp(j\beta_1)+V_{m2}\,exp(j\beta_2-j\frac{2\pi}{3})+V_{m3}\,exp(j\beta_3+j\frac{2\pi}{3})=0\ ,\quad j=\sqrt{-1} \quad (12)$$

Figure 9 shows the phase-phase voltages of the full-bridge inverter with frequency deviations. In this figure, the resonant frequencies, f_{r1}, f_{r2} and f_{r3} are 25 kHz, 26.5 kHz and 25 kHz, respectively (+6% deviations for f_{r2}). The quality factor of each resonant tank is approximately 20 and the DC-link voltage, V_{in}, is 50 V. In Figure 9(a), a conventional PLL tracks the resonant frequency of f_{r2} at steady state condition, hence the switching frequency is 26.5 kHz.

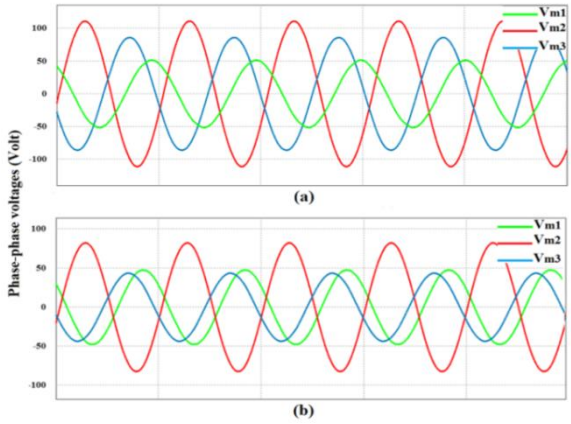

Figure 9

Phase-phase voltage of full bridge parallel resonant inverter: (a) the switching frequency is 26.5 kHz; (b) the switching frequency is 25.5 kHz

Figure 9(b) shows the phase-phase voltages of the full-bridge inverter with the same tolerances. In Figure 9(b), the PLL tracks the average value of the three resonant frequencies, 25.5 kHz, by using the proposed PLL.

Comparing Figure 9(a) and Figure 9(b), it can be concluded that the voltage stress of the inverter is reduced by 20% when the switching frequency is equal to the average value of the resonant frequencies, 25.5 kHz. Hence, for high quality factor (or light-load) conditions (Q>5), the voltage stress of the inverter is significant when the resonant inverter tuning is based on single-phase tuning or conventional PD's.

It can be proven that the minimum value of the voltage stresses occurs when the equation (13) is satisfied. The equation (13) shows a condition that the switching frequency is set to the average value of the resonant frequencies. In the next section, this condition and the performance of the proposed PLL are described in more details.

$$min\{max(V_{m1},V_{m2},V_{m3})\} \Leftrightarrow \beta_1+\beta_2+\beta_3=0 \tag{13}$$

Without loss of generality, consider that the switching frequency of the inverter is tuned by using a conventional PLL that tracks the resonant frequency of f_{r1}. Regarding equations (10) through (13), there is extra voltage stress. The extra stress is maximum for nonsymmetrical tolerances (e.g. ±0 %, ±0 % and ±6 %), and is minimum for symmetrical tolerances (e.g. +3%, -3% and ±0%). The voltage stress increases the current ripples of the DC-link inductor and decreases the net efficiency. The extra voltage stress is suppressed by using the proposed method, which satisfies the equation (13).

Figure 10 shows the stress reduction (in percentage) of the proposed technique for different quality factors and for nonsymmetrical and symmetrical tolerances. Figure 11 shows the voltage of the DC-link inductorwhen the full-bridge inverter is tuned by the conventional and proposed methods at quality factor of about 10 and nonsymmetrical tolerances. Regarding Figure 10 and Figure 11, the DC-link ripples are more affected by the voltage stress for a specific quality factor and frequency deviation.

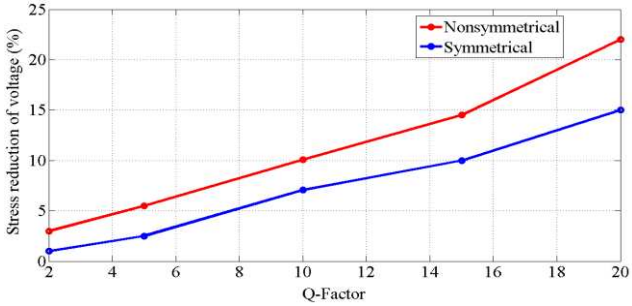

Figure 10

Percentage of stress reduction for the symmetrical and nonsymmetrical tolerances

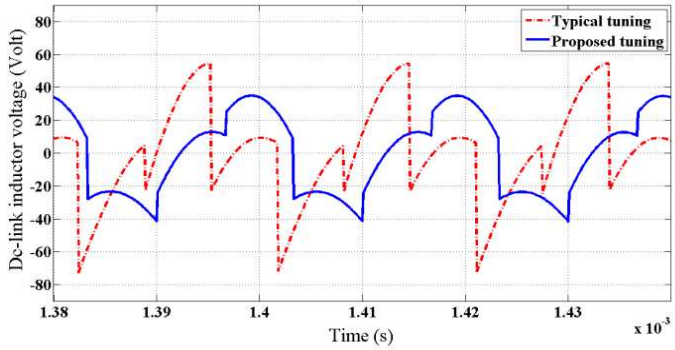

Figure 11

Voltage of DC-link inductor for the proposed and conventional techniques at quality factor of 10 for the full-bridge topology

Forlow quality factors, the system approximately works like a balanced three-phase system because the phase deviations are negligible, see Figure 8(b) and equation set (10). However, the switching frequency should be equal to the average value of the resonant frequencies to minimize the switching losses, negative sequences and DC-link current ripples.

3 The Proposed Resonant Inverter Tuning

PLL circuit consists of a Voltage Controlled Oscillator (VCO), Phase Detector (PD) and a Loop Filter (LF). There are three important parameters for a PLL circuit: VCO's gain K_V, center frequency f_c and LF parameters [25]. In this paper, the LFs are *RC* filterswith time constant of τ.

A three-phase PD is proposed which only uses the voltage of the switches and has no current sensor in the tuning loop. The PD directly connects to LF units to build a Multiplier PD mode [23-25]. To construct the three-phase PD, voltages of S_1, S_2, and S_3 (V_{S1}, V_{S2} and V_{S3}) are passed through comparators and then connected to a logic circuit to produce the phase error signals. According to comparators, the voltage of the switches are saturated in both positive and negative values to produce V_{S1+}, V_{S1-}, V_{S2+}, V_{S2-}, V_{S3+} and V_{S3-}. Figure 12(a) shows waveforms of V_{S1}, $V_{S1-}$and V_{S1+} when the inverter works at over the resonant frequency. Figure 12(b) and 12(c) show the voltage of the switches at over and under the resonant frequency for thehalf-bridge inverter and input voltage of 25 V.

Regarding Figure 12, the phase differences (β_1, β_2 and β_3) aresimplyproduced by using AND gates. For instance, to produce the β_1 when the inverter works at over the resonant frequency (or $\beta_1 < 0$),V_{S1-} and V_{S3+} are the inputs of the AND gate, see Figure 12(b).

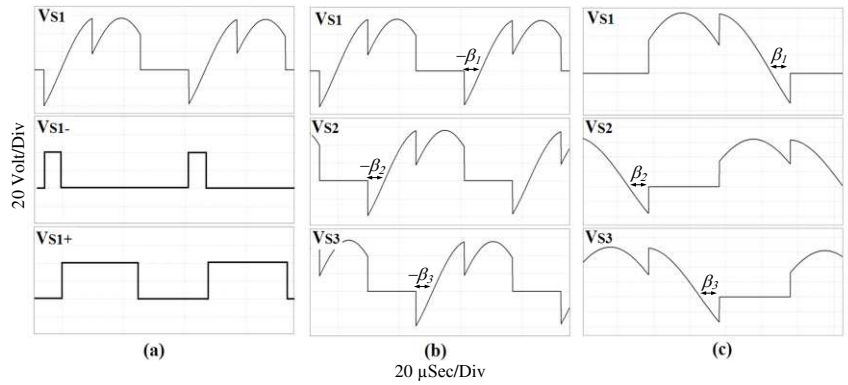

Figure 12

Switches' voltages: (a) voltage of S_1 and its positive and negative duration; (b) voltage of switches at over the resonant frequency; (c) voltage of switches at under the resonant frequency

Equation (14) shows the relationships between β_1 and voltage of the switches. The output of the AND gates are passed through Loop Filters (LF) to remove high frequency components.

$$\begin{cases} x_1 = V_{S1-} \,\&\, V_{S3+} = \beta_1 & , \quad \beta_1 < 0 \\ x_1 = V_{S1-} \,\&\, V_{S3+} = 0 & , \quad \beta_1 \geq 0 \\ x_2 = V_{S1-} \,\&\, V_{S2+} = 0 & , \quad \beta_1 \leq 0 \\ x_2 = V_{S1-} \,\&\, V_{S2+} = \beta_1 & , \quad \beta_1 > 0 \end{cases} \rightarrow \beta_1 = x_2 - x_1 \tag{14}$$

To produce the three-phase PD signals, there are six AND signals,$x_1 \ldots x_6$, which are implemented to produce the phase differences as follows:

$$\begin{cases} x_1 = V_{S1-} \,\&\, V_{S3+}\,,\; x_2 = V_{S1-} \,\&\, V_{S2+} & for\ \beta_1 \\ x_3 = V_{S2-} \,\&\, V_{S1+}\,,\; x_4 = V_{S2-} \,\&\, V_{S3+} & for\ \beta_2 \\ x_5 = V_{S3-} \,\&\, V_{S2+}\,,\; x_6 = V_{S3-} \,\&\, V_{S1+} & for\ \beta_3 \end{cases} \tag{15}$$

According to (15) and Figure 12, the output of phase detector, α is derived as follows:

$$\alpha = (\beta_1 + \beta_2 + \beta_3) = [(x_2 + x_4 + x_6) - (x_1 + x_3 + x_5)] \tag{16}$$

Figure 13 shows the proposed PD circuit with VCO and LF units. To analyze the performance of the PLL, the phase plot of thetank circuits must be linearized at their resonant frequencies as follows [21-23].

$$K_{\beta i} = -\frac{\partial \beta_i (j2\pi f)}{\partial f}\Big|_{f=f_{ri}} \tag{17}$$

The $K_{\beta 1}$, $K_{\beta 2}$ and $K_{\beta 3}$ are the slope of the phase curves near their resonant frequencies in rad/Hz. According to Figure 8 and considering that the deviations are below 3%, theslopes are similar for $|\beta_i| < 30^0$.

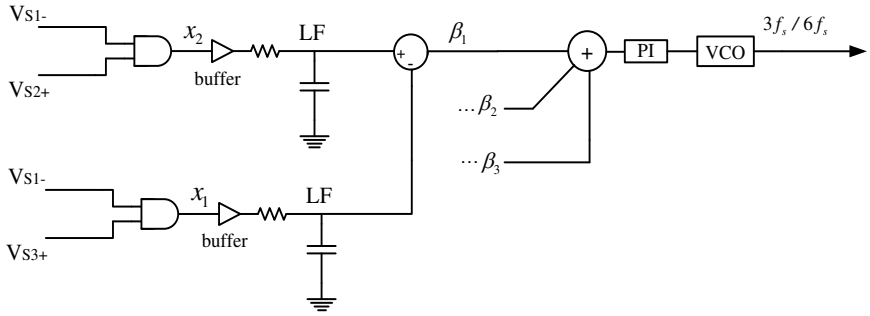

Figure 13
The proposed three-phase PD with VCO and LF units

$$\rightarrow \boldsymbol{K}_{\beta 1} = \boldsymbol{K}_{\beta 2} = \boldsymbol{K}_{\beta 3} = \boldsymbol{K}_{\beta}$$

Therefore, the phase differencescan be derived by equation (18) as follows:

$$\begin{aligned} \beta_1 &= K_\beta (f_{r1} - f_s) \\ \beta_2 &= K_\beta (f_{r2} - f_s) \\ \beta_3 &= K_\beta (f_{r3} - f_s) \end{aligned} \tag{18}$$

The f_s is the switching frequency of the inverter. Hence, the equation (16) is rewritten as follows:

$$\alpha = K_\beta (f_{r1} + f_{r2} + f_{r3}) - 3K_\beta f_s \tag{19}$$

At steady state condition, α isapproximately zero and hence, the switching frequency is derived as follows:

$$\alpha \to 0 \Leftrightarrow f_s = \frac{(f_{r1} + f_{r2} + f_{r3})}{3} \tag{20}$$

By designing a proper PI controller, αis close to zero at steady state condition. According to (20), the proposed PLL tracks the average value of the resonant frequencies. As seen from Figure 14, the output of the PD is passed through the PI controller. The output of the controller is connected to the VCO unit. According to Figure 12 and equation (16), it is worth noting that the high frequency component of the proposed PD is six times the switching frequency (or three times the conventional PD's) [21-25]. Therefore, the proposed method has fast dynamics and the tuning process occurs in less cycles.

Due to three-pulse and six-pulse operation of the half-bridge and full-bridge inverters, the center frequency of the PLL must be close to three times and six times of the resonant frequency. Figure 14 shows the switching sequences for 120^0 conduction mode for full-bridge and half-bridge topologies. Finally, the output of the VCO is connected to a sequential circuit to produce the proper switching sequences.

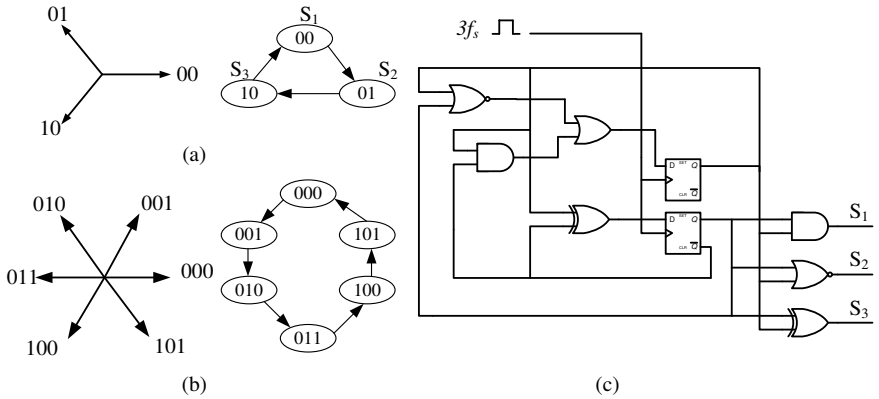

Figure 14

(a) The three-step performance of sequential circuitfor half-bridge inverter; (b) six-step performance of sequential circuitfor full-bridge inverter; (c) the sequential circuit used for half-bridge inverter

Figure 14(c) shows the proposed sequential circuit for the half-bridge topology. To show the PLL dynamics, simulation results are carried out by PSIM simulator for the half-bridge topology. The parameters of the inverter and the PLL are listed in Table 1. Figure 15(a) shows the voltage of $S_1$and the PLL dynamics at start-up. Figure 15(b) shows output signal of the phase detector controller (or input signal of the VCO unit) at start-up. In these figures, the center frequency f_c of the PLL is 65 kHz, which is approximately three times the resonant frequency. According to the resonant frequency, the final frequency of the VCO unit is close to 66 kHz.

In this simulation, the tolerances are less than 3% and the average value of the resonant frequencies is about 22 kHz. The parameters of the PI controller are set to achieve better dynamics. This simulation is done without power regulator. However, by using a power regulator, the voltage stresses of the switches are significantly reduced at start-up,as in [24]. As seen from Figure 15, the output voltage of the controller has three steps for each switching period, which is three times faster thanconventional PD's [21-25].

Table 1

Simulation parameters

Resonant tank parameters		Inverter Parameters		PLL specifications	
C_r	330nF	$L_{1,2,3}$	600µH	f_c	65 kHz
Q	≈ 5	V_{in}	50V	$\frac{P}{I}$	K_I= 5.5×10^4, K_P = 20
L_r	150µH	-	-	τ	330µSec
f_r	≈ 22 kHz	-	-	K_V	1000 (Hz/Volt)

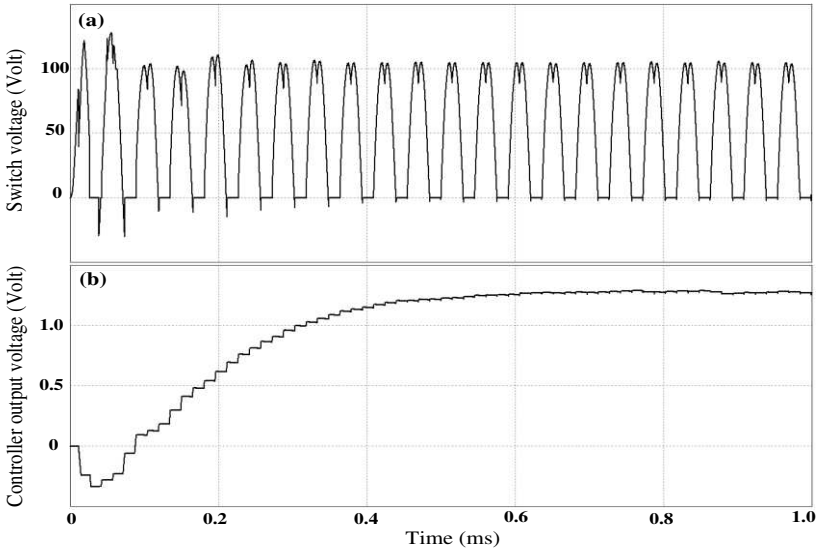

Figure 15

(a) Voltage of S_1 at start-up condition; (b) output signal of the PI controller at start-up condition

4 Experimental Results

A half-bridge inverterwas built and the performance of the inverter with the new PLL was investigated with operating frequency of 22 kHz. As mentioned, the structure of the PDis similar for the full-bridge and half-bridge inverters and the half-bridge topology is implementedfor simplicity. The parameters of the inverter and the PLL are listed in Table 2. In this prototype, the quality factor of the resonant tanks is investigated for 20 and 3. The quality factor of 20 is considered for the no-load condition. The center frequency of VCO is about 65 kHz for operating frequency of about 22 kHz.

Tolerance of theresonant inductor, L_r, is less than 1% and the resonant capacitors are metalized polypropylene film capacitor with maximum tolerance of 5%. Therefore, according to (6), the maximum frequency deviationis less than 3% for each resonant tank. In this prototype, the equivalent load resistances are in series with resonant inductors for mentioned quality factors.

Figure 16(a) shows the performance of the new PLL at start-up condition. In this figure, the PLL's center frequency is 65 kHz, which is approximately three times the average value of the resonant frequencies. The steady state switching frequency (or averaged value of three resonant frequencies) is about 22 kHz at quality factor of 20.

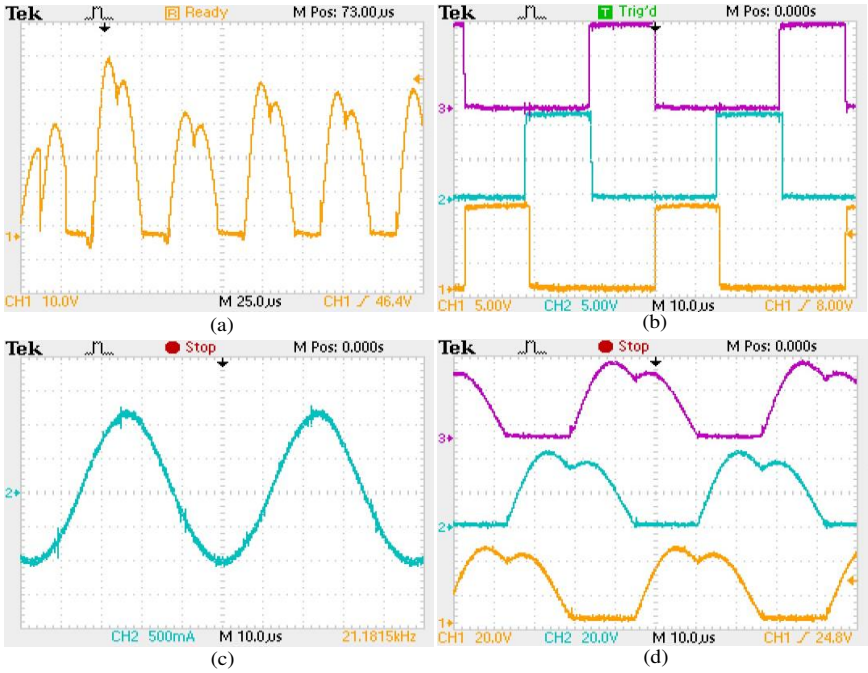

Figure 16

(a) Voltage of S_1 at start-up condition by using the proposed tuning loop and input voltage of 20 V (10 volt/div); (b) gate to source voltage of the switches, (5 volt/div); (c) resonant tank current at quality factor of about 3, (500mA/div); (d) voltage of the switches at steady state condition and input voltage of 20 V and quality factor of about 3, (20 volt/div)

Table 2

Inverter and PLL parameters

Load parameters		Inverter Parameters		PLL specifications	
C_r	≈ 330 nF	$L_{1,2,3}$	600 µH	f_{center}	≈ 65 kHz
Q	≈ 20 and 3	*Series diodes*	BY399	PI	$K_I \approx 6\times10^4$, $K_P \approx 15$
L_r	≈ 150 µH	Switches	IRFP540	τ	1000 µSec
f_r	≈ 22 kHz	Gate drivers	ICL7667	K_V	1000 (Hz/Volt)

The PI controller of the PLL circuit is designed to achieve minimum phase error at steady state condition while the transient response is suitable. The optimum parameters of the PI controller are listed in Table 2. Figure 16(b) and (d) show the gating signals and the voltage of the switches at quality factor of about 3 with 3% deviation. Figure 16(c) shows resonant tank current connected to S_1 at the quality factor of 3 and output power of about 50 W. Figure 17 shows the laboratory prototype of the current source parallel resonant half-bridge inverterwith the resonant inductors and capacitors.

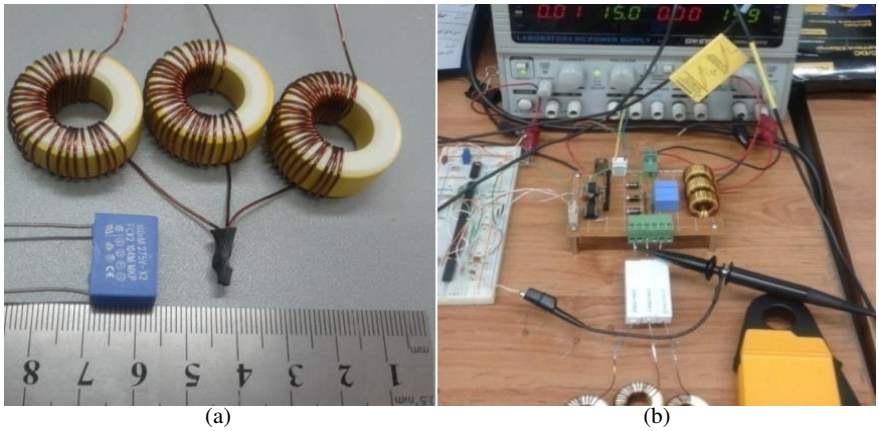

(a) (b)

Figure 17

(a) The three resonant inductors and the resonant capacitor; (b) laboratory prototype of the current source parallel resonant half-bridge inverter

Conclusion

In this paper, a new PLL circuit is proposed for three-phase current source parallel resonant inverters. The new PLL tracks the average value of three resonant frequencies according to the new phase detector performance. This helps to achieve less voltage stresses on the switches and lower distortions in DC-link current. The PLL is investigated in multiplier phase and frequency mode to achieve fast dynamics at transients. The new tuning circuit uses only the voltage of the switches to detect the phase error and there is no feedback from the load currents. Therefore, the circuit is simple, more reliable and cost effective. The new PLL can be used for both full-bridge and half-bridge topologies while the sequential circuit difference must be taken in consideration.

References

[1] H. R. E. Larico and I. Barbi: Three-Phase Weinberg Isolated DC–DC Converter: Analysis, Design, and Experimentation, IEEE Transaction on Industrial Electronics, Vol. 59, No. 2, 2012, pp. 888-896

[2] G. A. Covic, J. T. Boys, M. L. G. Kissin and H. G. Lu: A Three-Phase Inductive Power Transfer System for Roadway-Powered Vehicles, IEEE Transaction on Industrial Electronics, Vol. 54, No. 6, 2007, pp. 3370-3378

[3] S. V. G. Oliveira and I. Barbi: A Three-Phase Step-Up DC–DC Converter With a Three-Phase High-Frequency Transformer for DC Renewable Power Source Applications, IEEE Transaction on Industrial Electronics, Vol. 58, No. 8, 2011, pp. 3567-3580

[4] P. Alotto, A. Spagnolo and B. Paya: Particle Swarm Optimization of a Multi-Coil Transverse Flux Induction Heating System, IEEE Transaction on Magnetics, Vol. 47, No. 5, 2011

[5] J. Egalon, S. Caux, P. Maussion, M. Souley and O. Pateau: Multiphase System for Metal Disc Induction Heating: Modeling and RMS Current Control, IEEE Transaction on Industrial Application, Vol. 48, No. 5, pp. 1692-1699, 2012

[6] M. Daigavane, H. Suryawanshi and J. Khan: A Novel Three Phase Series-Parallel Resonant Converter Fed DC-Drive System, Journal of Power Electronics, Vol. 7, No. 3, 2007, pp. 22-232

[7] H. Matsumoto, Y. Neba, K. Ishizaka and R. Itoh: Model for a Three-Phase Contactless Power Transfer System, IEEE, Transaction on Power Electronics, Vol. 26, No. 9, 2011, pp. 2676-2687

[8] R. L. Andersen and I. Barbi: A Three-Phase Current-Fed Push–Pull DC–DC Converter, Transaction on Power Electronics, Vol. 24, No. 2, 2011, pp. 358-368

[9] L. Pang, Y. Wang and T. Chen: New development of traveling wave induction heating, IEEE. Transaction on Applied Superconductivity, Vol. 20, No. 3, 2010, pp. 1013-1016

[10] Y. Hwang, B. Hwang, H. Lin and J. Chen: PLL-based Contactless Energy Transfer Analog FSK Demodulator using High Efficiency Rectifier, IEEE Transaction on Industrial Electronics, Vol. 60, No. 1, 2013, pp. 280-290

[11] R. L. Lin and C. H. Wen: Three-Phase Electronic Ballast with Current-Equalization Function, Journal of Display Technology, Vol. 2, No. 4, pp. 378-385, 2006

[12] Z. Wang and H. Li: A Soft Switching Three-Phase Current-fed Bidirectional DC-DC Converter with High Efficiency over a Wide Input Voltage Range, IEEE Transaction on Power Electronics, Vol. 27, No. 2, 2012, pp. 669-684

[13] S. Lee, J. Park and S. Choi: A Three-Phase Current-Fed Push–Pull DC–DC Converter With Active Clamp for Fuel Cell Applications, IEEE Transaction on Power Electronics, Vol. 26, No. 8, 2011, pp. 2266-2277

[14] S. K. Changchien, T. J. Liang, J. F. Chen and L. S. Yang: Novel High Step-Up DC–DC Converter for Fuel Cell Energy Conversion System, IEEE Transaction on Industrial Electronics, Vol. 57, No. 6, 2010, pp. 2007-2017

[15] J. M. Kwon, E. H. Kim, B. H. Kwon and K. H. Nam: High-Efficiency Fuel Cell Power Conditioning System With Input Current Ripple Reduction, IEEE Transaction on Industrial Electronics, Vol. 56, No. 3, 2009, pp. 826-834

[16] B. Yuan, X. Yang, X. Zeng, J. Duan, J. Zhai and L. Donghao: Analysis and Design of a High Step-up Current-Fed Multiresonant DC–DC Converter With Low Circulating Energy and Zero-Current Switching for All Active Switches, IEEE Transaction on Industrial Electronics, Vol. 59, No. 2, 2012, pp. 964-978

[17] R. Casanueva, C. Brañas, F. J. Azcondo and F. J. Díaz: Teaching Resonant Converters: Properties and Applications for Variable Loads, IEEE Transaction on Industrial Electronics, Vol. 57, No. 10, 2010, pp. 3355-3363

[18] S. Jalbrzykowski and T. Citko: Current-Fed Resonant Full-Bridge Boost DC/AC/DC Converter, IEEE Transaction on Industrial Electronics, Vol. 55, No. 3, 2008, pp. 1198-1205

[19] A. L. Shenkman, B. Axelord and V. Chudnovsky: A New Simplified Model of the Dynamics of the Current-Fed Parallel Resonant Inverter, IEEE Transaction on Industrial Electronics, Vol. 47, No. 2, 2000, pp. 282-286

[20] M. K. Kazimierczuk, A. Abdulkarim: Current-Source Parallel-Resonant DC/DC Converter, IEEE Transaction on Industrial Electronics, Vol. 42, No. 2, 1995, pp. 199-208

[21] N. Margaris and V. Petridis: Voltage Pump Phase-locked Loops, IEEE Transaction on Industrial Electronics, Vol. 32, No. 1, 1985, pp. 41-49

[22] A. Namadmalan and J. S. Moghani: Tunable Self-Oscillating Switching Technique for Current Source Induction Heating Systems, IEEE, Transaction on Industrial Electronics, Vol. 61, No. 1, 2014, pp. 2556-2563

[23] H. Karaca and S. Kılınç: Nonlinear Modeling and Analysis of Resonant Inverter Tuning Loops with Voltage-Pump Phase-Frequency Detector, IEEE, Transaction on Power Electronics, Vol. 20, No. 5, 2005, pp. 1100-1108

[24] A. Namadmalan, J. S. Moghani and J. Milimonfared: A Current-fed Parallel Resonant Push-Pull Inverter with a New Cascaded Coil Flux Control for Induction Heating Applications, Journal of Power Electronics, Vol. 11, No. 5, 2011

[25] G. C. Hsieh and J. C. Hung: Phase-Locked Loop Techniques-A Survey, IEEE, Transaction on Industrial Electronics, Vol. 43, No. 6, 1996